

Solar Probe Plus

Report of the Science and Technology Definition Team (STDT)

PRE-PUBLICATION VERSION

February 14, 2008

Table of Contents

Solar Probe + Science and Technology Definition Team	iv
Executive Summary	ES-1
Our First Visit to a Star	ES-1
Solar Probe+ Science Objectives	ES-3
Baseline Mission	ES-5
Payload and Spacecraft	ES-5
Solar Probe+ and Human Exploration	ES-6
Summary	ES-7
1. Solar Probe+ and Human Exploration	1-1
2. Solar Probe+: Science Objectives and Measurements Requirements	2-1
2.1 Determine the structure and dynamics of the magnetic fields at the sources of the fast and slow solar wind	2-2
2.2 Trace the flow and elucidate the thermodynamics of the energy that heats the solar corona and accelerates the solar wind	2-11
2.3 What mechanisms accelerate and transport energetic charged particles?	2-20
2.4 Explore dusty plasma phenomena and their influence on the solar wind and energetic particle formation	2-27
3. Science Implementation	3-1
3.1 Minimum Criterion for Success	3-1
3.2 Baseline Payload	3-2
3.3 Supporting Scientific Activities	3 -11
4.0 Mission Implementation	4-1
4.1 Baseline Mission Design	4-2
4.2 Mission Concept of Operations	4-5
4.3 Mission Environment	4-7
4.4 Spacecraft Overview	4-9

4.5 Mechanical Design	4-12
4.6 Thermal Protection System	4-14
4.7 Thermal Control System	4-16
4.8 Power Subsystem	4-18
4.9 Avionics	4-23
4.10 Telecommunications	4-25
4.11 Data Management	4-27
4.12 Guidance and Control System	4-29
4.13 Propulsion System	4-31
4.14 Technical Challenges	4-32
5.0 References	5-1
Appendix A: Mass and Power Tables	
Appendix B: Environmental Mitigation	
Appendix C: Acronyms	

Solar Probe Science and Technology Definition Team

D. J. McComas, Chair
Southwest Research Institute
San Antonio, Texas, 78228-0510, U.S.A

L. W. Acton
Montana State University
Bozeman, Montana 59717-3840, U.S.A

M. Balat-Pichelin
PROMES-CNRS
B.P. 5 Odeillo
66125 Font Romeu Cedex, France

V. Bothmer
Institut für Astrophysik
Georg-August-Universität Göttingen,
37077 Göttingen, Germany

R. B. Dirling, Jr.
SAIC
Huntington Beach, California, 92649, U.S.A.

W. C. Feldman
Los Alamos National Laboratory
Los Alamos, New Mexico, 87545, U.S.A.

G. Gloeckler
University of Maryland
College Park, Maryland, 20742, U.S.A.

S. R. Habbal
Institute for Astronomy
University of Hawaii
Honolulu, 96822, U.S.A.

D. M. Hassler
Southwest Research Institute
Boulder, Colorado, 80302, U.S.A

I. Mann
Earth and Planetary Sciences
Kobe University
Nada, Kobe 657-8501, Japan

W. H. Matthaeus
Bartol Research Institute
University of Delaware
Newark, Delaware, 19716, U.S.A.

R. L. McNutt, Jr., *APL Study Scientist*
The Johns Hopkins University Applied Physics
Laboratory
Laurel, Maryland, 20723, U.S.A.

R. A. Mewaldt
California Institute of Technology
Pasadena, California, 91125, U.S.A.

N. Murphy
Jet Propulsion Laboratory
Pasadena, California, 91109, U.S.A.

L. Ofman
Catholic University of America
Washington, D.C., 20064, U.S.A.

E.C. Sittler, Jr., *GSFC Study Scientist*
NASA Goddard Space Flight Center
Greenbelt, Maryland, 20771, U.S.A.

C. W. Smith
University of New Hampshire
Durham, New Hampshire, 03824, U.S.A.

M. Velli
Dipartimento di Astronomia e Scienza del
Spazio
Università degli Studi di Firenze, 50125 Firenze,
Italy¹

T. H. Zurbuchen
University of Michigan
Ann Arbor, Michigan, 48109, U.S.A.

Support Staff and Ex Officio Members

A. A. Dantzler, *APL Study Lead*
The Johns Hopkins University Applied Physics
Laboratory
Laurel, Maryland, 20723, U.S.A.

J. D. Kinnison, *APL Engineering Team Lead*
The Johns Hopkins University Applied Physics
Laboratory
Laurel, Maryland, 20723, U.S.A.

¹Also at the Jet Propulsion Laboratory

M. Guhathakurta, *LWS Program Scientist*
NASA Headquarters
Washington D.C., 20546-0001, U.S.A.

O. C. St. Cyr, *LWS Senior Project Scientist*
NASA Goddard Space Flight Center

Greenbelt, Maryland, 20771, U.S.A.

W. S. Lewis, *Technical Writing Support*
Southwest Research Institute
San Antonio, Texas, 78228-0510

Solar Probe+: Executive Summary

Solar Probe+ will be an extraordinary and historic mission, exploring what is arguably the last region of the solar system to be visited by a spacecraft, the Sun's outer atmosphere or corona as it extends out into space. Approaching as close as $9.5 R_S^$ ($8.5 R_S$ above the Sun's surface), Solar Probe+ will repeatedly sample the near-Sun environment, revolutionizing our knowledge and understanding of coronal heating and of the origin and evolution of the solar wind and answering critical questions in heliophysics that have been ranked as top priorities for decades. Moreover, by making direct, in-situ measurements of the region where some of the most hazardous solar energetic particles are energized, Solar Probe+ will make a fundamental contribution to our ability to characterize and forecast the radiation environment in which future space explorers will work and live.*

Our First Visit to a Star

Two of the transformative advances in our understanding of the Sun and its influence on the solar system were the discovery that the corona is several hundreds of times hotter than the visible solar surface (the photosphere) and the development—and observational confirmation—of the theory of the corona's supersonic expansion into interplanetary space as a “solar wind.”

In the decades that have followed these important milestones in solar and space physics, the composition, properties, and structure of the solar wind have been extensively measured, at high heliolatitudes as well as in the ecliptic and at distances far beyond the orbit of Pluto. The corona and the transition region above the photosphere have been imaged with unprecedentedly high resolution, revealing a complex architecture of loops and arcades, while photospheric magnetography has uncovered the “magnetic carpet” of fine-scale flux bundles that underlies the corona. Observational advances have been accompanied by advances in theory and modeling, with a broad range of models offering plausible and competing scenarios to explain coronal heating and solar wind acceleration.

We now know more about the corona and the solar wind than ever before. And yet the two fundamental questions, raised in the 1940s by the discovery of the corona's million-degree temperature and in the early 1960s by the proof of the supersonic solar wind's existence, remain unanswered: *why is the solar corona so much hotter than the photosphere? And how is the solar wind accelerated?*

The answers to these questions can be obtained only through in-situ measurements of the solar wind down in the corona. A mission to provide these measurements, to probe the near-Sun particles-and-fields environment, was first recommended in 1958, at the dawn of the space age, by the National Academy of

Science’s “Simpson Committee.” Since then, NASA has conducted several studies of possible implementations of a Solar Probe mission, and a Solar Probe has remained at the top of various National Academy and NASA science priority lists. Most recently, the National Research Council’s “decadal survey” in solar and space physics recommended implementation of a Solar Probe mission “as soon as possible” (NRC, 2003), while NASA’s Sun-Solar System Connection Roadmap identified a Solar Probe as a “Flagship” mission that “is ready to fly and is our highest priority for new resources” (NASA, 2005).

The claim that a Solar Probe mission was “ready to fly” was supported by the most recent Solar Probe study, which was completed in 2005 [McComas *et al.*, 2005]. Beginning in March 2004, NASA’s Solar Probe Science and Technology Definition Team (STDT) worked closely with engineers at the Johns Hopkins University Applied Physics Laboratory (APL) to define a mission that could achieve those objectives. The mission that emerged from the study followed the basic structure of several previous studies: the 2005 study used a Jupiter gravity assist maneuver to place an RTG-powered spacecraft into a polar orbit about the Sun with a perihelion of 4 R_S and an aphelion of ~ 5 AU.* The spacecraft was protected by a tall, conical carbon-carbon composite heat shield and equipped with an integrated payload comprising in-situ and remote-sensing instruments. The baseline mission provided for only two brief solar encounters, roughly 5 years apart.

The APL engineering study demonstrated that the Solar Probe mission described in the 2005 report was technically feasible and acceptably low-risk; and the mission, as it was presented in various venues to members of the solar and heliospheric physics communities, enjoyed very broad support. Nevertheless, at a cost of \$1.1 billion in FY07 dollars, the 2005 Solar Probe was found to be too expensive to implement within NASA’s current funding environment. Recognizing the compelling nature of Solar Probe science, NASA’s Science Mission Directorate (SMD) requested a new study to determine if a mission could be designed that would achieve the Solar Probe core science while costing no more than \$750M in FY07 dollars. A further constraint—and technical challenge—was the SMD’s stipulation that Solar Probe not be powered by RTGs.

The following report presents the results of this new study, which was conducted by the same STDT that performed the 2005 study, again with significant support from the APL engineering staff. The new study has yielded a significantly re-designed mission that (1) can be implemented within the \$750M cost cap, (2) does not require RTGs for power, and (3) addresses the science objectives defined in the 2005 study. *The STDT found, in fact, that the new mission design, with its repeated near-Sun passes, offers significant advantages in both technical implementation and science return compared with the 2005 mission. The re-designed mission has therefore been christened “Solar Probe Plus” (written “Solar Probe+”).*

* R_S = solar radius = 6.96×10^5 km; AU = Astronomical Unit = $\sim 1.5 \times 10^8$ km or 215 R_S

Solar Probe+ Science Objectives

Observations, theory, and modeling provide a general picture of the corona and solar wind. At times of lower solar activity, the solar wind is bimodal, consisting of a dominant quasi-steady high-speed wind that originates in open-field polar coronal holes and a variable, low-speed wind that originates around the equatorial streamer belt (**Fig. ES-1**). With increasing activity, this orderly bimodal configuration of the corona and the solar wind breaks down, as the polar holes shrink and streamers appear at higher and higher heliographic latitudes. At these times, the bimodal wind structure is replaced by a complex mixture of fast flows from smaller coronal holes and transients, embedded in a slow-to-moderate-speed wind from all latitudes. The energy that heats the corona and drives the wind derives from photospheric motions and is channeled, stored, and dissipated by the magnetic fields that emerge from the photosphere and structure the coronal plasma. Several fundamental plasma physical processes—waves and instabilities, magnetic reconnection, turbulence—operating on a vast range of spatial and temporal scales are believed to play a role in coronal heating and solar wind acceleration.

Thus we have the general picture. But the devil—and the physics—is, as always, in the details. For example, the association of the fast and slow components of the solar wind with large-scale magnetic structures (coronal holes, streamers) in the corona is well established. However, to understand coronal heating and solar wind acceleration in coronal holes, it is necessary to know the geometry and dynamics of the expanding magnetic field and to determine the role of fine-scale structures (such as plumes and macrospicules) in coronal heating. In the case of the slow wind, a critical unknown is the morphology of the magnetic field in the regions where the wind forms. Similarly, the morphology of the magnetic field in active regions, which contribute to the solar wind at least during solar maximum, is also unknown. Thus a major science objective of the Solar Probe+ mission is to provide the critical in-situ data that will be used, together with remote-sensing observations of the photosphere and corona from other ground- and space-based assets, *to determine the structure and dynamics of the magnetic fields at the sources of the fast and slow solar wind.*

The precise mechanisms by which energy is transferred from the photosphere and subsequently dissipated to heat the corona and accelerate the solar wind are not known. For example, low-frequency Alfvén waves are thought to be launched into the corona by photospheric motions. What is the energy flux in these waves close to the Sun? How is the energy of the waves dissipated? Through phase mixing? Through resonant absorption by coronal loops? Through nonlinear cascade processes? Observations suggest that ion cyclotron waves play an important role in heating the corona and fast wind. But how and where are these waves generated? Are they produced locally by plasma instabilities, through turbulent

cascade from lower-frequency waves, or in the lower corona by reconnection? And generally, what is the role of reconnection (e.g., in nanoflares) relative to that of wave dissipation in coronal heating? To answer these and similar questions, Solar Probe+ will, as a second main objective, *trace the flow of energy that heats the corona and accelerates the solar wind.*

Solar Probe's third major science objective is *to determine what mechanisms accelerate and transport energetic particles* at the Sun and in the inner heliosphere (**Fig ES-2**). Two kinds of solar energetic particle (SEP) events occur during active periods, often both together: gradual events, in which particles are accelerated in the corona by shocks driven by fast coronal mass ejections (CMEs), and impulsive events, in which particles are accelerated by solar flares. In addition, even at the quietest times there is a continuous outflow from the Sun of particles of intermediate energies (suprathermal to >10 MeV). Mechanisms responsible for this outflow and their coronal origins are not known. Further questions concern the relative contributions of reconnection, shocks, and turbulence to particle acceleration in impulsive events, the source spectra, the identity and source of seed populations for gradual events, and the means by which energetic particles are transported to high latitudes. Accomplishment of this objective will not only advance our understanding of a fundamental plasma process, energetic particle acceleration, but will also significantly contribute to efforts to predict SEPs, which present one of the most serious threats to astronaut health and safety, especially outside low-Earth orbit.

The inner heliosphere is populated with dust grains originating from comets and asteroids. This inner heliospheric dust cloud, the source of the zodiacal light and the Sun's F-corona, has not been well characterized. Solar Probe's unique path near the Sun will make it possible to answer questions about the size and mass distribution of the dust, about its composition and origin, and about its interaction with the near-Sun plasma and gas environment. Of particular interest is the contribution of the dust to the "inner source" of energetic particles. As its fourth objective, Solar Probe+ will *explore dusty plasma phenomena in the near-Sun environment and their influence on the solar wind and energetic particle formation.*

To address these objectives, Solar Probe+ will travel closer to the Sun than any other spacecraft and **explore** the innermost region of our solar system. With the data it transmits back to Earth, solar and space physicists will answer questions that cannot be answered by any other means and will attain a **deep understanding** of phenomena and processes in this fascinating and critical region. And as with any great voyage into uncharted realms, Solar Probe+'s journey to the Sun holds the promise of many more unanticipated **discoveries**—new mysteries to challenge humankind's ever expanding knowledge of our home in the universe.

Baseline Mission

Although the Solar Probe+ science objectives remain the same as those established for Solar Probe 2005, the new mission design differs dramatically from the 2005 design (as well as from all previous Solar Probe mission designs since the 1970s). The 2005 and earlier missions involve one or two flybys of the Sun at a perihelion distance of $4 R_S$ by a spacecraft placed into a solar polar orbit by means of a Jupiter gravity assist. In contrast, Solar Probe+ remains nearly in the ecliptic plane and makes many near-Sun passes at increasingly lower perihelia. The baseline mission provides for 24 perihelion passes inside 0.16 AU ($35 R_S$), with 19 passes occurring within $20 R_S$ of the Sun (**Fig. ES-3**). The first near-Sun pass occurs three months after launch, at a heliocentric distance of $35 R_S$. Over the next several years successive Venus gravity assist (VGA) maneuvers gradually lower the perihelia to $\sim 9.5 R_S$, by far the closest any spacecraft has ever come to the Sun. The spacecraft completes its nominal mission with three passes, separated by 88 days, at this distance (**Fig. ES-4**). With a May 2015 launch, the Solar Probe+ prime mission will begin near the end of Solar Cycle 24 and end near the predicted maximum of Cycle 25 in 2022. During these ~ 7 years, Solar Probe+ will spend a total of 961 hours inside $20 R_S$, 434 hours inside $15 R_S$, and 30 hours inside $10 R_S$, sampling the solar wind in all its modalities (slow, fast, variable, transient) as it evolves with rising solar activity toward an increasingly complex structure (**Fig. ES-5**).

Payload and Spacecraft

Solar Probe+'s baseline payload is an integrated package of in-situ instruments and a white-light Hemispheric Imager (HI) for imaging coronal structures. The in-situ instrument complement is identical to that baselined for Solar Probe 2005 and includes a Fast Ion Analyzer (FIA), two Fast Electron Analyzers (FEAs), an Ion Composition Analyzer (ICA), an Energetic Particle Instrument (EPI), a Magnetometer (MAG), a Plasma Wave Instrument (PWI), a Neutron/Gamma-ray Spectrometer (NGS), and a Coronal Dust Detector (CD). Unlike Solar Probe 2005, Solar Probe+ carries only one remote-sensing instrument, the Hemispheric Imager. The change in orbit from polar to near-ecliptic allows for extensive simultaneous remote-sensing observations of photospheric and coronal features by ground-based, sub-orbital, and space-based assets as context for the in-situ measurements and thus eliminates the need for an on-board Source Region Imager included in the 2005 strawman payload. (The present study retains the resources previously allocated to the PSRI and reserves them for a possible additional instrument that may be proposed in response to the Solar Probe Announcement of Opportunity.)

The baseline Solar Probe+ is a 3-axis stabilized spacecraft designed to survive and operate successfully in the intense thermal environment that it will experience during its voyage around the Sun (Fig.

ES-6). The spacecraft's most prominent feature is the thermal protection system (TPS), a large, flat carbon-carbon shield 2.7-m in diameter. The TPS protects the spacecraft bus and instruments within its umbra during the solar encounters. Solar Probe+ is powered by two separate solar array systems. The primary arrays are used at greater heliocentric distances and are folded inside the TPS umbra as Solar Probe+ gets close to the Sun. At these times, secondary arrays, consisting of two moveable, liquid-cooled panels of high-temperature cells, are used. As the spacecraft moves even closer to the Sun, the secondary arrays are partially retracted behind the TPS to maintain constant temperature and power output. A lithium-ion battery is included as a secondary power source. The guidance and control system consists of three star trackers, an internally redundant inertial measurement unit, and a solar horizon sensor. Four reaction wheels provide attitude control, while a monopropellant hydrazine system is used for momentum control and trajectory correction maneuvers. The spacecraft is equipped with a high-gain antenna (HGA) mounted to a dual-gimbaled mast and two hard-mounted low-gain antennas (LGAs). The HGA is the prime antenna for the Ka-band science data downlink, while X-band uplink and downlink capability is provided through all antennas. Inside 0.59 AU, the HGA is stowed within the umbra and communications are maintained with the X-band LGAs. Science data collected during solar encounters are stored and downlinked once the spacecraft is beyond 0.59 AU.

The FIA, one FEA, and the ICA are mounted on a stand-off bracket on the ram side of the spacecraft. The bracket provides viewing near the edge of the umbra during solar encounters. The CD, EPI, second FEA, and HI are mounted directly to the spacecraft bus, while the NGS is located just behind the TPS. The MAG and PWI search coil are attached to the 2-m axial boom that extends from the bottom deck of the spacecraft and that also accommodates a solar horizon sensor used for attitude safing during solar encounters. The PWI consists of three 1.75-m antennas mounted 120° apart on the side of the bus.

Solar Probe and Human Exploration

SEP events present a serious radiation threat to human explorers living and working outside low-Earth orbit. Development of an SEP forecasting capability is critical to space radiation risk mitigation and management. By making the first direct measurements of the near-Sun regions through which all SEPs must travel, by directly sampling the regions where gradual SEPs are energized, and by identifying the seed populations for these dangerous particles, *Solar Probe+ will provide critical ground-truth data needed for the development of the predictive models that, combined with solar and heliospheric monitoring, will enable forecasting of the space radiation environment in support of human exploration.*

Summary

The mission described in this report is based on a detailed implementation study by the APL engineering team and a thorough review of the Solar Probe science objectives in light of the new mission design by the Science and Technology Definition Team. This study demonstrates that the re-designed mission fully satisfies the programmatic and cost requirements established by NASA's SMD. Thus, Solar Probe+ can be flown in the near-future, fully achieving all four science objectives while enjoying significant advantages, both scientific and technical, over previous Solar Probe mission concepts. *Solar Probe+ is an extraordinary mission of exploration, discovery, and deep understanding. It will journey to arguably the last unexplored region of the solar system and reveal how the corona is heated, the solar wind is accelerated, and solar energetic particles are created. It will solve these fundamental mysteries, a top priority science goal for many decades, and thereby transform our understanding of the Sun and its sister Sun-like stars.*

To understand the genesis of the heliospheric system, it is necessary to determine the mechanisms by which the solar corona is heated and the solar wind is accelerated and to understand how the solar wind evolves in the innermost heliosphere. These objectives will be addressed by a Solar Probe mission. Because of the importance of these objectives for the overall understanding of the solar-heliosphere system, as well as of other stellar systems, a Solar Probe mission should be implemented as soon as possible within the coming decade.

NRC, *The Sun to the Earth—and Beyond a Decadal Research Strategy in Solar and Space Physics* (2003)

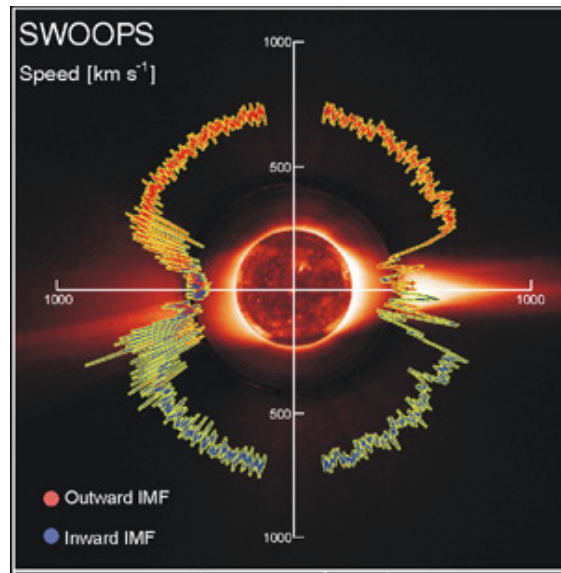


Figure ES-1. At solar minimum the solar wind is dominated by a high-speed flow from polar coronal holes, with a slower, variable flow emanating from the equatorial streamer belt (*McComas et al.*, 1998).

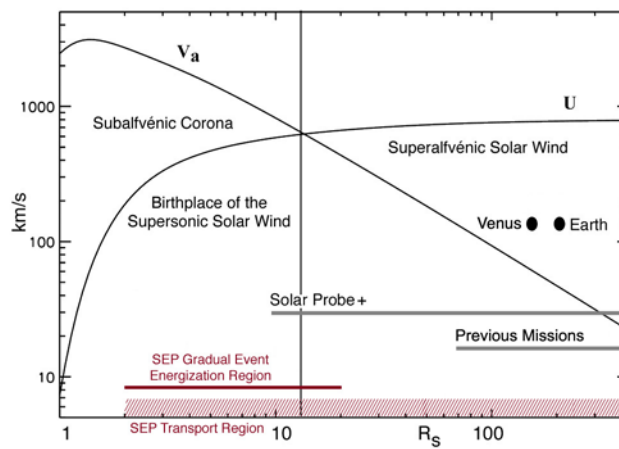


Figure ES-2. Model profiles of the solar wind speed (U) and the Alfvén wave speed (V_a) with distance from the Sun. The vertical bar separates the source, or sub-Alfvénic, region of the wind from the supersonic, super-Alfvénic solar wind flow. Solar Probe+ will be the first mission to fly inside the solar wind source region.

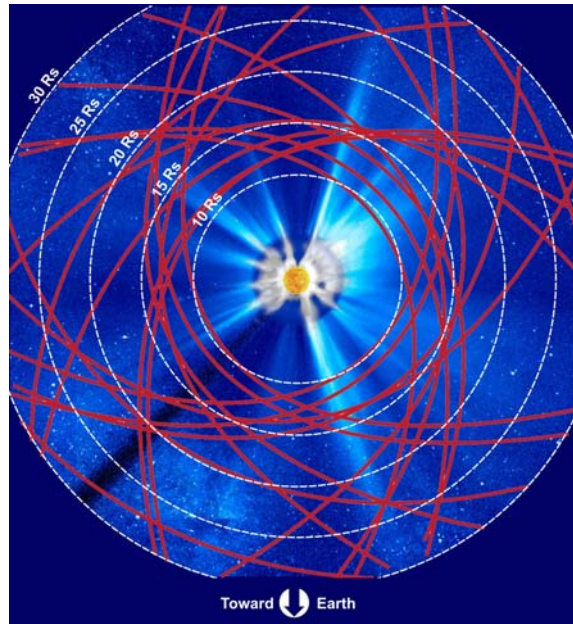


Figure ES-3. A simulated view of the Sun and inner heliosphere from above, illustrating the trajectory of Solar Probe+ during its multiple near-Sun passes inside $30 R_S$. The spacecraft will spend close to 1000 hours within only $20 R_S$ of the Sun. The spacecraft's near-ecliptic orbit allows repeated measurement of the slow wind from the streamer belt as well as of the fast wind from equatorial extensions of polar coronal holes.

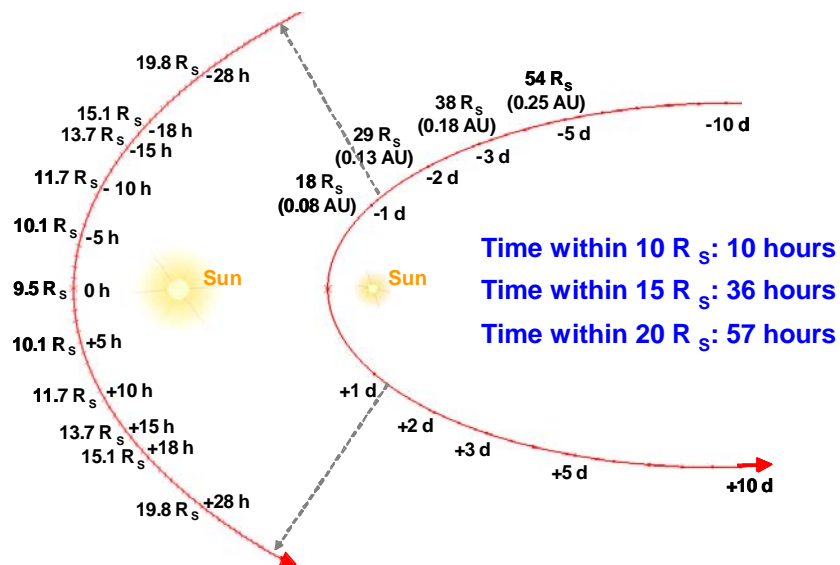


Figure ES-4. The trajectory of the Solar Probe+ during one of its minimum perihelion passes. With three such passes during its prime mission, Solar Probe+ will gather a total of 30 hours worth of data inside $10 R_S$.

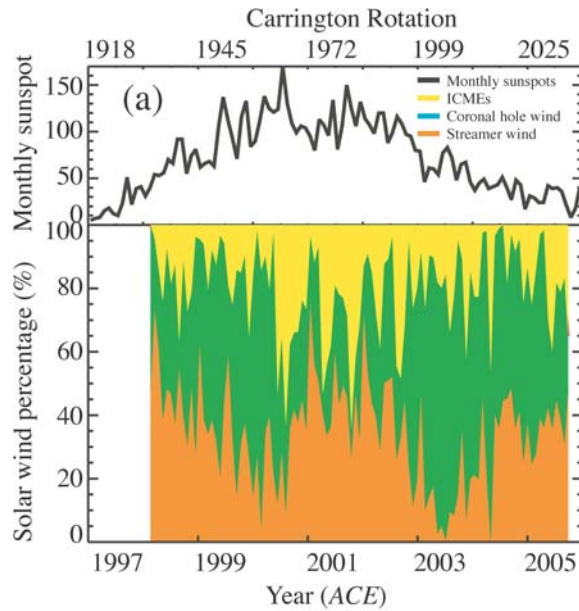


Figure ES-5. Observations from the Advanced Composition Explorer (ACE) during the rising phase, peak, and declining phase of Solar Cycle 23 show how the percentage of solar wind from different sources observed in the ecliptic varies with solar activity (yellow = transient wind; green = fast wind from coronal holes; red = wind associated with coronal streamers). From its near-ecliptic orbit Solar Probe+ will, over its numerous near-Sun perihelia, repeatedly sample the wind from all solar sources, producing an extensive set of observations of the wind in both its quasi-stationary and transient modes (*Zhao and Zurbuchen, 2008*).

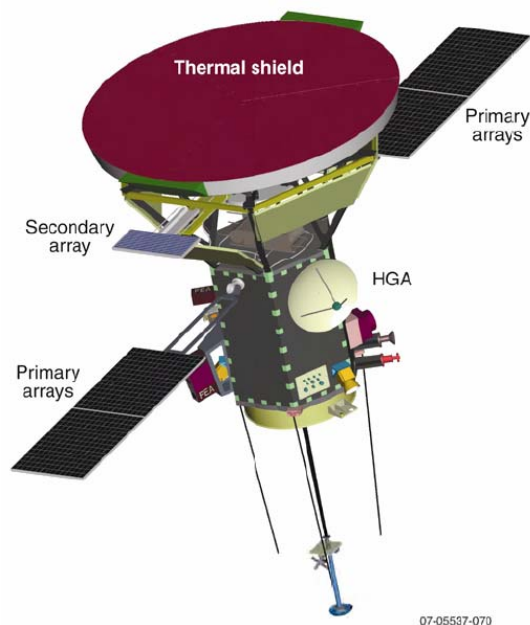


Figure ES-6. The re-designed Solar Probe+ spacecraft is based on rigorous engineering studies that demonstrate the technical feasibility and affordability of the mission.

1. Solar Probe+ and Human Exploration

NASA's new "Vision for Space Exploration" calls for an "extended human expedition to the Moon" some time between 2015 and 2020 and for the eventual human exploration of Mars. One of the problems that must be solved for this vision to become reality is the problem of space radiation, which presents a serious threat to the health and safety of future human explorers. A number of major research initiatives are now under way to improve our understanding of the biological effects of radiation and to develop effective shielding materials and other mitigation strategies. *Another important aspect of space radiation risk reduction and management is the development of the capability to forecast the radiation environment, and here Solar Probe has a unique and significant contribution to make to human exploration.*

The two principal sources of space radiation with which astronauts traveling outside Earth's magnetosphere will have to contend are *galactic cosmic rays* and *solar energetic particles*. Galactic cosmic rays (GCRs) are very energetic particles that are accelerated by a variety of processes within the galactic environment and then propagate into the solar system. Most of the GCR flux is filtered by the outer heliosphere; the remaining GCRs enter the solar system, providing a radiation background whose levels are modulated by the heliospheric magnetic field, with the smallest fluxes observed around solar maximum. The variability in the continuous GCR background over the solar cycle is generally well documented. The most pressing practical challenge in reducing the GCR risk is the development of adequate and cost-effective shielding for spacecraft and shelters where astronauts can spend the majority of their time.

In contrast to the relatively steady fluxes of GCRs, solar energetic particle (SEP) events are episodic and thus unpredictable, and can expose astronauts and spacecraft systems¹ to intense fluxes of particles with energies >30 MeV for a periods of hours to days. The effects of an SEP event on the health of human explorers can be quite serious, depending on such factors as the total absorbed dose and the dose rate, which in turn depend both on physiological factors and on the characteristics of the SEP event (energy spectra, intensity, duration). Acute effects from exposure to SEPs range from dizziness, nausea, and headaches to radiation sickness and, in principle, even death. SEP events are divided into two types: short-lived *impulsive* events, in which the particles are accelerated in solar flares, and *gradual* events, in which the particles are accelerated at shocks driven by fast coronal mass ejections (CMEs) in the near-Sun coronal environment. Both processes operate together in some events, but generally speaking the

¹An SEP event in April 2002 may have led to the loss of Japan's Mars mission, Nozomi; another SEP event in October 2003 rendered the MARIE instrument on the Mars Odyssey spacecraft inoperative. The loss of the MARIE instrument is ironic, as it was designed to measure the radiation environment at Mars.

gradual events produce the largest fluences of particles and most dangerous radiation environments for astronauts. SEP events occur most frequently during a 6-7 year period centered on solar maximum.

One the largest SEP events recorded occurred in August 1972—during the Apollo program, but fortunately not during a mission. A recent study of the health effects of SEP exposure based on data from this event concludes that “the combination of high doses and high dose rates delivered to crews by solar particle events of the magnitude and duration of the August 1972 event is likely to produce significant acute effects, which could be mission- or even life-threatening unless a heavily shielded space is provided for use by the crew” (*Parsons and Townsend*, 2000). An extraordinarily intense event occurred on January 20, 2005, with a very hard proton energy spectrum extending up to 400 MeV. An astronaut, exposed during this event on the surface of the Moon and protected only by a space suit, would have received an estimated radiation dose of ~50 cSv, which would have been enough to cause radiation sickness (http://science.nasa.gov/headlines/y2005/27jan_solarflares.htm?friend).

In contrast to GCRs, solar energetic particle radiation presents a problem of monitoring and forecasting rather than shielding: “It is not too difficult a task to provide appropriate shielding or storm shelters to protect against exposure during SPEs, but surveillance methods to predict and detect solar particle events from *both* sides of the Sun relative to a spacecraft must be improved” (*NRC*, 1996). The risk to future astronauts will come from SEP events that catch them unawares as they are engaged in exploration activities away from the shielded living quarters, laboratories, or storm shelters of their lunar or martian bases. ***In such cases, monitoring and real-time forecasting are vitally important if astronauts are to receive the advance warning they need in order to have enough time to find shelter.***

Models that can provide real-time forecasting of SEP spectra and fluxes are currently being developed and refined (e.g., the Space Weather Modeling Framework at the University of Michigan). At present, however, the accuracy of such models is limited by their dependence upon assumptions about the physical conditions in the corona and inner heliosphere, between 2 and 20 R_S , where gradual SEP events originate. ***Solar Probe+ will explore this critical region for the first time (Figure 1-1).*** It will directly address how SEPs are accelerated and transported in this region, identify their seed populations, and establish the physical conditions (e.g., magnetic field structure, turbulence levels, Alfvén speed) under which these critically dangerous particles are generated (cf. Section 2.3 below). ***Solar Probe+ will thereby provide the “ground truth” for models that eventually will be run in real time to make global predictions, and it will thus play a truly enabling role in the human exploration of the Moon and Mars.***

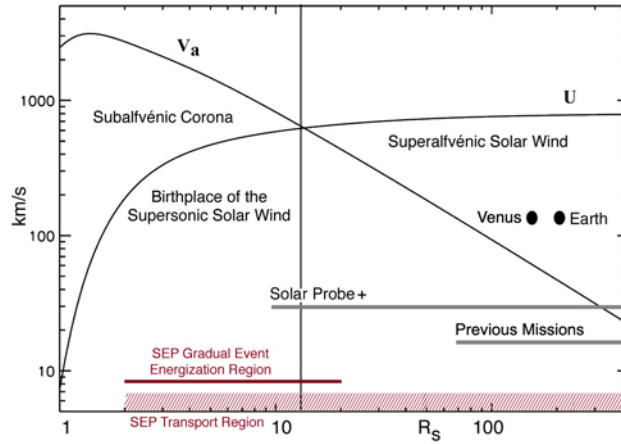


Figure 1-1. Model profiles of solar wind speed and Alfvén wave speed with distance from the Sun. The vertical bar separates the source, or sub-Alfvénic, region of the wind from the supersonic solar wind flow. Solar Probe+ will be the first mission to fly inside the solar wind source region and to sample directly the critical region of the outer corona where solar energetic particles (SEPs) are generated.

2. Solar Probe+ Science Objectives and Measurement Requirements

Remote-sensing observations from space-based platforms such as Yohkoh, Hinode, SOHO, STEREO and TRACE as well as from ground-based observatories, together with in-situ measurements by Helios, IMP, Ulysses, Wind, and ACE, have led to changing perspectives in our understanding of coronal heating and solar wind acceleration. As the time and space resolution of instrumentation has increased, the fundamental role played by the Sun's magnetic field in shaping dynamical processes on all scales in the three-dimensional heliosphere throughout the solar activity cycle has become more apparent. Significant progress has been made in our knowledge of coronal structures, particularly of fine-scale structures such as polar plumes, coronal bright points, and the Sun's "magnetic carpet"; and we have witnessed fundamental advances in our understanding of the nature of the solar wind, the association of its fast and slow components with specific coronal structures, and its variability with changing solar activity.

Important early clues about the bimodal structure of the solar wind came from the Helios mission, the only mission to explore the inner heliosphere as close to the Sun as 0.3-0.7 AU. Helios demonstrated that properties such as solar wind speed, ion temperatures, and turbulence amplitude increase with distance from the heliospheric current sheet or as a function of heliomagnetic latitude. In its three orbits about the Sun's poles Ulysses has explored the three-dimensional structure of the solar wind as it changes over the course of a solar activity cycle (**Figure 2-1**). Ulysses has shown that the fast solar wind, with a speed around 750 km/s, is the basic, quasi-steady outflow from the high-latitude solar corona during the minimum phase of the solar cycle and demonstrated that the fast wind originates from regions where the coronal electron temperature is relatively cool (**Figure 2-2**). This inverse correlation between flow speed and coronal electron temperature poses a fundamental challenge to one of the basic tenets of the original theory of the solar wind, which assumes high coronal electron temperatures and heat conduction. A further challenge to the original theory comes from SOHO measurements, which suggest that the open corona expands principally because of the very high, anisotropic temperatures of the coronal ions, with the minor species reaching temperatures of 10 MK at a few solar radii.

Unlike the fast wind, which originates in coronal holes, the slow solar wind is confined to regions emanating from the magnetic activity belt. SOHO observations suggest that the slow wind flows in a bursty, intermittent fashion from the top of helmet streamers, which were first seen to expand continuously, in X-rays, by Yohkoh. The organization into fast and slow components characterizes the solar wind around solar minimum. As the solar activity cycle progresses, however, Ulysses has shown that the simple bimodal structure gives way to a much more variable, but typically slower, solar wind at activity maximum, apparently originating not only from the much more sparse coronal hole regions and

quiet Sun, but also from coronal active regions. To whatever degree the various models of solar wind acceleration have succeeded in reproducing observations of the fast wind, still less success has been obtained in efforts to understand the acceleration of the slow wind.

A third type of flow arises from large eruptions of coronal magnetic structures, known as coronal mass ejections (CMEs). Their initiation requires an entirely distinct mechanism from the slow and fast wind. One of the important developments in solar and heliospheric physics during the last twenty-five years is the recognition that shock waves driven by fast CMEs can relatively often accelerate particles to energies exceeding 1 GeV and that such shock-driven “gradual” energetic particle events are distinct from “impulsive” events associated with solar flares. However, the identity of the seed particles and the physical conditions necessary for the acceleration of particles in gradual events are not known.

Although there are many models for various aspects of magnetic activity, coronal heating, and solar wind acceleration, the lack of magnetic field and detailed plasma measurements in the region inside 65 R_s does not allow their validation or falsification. Basic unanswered questions concern the dynamics of photospheric and coronal magnetic fields in the source regions of the solar wind; the storage, transport, and release of the mechanical energy required for coronal heating; the specific mechanism(s) for the conversion of energy between the magnetic field and thermal particles; and the sources of high-energy particles and the mechanisms by which they are accelerated. These questions motivate three broadly distinct but interlinked top-level Solar Probe+ objectives. A fourth top-level objective of an exploratory nature concerns the source, composition, and dynamics of dust in the inner solar system. In the following sections, these four main objectives are translated into specific scientific questions and basic measurement requirements.

The science objectives discussed in the following sections have been updated from those presented in the 2005 Solar Probe STDT report (*McComas et al.*, 2005) to reflect the changes in mission design resulting from the 2007 engineering study conducted by APL in concert with the STDT, as well as new results obtained since publication the earlier report. In our review of 2005 objectives, the re-convened STDT found that no substantive changes were required and further that the new mission implementation, with its multiple near-Sun encounters, could not only achieve all of the original Solar Probe objectives but also offered significant advantages over the previous design (see sidebar).

2.1 Determine the structure and dynamics of the magnetic fields at the sources of the fast and slow solar wind

In-situ measurements of the solar wind by Ulysses, Helios and other spacecraft have confirmed the origin of fast wind streams in coronal holes and demonstrated the overall association of wind speed and coronal

structure throughout the solar activity cycle (**Figure 2-1**) (McComas *et al.*, 2003). However, while the properties of the fast and slow wind in interplanetary space are well-established, their source regions have been explored only via remote sensing observations, which have revealed that the solar corona, even at solar minimum, displays a rich variety of dynamic magnetized structures over a wide range of temporal and spatial scales. Its orbit in the near-ecliptic plane will enable Solar Probe+ to make in-situ measurements both of the slow wind associated with the equatorial streamer belt and of the high-speed streams emanating from the low-latitude extensions of coronal holes. While not required for mission success, correlation of Solar Probe+'s plasma and magnetic field measurements between $30 R_S$ and $9.5 R_S$ with remote-sensing observations of the photospheric magnetic field and corona by assets such as Solar Dynamics Observatory (launch planned for 2008) and Solar Orbiter (launch planned for 2015) as well as numerous ground-based assets will be used to relate the solar wind measured in situ to the source regions at the Sun.

2.1.1 How does the magnetic field in the solar wind source regions connect to the photosphere and the heliosphere? The geometry of the magnetic field expansion in the inner corona, from the photosphere out to a few solar radii, plays a fundamental role in determining density distribution and solar wind speeds, as the field lines self-consistently define the flow tubes along which mass and energy flux are conserved. Close to the Sun, SUMER and MDI observations from SOHO suggest that the source of the fast solar wind is associated with the strong supergranular network magnetic fields in coronal holes (Hassler *et al.*, 1999, **Figure 2-3**) and, in particular, with regions of large-scale, locally unbalanced, net positive (≥ 10 G) magnetic field, which must rapidly fan out to fill the coronal hole (McIntosh *et al.*, 2006). Non-radial divergence of the magnetic field in both solar latitude and solar longitude on larger, coronal scales is a fundamental parameter of the solar wind flow, (e.g., Feldman *et al.*, 1996) as it determines the areal expansion along flux tubes, which has been shown to be inversely correlated with the asymptotic solar wind speed (Wang and Sheeley, 2003 and references therein). With accurate models of the coronal magnetic field, in-situ observations of the slow solar wind can be mapped to the wind's coronal source. Using multiple in-ecliptic perihelion passes, Solar Probe+ will measure the longitudinal dependence of the expansion of the solar magnetic field in a wide range of structures. *In-situ measurements by Solar Probe+ of the magnetic field in the inner heliosphere coupled with remote-sensing observations of the underlying photospheric field (e.g., from SDO and Solar Orbiter) will allow a complete description of magnetic field and solar wind expansion free from unknown parameters. These measurements will provide both a test of existing models of coronal structure and rigorous constraints on future coronal models.*

The magnetic network in the quiet Sun (i.e., that part of the corona that is distinct from coronal holes and excludes active regions) looks remarkably similar to the network in coronal holes in spectral lines formed at lower, transition region temperatures, while it is harder to distinguish in lines formed at 10^6 K. If a similar coronal heating mechanism is at work in both the quiet Sun and coronal holes, any difference in their appearance is presumably related to the magnetic field topology, including, perhaps, its time dependence. The larger densities, apparently higher electron temperature, and different chemical composition of the quiet Sun would then be the result of a larger filling factor of closed magnetic field lines compared with that in coronal holes. While the imprint of coronal holes and equatorial helmet streamers is manifest in the solar wind in the form of fast and slow streams and embedded plasma sheets, the fate of the quiet Sun corona is unknown. Is the plasma in the quiet Sun confined by closed magnetic field lines, so that the fast wind is entirely of coronal hole origin? Or is there a mass loss from the quiet Sun as well, and if so, what is its speed and how does it merge with the surrounding solar wind? Studies of the photospheric magnetic field show that coronal holes are embedded in predominantly unipolar regions, which are far larger in extent than the area of coronal holes (**Figure 2-4**). By sampling the corona in the ecliptic plane, as a function of longitude over many orbits, the transition from fast wind from coronal holes to the wind from the quiet Sun can be repeatedly explored. By sampling different longitudes at the same latitude, the transition from fast to slow wind can also be measured.

The magnetic field in active regions above sunspots provides the strongest confinement of hot plasma in the corona and is seen as bright x-ray loops, which often end in cusp-like shapes at their summit. At greater heights, these develop into streamers, which at solar minimum are large and elongated and form a belt around the solar magnetic equator. The equatorial streamer belt is thought to be the source of the slow wind. Remote-sensing observations by SOHO/UVCS of the EUV emission lines of minor ions, combined with multi-fluid models, provide some clues about the source regions of the slow solar wind in coronal streamers, but the magnetic field topology in these regions and the role it plays in plasma outflow are unknown. Coronal observations have shown that the mid-latitude regions of the streamer belt can map to the equatorial current sheet with magnetic signatures that can be observed inside the Alfvén critical point ($r \sim 15 R_S$) and that Solar Probe+ will be able to measure during several of its perihelion passes.

The complexity of the coronal magnetic field structure increases with increasing activity during the solar cycle. At activity maximum, disk observations show the existence of very complicated loop structures, and images of the extended corona show streamers protruding from the solar surface not only in the equatorial regions but at all latitudes around the disk as well (**Figure 2-5**). *Solar Probe+ will determine where the slow solar wind forms in and around streamers and whether specific magnetic signatures, such as embedded current-sheets, are associated with its formation. Further, studies of solar wind sources during periods of solar maximum indicate a contribution to the wind from inside*

active regions as well. With multiple passes in the near-ecliptic plane, Solar Probe+ will provide in-situ data that can be correlated with magnetographic data and, possibly, supporting EUV imaging and spectral observations from Solar Orbiter or other space-based platforms to determine the topology of magnetic field lines within active regions that give rise to solar wind flow

Solar Probe+ will travel many times over the low-latitude extensions of polar coronal holes as well as over equatorial coronal holes, the quiet Sun, and the active solar corona at distances between 30 and 9.5 R_s under both quiet and active conditions. It will trace the origin of the fast and slow wind and correlate the flow speed with closed/open magnetic field line topologies, as determined indirectly through the in-situ measurement of such parameters as electron and energetic particle bi-directional streaming and directly through remote-sensing observations: Solar Probe+ viewing of the white-light corona to trace field lines in the plane of the Solar Probe+ orbit, tomographic images from the Heliospheric Imager to identify coronal structures in the local spacecraft environment, and observations of the photosphere and photospheric magnetic fields to identify and locate the source region structures.

At present, relating the solar wind to the coronal magnetic structures in which it originates involves mapping the measured photospheric field out to some radius and extrapolating the solar wind flow radially backward to this same radius, where a boundary condition—typically that the magnetic field be radial—is imposed. The radius where the connection between solar wind backwards extrapolation and solar magnetic field forward extrapolation are matched is typically located at $\sim 2\text{--}3 R_s$. ***In-situ magnetic field measurements by Solar Probe+ during multiple fast longitudinal perihelion passes will provide definitive ground truth for such mapping and data from the equatorial passages will allow a better reconstruction of the magnetic field from the Sun into interplanetary space.***

In-situ measurements of the heliospheric magnetic field suggest a global structure that is generally similar to that predicted by Parker (1958), with a spiral structure caused by the combination of solar wind expansion and solar rotation and a warped current sheet separating the northern and southern polarities. However, Ulysses observations of the magnetic field orientation in co-rotating rarefaction regions have shown large deviations from Parker's model (Murphy *et al.*, 2002; Schwadron, 2002). Further evidence that the field deviates from the Parker model at large distances from the Sun came from the surprising detection by Ulysses of solar energetic particles at higher latitudes caused by shocks associated with corotating interaction regions (CIRs) formed at lower latitudes (McKibben *et al.*, 2001). It has been suggested that the observed departures from the Parker spiral result in part from the rigid rotation of coronal holes, which implies efficient reconnection between the open coronal hole field lines and the quiet Sun and the resulting diffusion of open field lines across coronal hole boundaries (Fisk, 1996; Fisk and Schwadron, 2001). The Alfvén critical point defines the effective co-rotation distance of the solar coronal plasma, as the angular momentum loss per unit mass is exactly $L = \Omega R_A^2$. The in-situ plasma

measurements should allow observation of the azimuthal flow (*Pizzo et al.*, 1983; *Marsch and Richter*, 1984), allowing the transfer of angular momentum to the solar wind and its relation to the spiral field to be determined. In-situ measurements by Solar Probe+ of the plasma and magnetic field as close as $9.5 R_s$ over many equatorial passes will help test such theories of the heliospheric magnetic field.

Measurement Requirements

- Continuous in situ magnetic field and plasma velocity measurement inside 0.3 AU
- Density temperature and composition of solar wind as a proxy for individual flow tubes
- Electron distribution function (bidirectional streaming as evidence of closed magnetic field line topology and correlations with composition and wind speed and magnetic field)
- All sky coronagraph images from multiple vantage points and photospheric magnetic field measurements.

2.1.2 How do the observed structures in the corona evolve into the solar wind? The outer solar atmosphere is structured by the magnetic field over a wide range of scales. Active regions and the quiet Sun display extended arcades and loops with thicknesses down to present observational resolution limits of a 1000 km or less, merging into the helmet streamers observed over the activity belt in coronagraph images. White light and UV coronagraph-spectroscopic observations also show coronal holes to be far from featureless as well. Bright striations, or plumes, can be traced all the way from the solar surface out to $30 R_s$ (**Figure 2-6**). Plumes have also been observed within equatorial coronal holes (*Del Zanna and Bromage*, 1999), which are also expected to be a source of high-speed wind (*Miralles et al.*, 2004).

The relationship of plumes to the fast wind is poorly understood. They appear above X-ray bright points in the coronal holes, and are denser by factors of 2 or more than the surrounding regions. UV lines in the plumes appear to be narrower (i.e., the plumes are cooler) than in the darker lanes separating them, while measurements of outflows suggest that the dark lanes are preferential outflow regions (*Teriaca et al.*, 2003). Earlier measurements also revealed an apparent large FIP effect in plumes, thus excluding the possibility that they could be the source of the fast wind. However, more recent analyses using SOHO/CDS data have shown that plumes do not have a significant FIP effect, contradicting the earlier observations (*Del Zanna et al.*, 2004). Moreover, the scale height temperature in plumes seems to be too high to allow them to remain in static equilibrium (*Wilhelm et al.*, 1998), and dynamic wave activity, suggestive of acceleration mechanisms, has been observed in plumes by SOHO/EIT (*DeForest and Gurman*, 1998; *Ofman et al.*, 1999) and SOHO/UVCS (*Ofman et al.*, 1997; 2000). Finally, Doppler

dimming measurements using SOHO/SUMER in the height range $1.05\text{--}1.35 R_s$ have found outflow velocities in plumes of order 60 km/s, exceeding those in the interplume regions (Gabriel *et al.*, 2003).

Fine-scale structures are observed in the fast wind as well as in coronal holes, including the so-called microstreams and pressure-balanced structures. These are fluctuations in radial velocity that last about sixteen hours in the spacecraft frame and have a magnitude on the order of 50 km/s. Such structures may be a remnant of the original acceleration process (see Section 2.1.3). *By flying through the equatorial coronal holes over a range of distances from 30 to $9.5 R_s$ Solar Probe+ will observe and cross ubiquitous fine scale structures, estimate their filling factor and contribution to the overall solar wind flow, and assess the expansion factors of the flow tubes carrying the solar wind flow. These observations will make it possible to clarify how microstreams form and evolve and to determine what their relationship to coronal fine-scale structures is.* Achieving this objective will require both in-situ measurement of the magnetic field and plasma velocity and full distribution function (density temperature and composition of solar wind) to identify individual flow tubes and use of the tomographic reconstruction technique of the Heliospheric Imager, which will provide information on the filling factor and geometrical distribution of plumes. Coordinated imaging of the solar disk can provide a link between features on the solar surface and those measured by the Solar Probe+, thus helping to identify the sources of the fast and slow wind.

The LASCO and UVCS telescopes on the SOHO mission have made important contributions to our knowledge of the origins of the slow solar wind streams around helmet streamers (**Figure 2-7**). Sequences of LASCO difference images obtained in 1996 (sunspot minimum) give the impression of a quasi-continuous outflow of material in “puffs” from the streamer belt (Sheeley *et al.*, 1997). A quantitative analysis of moving features shows that they originate above the cusp of helmet streamers and move radially outward, with a typical speed of 150 km/s near $5 R_s$, increasing to 300 km/s at $25 R_s$ (**Figure 2-8**). The average speed profile is consistent with an isothermal corona at the temperature $T \approx 1.1 \times 10^6$ K (SOHO/UVCS measurements indicating a temperature 1.6×10^6 K in the streamer core, at activity minimum) and a critical point near $5 R_s$. The ejection of material may be caused by loss of confinement due to pressure-driven instabilities as the heated plasma accumulates or to current-driven instabilities (tearing and or kink-type instabilities) in the sheared field of the streamer. Sheeley *et al.* (1997) conclude that the features they observe trace the wind motion like “leaves in the wind.” *Solar Probe+ will cross the paths of these ejecta from streamers multiple times and will ascertain whether the ejection of coronal material occurs in a continuous flow or whether the puffs are in fact disconnecting plasmoids. If the latter, Solar Probe+ will determine the magnetic field configuration of the plasmoid as well as the magnetic morphology at the point of disconnection in the corona.*

Comparison of radio-science data from the Galileo spacecraft with SOHO/UVCS images clearly shows the association of the slow wind with streamer stalks, that is, with the regions above the cusps of helmet streamers that include the current sheet (*Habbal et al.*, 1997). It is not known, however, whether there is a single current sheet that runs along the nearly equatorial strip of maximum brightness in the white corona, i.e., along the streamer belt (as surmised by *Wang et al.* [1997]), or whether there are a number of stalk/sheet structures of finite longitudinal extent. Nor is the structure of current sheets in streamer stalks known. Do they have a simple structure, or are they made up of multiple sheets in a more complex magnetic field morphology, as is suggested in part by SOHO/UVCS measurements (*Noci et al.*, 1997) and multiple current sheet crossings in situ (*Smith*, 2001)? Solar Probe+ will cross through the stalks of streamers in the ecliptic plane and determine whether or not they are always associated with current sheets. As it crosses the streamer stalks, the spacecraft will also be able to characterize the transition from the slow streamer-associated wind to the faster ambient wind.

During periods of maximum activity the solar wind flow is much more variable and structured than the simple bimodal case found at solar minimum. The solar wind speed is typically lower, with the exception of very high speed CME-driven flows, and the source regions of the wind are more uncertain. The quasi-stationary (non-CME driven) flows appear to originate not only from coronal holes and their boundaries, but also from active regions, which are associated with both the slower and moderately fast winds. The solar wind from active regions seems to be structured into sub-streams separated by distinctive structures such as magnetic holes, plasma sheets, or lower entropy regions (*Neugebauer et al.*, 2002).

White-light heliospheric images by Solar Probe+ within 30 R_s over a wide range of solar longitudes will reveal the geometrical distribution of fine-scale structures in low-latitude coronal holes, the plasma structures enveloping active regions and helmet streamers, and their filling factors, while in-situ measurements of plasma and magnetic field properties will clarify magnetic field morphology, the nature of plasma/current sheets, and the source regions of solar wind. Additionally, Solar Probe+ will be able to measure the extent to which streamers are disturbed by the passage of CMEs and will provide the observations needed to substantially improve our understanding of the near-Sun evolution and internal structure of CMEs.

Measurement Requirements

- In-situ magnetic field and plasma velocity and full distribution function measurements (density temperature and composition of solar wind as a proxy for individual flow tubes)

- Electron distribution function (bidirectional streaming as evidence of closed magnetic field line topology and correlations with composition and wind speed and magnetic field)
- Photospheric magnetic field measurements
- Heliospheric Imager measurements of coronal structure

2.1.3 Is the source of the solar wind steady or intermittent? As observed in-situ at large distances from the Sun, the solar wind appears as a continuous, if structured, plasma outflow. Its quasi-steady character may be a property of the outflow at the solar source. However, the apparently quasi-stationary wind may also result from a number of spatially limited, impulsive events that are distributed over smaller scales (Neugebauer, 1991; Feldman *et al.*, 1997).

There is abundant evidence for the intermittent or “pulsed” (Feldman *et al.*, 1997) character of the high-speed wind: observations of microstreams and persistent beam-like features in the fast wind (**Figure 2-9**); interplanetary scintillation measurements of field-aligned density structures having a 10:1 radially-aligned axial ratio and apparent field-aligned speeds ranging from ~400 to ~1280 km/s (Coles *et al.*, 1991; Grall *et al.*, 1996); and remote sensing observations of the chromosphere, transition region, and corona revealing explosive, bursty phenomena (microflares) associated with magnetic activity over an extremely wide range of energy and time scales. Feldman *et al.* (1996, 1997) have interpreted the fine-scale structures observed in the fast wind as remnants of spicules, macrospicules, X-ray jets, and H-alpha surges and hypothesize that the fast wind results from the superposition of transient reconnection-generated jets. Similar phenomena have been observed for equatorial extensions of the polar corona holes (Miralles *et al.*, 2004). ***If this hypothesis is correct, then the heating of the corona leading to its time-dependent acceleration to form an ensemble of outward-going jets could be accompanied by the annihilation of oppositely-directed magnetic flux bundles clustered near the magnetic network, in turn leading to transient hard X-ray and gamma-ray bursts, along with neutron production in the 1 to 10 MeV energy range, which could be detected by Solar Probe+.***

For the slow solar wind, evidence in favor of an intermittent origin is even more abundant. As mentioned above, blobs of plasma appear to be lost by helmet streamer structures overlying active regions and various mechanisms have been proposed for this process. At solar maximum, an important and definitely intermittent solar wind component is present in the form of CMEs and the fine-scale structure of the solar wind from active regions suggests at least a spatially structured origin for the various flow streams. More generally, smaller CME-like events at all scales could contribute significantly to the solar wind throughout the activity cycle.

Recent models of the solar wind (e.g., Feldman *et al.*, 1996;1997; Fisk, 2003; Schwadron and McComas, 2003) require an intermittent, bursty origin for the solar wind, as the mass flux is lost by the

reconnection of closed loops to open field lines. Loops may act as plasma storage deposits, accumulating energy and matter that will be injected in the solar wind. For a given energy flux, hotter loops contribute a larger mass flux, and therefore the asymptotic wind speed is lower. The inverse correlation of electron temperature and solar wind speed inferred from in-situ observations (*Gloeckler et al.*, 2003) may thus be an intrinsic signature of the loops that are the source of solar wind. In this view, all solar wind material comes from plasma that was once confined in coronal loops and has therefore been injected into the wind via magnetic reconnection with open field lines (*McKenzie and Mullan*, 1997). This view is also supported by in-situ measurements of the abundance of elements with a low first ionization potential (FIP bias), whose coronal accumulation can only occur in loops. FIP bias is close to 2 in the fast wind or high-latitude region and greater than 3 everywhere else (*Zurbuchen et al.*, 2002), evidence that the fast wind comes from small, short-lived loops, while slower wind may come from larger, longer-lived structures.

Direct, in-situ measurements of the structure of the solar wind during multiple perihelion passes, of the ion and electron distribution functions, and of elemental abundance variations close to the Sun will provide the data required to test these models. Solar Probe+ will directly measure both the electron distribution function and flow speeds of minor ions in equatorial extensions of coronal holes and directly sample composition differences on closed and open fields. By continuous direct sampling the plasma flow, Solar Probe+ will be able to assess the spatial and temporal character of the filling factor of the solar wind, while imaging the coronal structures that it will cross above 10 R_{\odot} . It will measure how microstreams in the fast wind change and whether they merge with pressure-balanced or other density-enhanced plume-like and or filamentary structures. The time-dependent variability observed in the wind might also increase close to the Sun, revealing signatures of multiple sources such as bursty events or micro-CME's.

Measurement Requirements

- In-situ magnetic field and plasma velocity at high cadence in inner heliospheric regions (below 20 R_{\odot})
- Solar wind density, temperature, and composition
- Electron distribution function (bidirectional streaming as evidence of closed magnetic field line topology and correlations with composition and wind speed and magnetic field); strahl; and high-energy tails of proton and helium distribution functions at high cadence.
- Neutron and gamma-ray detection
- Energetic electrons and ions

2.2 Trace the flow and elucidate the thermodynamics of the energy that heats the solar corona and accelerates the solar wind

The solar corona loses energy in the form of radiation, heat conduction, waves, and the kinetic energy of the solar wind flow. It is estimated that the energy flux required to balance such losses from the corona varies from $\varepsilon = 10^7$ erg/cm²/sec for active regions to $\varepsilon = 5\text{-}8 \times 10^5$ erg/cm²/s for coronal holes and streamer belt cusps (*Withbroe and Noyes, 1977*). This energy must come from mechanical energy residing in photospheric convection, the solar magnetic field acting both to channel and store this energy in the outer atmospheric layers. However, the mechanisms by which the energy is transferred and dissipated to generate the hot corona, solar wind, and heliosphere throughout the Sun's activity cycle remain one of the fundamental unanswered questions in solar and heliospheric physics.

Remote-sensing measurements of the solar corona and in-situ measurement of particle distribution functions in the fast and slow solar wind streams have shown that the heating process is correlated with magnetic structure, and at solar minimum, with the basic bimodal nature of the solar wind. SOHO/UVCS observations using the Doppler dimming technique (*Li et al., 1998; Kohl et al., 1998*) (**Figure 2-10**) and interplanetary scintillation measurements (*Grall et al., 1996*) indicate that the high speed solar wind is rapidly accelerated near the Sun, reaching speeds of the order of 600 km/s within 10 R_s (*Grall et al., 1996, Figure 2-11*). Observations of comet C/1996Y1 confirm a most probable speed of about 720 km/s for the solar wind at 6.8 R_s (*Raymond et al., 1998*). Such rapid acceleration appears to result from the extremely large and anisotropic effective temperatures in the lower corona that have been deduced from measurements by SOHO/UVCS. These temperatures are much higher perpendicular to the magnetic field. The fast solar wind measured in situ shows what may be a relic of this anisotropy, which is smaller than that inferred from coronal observations, but persists in the distance range from 0.3 to 5 AU. Proton, alpha-particle, and minor ion distribution functions in the fast wind also present a non-thermal beam-like component whose speed is comparable to the local Alfvén speed. All these properties suggest that Alfvén or ion-cyclotron waves play a major role in coronal heating and solar wind acceleration. It is difficult, however, to separate remnant signatures of solar wind acceleration from in-situ processes. Measurements close to the Sun are required to distinguish the effects of in-situ processes and obtain a more direct measure of the acceleration mechanism(s).

The different properties of the turbulence observed in the fast and slow solar wind are further evidence of the role played by turbulence and wave-particle interactions in coronal heating. Fast streams contain stronger fluctuations in transverse velocity and magnetic fields, and display a higher degree of correlation between the velocity and magnetic fluctuations (often described as a well-developed spectrum of quasi-incompressible Alfvén waves propagating away from the Sun). In the slow wind, this correlation

occurs at a much lower level, while larger fluctuations in density and in the magnitude of the magnetic field are present, indicating a more evolved MHD turbulent state there. This difference in turbulence state between fast and slow wind streams, together with the fact that slow wind distribution functions are much closer to equilibrium, suggests that the outward propagating wave flux contributes to the heating of the steady fast wind, while the slow wind is heated much more variably. It is not known, however, how the turbulent flux increases toward the Sun, whether it is sufficient to power coronal heating and solar wind acceleration, and how it is driven by time-dependent events in the photosphere, chromosphere, transition region, and lower corona.

By providing the first in situ measurements of the distribution functions, waves, turbulence, and electromagnetic fields from 0.3 AU to 9.5 R_s , and by correlating them with plasma and magnetic field structures, Solar Probe+ will be able to answer the basic questions of how the solar corona is powered, how the energy is channeled into the kinetics of particle distribution functions in the solar corona and wind, and how such processes relate to the turbulence and wave-particle dynamics observed in the heliosphere.

2.2.1 How is energy from the lower solar atmosphere transferred to, and dissipated in, the corona?

An abundant amount of mechanical energy is available in photospheric motions. The question is: How is this energy transmitted upwards and dissipated in the right place, within a few solar radii of the surface, to heat the corona? The coincidence of magnetic and thermal structures suggests that the magnetic field plays a fundamental role in channeling, storing, and dissipating the energy, both via the emergence of photospheric flux tubes and through their continuous distortion and convection by the photospheric velocity fields. Photospheric motions on different time-scales have different effects, which may be broadly divided into two categories: power at periods below a few minutes propagates in the form of MHD waves (AC), while power at lower frequencies is stored by currents or gradients in the coronal magnetic field (DC) (*Hollweg, 1974;1978*).

Because of the high coronal temperatures, the resistivity of the coronal plasma is weak (i.e., magnetic Reynolds numbers are of order $S \sim 10^{12}$ based on collisional resistivity). Weak resistivity implies that the dissipation of MHD waves must occur via the development of steep gradients and small scales—through nonlinear steepening or a turbulent cascade, for example, or through phase-mixing (*Heyvaerts and Priest, 1983*) and resonant absorption (*Ionson, 1978*). In the case of energy stored in DC currents, dissipation occurs by means of current sheet collapse and magnetic reconnection. Ultimately, both mechanisms require large electric fields, so that particle acceleration occurs, resulting in non-thermal particle distributions.

Whether the solar corona is heated by low-frequency waves resulting from motions naturally arising in the photosphere or whether the dominant energy source resides in the currents stored via slower field line motions has been the subject of strong debate. Among the MHD waves, only Alfvén waves would appear to survive the strong gradients in the chromosphere and transition region, because slow modes steepen into shocks while fast modes suffer total reflection. Transmitted waves propagate at large angles to the radial direction, since a 100 s wave with an Alfvén speed of 2000 km/s has a wavelength along the direction of the field of 2×10^5 km, while the perpendicular coherence will be at most 10^4 km. Longer-period waves must have an even larger ion anisotropy. Waves reaching the lower corona must therefore be shear Alfvén waves, although discrete coronal structures such as loops and plumes might channel surface waves and propagate energy as global oscillations as well. Recently, Alfvén waves have been observed directly in the chromosphere (*DePontieu et al.*, 2007) and in the lower solar corona by the Hinode satellite (*Ofman and Wang*, 2007; *Okamoto*, 2007). Ubiquitous upward propagating Alfvén waves have also been recently detected in the inner corona by ground-based coronagraph using the Coronal Multi-Channel Polarimeter (CoMP) (*Tomczyk et al.*, 2007). Estimates for the energy flux in these waves are now yielding values compatible with the requirement for coronal holes and the fast wind, although information on the coronal power spectrum is lacking (see Section 2.2.3).

Several mechanisms for the dissipation of waves have been proposed, among which phase-mixing (*Heyvaerts and Priest*, 1983) and resonant absorption (*Ionson*, 1978) are the most widely invoked. Both processes rely on gradients in coronal structures or, more generally, on the presence of non-uniform phase speeds, resulting in the corrugation of wave-fronts and the development of small scales as the waves propagate. It is not clear, however, that wave dissipation by either process could occur within the distance required to produce the high-speed wind (i.e., $1.5 R_s$ from the coronal base in open field regions) (*Hansteen et al.*, 1997). Phase mixing and resonant absorption might play a specific role in coronal structures such as plumes, where guided surface and slow mode waves have been remotely observed and modeled (*Ofman et al.*, 2000). Alternatively, the upward-transported waves may drive low-frequency turbulence and a quasi-perpendicular cascade involving counter-propagating waves (*Matthaeus et al.*, 1999) to provide the source for extended heating at smaller scales needed to drive the fast wind from coronal holes. In any of these scenarios, the details of the kinetic processes that convert small-scale fluid motions into thermodynamic internal energy remain to be discovered.

Parker (1988) argued that most of the energy reaching the corona must come from the slow displacement of closed field lines in low-lying loops, which are tangled until they spontaneously develop current sheets and then reconnect, resulting in elementary dissipation events known as nanoflares. In this scenario, the energy for coronal heating is stored in presently unmeasured coronal magnetic field fluctuations. On the basis of coronal heating energy requirements, Parker estimated that 10^{24} ergs must be

released per elementary event. MHD numerical experiments have shown how power-law distributions in energy release are a natural outcome of the Parker scenario, with indices not far from those observed in x-ray flaring events (*Georgoulis et al.*, 1998). The original nanoflare heating scenario has been strongly debated, observational work having focused mostly on the power law index characterizing the distribution of the panoply of small-scale energetic events observed in the corona, transition region, and network. However, extrapolating the data to lower energies and inferring the total contribution of such events to coronal losses is subject to strong uncertainties (*Cargill and Klimchuk*, 2004). The direct detection of nanoflares is beyond the scope of the Solar Probe+ mission. However, *the detection of energetic particles and their spectra, as well as the measurement of the coronal magnetic field and its fluctuations at perihelion, where confined coronal plasma may be traversed, will provide important indirect evidence for the lower energy scales to which bursty events extend.*

Recently the role of low-lying loops and reconnection at transition region heights due to photospheric dragging of network and intra-network fields (magnetic carpet vs. canopy) has been stressed as a potential source of energy, in the form both of direct heat and of waves launched by reconnection (*Axford and McKenzie*, 1992; *Schrijver et al.*, 1997; *Longcope et al.*, 2003; *Fisk*, 2003). High-frequency modes of this type (e.g., ion cyclotron waves) (*Marsch and Tu.*, 2001) can propagate into the corona, where they can drive the heating of both protons and minor ions (see Section 2.2.2 below). Similar phenomena may be involved in the polar radial magnetic field inversions observed by the Ulysses spacecraft (*Yamauchi et al.*, 2004). Reconnection, buffeting of field lines associated with photospheric oscillations, or direct field line dragging by photospheric velocity fields have also been invoked to account for the formation of chromospheric and coronal features such as spicules and macrospicules (*Sterling*, 2000), although no theory has yet been able to completely describe such phenomena.

With a comprehensive measurement of plasma and electromagnetic fluctuations in the inner solar wind ($<20 R_S$), *Solar Probe+ will determine how the energy that powers the corona and wind is dissipated and what the dominant dissipative structures are as well as the frequency spectrum of electromagnetic fluctuations.* Small-scale magnetic reconnection, of both the “anti-parallel” and “component” types, occupies an important place in the closed field line Parker mechanism and in open field line cascade and phase mixing models. *An important set of investigations on Solar Probe+ will therefore be the multi-instrument detection of signatures of small-scale reconnection, such as bi-directional plasma jets, accelerated particles, magnetic field, and velocity gradient correlations along the trajectory.*

Energy transport and dissipation mechanisms strongly depend on the mean free path of particles in the coronal plasma, which varies drastically both with distance from the Sun (from the base of the corona to the supersonic solar wind), as well as across coronal structures (coronal holes to helmet streamers).

This dependence has led to the suggestion that coronal heating arises from energy stored in non-thermal wings of particle distribution functions generated between the chromosphere and transition region or, more generally, in the region where the solar atmospheric plasma changes from collisional to collisionless. The higher temperatures and subsequent outflows would then arise naturally through velocity filtration by the Sun's gravitational potential (Scudder, 1994).

By measuring electron and ion distribution functions up to large energies as a function of distance from the Sun in the inner heliosphere, *Solar Probe+ will be able to assess the contribution of the velocity filtration mechanism to shaping coronal distribution functions. Solar Probe+ will clarify the relative role of reconnection compared to other heating mechanisms and will for the first time identify the coronal regions above which Coulomb collisions are negligible.*

The abundance of elements with a low first ionization potential (e.g., Mg, Fe) is enhanced in the slow solar wind relative to their photospheric abundances (the “FIP effect”). The FIP effect is less pronounced in the fast wind. The differences between the slow and fast winds with respect to composition and the FIP effect provide clues about the underlying heating and acceleration mechanism. Solar Probe+ will be able to measure for the first time the heavy ion abundances in the solar wind acceleration region and provide the data necessary to differentiate between the heating and acceleration mechanisms responsible for the slow and fast wind.

Measurement Requirements

- Magnetic field, velocity field, and density fluctuations and their spectra
- Particle distribution functions of protons, electrons, alpha particles, and possibly minor ion species; suprathermal populations
- Compositional variation of the solar wind across structures (FIP effect).
- High-cadence 3-axis electric and magnetic field plasma wave measurements with sufficient temporal resolution to resolve the expected proton gyroperiod at 9.5 R_S (~100 Hz).
- Coherent structure identification using plasma wave electric and magnetic field wave-form data

2.2.2. What coronal processes shape the non-equilibrium velocity distributions observed throughout the heliosphere? The significant broadening of minor ion emission lines observed in coronal holes with Spartan and UVCS on SOHO results from unresolved ion motions and is indicative of high temperature anisotropies in the coronal holes, with preferred heating in a direction perpendicular to the radial and preferential acceleration of minor ions over neutral hydrogen, which in the lower corona should be strongly coupled to protons (Li *et al.*, 1998; Kohl *et al.*, 1998). Smaller broadening and temperature

anisotropy of minor ions was observed in equatorial streamer belt at solar minimum (*Strachan et al.*, 2002). Preferential heating of minor ions with respect to protons and temperature anisotropies is also observed in the fast solar wind, where in-situ measurements have shown that the perpendicular temperature in the thermal core component of the proton velocity distribution is higher than the parallel temperature. In-situ measurements have also shown that the magnetic moment is not conserved, implying that plasma turbulence heats the ions significantly in directions perpendicular to the magnetic field from 0.3 out to 1 AU and beyond. Whether this turbulent heating is the primary energy source closer to the Sun, however, is unclear; also, because the temperatures determined from remote sensing techniques are indirect and are dependent on empirical modeling, discriminating turbulent bulk perpendicular and parallel motions from real temperatures requires direct measurement. ***By carrying out such measurements inside 0.3 AU for protons, helium, and minor ions, Solar Probe+ will clarify the role of turbulence and wave-particle interactions in shaping the particle distribution functions. Solar Probe+ temperature data will also provide a yardstick for future remote sensing temperature observations.*** We emphasize that remote sensing measurements of the Lyman-alpha line determine properties of the neutral hydrogen distribution, whose coupling to protons depends crucially on the density profiles; semi-empirical models of the solar wind require an average mean proton temperature of at least 3 MK between 2 and 4 R_{\odot} , and it is expected that the temperature does not drop significantly by 10 R_{\odot} . The ***Solar Probe+ will for the first time measure the proton temperatures in the corona directly (perhaps approaching or passing beyond the temperature maximum at low latitudes), leading to an understanding of the energetically dominant wave-particle interaction properties.***

In addition to the core component, the proton distribution in the fast solar wind has an accelerated beam component whose drift speed is comparable to the Alfvén speed, which is close to the alpha particle drift speed with respect to the protons (*Feldman et al.*, 1974; *Marsch et al.*, 1982; *Tu et al.*, 2004). (The two principal explanations put forward for the presence of such beams are direct generation—in the jet superposition picture of solar wind formation (Section 3.1.3)—and wave-particle interactions in the solar wind acceleration region. The relative drift of protons and alpha particles is observed beyond 0.3 AU in the solar wind, and should reach enormous values if it remains close to the Alfvén speed approaching the Alfvénic point. Solar Probe+ measurements of the shape of the proton and alpha-particle distribution functions will describe this phenomenon below 0.3 AU and determine how this drift originates, yielding clues about the responsible mechanisms.

In-situ measurements of the solar wind and remote sensing observations of coronal holes (Section 2.2.1) strongly implicate resonant interaction with ion cyclotron waves as the mechanism responsible for heating and accelerating coronal hole ions to generate the fast solar wind. The evidence pointing to this mechanism includes observations of extended proton heating, minor ion heating, equal thermal ion

velocities, and greater-than-mass-proportional ion temperatures. A natural process that might lead to these effects is “cyclotron sweeping” (Hollweg and Isenberg, 2002), which relies on the gradual decrease with distance from the Sun of the ion-cyclotron frequency relative to the Alfvén wave frequency. Minor ions, with resonance at lower frequency, would therefore come into resonance closer in the corona, and naturally tap higher-energy regions of the turbulent spectrum, assuming a standard, decreasing shape for energy as a function of frequency. Although this process may work for minor ions, its efficiency is dramatically reduced for protons (Isenberg, 2004), calling its relevance into question as a whole. ***Solar Probe+ measurements of the high-frequency wave spectra and wave-mode analysis, together with proton and alpha-particle distribution functions, will determine the relevance of ion-cyclotron waves in regulating solar wind acceleration processes.***

Other possibilities exist for converting collective plasma energy into thermal energy, thereby shaping plasma distribution functions: in addition to the cyclotron mechanisms discussed above, which feed on fluctuations that vary along the magnetic field, there are also a variety of processes that are powered by cross-field perpendicular fluctuations. Among these are oblique wave damping or Landau damping, weakly collisional and/or compressive damping, and mechanisms involving nonlinear dynamics of current sheets that might be formed by small-scale shears or reconnection activity. The last-mentioned include kinetic (lower hybrid) plasma turbulence, electron solitary structures, mode conversion, and nonlinear beam instabilities. As an example, in the solar wind, there is evidence that the dissipation of kinetic Alfvén waves at large perpendicular wavenumbers, due at least in part to Landau damping and gyroresonant effects, contributes significantly to plasma heating (Leamon et al., 1998).

Solar Probe+ data will allow identification of the heating mechanisms that operate in the corona and of their relative contributions to coronal heating. Do these same processes occur inside 20 R_s ? What are the properties of both high- and low-frequency fluctuations responsible for wave-particle interactions and turbulence? ***Solar Probe+ will measure the proton and alpha particle distribution functions and the temperatures of minor ion species and their anisotropies and will determine their relationship to fluctuations in the magnetic field and the bulk velocity field. Solar Probe+ will thereby identify the basic interactions shaping the distribution functions in the solar wind acceleration region, providing the ground truth knowledge needed to answer the most basic questions about energy dissipation and heating in the corona.***

Measurement Requirements

- Particle distribution functions, protons, electrons and alphas, possibly minor ion species

- Magnetic, velocity, density and temperature fluctuations in the MHD range (below the proton cyclotron frequency)
- Plasma wave measurements at high cadence, electric field measurements.

2.2.3. How do the processes in the corona affect the properties of the solar wind in the heliosphere?

The fast wind displays Alfvénic turbulence, i.e., fluctuations sharing many properties of large-amplitude Alfvén waves propagating away from the Sun (including nearly vanishing magnetic pressure fluctuations), but with a flat frequency (f) spectrum, $E_f \sim 1/f$. The origin of the shape of this “flicker noise” spectrum is not understood, although it is suggestive of the presence of scale-invariant processes, such as reconnection, in the lower corona (*Matthaeus and Goldstein, 1986; Matthaeus et al., 2007*). At higher frequencies the spectrum gradually steepens, which is presumably associated with an active turbulent cascade. The break point between the two spectral forms is, roughly, at the measured correlation scale of the fluctuations, which gradually evolves towards lower frequency with increasing heliocentric distance.

Is the lower-frequency $1/f$ spectrum a remnant of the wave flux that contributes to plasma heating in the lower corona? The existence of a broad spectrum is evidence in itself of significant dynamic evolution, for otherwise significant traces of transmission through the coronal cavity should be found, in the form of preferred frequencies or broad “lines” in the spectrum (*Velli, 1993*). Steepening of the $1/f$ spectrum may occur as a result of an ongoing non-linear cascade (*Tu, Pu, and Wei, 1984*) and/or wave dissipation, as demonstrated by multi-fluid modeling of the solar wind (*Ofman, 2004*).

The spectral slope at different coronal heights evolves with distance, subject to expansion and driving effects, which affects the radial dependence of dissipation. Models starting from the chromosphere (*Verdini and Velli, 2007*) demonstrate that the initial spectrum of Alfvén waves in the photosphere cannot be constrained by in-situ data collected in the far solar wind, since local processes contribute to its shaping there. Only observations close to the solar surface will help in constraining the shape of the Alfvénic spectrum with relevant implications on the role of turbulence in the acceleration of the solar wind and the heating of the corona.

If the very low frequency solar wind fluctuations are remnants of coronal heating, then Solar Probe+ will encounter and detect additional required factors, such as a flux of “inward” type Alfvénic fluctuations, a possible component of compressive fluctuations, and signatures of an incompletely understood mechanism for containing the inward waves in the presence of the turbulence near the Alfvénic critical point. *There has been some debate as to whether signatures of the global solar oscillations, such as the 5-minute photospheric p-modes, survive in the solar wind, as measurements are very close to the noise level as measured in-situ [Thomson et al., 1995; Roberts et al., 1996;*

Thomson et al., 1996]. Solar Probe+ measurements will contribute to the resolution of this controversial question by determining whether such oscillations are present in the corona, before there is time for non-linear dynamics to smooth them out.

Simple extrapolation, along with interplanetary scintillation observations (Canals et al., 2002), suggests that Solar Probe+ will observe rms velocity field fluctuations of about 200 km/s at the Alfvénic critical point, while at the base of the corona limits obtained from spectral line-widths indicate a turbulent velocity near the transition region of 30 km/s (Chae et al., 1998, **Figure 2-12a**). Observations of fluctuation amplitudes from the Sun out to 1 AU are summarized in **Figure 2-12b** (Cranmer and van Ballegoijen, 2005). Such measurements appear to be broadly consistent with an Alfvén wave propagation that is modified very little by non-linear effects, in which case there would be little or no contribution from these waves to coronal heating. *Solar Probe+ will unequivocally determine whether the currently observed fluctuations are in fact one of the principal agents in the coronal heating and wind acceleration process.*

By measuring the fluctuations of velocity, density, temperature, and magnetic fields from 0.3 AU down to 9.5 R_s , Solar Probe+ will determine how the Alfvénic turbulence observed in high speed solar wind streams is generated and how it evolves, how much energy is available, how it is distributed in space and time, and what wave-modes and/or structures are excited. Solar Probe+ will also ascertain whether the observed in-situ fluctuations are indeed the remnant of the coronal heating process and will determine how their evolution is coupled to the evolution of the thermodynamic properties of the plasma itself, principally temperature, density, velocity and average magnetic field. Moreover, beyond their importance for addressing fundamental questions in solar physics, *Solar Probe+'s measurements of the properties of turbulence and nonlinear plasma dynamics in the corona and solar wind will be a watershed for all of astrophysics, where these phenomena are invoked over widely different contexts, from accretion disks to the collisionless shocks occurring in galaxy-cluster formation.*

Apart from determining the initial conditions for the origin the solar wind turbulent spectra, coronal processes have a large impact on other solar wind properties. For example, the composition of the solar wind and its variation with wind speed, which also follows a bimodal pattern, show that the slow wind is enhanced in low first ionization potential (FIP) elements with respect to photospheric values (Zurbuchen et al., 2002). This results most probably from the longer confinement time, in or around closed coronal loop type structures, of the slow solar wind plasma (Section 2.1.3). Solar Probe+ will measure the abundances of heavy ions in the slow and fast wind close to the Sun, ions that to date have been observed only remotely or far from the Sun in situ. Solar Probe+ may also be able to detect light FIP elements, such as Na, which, due to their low abundance, have not been observed so far. The measurement of the FIP

effects in these elements can provide strong constraints on the mechanism responsible for the FIP effect and yield clues to the ionization processes in slow and fast solar wind plasma.

The outer solar corona between 10 and 20 R_S is the region where the velocity gradients between the fast and slow speed streams develop, determining the initial conditions for the development, further out, of corotating interaction regions (CIRs). *In repeatedly sampling this critical distance range for the first time, Solar Probe+ will obtain precise measurements of the plasma flow, magnetic field, and their gradients. These measurements will make it possible to determine the initial conditions for the development of heliospheric structure, enabling a predictive approach to mean global heliospheric structure based on actual coronal measurements.*

Measurement Requirements

- Basic plasma (proton, alpha particles, minor ions) and magnetic field measurements.
- Plasma wave electric field measurements to above the plasma frequency for quasi-thermal noise spectroscopy and high-resolution electric and magnetic field wave-form data for electromagnetic fields.
- Plasma wave electric and magnetic field measurements up to the proton cyclotron frequency.
- Electron temperature gradient, density gradient, electric field/ interplanetary potential.
- Correlation with underlying photospheric magnetic structure from magnetograph.

2.3. What mechanisms accelerate and transport energetic charged particles?

The current paradigm (e.g., Reames, 1999) defines two general classes of solar energetic particle (SEP) events. Gradual events are accelerated by CME-driven shocks and are characterized by roughly coronal abundances and charge states. Impulsive events are generally much smaller events associated with impulsive x-ray flares and are characterized by enrichments in ^3He , heavy ions such as Fe, and electrons, with charge states characteristic of temperatures ranging from ~ 5 to 10 MK. This paradigm distinguishes between two separate acceleration processes and acceleration sites, both driven by eruptive events on the Sun: a) CME-driven shock acceleration starting in the high corona and continuing into interplanetary space and b) acceleration at the flare site, presumably driven by magnetic reconnection. Both processes are known to operate in larger SEP events, and studies at 1 AU during Solar Cycle 23 present a complex picture of events that often exhibit characteristics of both gradual and impulsive SEP events (e.g., Cohen *et al.*, 1999; Cane *et al.*, 2003; Tylka *et al.*, 2005). In addition to such transient energetic events, observations at 1 AU show a continual outflow of intermediate-energy particles from the Sun extending

from suprathermal energies to >10 MeV/nucleon. The mechanisms responsible for the acceleration of these particles are not known.

Determining characteristics of the seed particle populations and distinguishing the various acceleration processes occurring at the Sun on the basis of data acquired only at 1 AU or beyond is difficult. Transport through the interplanetary medium washes out the time structure, reduces the intensities by orders of magnitude, and leads to mixing of particles from different acceleration sites. Solar Probe+ measurements, made at distances as close to the Sun as $9.5 R_S$, will not suffer from transport effects because the Probe+ will sample energetic particles close to their acceleration sites on the Sun and will explore, in situ, acceleration sites in the corona and inner heliosphere. In particular, recent results from ACE, SOHO, and WIND point to the increasing importance of the high corona ($2 R_S < r < 20 R_S$) as an acceleration site for energetic ions and electrons—a region that Solar Probe+ will sample directly. These measurements will address key questions important for understanding solar energetic particle acceleration and transport. The following discussion presents examples of how Solar Probe+ can address these questions.

2.3.1 What are the roles of shocks, reconnection, waves, and turbulence in the acceleration of energetic particles? In ^3He -rich SEP events, abundance ratios of $^3\text{He}/^4\text{He}$ commonly exceed that in the solar wind ($\sim 5 \times 10^{-4}$) by 3 orders of magnitude or more. In addition, heavy nuclei abundances (relative to coronal values) tend to increase with increasing mass, resulting in roughly tenfold enhancements of Fe/O and in enhancements of “ultraheavy” ($Z > 30$) elements by factors as large as 10^2 to 10^3 (Reames, 2004; Mason *et al.*, 2004; see **Figure 2-13**). Explanations of this highly selective fractionation have generally focused on plasma processes that heat and/or accelerate ions in a certain range of charge/mass ratio, including models based on electromagnetic ion-cyclotron waves (see, e.g., the review by Miller [1998]). However, Mason *et al.* (2004) have suggested that these processes fail to account for the overall composition pattern and suggested that coronal shocks may be the accelerating agent in impulsive SEP events. The small-scale, randomly occurring “component” reconnection that typifies microflares may be an indicator of a scale-invariant dissipation process that not only heats coronal plasma (see Section 2.2.1), but also produces a stochastic component of the electric field that contributes to particle acceleration. The production of these dissipative structures may be related to the small-scale termination of the cascade of plasma turbulence that connects large with small scales and may be distributed throughout the heliosphere (Matthaeus and Lamkin, 1986; Ambrosiano *et al.*, 1988).

About 1000 impulsive SEP events/year are estimated to occur on the Sun during solar maximum, but the number may be much larger because many small events undoubtedly go undetected at 1 AU. **Figure 2-14** shows a series of ~ 10 events observed at 1 AU during a several day period. Observations of the same

^3He -rich SEP event by IMP-8 at 1 AU and by Helios at 0.32 AU show that the event is ~ 100 times more intense at 0.32 AU and much more localized in time (**Figure 2-15**). Observed even closer to the Sun, these events will appear as intense bursts of only minutes in duration. *With simultaneous solar observations from 1 AU, it should be possible to trace events observed by Solar Probe+ to the flare site, to measure the flare properties, and to obtain the underlying magnetic field configuration. In addition to composition measurements, Solar Probe+ will measure near-relativistic ($V > 0.1 c$) electrons from these events within a fraction of a minute of their release.* These electrons are particularly important for untangling acceleration processes because their acceleration sites can be sensed remotely by microwave radio emission or hard x-rays.

Solar Probe+ may also observe gamma rays and neutrons from impulsive solar flare events, providing information on accelerated particle components trapped on closed coronal field lines. These particles never escape the Sun to the interplanetary medium yet account for more than 90% of ions accelerated in impulsive events. The neutron measurements must be made as close to the Sun as possible because their flux intensities decrease drastically with increasing heliocentric distance for several reasons owing principally to the finite neutron lifetime and the spread in radial distance for a given neutron energy. This latter effect is caused by the fact that neutrons, unlike photons, travel at speeds that decrease with decreasing energy. As shown in **Figure 2-16**, the net reduction in flux for 1 MeV neutrons between detection at 0.05 AU (close to the perihelion of Solar Probe+) and at 1 AU amounts to ~ 9 orders of magnitude. At $10 R_s \sim 1 \text{ MeV}$ (10 MeV) neutron intensities are $\sim 1 \times 10^9$ (1×10^5) times greater than at 1 AU.) This factor reflects differences in neutron flux intensity at given energy, E , and radial distance, R , for a given flux intensity produced at the Sun.

Among the most interesting discoveries in the last few years was that of suprathermal power law tails with spectral index of -5 in the velocity distributions of solar wind ions (Gloeckler *et al.*, 2000; Gloeckler, 2003; Krimigis *et al.*, 2004; Simunac and Armstrong, 2004; Decker *et al.*, 2006; Gloeckler and Fisk, 2007). Not only are such tails observed downstream of shocks, but they are also seen during quiet times far away from shocks, and, in particular, in the most quiet solar wind from polar coronal holes during solar minimum. All solar wind species that have been measured exhibit suprathermal tails. Such tails are observed at 1 AU with ACE (**Figure 2-17**) and Wind, at different latitudes and from 1.4 to ~ 5 AU with Ulysses and at ~ 100 AU with the Voyagers in the heliosheath. The suprathermal ions are important as a seed population for SEPs; moreover, their presence in the solar wind may be indicative of continuous particle acceleration at the Sun or in the inner heliosphere. There is evidence, for example, that ^3He is continuously accelerated at the Sun, even during the quietest periods, suggesting that more or less continuous acceleration may be occurring in microflares such as those reported by RHESSI (Krucker *et al.*, 2002).

With its multiple orbits, Solar Probe+ is ideally suited to study suprathermal tails in regions never visited before by any other spacecraft and over a good fraction of the solar cycle. These -5 power law tails are bounded, starting at low energies at a few keV (corresponding to about twice the solar wind speed) and gently rolling over, and becoming steeper, at energies around several MeV for protons, and below 1 MeV/nucleon for iron. *Fisk and Gloeckler (2006, 2007)* have proposed a stochastic acceleration process, subject to thermodynamic constraints, to explain the observations, in particular the power law spectra with a -5 spectral index. In their scenario, the tails are accelerated from a core distribution that extends to twice the solar wind speed. Measuring the characteristics of these tails under various solar wind flow conditions, in the turbulent regions downstream of shocks, but also in the most quiet solar wind is imperative for understanding how particle acceleration starts and for revealing the characteristics of seed particles accelerated by shocks to much higher energies. Solar Probe+ will do what has not been possible previously, namely study the formation and evolution of suprathermal tails with distance in the most inner heliosphere. Only with such observations can we hope to answer questions such as: Where and under what circumstances are these tails formed? Do the high-energy cutoffs change with distance, and if so how? How exactly does the pressure in the tails depend on the pressure in the core particles and how does this change with changing levels of solar wind turbulence? Does the proposed stochastic acceleration mechanism account for the observed power law spectrum?

Solar Probe+ will explore the inner heliosphere between $30 R_S$ and $9.5 R_S$, where the particle intensities are orders of magnitude larger than at 1 AU. In this critical region, Solar Probe+ plasma, fields, and energetic particle instruments will be used to investigate the mechanisms responsible for solar energetic particle and suprathermal ion acceleration, while gamma-ray and neutron measurements will reveal the occurrence of sporadic and/or continuous particle acceleration on the Sun. Neutron observations close to the Sun may also reveal evidence of small microflares ($\sim 10^{26}$ ergs), which have been suggested as a principal source of energy for heating the corona (see Section 2.1.3). Solar Probe+ measurements will be over a good fraction of a solar cycle, allowing acceleration processes to be studied at different levels of solar activity.

Measurement Requirements

- Composition and energy spectra of energetic ions and electrons
- Suprathermal ions and electrons
- Neutron and gamma-ray energy spectra
- In-situ magnetic field and solar wind properties
- Photospheric magnetic field measurements and, if available, EUV observations from Solar Orbiter.

2.3.2 What are the seed populations and physical conditions necessary for energetic particle acceleration? SOHO has observed more than 10,000 CMEs since 1996, but there have been only about 100 large SEP events at Earth during this same time period (particle intensities $>10/\text{cm}^2\text{sr} > 10 \text{ MeV}$). The acceleration mechanism (1st-order Fermi acceleration) in gradual SEP events is generally well understood, but we lack information on the conditions close to the Sun where particles are accelerated to high energies. Moreover, it is known that faster CMEs can form shocks more easily and that shocks driven by fast, wide CMEs accelerate particles more efficiently. It remains a mystery, however, why, for a given CME speed, the peak intensity of $>10 \text{ MeV}$ protons can vary by a factor of $\sim 10^4$ (Kahler, 2001).

To forecast large SEP events reliably, it is necessary to determine why some CMEs accelerate particles more efficiently than others. The suggested possibilities include: (1) the presence or absence of a pre-existing population of suprathermal ions, left over either from a previous gradual event (e.g., Kahler 2001; Mewaldt *et al.*, 2006) or from small impulsive flares (Mason *et al.*, 1999); (2) the presence or absence of successive, interacting CMEs (Gopalswamy *et al.*, 2002); (3) pre-conditioning and production of seed-particles by a previous CME (Kahler, 2001; Gopalswamy *et al.*, 2004); (4) possibly reduced injection efficiency, but faster acceleration at quasi-perpendicular (as opposed to quasi-parallel) shocks (Tylka *et al.*, 2005); and (5) variable contributions from flare and shock-accelerated particles (Cane *et al.*, 2003; 2006), including acceleration of associated flare particles by the shock (Li and Zank, 2004; Cliver *et al.*, 2004).

Timing studies have shown that gradual SEP events are first accelerated at distances between ~ 3 and $\sim 12 R_S$ (Kahler, 1994; Mewaldt *et al.*, 2003). Formation of the CME-driven shock requires that $v_{\text{cme}} > v_{\text{sw}} + v_{\text{fast}}$, where $v_{\text{fast}} \approx (v_A^2 + c_s^2)^{1/2}$, v_A is the Alfvén speed and c_s is the sound speed (see e.g., Kahler and Reames, 2003). It has therefore been suggested that SEPs originate beyond $\sim 3 R_S$ because there is a peak in the Alfvén velocity at $\sim 3 R_S$, such that it is only beyond this radius that shocks can be easily formed and sustained for typical CME speeds (e.g., Gopalswamy *et al.*, 2001; **Figure 2-18**). In MHD simulations of SEP events driven by coronal shocks (e.g., Zank *et al.*, 2000; Sokolov *et al.*, 2004) it is necessary to assume or model a variety of conditions in the region where gradual SEP events originate, including the magnetic field and density profiles, the solar wind and Alfvén speeds, the density of seed particles, and turbulence levels that determine the particle diffusion coefficient. *Solar Probe+ will (1) measure the solar wind and magnetic field close to the Sun in the critical region from <10 to $60 R_S$; (2) monitor the density and composition of suprathermal seed particles in the high corona and inner heliosphere; and (3) measure the spectrum of magnetic turbulence directly, thus providing needed constraints on simulations of SEP events.* These measurements will extend over a period of almost 7 years in a series of 24 passes with perihelia that range in distance from 30 to $9.5 R_S$, including both solar minimum and solar

maximum conditions. This data set will make it possible to map out the range of conditions that occur in the inner heliosphere where gradual SEP events are accelerated, and make it possible to relate these conditions to the observed SEP intensity, energy spectrum, and composition.

Over the course of its ~7-year mission Solar Probe+ is expected to observe ~80 SEP events with peak particle intensities characteristic of SEP events at 1 AU that are recorded by NOAA (>10 particles/cm²sr-s with $E >10$ MeV). This estimate takes into account the frequency and size distribution of events measured by NOAA's GOES satellites from 1976-2007 and includes an extrapolation of the radial variation in the proton peak intensity in SEP events (proportional to $R^{-2.4}$) as determined from Helios data (Lario *et al.*, 2005). Approximately 45% of these events would be expected to be observed inside 0.3 AU (~60 R_S) and ~20% of these events may be observed inside ~30 R_S . ***For a large fraction of these SEP events, Solar Probe+ will encounter the CME-driven shock between ~10 R_S and ~60 R_S , allowing in situ studies of shock acceleration in a previously unexplored region.*** In addition, Solar Probe+ measurements of the ambient conditions that exist prior to such events will be of enormous value to our efforts to understand SEP acceleration and transport. If it should prove possible to extend the Solar Probe+ mission an additional 2 years (at the peak of the solar cycle 25), the number of large SEP events observed inside 0.3 AU would be approximately doubled.

In addition to observing CME-driven shock acceleration close to the Sun, Solar Probe+ is expected to observe >1000 smaller SEP events associated with impulsive x-ray flares. Further, Solar Probe+ will almost certainly observe a significant level of the continuous particle acceleration events, the intensity of which is too small to be detected at 1 AU but will be orders of magnitude greater in the near-Sun region. ***Capturing large SEP events will yield valuable data for improving space weather predictions, while measurements of the expected low-level activity during solar quiet times will provide definitive information on the unknown details of near-Sun particle acceleration, escape from the corona, and interplanetary transport.***

Measurement Requirements

- Basic plasma (proton, alpha particles) and magnetic field measurements, and their gradients
- Major and minor ion distribution functions extending to high-energy tails.
- Composition and spectra of ions extending from energies through ~100 MeV/nuc, including ³He
- Plasma wave electric field measurements to above the plasma frequency for quasi-thermal noise spectroscopy.
- Plasma wave electric and magnetic field fluctuation spectra,
- Correlation with underlying photospheric magnetic structure

- Remote sensing of active regions, flares, and CMEs

2.3.3 How are energetic particles transported radially and across magnetic field lines from the corona to the heliosphere? In some cases solar energetic particles arrive at 1 AU in a nearly scatter-free beam, while in other cases the transport is very diffusive, indicating a great deal of particle scattering on magnetic field irregularities between the Sun and 1 AU. In a recent study, *Mason et al.* (2006) demonstrated that pitch-angle scattering also affects the relative composition of the arriving particles. The large number (>1000) of small impulsive events that Solar Probe+ is expected to observe will be especially useful for studying particle transport because they originate from a point source, and observations of SEP events at a range of radial distances and longitudes from the flare site should make it possible to isolate the relative role of transport along and across the average magnetic field. *Solar Probe+ will encounter energetic particles at distances from the Sun ranging from 10 R_S to 0.7 AU and will determine how scattering properties from the corona into the solar wind vary with magnetic field intensities and turbulence levels.*

Energetic electrons are observed in both impulsive and gradual SEP events. Because of the electrons' near-relativistic velocities, the onset times of electron events at 1 AU are often used to deduce SEP release times near the Sun for comparison with their associated electromagnetic signatures. Surprisingly, the deduced release times almost always appear to be delayed by ~10 minutes with respect to electromagnetic signatures such as soft x-ray and optical emissions from flares and associated radio emissions (e.g., *Krucker and Lin*, 2000; *Haggerty and Roelof*, 2002). This discrepancy has resulted in considerable debate concerning its cause—whether storage and subsequent release of the electrons, longitudinal propagation of the acceleration mechanism from the flare site to the injection site, or radial transport of the acceleration mechanism in the form of a CME-driven shock (*Haggerty and Roelof*, (2002). *Close to the Sun propagation delays will be minimized, and energetic electron measurements combined with interplanetary magnetic field observations will reveal where and how particles are released from the Sun and/or accelerated in interplanetary space.*

Measurement Requirements

- High-energy ions and electrons
- In situ vector magnetic field
- Photospheric EUV and magnetic field measurements
- Remote sensing of active regions, flares, solar radio bursts, and CMEs.

2.4 Explore dusty plasma phenomena and their influence on the solar wind and energetic particle formation

The origin of dust in the inner solar system is not well understood. The ultimate sources of the dust population are thought to be the release of dust from comets and asteroids and the breakup of meteoroids (**Figure 2-19**). Subsequent dust-dust collisions lower the average mass of the dust particles. Dust orbital motion combines with Poynting-Robertson deceleration to increase the dust number densities towards the Sun (*Burns et al.*, 1979). As recent analysis of photometric observations has shown, the dust distribution is also influenced by the gravity of planets (*Leiner and Moster*, 2007). Inward from 1 AU, the fragmentation of cometary meteoroids locally is believed to produce a majority of dust particles (*Grün et al.*, 1985; *Ishimoto*, 2000; *Mann et al.*, 2004). Dust that is freshly released from cometary meteoroids has distinctly different optical properties from the dust of the “background” cloud (*Ishiguro et al.*, 2007); Solar Probe+ dust measurements should therefore be able to identify dust components with distinctly different compositional characteristics. Dust particles attain electric surface charge through photo-ionization, electron emission, and interaction with the solar wind. While larger (>1 micron) particles move primarily in Keplerian orbits, smaller charged grains are deflected by the interplanetary magnetic field. The degree of deflection depends on the surface charge, which has not yet been directly measured for dust particles in space, and on the magnetic field magnitude and direction and their variation in time (*Mann et al.*, 2000). In addition, dust dynamics is likely to be influenced by events such as coronal mass ejections, which may even lead to dust destruction (*Misconi*, 1993, *Ragot and Kahler*, 2003).

The interaction of dust in the inner heliosphere and the solar wind plasma influences not only the dust population but the local plasma and gas environment as well. Notably, dust grains in the inner heliosphere are important as a source of pickup ions, protons as well as heavier species, which differ from the solar wind in their charge state and velocity distribution. These “inner source” pickup ions are potential candidates for subsequent acceleration and may contribute to the anomalous cosmic ray population [*Cummings et al.*, 2002]. The interaction of the solar wind with dust particles also generates energetic neutral atoms (ENAs), which can be detected from Earth orbit (*Collier et al.*, 2001); smaller variations in this ENA flux may be due to structures in the dust population (*Collier et al.*, 2003).

Although the dust supply from the frequently observed sungrazing comets is negligible, they provide an impressive example of the fate of solar system objects in the inner solar system and in the vicinity of the Sun. They also illustrate how the presence of small bodies can influence the local environment. For example, SOHO/UVCS observations of the sungrazing comet C/2001 C2, at heliocentric distances of 4.98 and 3.60 R_s , revealed sequential fragmentation events along the comet’s path and provided evidence for the creation of a population of neutral hydrogen through the exchange of charge between

coronal protons and material sublimated from pyroxene dust grains as well as between coronal protons and atoms created from the photodissociation of water (*Bemporad, 2005*).

Despite some valuable observations (e.g., from *Helios* and *Ulysses*), much of our understanding of dust in the inner heliosphere is theoretical and model-based, and many basic questions remain open, awaiting detailed measurement of the near-Sun dust population. What, for example, are the mass distributions and fluxes of dust particles as a function of distance from the Sun? How are dust fluxes correlated with fluxes and velocity distributions of pickup ions? What are the major elemental compositions and bulk density of the dust and how do they vary with distance from the Sun? In-situ observations with *Solar Probe+* will be crucial in resolving many of the present uncertainties regarding dust origin, its composition, and spatial distribution. Since dust is a common component of interstellar material as well as most likely of other stellar systems, *Solar Probe+* results will have a direct bearing on certain astrophysical problems, with the near-Sun dust cloud serving as an analogue for circumstellar dust clouds, for example.

2.4.1 What is the dust environment in the inner heliosphere? Because of current observational limitations, there are great uncertainties in our knowledge and models of the spatial distribution of dust in the inner heliosphere and even at 1 AU. Brightness observations of dust are limited by line-of-sight geometry and biased by large dust grains. Thus they do not reveal the complex dynamics of small dust particles nor do they allow their size distribution and composition to be derived. Given these and other observational limitations, the mass distribution of dust at 1 AU is described by the interplanetary flux model (IFM) (*Griin et al., 1985*). It is assumed that the IFM can be extrapolated inward to give an estimate of the mass distribution in the near-Sun environment. The radial dependence consistent with observations at 1 AU is flat inside $10 R_{\odot}$ with an inner cutoff at $2 R_{\odot}$ and an approximate r^{-1} decrease beyond $10 R_{\odot}$. Most ($\sim 90\%$ at 1 AU) of the dust is believed to be concentrated near the ecliptic plane (which takes 23% of the volume of the sphere), where it can be extensively sampled by *Solar Probe+*. At high latitudes, a second, spherically symmetric component with a steeper increase toward the Sun is assumed. This picture is consistent with zodiacal light observations and based on the hypothesis that comets and asteroids and meteoroids from comets and asteroids are the main sources of the dust cloud (*Mann et al., 2004*).

One recent study suggests that the density at 1 AU may be enhanced by up to a factor of 3 in the middle mass range (*Love and Brownlee, 1993*) compared to that given by the interplanetary flux model. In addition, mutual collisions may increase dust densities for masses smaller than 10^{-7} g compared to the distribution extrapolated from 1 AU (*Mann et al., 2004*). Number densities near the Sun may thus exceed those given by the present model by an order of magnitude. Moreover, since part of the collisional

evolution takes place in meteoroid trails, the dust distribution in the inner solar system may not be homogeneous within the cloud (*Mann and Czechowski, 2005*).

Coronal observations show that the dust number density is influenced by sublimation inward from 10 R_s , but there is no feature that indicates the beginning of the dust free zone outside 2 R_s . This implies that some species survive to this distance or even closer (see the following section). Although Solar Probe+ will not reach distances where the dust-free zone is expected, it will cross regions where volatiles and significant amounts of the other dust compounds sublimate.

Solar Probe+ will characterize the near-Sun dust environment by determining how the mass distribution of dust and impact directions vary along the spacecraft trajectory and how the observed impact signals vary with the mass and impact parameters of the dust particles. Solar Probe+ dust measurements will likely require substantial revision of the paradigm of a homogeneously distributed dust cloud that is stable in space and time.

2.4.2 What is the origin and composition of dust in the inner heliosphere? While the sources of dust are thought to be mainly comets and asteroids, it is not clear how much each source contributes. Collision models suggest that the contribution of cometary dust to the inner heliospheric dust population is greater near the Sun than in the outer solar system beyond 1 AU. Little is known about the composition of dust. Laboratory studies, both past and ongoing, on dust samples (e.g., interplanetary dust collected in the stratosphere and dust currently collected during space missions) provide important information about the collected species, but the samples are limited to those dust particles that survive the collection process and, moreover, there are spatial biases. In-situ spacecraft measurements have so far not been successful in determining dust composition, but some relevant data on element abundances have been obtained during flybys at comet Halley (*Kissel et al., 1987*). These Halley data suggest that cometary dust has a completely different composition from cometary material, namely a high abundance of the elements CHON, as well as an extremely low density, i.e., a porous structure (**Figure 2-20**). Even less is known about the composition of the dust material close to the Sun. If dust originates from comets, dust grains should be rich in the elements C, H, O, N, which according to some models form organic refractory compounds. In addition to C, H, O, N, the dust is expected to consist to a great extent of silicates and components such as sulfides and metal oxides. Solar wind and suprathermal solar particle material will also be implanted in the surface of grains, enriching the grains in noble gases such as He and Ne. (If the energy of the impinging ions significantly exceeds that of the solar wind, then they will simply pass through the grains). This implantation process should lead to the production of molecules such as OH, H₂, NH, and other light molecular species near the surface of the grains. Ulysses observations of pickup ions at distances of several AU suggest that this is in fact the case. Finally, it has been proposed that an

accumulation of silicon nano-dust forms near the Sun (*Wimmer-Schweingruber and Bochsler, 2003; Habbal et al., 2003*)¹, a suggestion that is currently under critical debate (*Mann et al., 2004; Mann and Czechowski, 2005*). Recent investigation of the dust sublimation sequence has shown that most likely the metaloxides are the last component to sublime and that the nanoparticles that form in the inner solar system are stable against radiation pressure ejection and more likely ejected by Lorentz force, serving as an indicator for solar magnetic field interactions (*Mann et al., 2007*). Aside from this, the composition and evolution of cometary carbon compounds is not well studied and Solar Probe+ provides a unique opportunity for in-situ studies of cosmic dust along its sublimation path.

Sublimation releases material from the dust grains into the solar wind, where it is converted into pickup ions (see Section 2.4.4). The sublimation of meteoritic silicates produces highly refractory metal oxides that can survive at distances as close to the Sun as 2 R_{\odot} . It is not known at what distance from the Sun CHON materials sublime. They are clearly not highly volatile, however, since otherwise they would sublime in the vicinity of the comet.

Solar Probe+ measurements of pickup ions created from material released from the dust by sublimation will provide information about the composition of dust. This information, combined with measurements of spatial variations of dust fluxes, will help establish the relative contributions of the sources of the dust cloud as well as dust composition.

2.4.3 What is the nature of dust-plasma interactions and how does dust modify the spacecraft environment close to the Sun? As indicated in the preceding sections, the interaction of the dust with solar wind plasma significantly affects the dynamics and distribution of the dust—e.g., through charging, the Lorentz force, the pseudo Poynting-Robertson effect, and ion drag. In addition to its interaction with the quasi-stationary wind, the near-Sun dust population also interacts with and is influenced by transient events such as CMEs (*Ragot and Kahler, 2002*). Collisional evaporation, particularly in cometary meteoroid trails, is expected to influence the solar wind parameters measured locally. For example, a recent study shows that dust collisions in the inner solar system can produce some of the heavy species in amounts comparable to the observed inner source fluxes (*Mann and Czechowski, 2005*). The material released in such collisions may be responsible for the enhancements of the interplanetary field measured by Ulysses in association with meteoroid trails (*Jones et al., 2003, Figure 2-21*). These enhancements—

¹ Some solar eclipse observations have been interpreted as evidence for the existence of silicon nano-particles near the Sun (*Habbal et al., 2003*). If true, this finding would be interesting for astrophysical studies, since it has been suggested that silicon nano-particles play a role in the extended red emission (ERE) observed in the diffuse interstellar medium (*Witt et al., 1998; Zubko et al., 1999*). More recent attempts to search for features of silicon nano particles, on the other hand, were not able to detect their signature (*Singh et al., 2004*). The majority of solids thought to be present in cosmic dust sublime within 0.1 AU of the Sun, with some refractory compounds such as metal oxides (e.g., MgO) (*Mann and Murad, 2005*) surviving as close as a few solar radii to the Sun.

which last for minutes to hours, are clustered in space, and occur more frequently in the inner solar system—may be the result of mass loading of the solar wind plasma induced by collisional vaporization in the dust trails (Mann and Czechowski, 2005). It is still an open question how noble gases observed in the inner source are produced, with the solar wind surface interactions being a distinct possibility.

Dust impacting the spacecraft will influence the plasma environment of the spacecraft and may bias plasma and field measurements. Signals due to impact-generated ion cloudlets have been observed by plasma experiments on several spacecraft in the vicinity of planetary rings (Gurnett *et al.*, 1983; Meyer-Vernet *et al.*, 1986), in the interplanetary medium (Gurnett *et al.*, 1997), and during encounters with the comets Giacobini-Zinner, Halley, and P/Borrelly (Neubauer *et al.*, 1990; Oberc and Parzydlo, 1992; Tsurutani *et al.*, 2003).

Dust fluxes are expected to be especially high near the Sun. ***Solar Probe+ will measure these fluxes and characterize the near-Sun dust environment and its effects on in-situ plasma measurements.***

2.4.4 What are the physical and chemical characteristics of dust-generated species? Neutral and ionized material is released from dust grains by various mechanisms, including vaporization, sublimation, desorption, or direct collisions, and moves at speeds comparable to those of the dust grains (~50 km/s and higher). The neutral gas is quickly ionized by the solar wind and photons and, along with the ionized gas, is picked up by the solar wind to form part of the “inner source” pickup ion population (Geiss *et al.*, 1996; Gloeckler and Geiss, 1998; 2001). Inner source pickup ions, discovered with Ulysses, have provided limited knowledge concerning the composition of the gas released from dust and constraints on the spatial distribution and fluxes of dust grains. One of the surprising results has been the detection of noble gases and light elements in the inner source pickup ions having a composition remarkably similar to that of the slow solar wind. Molecular ions in the mass range up to ~40 amu have also been detected. These measurements imply that recycling of solar wind particles through adsorption and desorption constitutes an important mechanism for the origin of the inner source pickup ions. However, the fluxes of dust required to account for the amounts of observed pickup ions exceeds by orders of magnitude the fluxes deduced from zodiacal light observations. Further progress in resolving the origin of inner source pickup ions will require in-situ measurements close to the Sun as well as better models of dust microphysics. ***Solar Probe+ will measure both the dust fluxes and pickup ion densities and composition as a function of radial distance and longitude with sufficient resolution, sensitivity, and dynamic range to characterize the species generated from the dust grains near the Sun and to elucidate the mechanisms by which material is released from the dust.***

Measurement Requirements

- Spatial variation of dust flux as a function of radial distance and latitude from $4 R_S$ to 5 AU
- Distribution functions and composition of inner source pickup ions
- Solar wind bulk parameters
- Solar wind ion composition
- Plasma wave electric field measurements
- Energetic particle spectra and composition
- Magnetic field orientation and strength.

Sidebar: Solar Probe 2005 (Polar) and Solar Probe+ (In-ecliptic): Science Objectives

The new Solar Probe mission (Solar Probe+) defined in this report places the spacecraft in a radically different orbit, confined to within a few degrees of the ecliptic plane and with a closest approach farther from the Sun (9.5 vs 4 R_s) than was envisioned in previous Solar Probe studies, including the 2005 report compiled by the present STD. The STD conducted a trade study to assess the impact of the changed mission design on Solar Probe science and determined that the new concept would allow all of the scientific goals to be attained and, in fact, presented a number of significant advantages over the old design, largely because of the far larger number of passes (21 instead of 2 inside of 30 R_s) and much greater data sampling in this region (over 2100 hours instead of ~160) (Table).

Objective 1: Determine the structure and dynamics of the magnetic fields at the sources of the fast and slow solar wind. Owing to its near-ecliptic orbit, Solar Probe+ will not be able to sample the fast wind directly above its polar source region nor will it be instrumented to measure the photospheric magnetic field. However, the new mission design compensates for the lack of in situ measurements of the fast wind in the polar regions by the length of time that the spacecraft spends in the ecliptic plane inside 20 R_s (over 950 hours, distributed over 7 years), which will allow extended measurement of the equatorial extensions of high-latitude coronal holes well as equatorial coronal holes. Moreover, the lower spacecraft speed in the inner heliosphere—from about 110 km/s for perihelia at 20 R_s to 195 km/s at 9.5 R_s —allows better sampling of the structures, such as plumes, inside the equatorial extensions of the coronal holes. Measurements of the photospheric magnetic field inside such holes will be available from ground-based observatories and possibly from space-based platforms as well (e.g., SDO). (In the 2005 mission design, the PSRI could, for thermal reasons, not even be used at radial distances <20 R_s .) At a radial distance of ~35 R_s , there are two periods per orbit (one inbound, one outbound) where Solar Probe+ will be in quasi-corotation and will cross a given longitudinal sector slowly. In these intervals, the spacecraft will be able to sample the solar wind for significant radial distances along a field line before moving across the sector. These measurements will yield additional important information on the spatial/temporal dependence of structures in the solar wind and on how they merge in the inner heliosphere.

In the case of the investigation of the slow wind and heliospheric current sheet, the greater perihelion distance means that the spacecraft will cross fewer closed field lines. However, the 2005 Probe, in polar orbit, would pass through the streamer belt in 1-2 hours, depending on the geometry of the corona during transit. In contrast, Solar Probe+, orbiting in the ecliptic, will remain inside the streamer belt for a significant fraction of the 3 encounters inside 9.5 R_s (30 hrs) and the previous 5 below 12 R_s (50 hrs). The extensive sampling of the streamer belt region enabled by the new mission design more than compensates for the increase in the minimum perihelion distance.

Objective 2: Trace the flow and elucidate the thermodynamics of the energy that heats the solar corona and accelerates the solar wind. Solar Probe 2005 was expected to encounter the fast wind from polar coronal holes continuously between 6 and 9 R_s , providing ~15 hours worth of in-situ measurements of the fast wind. In contrast, with 80 hours inside 12 R_s and over 400 hours inside 15 R_s (the likely extent of the region where the solar wind flow is sub-Alfvénic), the amount of time Solar Probe+ spends in the fast wind is likely to exceed 20 hours (inside 12 R_s) and 100 hours (inside 15 R_s). These regions lie outside the most-probable ion and electron temperature maxima for a coronal hole, but are still within regions where Alfvénic turbulence is expected to peak, thus allowing definite confirmation/exclusion of the role of low-frequency fluctuations in heating and accelerating the fast wind. The extensive amount of data obtained by Solar Probe+ during these intervals will enable a more detailed understanding of how the plasma distribution functions evolve in the fast wind, which should compensate for the lack of a much smaller set of data that Solar Probe 2005 would acquire between 4 and 9.5 R_s .

Solar Probe+ will perform a much more comprehensive exploration of the streamer belt, although at greater distances, than Solar Probe 2005. Subsonic regions may survive, although with a smaller volume coverage than at 4 R_s (analogously to the filling factor of closed field lines). This loss again is more than compensated by the increased amount of observing time that Solar Probe+ will spend in the explored regions. The role of reconnection and jets and instabilities in the heating and acceleration of the slow wind will therefore be adequately addressed.

Objectives 3 (energetic particles) and 4 (cosmic dust)

The new mission design is significantly better for the remaining two science objectives. Both will benefit from the significant amount of data that Solar Probe+ will acquire during its multiple near-Sun passes. Solar Probe+ will not be able to explore the dust cloud out of the ecliptic plane; however, 90% of the dust resides in the ecliptic, and will be extensively sampled by Solar Probe+, enabling a much more thorough characterization of the cosmic dust population in the inner heliosphere than would have been possible with Solar Probe 2005.

Distance (R_s)	Time (Hrs)	
	2005 Study	2008 Study
<10	36	30
<15	64	434
<20	94	961
<30	164	2149

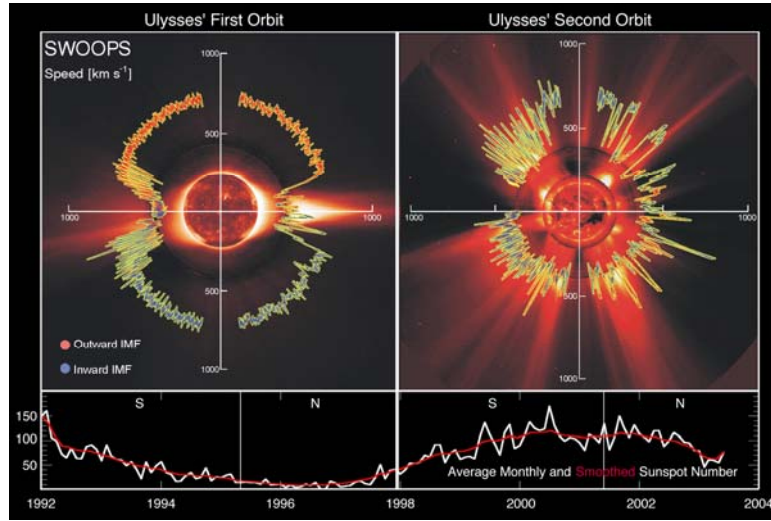


Figure 2-1. Plots of solar wind speed as a function of heliographic latitude illustrating the relation between the structure of the solar wind and coronal structure at solar minimum (left) and solar maximum (right). (Ulysses SWOOPS solar wind data are superposed on composite solar images obtained with the SOHO EIT and LASCO C2 instruments and with the Mauna Loa K-coronameter. [McComas *et al.*, 2003]).

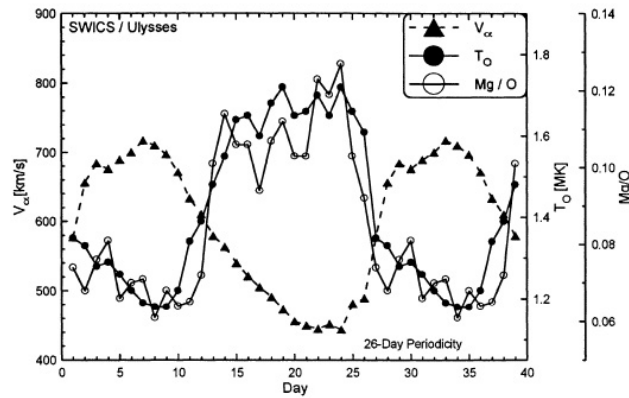


Figure 2-2. Solar wind speed, freezing-in temperatures determined from O^{7+} -to- O^{6+} abundances, and magnesium-to-oxygen ratios as a function of time measured by Ulysses during a low-latitude crossing of alternating high- and low-speed streams. The anti-correlation of wind speed with electron temperature as determined from the freezing-in temperature is dramatic, calling into question the role of thermal electrons in driving the solar wind. (Geiss, Gloeckler, and v. Steiger, 1995).

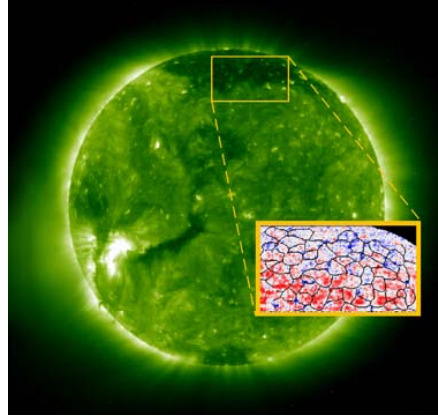


Figure 2-3. Polar coronal holes, such as that seen in this SOHO/EIT image, are the source of the fast solar wind. SUMER measurements of Doppler-shifted coronal emission lines superposed on the magnetic network (inset) suggest that the high-speed outflow from coronal holes is associated with the chromospheric network (*Hassler et al., 1999*). Local measurements of outflows from the equatorial extension of coronal holes will provide the data needed to test the hypothesis that the primary source region for the fast solar wind is in the magnetic network.

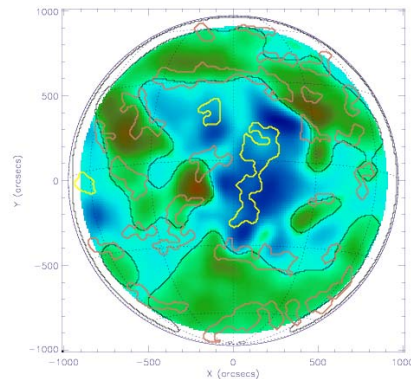


Figure 2-4. Black line is the neutral line separating magnetic field regions of opposite polarity (green and blue). The darkest colors correspond to the strongest magnetic flux imbalance. Yellow contours are coronal holes. Pink contours are filaments. [Courtesy I. Scholl]

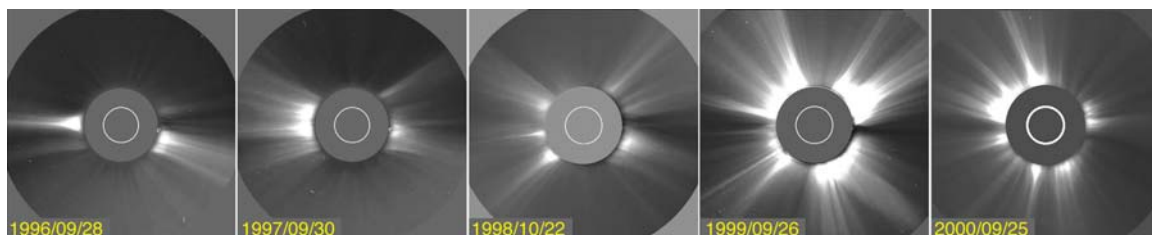


Figure 2-5. SOHO/LASCO C2 images showing the evolution of the streamer belt during the rising phase of Solar Cycle 23. With increasing activity, polar coronal holes shrink and streamers appear at higher and higher heliolatitudes. The solar wind loses its orderly bimodal character and becomes a complicated mixture of fast flows from small coronal holes and transients embedded in a moderate-to-slow wind from all latitudes.

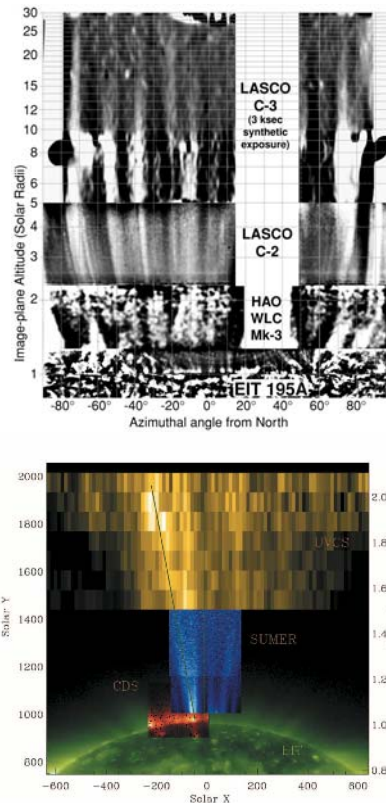


Figure 2-6. Top: A composite image showing the polar plumes and interplume regions from the surface out to a distance of $30 R_S$ (DeForest *et al.*, 2001). Such plumes have also been observed within equatorial coronal holes (Del Zanna and Bromage, 1999). Bottom: Composite showing detailed plume structure in the lower corona (Teriaca *et al.*, 2004). It is unknown how coronal plumes are formed, how their density structures are maintained in the solar wind, and what their fate in the more distant heliosphere is, as in-situ measurements from 1 AU are unable to identify them.

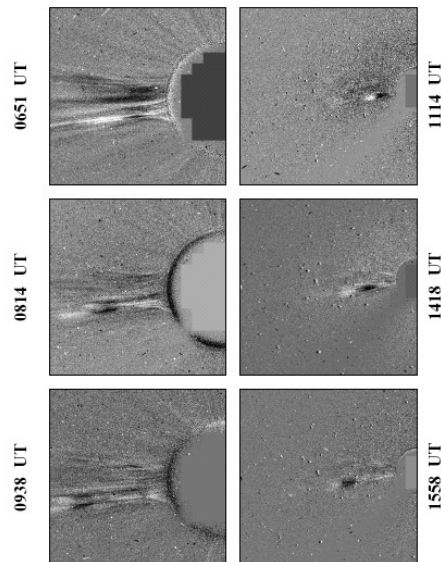


Figure 2-7. Difference images from the SOHO/LASCO coronagraphs showing the expulsion of material from the streamer belt (Sheeley *et al.*, 1997). These images show how dynamic the release of mass from the magnetically confined corona may be.

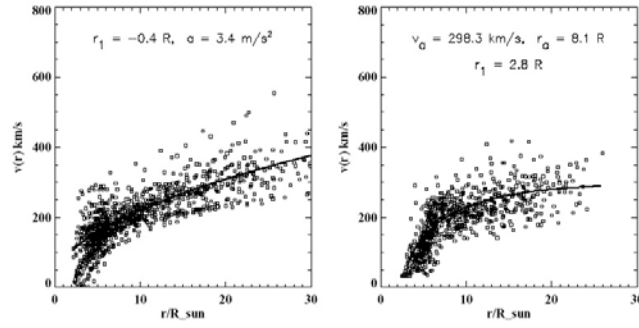


Figure 2-8. Scatter plots of the speed of density perturbations, or plasma puffs, as determined from difference images from the SOHO/LASCO instrument, as a function of distance from the Sun, together with a best fit for the radial velocity profile (*Sheeley et al., 1997*). The plasma puffs serve as tracers of the slow solar wind, which experiences acceleration over a more (top panel) or less (bottom panel) extended radial distance from the Sun. Local measurements of densities and speeds within this full distance range can determine the contribution of plasmoids to the overall mass flux from the Sun.

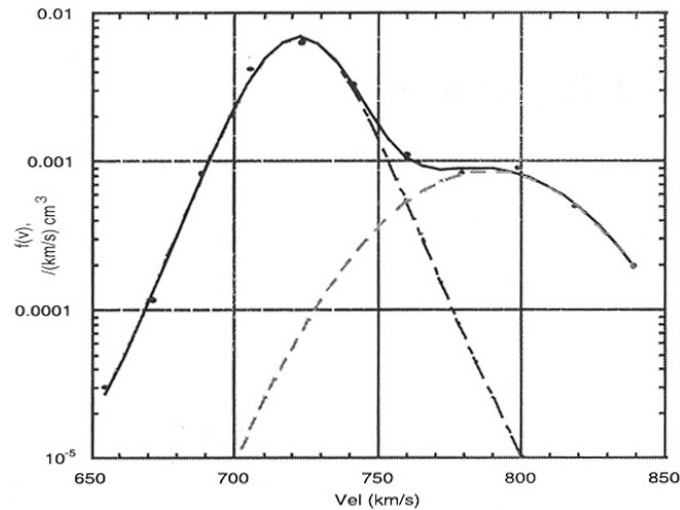


Figure 2-9. Two-beam model fit to the logarithm of phase space density for the Ulysses proton spectrum in the high-speed solar wind (*Goldstein et al., 2000*). A proton beam with a drift speed of about 50 km/s, i.e., the Alfvén speed, gives the best fit. Continuous plasma measurements inside 65 R_S can be used to determine where this beam forms and whether it is the direct remnant of the acceleration mechanism or is produced in-situ by wave-particle interactions.

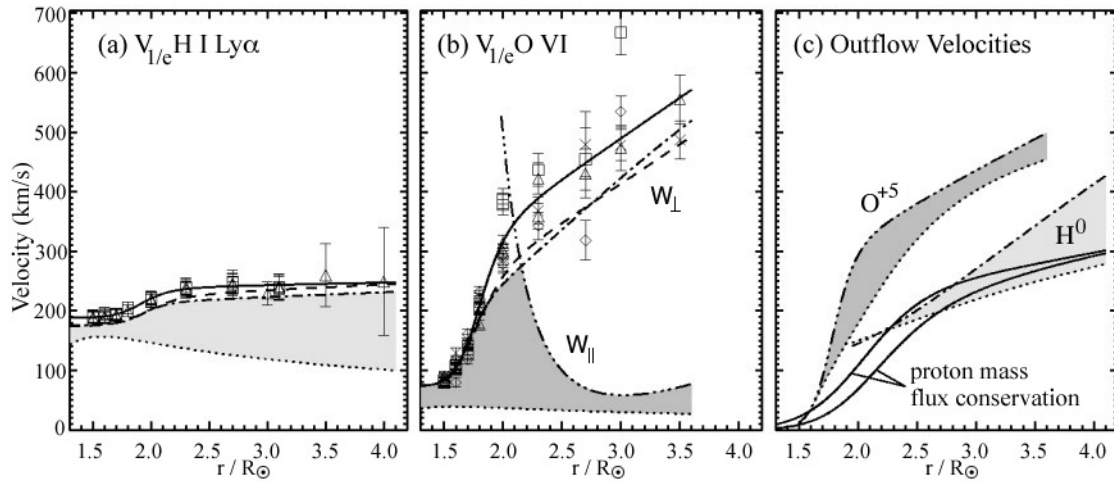


Figure 2-10. SOHO/UVCS emission line width observations show anisotropic velocity distributions of neutral hydrogen (a proxy for protons) and O^{5+} and preferential acceleration of minor ions relative to the hydrogen atoms. Shaded areas indicate uncertainties due to thermal broadening. Preferential acceleration of the minor ions may result from ion-cyclotron resonance or from wave-particle interactions involving nonlinear Alfvén waves (Kohl *et al.*, 1998).

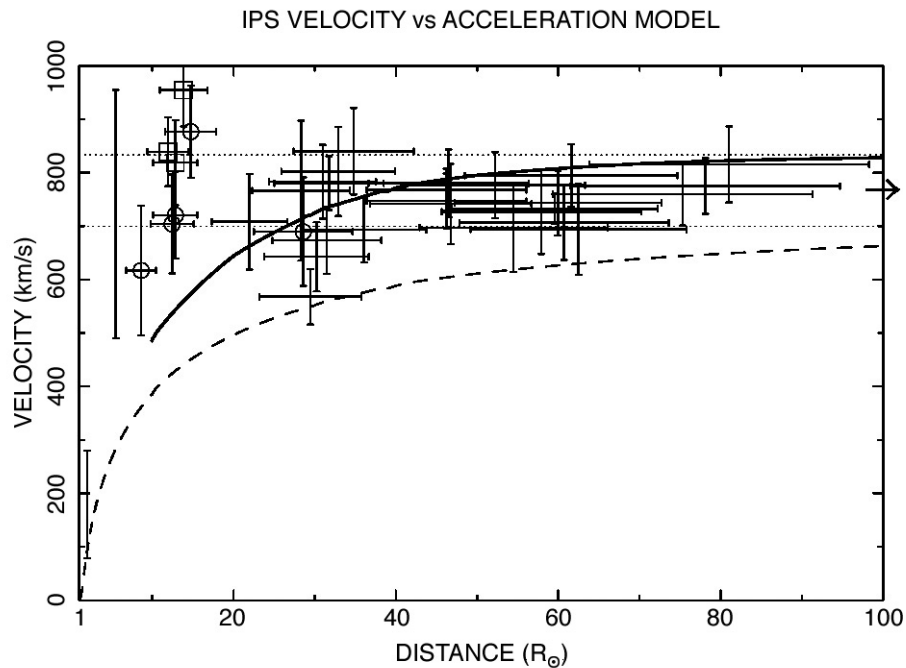


Figure 2-11. Apparent flow speed of the fast wind vs. distance determined from radio scintillation measurements by EISCAT, VLBA, and Spartan 201-01, showing rapid acceleration of the solar wind at distances $\leq 10 R_S$ (Grall *et al.*, 1996). These measurements rely on the phase shifts in radio signals caused by the movement of density structures across the line of sight, and therefore contain the effects of compressive waves.

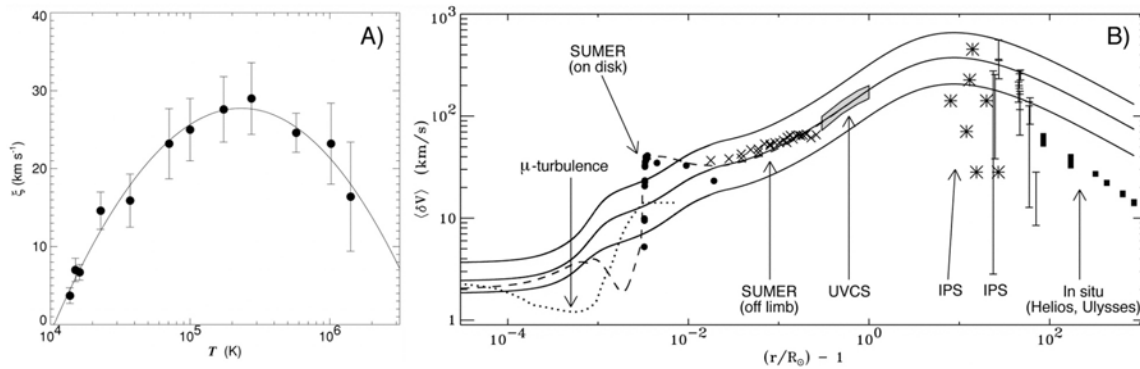


Figure 2-12. a) Non-thermal component to line model broadening in the solar atmosphere as a function of temperature showing a maximum around 30 km/s at transition region heights (*Chae et al.*, 2002). **b)** Composite of observations of magnetic field and velocity field fluctuation amplitude with height in the solar atmosphere (*Cranmer and van Ballegoijen*, 2005). Note the gap between the data labeled UVCS and IPS, where in situ measurements of velocity and magnetic field fluctuations are needed to clarify the role of such fluctuations in coronal heating and solar wind acceleration.

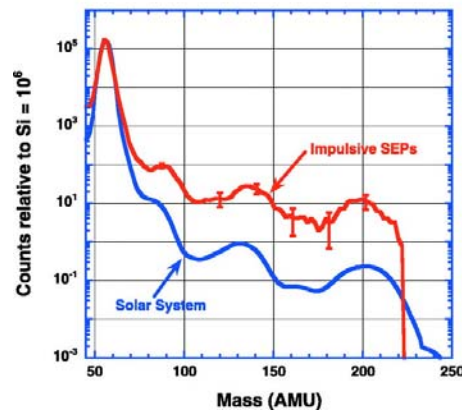


Figure 2-13. Nuclei with mass >90 ($Z > 40$) are overabundant in impulsive SEP events (compared to solar material) by factors ranging from ~ 10 to ~ 50 when normalized to Fe. Since Fe is itself overabundant by a factor of ~ 10 , the $Z > 40$ overabundance is even greater when normalized to He or oxygen (observations by *Mason et al.* [2004]). The origin of these overabundances is not understood.

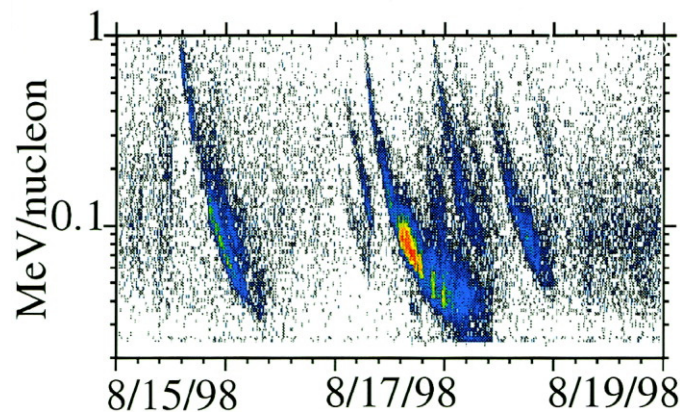


Figure 2-14. Energy vs. time plot showing a series of impulsive events observed by ACE in 1998 (*Mason et al.*, 1999). Because of velocity dispersion, the highest energy particles arrive first.

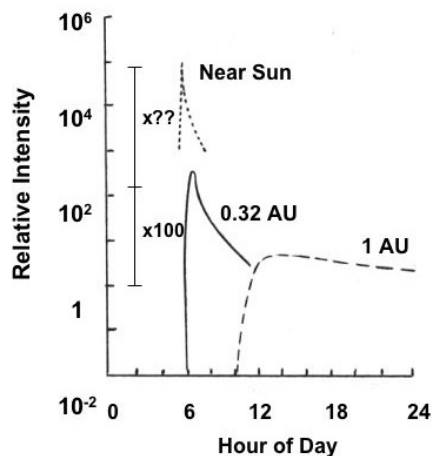


Figure 2-15. Time profiles of an impulsive ^3He -rich event observed at 1 AU on May 17, 1979 by ISEE-3 and at 0.32 AU by Helios-1 (based on data in *Mason et al.* [1989]). Both spacecraft were magnetically well-connected to the flare site. Note that the peak intensity is ~ 100 times greater at 0.32 AU. Closer to the Sun the event will be even more localized in time.

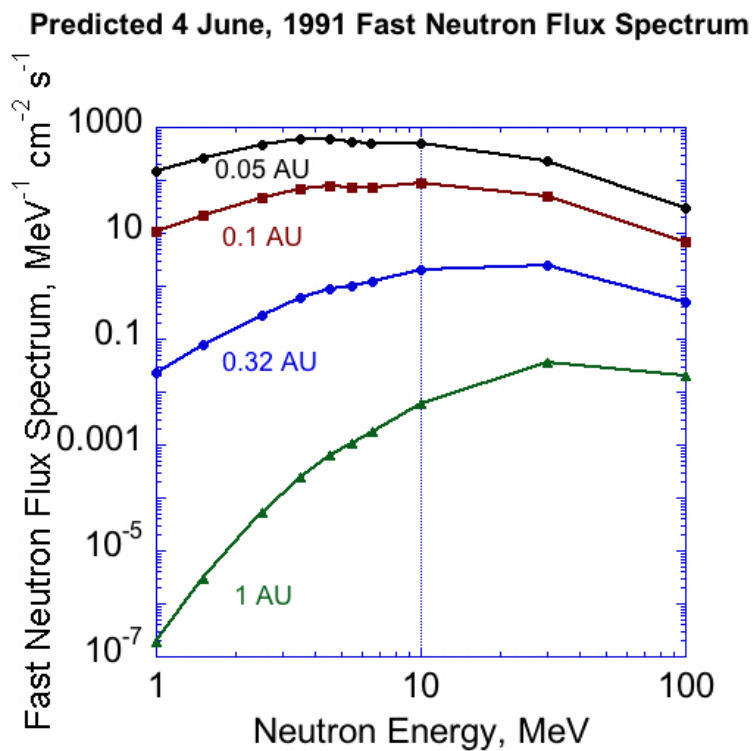


Figure 2-16. Neutron flux as a function of neutron energy and distance from the Sun for the solar flare that occurred on 4 June, 1991 (*Murphy et al.*, 2007). The increase in flux with decreasing radial distance illustrates the great advantage of making neutron measurements as close to the Sun as possible and the benefit of using Solar Probe Plus as a neutron measurement platform.

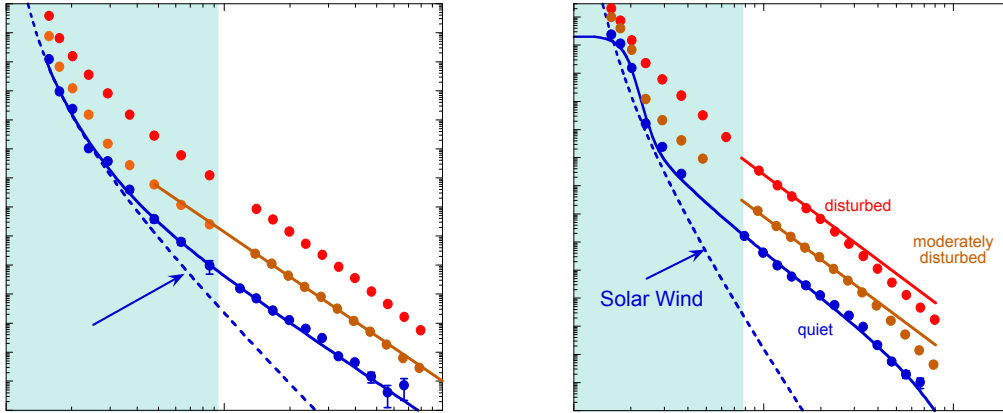


Figure 2-17. Velocity distributions of H and He measured with the ULEIS and SWICS instruments on ACE during quiet times, moderately disturbed and disturbed times. Power law tails (in the solar wind frame), with spectral index -5 , extend to $W \approx 50$ (2.5 MeV).

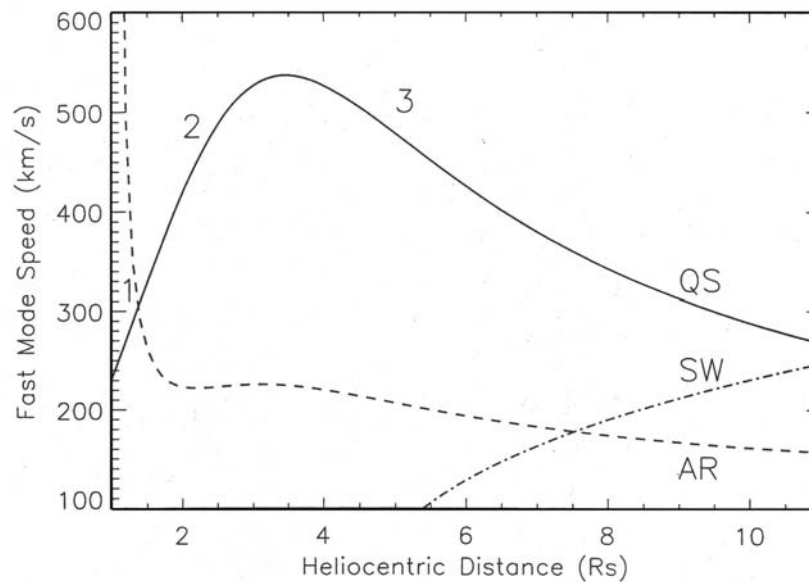


Figure 2-18. Estimated speed profile of the fast magnetosonic mode (V_{fast}) in the quiet Sun (QS) and in the active region (AR) coronas (from Gopalswamy et al., 2001). The Alfvén speed is expected to vary with location and time by as much as a factor of 3 (see also Figure 1-1). Conditions for shock formation differ in the three regions marked 1, 2, and 3. A CME can form a shock if the CME speed exceeds the sum of V_{fast} plus the solar wind speed (SW), one estimate for which is shown above. Shocks formed inside $\sim 3 R_S$ will not propagate into the quiet corona beyond $\sim 3 R_S$ unless they have speeds greater than ~ 540 km/s; however, the CME driver could form a new shock once beyond the peak. The height of the peak in the V_{fast} curve depends on the actual density and magnetic field values in a given location, but the shape of the curve will be the same. Measurement of these quantities and their variability near the Sun would reveal where and how easily shocks can form and would provide ground truth for models of SEP acceleration by fast CMEs.

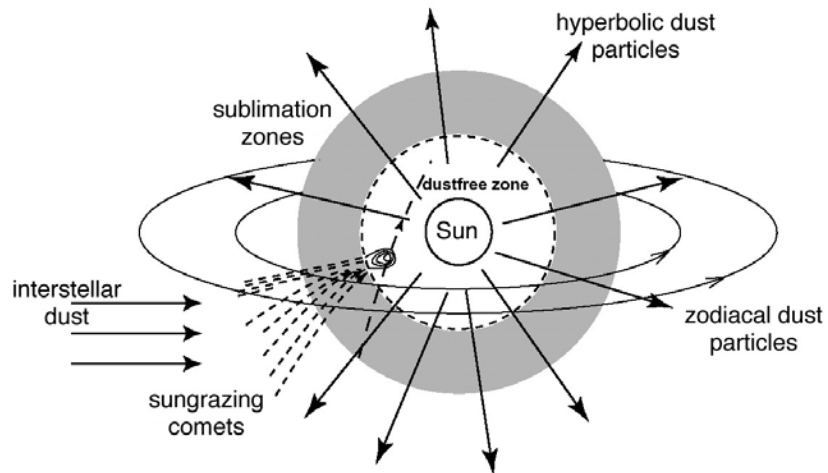


Figure 2-19. Sketch illustrating the dust environment near the Sun. Most of the dust near the Sun is bound in Keplerian, roughly circular orbits near the ecliptic, although some dust particles are ejected by radiation pressure on hyperbolic trajectories as b-meteoroids. Comets and asteroids are the principal sources of the solar dust cloud, with smaller contributions from sungrazing comets and interstellar dust. (Mann *et al.*, 2004)

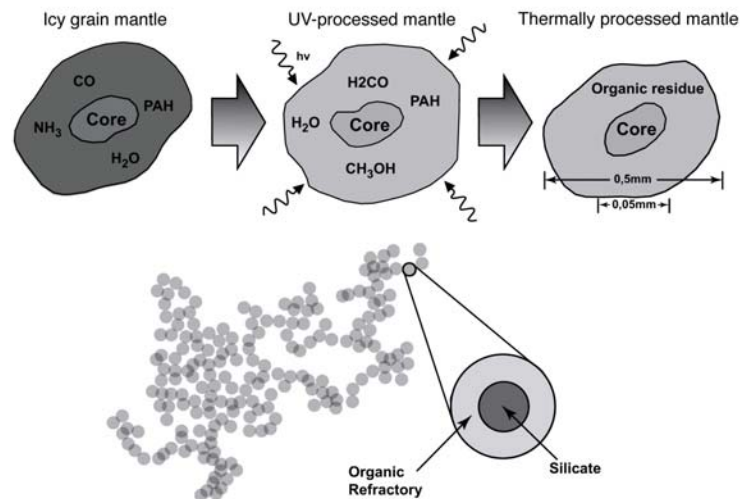


Figure 2-20. Sketch illustrating the evolution of a cometary dust grain. Cometary dust grains are produced by collisions in meteoroid streams inward from 1 AU. By sampling pickup ions created from the sublimated material, it is possible to obtain information about the composition of the organic refractory materials in comets.

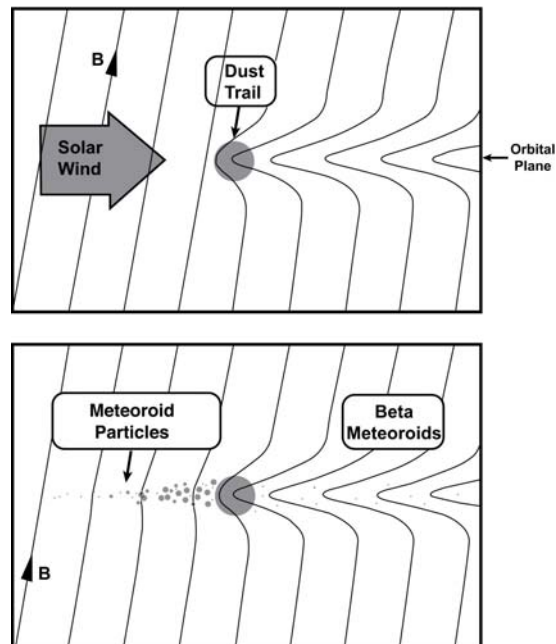


Figure 2-21. Cross-sectional sketch of cometary dust trail illustrating the formation of an interplanetary field enhancement (IFE). Such IFEs have been observed with Ulysses and correlated with meteoroid trails (cf. *Jones et al.*, 2003). It is hypothesized that the IFEs result from mass loading of the solar wind by material produced by collisional vaporization in dust trails.

3. Science Implementation

The Solar Probe+ science objectives will be addressed through a combination of in-situ and remote-sensing observations made from a near-ecliptic heliocentric orbit at progressively closer distances to the Sun, with the spacecraft achieving a minimum perihelion distance of $\sim 9.5 R_S$ roughly six and a half years after launch (**Figures 3-1**). The Baseline Mission provides for 24 passes inside 0.16 AU ($35 R_S$), with 19 passes reaching inside $20 R_S$ of the Sun. The first near-Sun pass will occur three months after launch, at a heliocentric distance of $35 R_S$. During the final phase of the prime mission, the spacecraft will make three passes, separated by 88 days, at the minimum perihelion distance of $\sim 9.5 R_S$. Thereafter, in any extended mission, Solar Probe+ will add four additional passes to a perihelion of $\sim 9.5 R_S$ each year. The phasing of the Solar Probe+ orbit with respect to the Earth during the minimum perihelion passes will allow for simultaneous remote-sensing observations of coronal and photospheric features by ground-based, sub-orbital, and space-based assets (see Section 3.3 below). With a May 2015 launch, the Solar Probe+ prime mission will begin near the end of Solar Cycle 24 and end near the predicted maximum of cycle 25 in 2022. During these ~ 7 years, Solar Probe+ will spend a total of 961 hours inside $20 R_S$, 434 hours inside $15 R_S$, and 30 hours inside $10 R_S$, guaranteeing sampling of all types of solar wind (**Figure 3-2**).

Solar Probe+ will make in-situ measurements of plasma, suprathermals, energetic particles, magnetic fields, waves, neutrons/ γ -rays, and dust in the near-Sun environment, while hemispheric white-light imaging of the corona will provide context for the in-situ measurements. (The baseline payload is described below, in §3.2). The measurements required to address the four Solar Probe+ science objectives are listed in the preceding section, at the end of the discussion of each subquestion. They are summarized in the Traceability Matrix (**Table 3-1**), which also briefly suggests investigative strategies that might be employed in answering the subquestions. The STDT followed a strict traceability process to derive measurement requirements from the science objectives and subquestions and instrument specifications from the measurement requirements. Measurements that are *required* to address a specific question are identified in the Traceability Matrix by the letter “R,” while “S” denotes *supporting* measurements. As can be seen from the Traceability Matrix, Solar Probe+ will address each science question with multiple kinds of measurements, thus ensuring comprehensiveness and providing redundancy and resiliency in the event that a particular instrument should fail.

3.1 Minimum Criterion for Success

Science objectives 2.1, 2.2, and 2.3 relate directly to Solar Probe+’s overall goal: to determine how the Sun’s corona is heated and how the solar wind is accelerated. Thus the STDT recommends that the following requirement be established as the minimum success criterion for the Solar Probe+ mission: ***Solar Probe+ must make measurements that address any two of the three questions under each of the***

first three science objectives (2.1, 2.2, and 2.3). The Baseline Mission (three passes with perihelion at $<10 R_S$) will provide the richest scientific yield, enabling comparative studies of the corona and solar wind at two different phases of the activity cycle. However, the STDT considers that the minimum success criterion can still be satisfied by the first solar pass reaching below $10 R_S$ and at least 500 hours within $20 R_S$.

3.2 Baseline Payload

To meet the Solar Probe+ science objectives, the STDT recommends an integrated payload comprising in-situ and remote-sensing instruments serviced by a common data processing unit (DPU) and low-voltage power supply (LVPS). The use of a common DPU/LVPS reduces mass, power, cost, and complexity through the sharing of resources among the instruments. As pointed out in the 1999 and 2005 Solar Probe reports [Gloeckler *et al.*, 1999; McComas *et al.*, 2005], development of the payload as an integrated package under the direction of a single principal investigator provides streamlined and efficient project management and effective cost and schedule control. A single integrated payload has been assumed in the engineering study and cost estimate and was instrumental in achieving the aggressive cost cap provided to the STDT for this study.

Solar Probe+'s in-situ instrumentation consists of a Fast Ion Analyzer, two Fast Electron Analyzers, an Ion Composition Analyzer, an Energetic Particle Instrument, a Magnetometer, Plasma Wave Instrument, a Neutron/Gamma ray Spectrometer, and a Coronal Dust Detector. The remote-sensing instrument is a Hemispheric Imager for white-light imaging of coronal structures. The specifications for each instrument and their rationale are discussed in the sections that follow.

Tables 3-2 and **3-3** summarize, respectively, the instrument specifications and resource requirements for the baseline payload. To determine the instrument specifications the STDT translated the Solar Probe+ science objectives into measurement requirements (cf. **Table 3-1**) and these into specific sensitivity, range, and resolution requirements. The mass, power, and data rate allocations shown in **Table 3-3** are based on those of past or existing instrumentation or components. In addition to the core payload

Resolving Space-Time Ambiguities

Distinguishing between spatial structures and temporal variations is a well-known problem in the interpretation of in-situ data acquired from a single spacecraft. In the case of Solar Probe, this problem will be resolved by 1) imaging the local corona with an onboard wide-angle white-light coronagraph and 2) remotely observing the corona and underlying regions from Earth-based and near-Earth imagers, while simultaneously performing in-situ measurements of the coronal plasma and fields. At $30 R_S$, Solar Probe will already be embedded in both large- and small-scale coronal structures such as plumes and streamers (cf. Figure 2-5). The Probe's white-light Hemispheric Imager (Section 3.2.8) will image these structures and the local environment through which the spacecraft is flying, and the resulting images can then be analyzed together with the simultaneous remote observations and in-situ data to distinguish spatial from temporal effects. In addition to this technique, it will be possible to perform statistical studies using the data sets from the 24 perihelion passes to establish which features in the in-situ data are indicative of spatial structures and which result from temporal variations.

specified by the STDT, Table 3-3 also includes resources for an additional experiment. While the STDT discussed several possible measurements that might enhance the core payload (e.g., an EUV spectrograph or a neutral solar wind sensor), it is our intention that NASA should compete this additional instrument without specifying the type of observations and select the best addition to the core science.

3.2.1 Fast Plasma Instrumentation. The Solar Probe+ Fast Plasma Instrumentation consists of a single Fast Ion Analyzer (FIA) and a pair of Fast Electron Analyzers (FEAs). The FIA and one of the FEAs are mounted, together with the ICA, on a bracket on the +X/-Y side of the spacecraft; this bracket provides viewing to near the edge of the heat shield umbra during closest approach to the Sun and is angled so that the instrument apertures point into the ram direction. This close mounting, combined with the large aberration angles of the solar wind allow good viewing of most of the ion distribution functions when Solar Probe+ is near the Sun. At greater heliocentric distances the Solar Probe+ spacecraft can be slightly off-pointed from the center of the Sun, again allowing good viewing of the ions. The second FEA is mounted on the anti-ram side of the spacecraft body, pointing 180° away from the first. While the mission-unique aspects of Solar Probe+ will require new designs for the FIA and FEA instruments, the basic designs and subsystems can be drawn from a wide variety of previous heritage missions such as Helios, Ulysses, and ACE.

Fast Ion Analyzer (FIA). The FIA should be capable of measuring two- and three-dimensional distribution functions for protons and alphas over the energy/charge range of 50 eV/q to 20 keV/q. This energy range covers the lowest and highest expected speeds for 100 km/s protons and 1400 km/s alpha particles, respectively. FIA's 3D temporal resolution of 3 seconds and 0.1 second for two-dimensional distribution functions allows identification of boundaries in the solar wind down to ~1000 km near perihelion and wave modes (e.g., the gyrofrequency is ~30 Hz over the poles). The energy resolution ($\Delta E/E$) should be ~5%, which does a good job of resolving the supersonic solar wind beam all the way out to perihelion. The sensitivity and dynamic range need to be adequate to measure 2D (energy and one angle) ion distributions in 0.1 s at 20 R_S without saturating the detectors all the way into perihelion. The FIA's field of view needs to observe as much of the ram side of the viewing space as possible. For example, a top-hat analyzer with an ~330° fan in the X-Y plane (with some obscuration by the spacecraft) that deflects over 90° ($\pm 45^\circ$) in the X-Z plane, extending upward from the edge of the heat shield obscuration, provides adequate coverage. To resolve the ion distributions everywhere from 1 AU into perihelion, FIA's angular resolution needs to be ~5° around the solar wind beam and ~30° over the remainder of its field-of-view (FOV).

Fast Electron Analyzer (FEA). The FEAs should be capable of measuring two- and three-dimensional electron distribution functions over the energy range from ~1 eV to 5 keV. This energy range covers from the lowest energy photoelectrons, through the thermal, core population and well up into the suprathermal halo population. The FEAs' 3D temporal resolution of 3 second (0.1 second for two-

dimensional distribution functions of energy and one angle) is matched to the FIA to help resolve plasma conditions and structures on the same scales. The energy resolution ($\Delta E/E$) should be approximately 10%, which does a good job of resolving the hot electron distributions. Like the FIA, the FEA requires a sensitivity and dynamic range adequate to measure the 2D distributions in 0.1 s at 20 R_S without saturating the detectors all the way into perihelion. Together the FEA need to observe as much of 4π sr as possible; all-sky imagers and deflecting top-hat analyzers are both appropriate approaches for achieving the needed FOVs. To resolve possibly very narrow halo electron beams (the strahl), the FEAs need angular resolutions that approach 3° in at least one dimension at higher energies around the magnetic field direction (this information is supplied real-time from the magnetometer via the payload DPU), while $\sim 30^\circ$ angular resolution is adequate to measure the remainder of the halo population and the core and photoelectron populations at lower energies.

3.2.2 Ion Composition Analyzer (ICA). The Ion Composition Analyzer (ICA) is mounted, together with the FIA and one FEA, on the bracket referred to above. The ICA should be capable of measuring two- and three-dimensional distribution functions of He and heavy ions in the solar wind, over an energy range from ~ 100 eV/q to ~ 60 keV/q and a mass range from 2 to $> \sim 60$ amu. The required energy range covers all major solar wind species that will be observed during the solar encounter. ICA's 3D temporal resolution of 10 seconds (at 20 R_S) permits temporal and spatial effects to be distinguished and allows comprehensive assessment of the non-thermal properties of the distribution functions that are generally expected from various solar wind acceleration and heating mechanisms. Furthermore, with the required mass range the ICA will measure species with low ionic charge states (i.e., He^+) and high masses (i.e., SiO_2), such as those produced from neutral sources in the inner heliosphere or created by the solar wind's interaction with dust near the Sun (e.g., inner source pickup ions). The energy resolution ($\Delta E/E$) should be $\sim 5\%$, sufficient to resolve the supersonic solar wind beam out to aphelion. The sensitivity should be sufficient to measure He/O ratios every 10 seconds at 20 R_S , which can be achieved by scaling from 1 AU observations of solar wind composition and charge states. The dynamic range should be $\sim 10^4$. The ICA field of view (FOV) needs to observe as much of the ram side of the viewing space as possible due to the large amount of variability expected due to turbulence or waves in the outer corona. This can be achieved, for example, with a tophat and swept field of view, or with an instrument with large instantaneous FOV as done on MESSENGER, provided that the edge of the FOV extends to close to the heat shield. To resolve the ion distributions everywhere from 1 AU to perihelion, ICA's angular resolution needs to be $\sim 10^\circ$ around the solar wind beam and $\sim 20^\circ$ over the remainder of its FOV.

3.2.3 Energetic Particle Instrument (EPI). The Solar Probe+ Energetic Particle Instrumentation (EPI) consists of a Low-Energy sensor (EPI-Lo) and a high energy sensor (EPI-Hi). Both packages are to be

mounted on the spacecraft body, where they view particles incident from both the sunward and anti-sunward hemispheres.

EPI Low-Energy Instrument (EPI-Lo). The EPI low-energy instrument is required to measure the composition and pitch-angle distributions of energetic particles. The composition includes hydrogen to iron as well as energetic electrons. As a minimum the detector should be able to make the ion measurements from ~ 20 keV/nucleon to ~ 1 MeV/nuc and the electron measurements from ~ 25 keV to ~ 1 MeV. Composition measurements should discriminate protons, ^3He , ^4He , C, O, Ne, Mg and Si, and Fe. The measurements should have sufficient angular spread and resolution to enable pitch-angle measurements of the differential particle fluxes for a (nominal) radial magnetic field. A “slice” field of view of $\sim 10^\circ$ wide and $>120^\circ$ and at least 5 angular bins would suffice; at least 120° coverage and an angular resolution of no worse than 30° are required. The wider opening should be aligned with the spacecraft axis with the field of view just clearing the thermal protection system. Larger solid angle coverage and better species resolution are, of course, preferred. The preferential mounting is with the instrument field of view in the ram direction (or as close thereto as possible) to enhance the coverage of the particle population via the aberration due to the spacecraft velocity (at a $10 R_S$ perihelion, the spacecraft speed is ~ 200 km/s and an energy of 20 keV/nuc corresponds to a speed of ~ 2000 km/s). The sensitivity should be at least $\sim 1 \text{ (cm}^2 \text{ ster s keV)}^{-1}$. Timing resolution should be no worse than 1s for e^- , 5s for protons, and 30s for heavier nuclei. The capabilities described here can be achieved with energetic particle instruments of the type currently being flown on MESSENGER, STEREO, and New Horizons.

EPI High-Energy Instrument (EPI-Hi). The EPI high-energy instrument (EPI-Hi) is required to measure the composition and energy spectra of energetic nuclei with $1 \leq Z \leq 26$ from ~ 1 to 100 MeV/nuc, as well as energetic electrons from ~ 0.3 to 3 MeV. The source of the energetic ions to be observed over the course of the Solar Probe+ mission range from quiet-time intensities of cosmic rays, to low-energy ions accelerated in CIRs and transient interplanetary shocks, to ions accelerated in small, impulsive events associated with solar flares, to solar energetic particles accelerated in large gradual events associated with CME-driven shocks. As a minimum, the charge resolution should be sufficient to measure differential intensities of H, He, C, N, O, Ne, Mg, Si, and Fe, although minor species are also of interest. It would also be very useful (but is not required to satisfy the minimum science requirements), to extend composition measurements (of element groups) to include nuclei with $30 \leq Z \leq 83$ that are found to be enhanced in some SEP events associated with impulsive solar flares. It is required that ^3He and ^4He be separately identified whenever the $^3\text{He}/^4\text{He}$ ratio exceeds 1%. Assuming that onboard particle identification is used to sort species into a matrix of species versus energy bins, the energy resolution of these bins should be no worse than six intervals per decade.

Near the Sun it can be expected that energetic ions may be highly anisotropic and beamed along the interplanetary magnetic field, which is expected to be on average radial at closest approach, but could be highly variable. It is therefore desirable for the EPI-Hi instrument to sample as much of 4π sr as possible,

including, in particular, the forward hemisphere. As a minimum EPI-Hi should be able to observe particles with pitch angles ranging from 30° to 120° with respect to the spacecraft Z-axis with an angular resolution no worse than 30°. EPI-Hi should have sufficient directional information so as to be able to determine the magnitude and direction of 3D anisotropies.

Although not well known, it is expected that the intensity of impulsive SEP events will scale with distance from the Sun (R) approximately as R^{-3} (cf. *Reames and Ng*, 1998, and references therein), while the Helios data indicate an $\sim R^{-2.4}$ scaling for the peak intensity of gradual SEP events (*Lario et al.*, 2005). To observe particle populations that range from quiet-time levels near 1 AU to solar energetic particle (SEP) events near the Sun requires a dynamic range of $\sim 10^7$. The peak intensity of a typical impulsive event at 1 AU is ~ 1 to 10 protons/cm²-sr-sec >1 MeV. Scaling this to 10 R_s by R^{-3} suggests that intensities up to $\sim 3 \times 10^5$ protons/cm²-sr-sec >1 MeV should be measurable. For gradual events it is expected that several events with peak intensities ~ 5 -10 times greater than the largest of solar cycle 23 (e.g., the Bastille Day event) will be observed (proton intensities of $>10^5$ protons/cm²-sr-sec >10 MeV). Particle intensities should be measured with a timing resolution that is no worse than 1-s for electrons, 5 s for H, and 30s for $Z \geq 2$ nuclei. There is considerable heritage for energetic particle instruments in the 1 to 100 MeV/nucleon energy range. Instrument designs that could be adapted to meet these requirements (assuming modern, low-power, low-mass electronics) have flown on Helios, Voyager, ISEE-3, Ulysses, Wind, ACE, and STEREO.

3.2.4 DC Magnetometer. The Solar Probe+ DC Magnetometer (MAG) will provide context and definition of local magnetic structure and low-frequency (< 10 Hz) magnetic fluctuations. MAG consists of one or more 3-axis sensors mounted close to the end of a deployable, non-retractable axial boom extending from the bottom deck of the spacecraft.

The MAG sensor will be located close to the search coil component of the Plasma Waves Instrument (PWI), making it necessary for both to work together to provide a suitable measurement environment. Close collaboration between the two teams is critical to containing cross contamination of the instruments and providing for the success of the mission. Signatures of plasma processes at the proton inertial scale, which result in the conversion of magnetic energy into heat, fall within the frequency range of the PWI; and only two suitably configured instruments will be able to provide the needed plasma diagnostics.

MAG Performance. Photospheric structures with scale sizes of 10s of km will have scale sizes of 100s of km if they are coherent out to the orbit of Solar Probe+. A sample rate of 20 Hz gives a spatial resolution of approximately 30 km at $\sim 10 R_s$, which will provide minimal resolution of the magnetic structures. A burst or snapshot mode of higher time resolution is used for comparison with the PWI. Data telemetry compression to 16 bits/component (dynamic range 65536) will permit adequate retention of measurement resolution. Total telemetry dedication of 960 bits/sec will permit adequate download of continuous 20 Hz vector measurement plus snapshot buffer.

Extrapolation of Helios data acquired at distances ≥ 0.3 AU indicates an average IMF of approximately 260 nT at 20 R_s . Various measurements and theories suggest that, within some regions and structures, the magnetic field might be as high as 1 G at 10 R_s . MAG should be capable of switching sensitivity ranges. Several ranges are needed, with the most sensitive being $|B| < 0.1$ nT and the high-field range $|B|$ significantly larger than 1 G. With some adjustment to accommodate the upper range, this requirement could be met with magnetometers commonly flown on magnetospheric missions today.

Magnetic Cleanliness. For an expected field of ~ 250 nT, a DC cleanliness requirement at the magnetometer of 10 nT would be reasonable, with a low-frequency AC requirement of 1 nT. Given the small size of the spacecraft and short boom, cooperation between the instrument and spacecraft teams in controlling magnetic contamination is imperative and the spacecraft will need to enforce a minimal magnetic cleanliness program. This program need not add significant cost, but cleanliness must be addressed to achieve the core science goals of the mission.

3.2.5 Plasma Wave Instrument (PWI). The PWI sensors consist of a 3-axis search coil for detecting magnetic field fluctuations and a 3-element electric field antenna. The search coil sensor is mounted on the aft spacecraft boom, separated from the DC magnetometer and other instruments to minimize contamination of the search coil data. The electric field antenna is mounted on the base of the spacecraft, with the three antenna elements separated by $\sim 120^\circ$. Each element is ~ 1.90 m long, with the last meter electrically isolated from the inner part of the antenna. The antenna inclination to the spacecraft axis is fixed such that the last meter of all antennas extend beyond the umbra at closest approach. This arrangement allows the maximum separation between the outer antenna segments to facilitate quasi-thermal noise spectroscopy measurements inside 20 R_s . Having the end segments of the antenna elements sunlit enables low frequency ($< \sim 3$ kHz) plasma waves to be sampled. Characterizing waves in this frequency range will provide insight into processes at and below the ion inertial scale.

Plasma wave instruments with the necessary capabilities have been implemented on numerous missions, including Cluster, Polar, FAST, and Geotail. Similar antenna concepts have been used on these missions, however they were not designed to work in the thermal environment expected for Solar Probe+. In order to be accommodated safely on the spacecraft the PWI antenna will need to be made from a refractory material that will operate at temperatures up to 1500 °C. As with any hardware that extends out into solar illumination anywhere near perihelion (because such items have a mission critical effect on the thermal environment), the PWI flight antennas must be implemented and controlled as an integrated part of the overall thermal protection system.

Search Coil Magnetic Field Measurements. The PWI magnetic field experiment should operate in the frequency range ~ 1 Hz to 80 kHz, allowing overlap with the DC magnetometer at low frequencies and to measure fluctuations beyond the ion cyclotron frequency at high frequencies (The sensitivities of the

search coil and DC magnetometer are expected to be equivalent at approximately 10 Hz). The strawman instrument samples in frequency space at 40 channels per decade, with cross-spectral power between the field components at 20 channels per decade. Bursts of waveform data also collected at a cadence of up to 60 s to allow detailed study of small-scale processes in the near-Sun plasma.

Electric Field Measurements. The PWI electric field experiment should measure fluctuations in the electric field from close to DC to above the plasma frequency (1Hz to 10MHz was chosen for the strawman instrument) so as to return information on low-frequency wave, turbulence and small-scale structures and to diagnose plasma parameters (density and temperature) using the technique of quasi-thermal noise spectroscopy (QNS). QNS requires sampling total electric field fluctuations from low frequency to above the plasma frequency. The strawman instrument has a sampling density of 40 samples per decade, a temporal sampling period of 0.1 s to allow rapid sampling of plasma parameters local to the spacecraft. A sensitivity of 2×10^{-17} V/m²/Hz at 10 MHz provides adequate signal to noise for QNS measurements. The strawman instrument returns three-axis measurements sampled at 40 samples per decade, and as with the magnetic field, cross spectra between components are returned. In the low frequency regime (<10kHz) cross spectra between E and B are measured to facilitate identification of wave modes. Waveform data that allow the study of small-scale phenomena are returned as burst mode data with a 60-s cadence.

3.2.6 Neutron/Gamma-Ray Spectrometer (NGS). The NGS detector should be capable of detecting, and positively identifying neutrons and gamma-rays from the Sun having energies that range up to ~10 MeV. The neutron component should be capable of intrinsic energy resolution sufficient to separate neutrons having energies below and above 1 MeV, and better than 50% energy resolution for neutron energies between 1 and 10 MeV. This last requirement is needed to separate quasi-steady-state neutron emission from transient neutron emission. The NGS will measure the products of the acceleration of protons (via neutrons and gamma rays) and electrons (via gamma-rays) as they interact with the dense low chromosphere and photosphere. If microflares or nanoflares play a significant role in coronal heating, these signatures of particle acceleration will be present. Their spectrum and time variation provide information on the acceleration processes(s).

Upward-propagating protons and electrons may be directly detected, although the probability of crossing the appropriate field lines at the critical time may be small. The neutron and gamma detection suffers no such restriction. Furthermore, Solar Probe+'s close passage to the Sun provides tremendous advantage for detection of low-energy neutrons because of their short lifetimes as well as for spectroscopy of faint gamma-ray bursts. These observations will, for the first time, provide solid statistical knowledge of the frequency of energetic particle acceleration in small solar flares.

A detection of a burst of gamma rays would help refine the energy spectrum of transient neutrons through use of the measured time of flight between neutron arrival times and the time of the gamma burst. The detection sensitivity of the NGS should be sufficient to measure neutrons produced by flares that release greater than 10^{24} ergs.

A broad-band analysis of the gamma-ray spectrum can provide a measure of the electron and ion components that will complement the detection of neutrons. The neutron measurements are most sensitive to the lowest-energy heavy-ion interactions, while the ion-induced gammas sample higher energies that may be present in the ion population. Bremsstrahlung from accelerated electrons will manifest themselves in a continuum spectrum that is distinguishable from that of the ion-induced gammas.

NGS Performance. To adequately resolve the onset and duration of a gamma-ray burst requires a sample period of 4 seconds in each of 64 energy bins encompassing an energy band of 0.1 to 10 MeV. The neutron channel will require a sample period of 16 seconds over a neutron energy range of 0.05 to 20 MeV, also with 64-channel spectra. The detector must be able to distinguish between fast neutrons and gammas and should possess an unambiguous neutron-detection channel. A spectral resolution better than 50% will allow broad-band analysis of the gammas and neutrons, sufficient to resolve the bremsstrahlung, nuclear and neutron components. Both neutron and gamma-ray spectrometer functions must efficiently reject charged particles.

Based upon extrapolation of measurements at 1 AU, an appropriate sensitive area for the gamma-ray spectrometer is 75 cm^2 at 1 MeV, providing a sensitive area of $3 \times 10^5 \text{ cm}^2$ when scaled to 1 AU. The neutron spectrometer in the context of the spacecraft must have an effective area of 75 cm^2 at 1 MeV. The placement of the NGS on the spacecraft will be studied pre-Phase A; mounting just under the heat shield is desirable. Heritage instruments for the Solar Probe+ NGS include those flown on Lunar Prospector, Mars Odyssey, and MESSENGER.

3.2.7 Coronal Dust Detector (CD). The CD should be compact and lightweight and must be able to cope with the near-Sun thermal and particle environment. The CD assumed for this study is an impact ionization detector based on the Mars Dust Counter (*Igenbergs et al.*, 1998). Such devices measure ions and electrons produced by the impact of dust particles on the detector's target area to derive particle mass and have been successfully flown on Ulysses, Hiten, Galileo, and Nozomi (e.g., *Grün et al.*, 1992; *Sasaki et al.*, 2002). The CD is mounted on the bus and positioned to be exposed to the maximum dust flux. For an aperture area of 140 cm^2 , the dust model described in the previous STDT report [*McComas et al.*, 2005; Appendix B] predicts that $>10^6$ particles of masses larger than 10^{-17} g and up to 10^8 particles of masses larger than 10^{-19} g would be detected at the high impact velocities that Solar Probe+ will experience. Independent pointing and special pointing accuracy are not required

The CD will be operated continuously. Only modest telemetry allocation is required. The CD should have an external cover to be removed after launch. No special cleanliness is required, but purging with N_2

should be considered. Issues to be addressed for further development of the CD are the high-voltage parts and the influence of the radiation environment and outgassing from the heat shield on the measurements. Measurement of particle mass is standard for impact ionization detectors but has not yet been demonstrated for the high impact speeds that the Solar Probe+ CD will experience.

Although a single sensor has been assumed in the payload design, we have conservatively included enough mass to accommodate a second sensor mounted at a different location on the spacecraft to provide a second look direction. The allocated power is adequate to two alternately operated sensors. Measurements from two sensors on different spacecraft locations can be used to distinguish between particles in prograde and retrograde motion as well as between particles in near-ecliptic and out-of-ecliptic orbits. If resources permit, an alternative to two sensors would be a single detector with time-of-flight (TOF) capability. This would enable TOF measurement of the impact-produced ions, yielding mass spectra and allowing the elemental composition of the dust to be derived.

3.2.8 Hemispheric Imager (HI). HI is a broadband, very wide-angle, white light coronagraph with a $\sim 160^\circ$ FOV to image the local spacecraft environment and provide tomographic imaging of coronal structures as Solar Probe+ flies through the corona. HI will also be able to observe CMEs and other dynamic structures as they evolve. Coronal tomography is a *fundamentally* new approach to coronal imaging (similar to a medical CAT scan) and is possible only because the imaging is performed from a moving platform close to the Sun, flying through coronal structures and imaging them as it flies by and through them. HI observations of the 3D coronal density structure are required to resolve ambiguities in the interpretation of spatial and temporal changes seen in the in-situ measurements. HI heritage stems from the all-sky coronagraph on SMEI, the HI wide-angle coronagraph on STEREO, and instrument prototypes developed as part of earlier Solar Probe proposals.

The HI's FOV and resolution derive from the need to provide context for the in-situ instruments and to be able to reconstruct the 3D density structure of the corona tomographically. The 160° FOV is sufficiently large to view the corona from near the solar limb to beyond the zenith. A wide-angle view is particularly important for imaging faint coronal features because the coronal intensity contrast is greatest *along* flux tubes and other magnetic structures near the zenith. The spatial resolution required to image small-scale coronal structures is of order 1° . The temporal cadence required to provide continuous observations and sufficient data for 3D tomographic reconstruction is ~ 90 s at perihelion.

3.2.9 Common Data Processing Unit (CDPU). The Common Data Processing Unit (CDPU) integrates the data processing and low voltage power conversion for all of the payload science instruments into a fully redundant system that eliminates replication, increases redundancy, and reduces overall payload resources. The CDPU consists of redundant sides (A & B), each of which contains a processor board, a low-voltage power supply board, a low-voltage distribution board, a serial instrument interface board, and

a custom instrument interface board. The processor board should employ a high-speed 32-bit processor and at least 2 Gbit of memory to service the instrument interface boards and perform all of the control and data processing that each instrument requires. This includes real-time control and servicing as well as processing of acquired data through Fast Fourier Transform (FFT), compression, and custom algorithms that the instrument teams specify. The low-voltage power supply board and low-voltage distribution board should efficiently convert the primary spacecraft power bus using DC-DC converters to the secondary voltage rails required by the instrument electronics and distribute those voltage rails to the science instruments. The serial instrument interface board is used for instruments whose front-end electronics produce results in digital form. This information will be transmitted serially from the instrument to the CDPU, buffered in memory on the interface board, and processed by the CDPU software. Other instruments require discrete control and analog conversion to process the data produced by their front-end electronics. The custom instrument interface board services these instruments, providing the control, processing, and data buffering required to integrate each instrument.

The CDPU provides a unified interface to the payload for the spacecraft. The spacecraft selects which side of the CDPU will be powered, leaving the redundant side off as a cold spare. The payload CDPU communicates with the spacecraft over a MIL-STD-1553 bus, accepting commands and producing CCSDS packets ready for final processing by the spacecraft for telemetry to the ground.

3.3 Supporting Scientific Activities

Each of Solar Probe+’s perihelion passes is analogous to a planetary flyby in that the most unique observations that justify the mission will be carried out over several days around each perihelion. To obtain the maximum scientific return from this “burst” of observations, the Solar Probe+ mission needs to be supported by (1) theory and modeling and (2) a coordinated campaign of observations by relevant ground-based, sub-orbital, and space-based assets during the Probe+’s perihelion passes.

3.3.1 Theory and Modeling. Experience has shown that a broad involvement of the scientific community in targeted theoretical and computer modeling studies, both before and after the period of intense data gathering, multiplies by a significant factor the scientific return from exploratory space missions. To facilitate broad community participation in the Solar Probe+ mission, the Solar Probe STDT recommends that NASA establish a competitive Solar Probe+ Affiliated Scientist (SPAS) theory and modeling program. Affiliated Scientists should be fully involved early enough in the mission that their work can contribute to operational decisions. The SPAS program should provide for semi-annual meetings of Affiliated Scientists and Solar Probe+ investigators and for several community workshops on specific aspects of Solar Probe+ science (e.g., magnetic reconnection and turbulence, plasma acceleration, etc.).

We envision NASA support for 8-12 Affiliated Scientists and/or small subject teams, with an equivalent number supported by other national and international agencies.

3.3.2 Solar Probe+ Observation Campaign. Solar Probe+'s many perihelion passes, especially the final three at $9.5 R_S$ will be such a unique, exciting, and important scientific opportunity for the solar and space physics and astrophysics communities that all relevant national and international scientific assets should be dedicated to providing supporting observations in a coordinated campaign. This campaign should also provide, as part of its education and public outreach component, for the participation of amateur solar astronomers from around the world.

The three perihelion passes at $9.5 R_S$ will be phased with respect to Earth such that the coronal features being sampled in-situ by Solar Probe+ can be observed simultaneously from Earth. A wide range of ground-based, sub-orbital, and space-based observations will thus be able provide unique and important contextual information for the Solar Probe+ measurements, substantially enhancing the science return from Solar Probe+.¹ Conversely, the remote observations will benefit from the unique ground-truth measurements provided by Solar Probe, which will allow benchmark calibrations of many observational techniques that rely on important but hitherto unverified assumptions about the near-Sun environment.

The planning and coordination of the Solar Probe+ minimum perihelion pass campaign should be the responsibility of the Solar Probe+ team and Affiliated Scientists. Funding for specific ground-based and/or suborbital solar observations should be provided by the Solar Probe+ project. We anticipate that support for other campaign activities will be provided by COSPAR, the International Astronomical Union, the National Science Foundation, and other national and international scientific agencies.

¹Powerful new solar observatories such as the Advanced Technology Solar Telescope, the Frequency Agile Solar Radio telescope, and Solar Orbiter are expected to be operational at the time of the Solar Probe encounter.

			Measurements/Instruments						
			PLASMA DISTRIBUTION ; COMPOSITION : SUPRATHERMALS (FIA, FEA, ICA)	ENERGETIC PARTICLES (EPI)	PLASMA WAVES (PWI)	VECTOR MAGNETIC FIELD (MAG)	NEUTRON/GAMMA-RAY EMISSIONS (NGS)	CORONAL DUST (CD)	WHITE LIGHT IMAGING (HI)
Science Objectives	Objective Questions	Strategy							
2.1 Determine the structure and dynamics of the magnetic fields at the sources of the solar wind	a. How does the magnetic field in the solar wind source regions connect to the photosphere and the heliosphere?	Coordinate in-situ observations and remote-sensing of corona (high-cadence white-light imaging < 20R _S); intercompare in-situ measurements along the orbits.	R	S	S	R			R
	b. How do the observed structures in the corona evolve into the solar wind?	Identify in-situ signatures of density and magnetic field structures or boundaries and compare with coronal structure as observed with remote sensing.	R	S	S	R			R
	c. Is the source of the solar wind steady or intermittent?	Perform statistical study of temporal andradial variations of composition and plasma and field data of various types of solar wind; relate to filamentary structure and filling factors.	R	S	S	R	S		R
2.2 Trace the flow of the energy that heats the solar corona and accelerates the solar wind	a. How is energy from the lower solar atmosphere transferred to and dissipated in the corona?	Characterize the turbulence and energy budgets and their evolution along the orbits; compare with sources at the Sun and along the trajectory; search for signatures of candidate dissipation mechanisms at kinetic scales.	R	S	R	R	R		S
	b. What coronal processes shape the non-equilibrium velocity distributions observed throughout the heliosphere?	Compare measured electromagnetic fields and distribution functions of protons, electrons,and heavy ions and their variability	R	R	R	R			
	c. How do the processes in the corona affect the properties of the solar wind in the heliosphere?	Use measured amplitude and spectra of electromagnetic and plasma fluctuations to assess role of Alfvénic turbulence in coronal heating and solar wind acceleration; with modeling, determine origin of spectra (photospheric or coronal).	R	S	R	R			S
2.3 Determine what mechanisms accelerate and transport energetic particles	a. What are the roles of shocks, reconnection, waves, and turbulence in the acceleration of energetic particles?	Correlate energetic particle distributions and their temporal variations with shocks, signatures of reconnection, and properties of turbulence properties.	R	R	R	R	S		S
	b. What are the seed populations and physical conditions necessary for energetic particle acceleration?	Correlate suprathermal and energetic particle distribution functions with measured plasma and electromagnetic field properties.	R	R	R	R			
	c. How are energetic particles transported from the corona to the heliosphere?	Determine energetic article distribution functions and composition and turbulence properties along the trajectory, along with measured and modeled large-scale magnetic field.	R	R	R	R	S		S
2.4 Explore dusty plasma phenomena and their influence on the solar wind and energetic particle formation	a. What is the dust environment of the inner heliosphere?	Compare dust measurements with brightness patterns from coronagraph and models to characterize size distribution.			S	S		R	S
	b. What is the origin and composition of dust in the inner heliosphere?	Derive information about dust composition from measurements of dust-generated species and from sublimation sequence determined from size distribution as function of distance from the Sun.	R			S		R	
	c. What is the nature of dust-plasma interactions in the near-Sun environment?	Correlate plasma distribution functions, composition measurements, and dust properties.	R		S	S		R	S
	d. What are the physical and chemical characteristics of dust-generated species?	Measure composition of dust-generated species; correlate with dust, solar wind, and magnetic field data.	R			S		R	

Table 3-1 Traceability Matrix. All measurements/instruments are included in the Solar Probe+ Baseline mission. “R” denotes measurements required to address the question in whose row they appear; “S” denotes supporting measurements.

Table 3.2 Solar Probe+ Baseline Instrument Payload

Instrument	Parameter(s) or Quantity(ies) Measured	Sensitivity <i>Dynamic Range</i>	Spectral Range <i>Resolution</i>	Angular Range <i>Resolution</i>	Time Integration <i>Cadence</i>
Fast Ion Analyzer (FIA)	H, He distribution functions	2D distributions in 0.1s @20 R _S	50 eV- 20 keV $\Delta E/E \sim 0.05$	330° x 90° (2 orthogonal) 10° x 10° 90° back from heat shield (phi) x centered on ram direction; 80° perp to symmetry axis; 5° toward beam to 20° away from beam	3 s for 3D; 0.1 s for 2D
Fast Electron Analyzer (FEA)	Electron distribution function	2D distributions in 0.1s @20 R _S	1 eV- 5 keV $\Delta E/E \sim 0.1$	As close to 4 π less s/c obscuration ~3° (1D) near strahl 30° x 30° otherwise	3 s for 3D; 0.1 s for 2D
Ion Composition Analyzer (ICA)	Distribution functions of ³ He, ⁴ He, C, O, Mg, Si, Fe; composition of dust-related PUI from 2 to ~60 amu	Enable He/O in 10 s at 20 R _S	100 eV/q - 60 keV/q $\Delta E/E \sim 0.04-0.05$	120° x 120° 10° x 10°	10 s for He/O ratio at 20 R _S 60 s for heavy ions (e.g. Fe/O, charge states)
Magnetometer (MAG)	DC vector magnetic field	10 nT - 8 G 3-axis >10 ⁴	n/a	3° knowledge inside 20 R _S	20 samples/sec
Plasma Wave Instrument (PWI)	3-axis AC E- and B-fields	2 x 10 ⁻¹⁷ V/m ² /Hz	E: 10 Hz-10 MHz B: 10Hz -80 kHz 40 samples/decade	n/a	0.1 s for spectral data; 60 s for waveform data
Energetic Particle Instrument (EPI)	Differential fluxes of H, ³ He, ⁴ He, C, O, Ne, Mg, Si, Fe, and e ⁻	10 ⁶ protons/cm ² s sr with 0.2 - 1 MeV 5 x 10 ⁵ protons /cm ² s sr with >1 MeV	0.02 - 100 MeV/nuc for ions 0.03 - 3 MeV for e ⁻ 6 energy bins/decade	Capability to measure pitch-angle distributions and anisotropies. Minimum coverage: 30° to 150° wrt nominal magnetic field at 4 R _S with 30° resolution	5 s for H; 30 s for Z ≥ 2; 1 s for e ⁻
Neutron/γ-ray Spectrometer	Neutron, hard x-ray, and γ-ray spectra	Factor of 10 ⁴	0 - 20 MeV < 0.5 $\Delta E/E$ 0.02 - 10 MeV (power-law spectrum)	4 π FOV for both energy ranges	10 s integration both ranges 10 s cadence both ranges
Coronal Dust (CD)	Flux and mass spectrum; silicate vs. organic	m>10-15 g for $\Delta V=5$ km/s (smaller particles detected for larger ΔV)	0.05 - 50 μ m (1 fg - 1 μ g)	As close to 2 π less s/c obscuration	10 s 30 s
Hemispheric Imager (HI)	White light intensity	10 ⁻⁹ erg/cm ² /deg/s	white light n/a	160° x 160° less s/c obscurations ~0.2°	1 - 10 s 90 s

Table 3.3 Instrument Resource Requirements.

Instrument	Mass (kg)	Power (W)	Peak Data Rate (kbps)
Fast Ion Analyzer (FIA)	2.8	3.7	10
Fast Electron Analyzer (FEA) (2X)	5.0	7.2	20
Ion Composition Analyzer (ICA)	7.0	6.0	10
Magnetometer (MAG)	2.5	2.5	1.1
Plasma Wave Instrument (PWI)	5.0	5.0	3.5
Energetic Particle Instrument (Low Energy)	1.4	2.3	5
Energetic Particle Instrument (High Energy)	2.7	1.7	3
Neutron/Gamma Ray Spectrometer (NGS)	2.0	3.0	0.5
Coronal Dust Detector (CD)	1.5	3.8	0.1
Hemispheric Imager (HI)	1.5	4.0	70
TBD	5.0	4.0	70
Common DPU/LVPS	10.8	14.0	N/A
Total	47.2	57.2	123.2

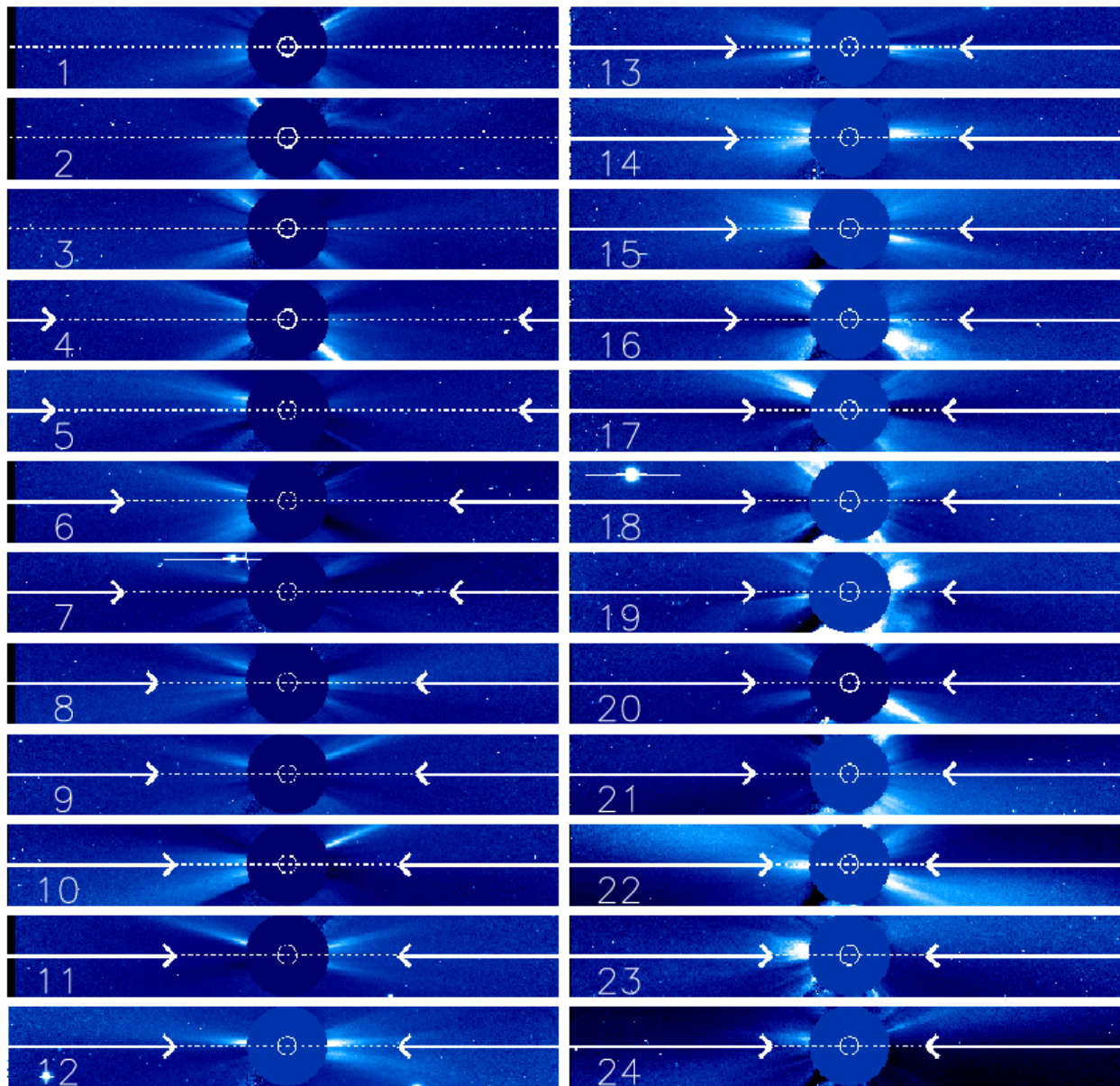


Figure 3-1. Representative coronal conditions for the first 24 Solar Probe+ perihelion passes for a launch circa 2015 May 26. Each panel is made from a LASCO C3 image taken at a time in the sunspot cycle corresponding to the time of the Solar Probe+ pass. Panels 11, 2007 Dec 11, and 12, 1997 March 18, are near solar minimum. Panel 24, 2000 April 4 is approaching sunspot maximum. North is at the top and east to the left in each panel. The thin horizontal lines indicate approximately the plane of the Solar Probe+ orbit and the crosses show the perihelion distance of each pass. Panels 17, 18, and 19 were times of SOHO attitude instability

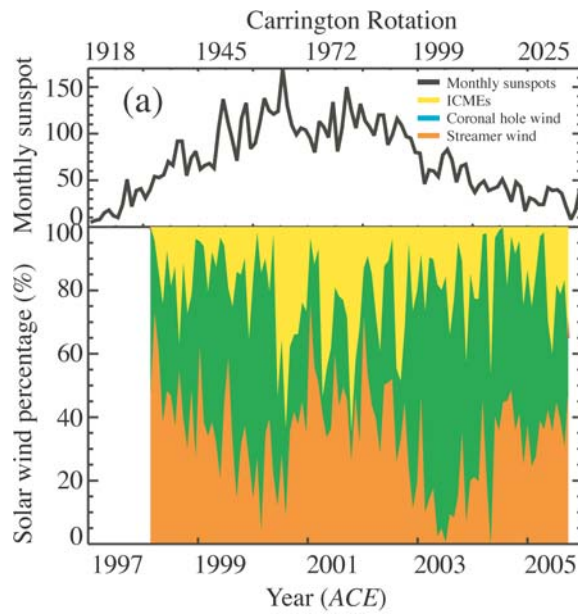


Figure 3-2. ACE observations during the rising phase, peak, and declining phase of Solar Cycle 23 show the percentage of wind from different solar source regions that is observed in the ecliptic (yellow = transient wind; green = fast wind from coronal holes; red = wind associated with streamers) [Zhao and Zurburchen, 2008]. This plot indicates the probability with which Solar Probe+ will be able to sample the different kinds of solar wind from its near-ecliptic orbit over the course of its 7-year mission.

4.0 Mission Implementation

NASA's Science Mission Directorate (SMD) tasked The Johns Hopkins University Applied Physics Laboratory (JHU/APL) to work with the existing STDT to design a technically feasible Solar Probe mission that could be implemented for a total mission cost of less than \$750M (FY07 dollars). In addition, according to the SMD's ground rules, the redefined Solar Probe mission must

- achieve the Solar Probe 2005 core science objectives
- not use radio-isotope thermoelectric generators (RTGs) for power
- be able to be accomplished in less than 10 years
- be ready for launch in 2015
- maintain mass and power margins of at least 35%

The APL engineering team worked closely with the STDT and with a team from NASA's Glenn Research Center to develop a new mission scenario and spacecraft design that would satisfy the SMD requirements. The new mission concept was judged to offer several advantages over the 2005 concept, in terms of both increased science yield and technical implementation, and so the revised mission was christened "Solar Probe Plus," written "Solar Probe+."

The mission concept for Solar Probe+ differs substantially from that described in the 2005 Solar Probe report, which called for Solar Probe to be placed into a solar polar orbit by means of a Jupiter gravity assist (JGA) maneuver and to perform one or two flybys of the Sun at a perihelion distance of 4 R_s . In contrast, Solar Probe+ will remain near the ecliptic, eliminating the need for a JGA, and execute 24 near-Sun passes with ever closer perihelia until it reaches a minimum perihelion distance of 9.5 R_s . Because the solar flux at this distance is significantly less intense than at 4 R_s , Solar Probe+ can use a Thermal Protection System (TPS) that is simpler and less massive than the one baselined for Solar Probe 2005. A further difference between the 2005 spacecraft design and the Solar Probe+ design is the use by the latter of solar arrays rather than RTGs to power the spacecraft over its entire trajectory.

In developing the concept for the Solar Probe+ mission, the STDT and APL engineering team made extensive use of previous studies and analyses conducted in support of the 2005 Solar Probe definition effort and subsequent studies including the follow-on *Solar Probe Thermal Protection Risk Mitigation Study*.¹ Numerous trade studies were performed as well, and risk reduction measures and cost savings options were identified.² ***The result is a technically feasible and affordable mission with acceptable risk***

¹*Solar Probe Thermal Protection System Risk Mitigation Study: FY2006 Final Report*, prepared by The Johns Hopkins University Applied Physics Laboratory under contract NAS5-01072, Laurel MD, November 30, 2006.

²Detailed discussions of the trade studies performed during the Solar Probe+ study as well as of studies and analyses planned for subsequent stages in the Solar Probe+ development effort can be found in the report of the APL

that can survive in the unique thermal and dust environment near the Sun and that will fully achieve all of the Solar Probe+ science objectives. The sections that follow describe this baseline Solar Probe+ mission. The key requirements that flow down from the science objectives and drive the mission and spacecraft designs are summarized below:

Mission Requirements

- At least three orbits with perihelion distance less than $10 R_S$
- A Sun-spacecraft-Earth encounter geometry that supports simultaneous Earth-based observations to support Solar Probe+ observations
- Minimum perihelion passes achieved within 10 years
- Return of full data collected in a perihelion pass in each orbit

Spacecraft Requirements

- Survive solar intensity during perihelion pass (~ 510 Suns)
- Provide reliable power over the distance range 0.044 AU – 1 AU
- Protect instruments and spacecraft systems from dust environment near the Sun
- Provide large total science data return (~ 128 Gbits per orbit)
- Accommodate significant payload mass (~ 50 kg) and power (57 W)
- Provide science boom for magnetometer and plasma wave search coils
- Provide actuations of instruments and antennas for proper placement and FOV orientations during science collection

4.1 Baseline Mission Design

The new programmatic and resource requirements placed by NASA's Science Mission Directorate on the Solar Probe mission required a thorough re-assessment of the mission design developed in previous Probe studies, including the most recent one (*McComas et al.*, 2005). The APL engineering team thus conducted a careful mission design trade study, in which several different mission scenarios and trajectories, including a Jupiter gravity assist (JGA) trajectory, were explored. Based on this study, and working in close consultation with the STDT, the APL team developed a new design for a baseline mission that fully meets all scientific, programmatic, and resource requirements for the Solar Probe mission. The new

engineering team, 2008 *Solar Probe+ Mission Engineering Study Report*, prepared under contract to NASA, Laurel MD, February 19, 2008.

mission concept not only allows Solar Probe+ to be implemented within the prescribed resource envelope but also significantly enhances the mission's science return by allowing repeated sampling of the near-Sun region as the level of solar activity changes from the declining phase of solar cycle 24 through solar minimum to the solar maximum of cycle 25 in ~2022.

4.1.1 Launch and Launch Vehicle Selection. Solar Probe+ will be launched from the Eastern Test Range at Cape Canaveral Air Force Station. The nominal launch period begins on May 21, 2015 and lasts through June 9, 2015. The launch energy C_3 required for the optimum launch date during this 20-day interval is $156 \text{ km}^2/\text{s}^2$. Based on an estimated launch mass of ~610 kg and launch vehicle performance calculations, an Atlas V 551 with a Star-48BV third stage has been baselined as the Solar Probe+ launch vehicle. As with other interplanetary missions, Solar Probe+ will be placed into a low-Earth parking orbit and coast for ~30 minutes before being injected into the desired heliocentric trajectory.

4.1.2 ΔV Budget. No deterministic ΔV is required throughout the entire Solar Probe+ mission. Except for the propellant budgeted for launch vehicle dispersion, navigational corrections, and momentum control, the entire ΔV necessary for achieving orbit will be supplied by the launch vehicle (**Table 4-1**).

4.1.3 Baseline Mission Trajectory. The baseline Solar Probe+ mission comprises 24 solar orbits with a 3.4° -inclination from the ecliptic over a 6.9-year period. During this interval, Solar Probe+ will perform seven Venus flybys to reduce the perihelion distance from $35 R_S$ to a minimum of $9.5 R_S$ (**Figures 4-1 and 4-2**). The first perihelion pass (at $0.16 \text{ AU}/35 R_S$) will occur only three months after launch. The baseline mission will end after Solar Probe+ has completed three near-Sun passes at $9.5 R_S$. The period of the final three orbits is 88 days. For a May 2015 launch, Solar Probe+ will arrive at $9.5 R_S$ in October 2021, 6.4 years after launch. The trajectory and timeline for one of the passes at $9.5 R_S$ are shown in **Figure 4-3**. The trajectories of the other near-Sun passes are similar, but involve greater flyby distances and slower flyby speeds. The position of Earth relative to the Sun and the spacecraft when Solar Probe+ passes through perihelion will change from orbit to orbit, allowing different viewing geometries for supporting Earth-based remote-sensing observations of the corona and photosphere, as illustrated in **Figure 4-4** for the three minimum perihelion passes.

Solar Probe+ will spend a significant amount of time in the near-Sun region, performing 3 to 4 near-Sun passes per year and gathering data over more than half of the 11-year solar cycle. In 21 of the 24

The key features of the Solar Probe+ mission design

- Launch in May 2015, with a prime mission of 6.9 years
- 7 Venus flybys to lower perihelion gradually to a minimum distance of 9.5 R_S
- First solar pass at ~ 0.16 AU (35 R_S) 3 months after launch
- A total of 24 solar passes during the prime mission, with 19 passes inside 20 R_S for a total of 961 hours in this region
- Extensive sampling of the inner heliosphere during rising phase of solar cycle
- Final phase of nominal mission consists of 3 passes at 9.5 R_S with an 88-day orbital period
- Extended mission with additional near-Sun passes requires no orbit maintenance maneuvers

In addition to enabling a greater science return than was achievable with earlier designs, the new trajectory design also offers several advantages in terms of mission implementation:

- Gradual lowering of the perihelion distance to 9.5 R_S reduces mission risk
- Elimination of the JGA maneuver removes the need for RTGs and allows for multiple solar encounters
- An aphelion of less than 1 AU ensures sufficient solar flux to power the spacecraft
- The solar flux at 9.5 R_S is $\sim 1/6$ that at 4 R_S , and the thermal environment correspondingly less severe, allowing solar arrays to be used to power the spacecraft even during the minimum perihelion passes

orbits, perihelion will occur inside 30 R_S ; and in 19 orbits, inside 20 R_S .³ (Solar Probe+ will spend 10 times the amount of time inside 20 R_S that Solar Probe 2005 would have spent in that region.) The total accumulated time that Solar Probe+ will spend inside 30 R_S , 20 R_S , 15 R_S , and 10 R_S is summarized in **Table 4-2**.

4.1.4 Comparison with 2005 Solar Probe Baseline Mission. As noted above, the Solar Probe+ mission concept is fundamentally different from that described in the 2005 Solar Probe study (as well as in all previous studies since the 1970s). The principal differences are summarized in **Table 4-3**. Based on the present study and the review of the Solar Probe science objectives, the STDT and APL engineering team judged that the new mission design will return more science with lower mission risk. With 24 near-Sun passes over a 6.9-year interval (compared with only 2 passes by Solar Probe 2005 over an ~ 8 year period), the new mission design allows extensive in-situ sampling of the near-Sun environment at changing levels of solar activity with concurrent supporting remote-sensing observations from other assets. From an operational standpoint, gradually lowering the perihelion distance over a number of orbits makes it possible to incorporate lessons learned during earlier passes into the operational planning for subsequent near-Sun passes and is significantly less risky than attempting to achieve the minimum perihelion distance during the first solar encounter, as was called for in the 2005 study.

³For comparison, the minimum perihelion of Helios B (launch 1976) was 0.289 AU (63 R_S), which is the closest any spacecraft has come to the Sun. ESA's Solar Orbiter mission, planned for launch in 2015, will have a minimum perihelion of ~ 0.22 AU (48 R_S).

4.2 Mission Concept of Operations

4.2.1 Launch and Early Operations. As noted above, Solar Probe+ will be launched from Cape Canaveral within a 20-day launch window on an Atlas V 551 with a STAR-48BV third stage. The nominal launch date is May 21, 2015. The spacecraft will be 3-axis stabilized by the launch vehicle and third stage for the entire launch ascent and third stage fly-out. No de-spin maneuver will be needed after third stage separation. After separation, Solar Probe+ will be in a Sun-pointing orientation. The low-gain antenna (LGA) will be used for communications until the high-gain antenna (HGA) is deployed and checked out.

The first Venus flyby will occur approximately 6 weeks after launch. During this period, spacecraft systems will be checked out, and preparations will be made for the Venus encounter. The interval between the first Venus encounter and the first near-Sun pass is allocated to science instrument checkout, solar encounter preparations, and the first changeover from the primary solar arrays to the secondary arrays (cf. Section 4.8.1). During the first 7 days after launch, DSN coverage will be continuous.

4.2.2 Mission Events From an operational perspective, Solar Probe+ orbits are broken into **perihelion** and **aphelion** segments (**Figure 4-5**). The bulk of the science measurements will be made during the perihelion segment, although some, lower cadence measurements will also be made during the aphelion segments. The data will be stored for downlink after each solar encounter. The HGA can be used during the aphelion portion of the orbit, nominally outside 0.59 AU. All trajectory correction maneuvers (TCMs), Venus flybys, and science data downlink also take place during this segment.

Solar Encounters. Solar encounters will begin ~10 days before perihelion and last until ~10 days after closest approach. At ~0.25 AU on the inbound leg of the orbit, Solar Probe+ will transition from standard to encounter configuration.⁴ While the spacecraft maintains the correct Sun-pointing attitude, the primary solar arrays will be retracted inside the TPS umbra and power will be provided by liquid-cooled secondary arrays, which are fully extended. As the spacecraft nears perihelion, the secondary arrays will be partially retracted behind the TPS shield, maintaining constant power. Prime science data will be collected during the entire 20-day encounter period; the instruments in use and the measurement rates will vary during this interval, with highest use near perihelion. The solar wind plasma instruments and the coronal dust detector face in the ram direction during the solar encounters. All science data will be stored for later downlink; however, the X-band link is maintained through the LGA for command uplink and

⁴This solar distance was chosen based on the performance of the MESSENGER solar arrays, which are capable of withstanding solar fluxes at distances up to 0.25 AU and are the basis for the primary arrays baselined for Solar Probe+.

housekeeping telemetry downlink except during solar conjunction. After closest approach, the secondary arrays will be slowly extended and, at 0.25 AU, the primary arrays will be unfolded. Once the spacecraft reaches 0.59 AU, the HGA, which was stowed behind the TPS during the inbound leg inside 0.59 AU, will be re-deployed and pointed toward Earth for data downlink. To simplify spacecraft attitude management and maintain the thermal protection attitude, the Solar Probe+ mission is designed to avoid burns during solar encounters.

Venus Flybys. Operational activities surrounding the seven Venus flybys will begin thirty days before each encounter and continue for 10 days after the encounter. Operations during the 40-day Venus encounter period are limited to 1) downlinking science data from the previous near-Sun pass; 2) analysis, execution, and evaluation of the pre-encounter navigation burn and a post-encounter burn to correct any residual errors; and 3) monitoring spacecraft health and safety during the encounter. TCMs for Venus flyby targeting will be executed before each Venus encounter (**Table 4-4**).

Data Downlink. The aphelion segment is designated primarily for the downlink of data collected during the most recent solar encounter. The Ka-band will be used for science data downlink to the DSN 34-m subnet via the spacecraft's HGA. Contact time will vary as the Sun-Probe-Earth angle changes but will average 10 hours per day. All data from one solar encounter will be downlinked before the next encounter. When the spacecraft is in contact with Earth, it will maintain Sun pointing and will roll as needed to point the HGA toward Earth. When it is not in contact, it will maintain the default pointing with ram-pointing instruments in their optimal attitude.

4.2.3 Navigation. Solar Probe+ has no special navigation requirements. Optical navigation is not required. Radiometric Doppler range and range rate data will be used for spacecraft trajectory determination. Delta-DOR tracking data may be used prior to the Venus flybys to enhance the orbit determination accuracy. From launch (L) to L+ 2 weeks, there will be continuous DSN tracking, followed with five 10-hour passes per week from L+2 to L+4 weeks. At each Venus (V) flyby there will be five 10-hour passes per week from V-5 to V-1 week and one 10-hour pass per day from V-1 to V+1 week.

4.2.4 Mission Operations. With respect to mission operations, the Solar Probe+ cost estimate developed by the APL team is based on the following assumptions:

- A modular approach to mission operations, in which operations for recurring events (solar encounters, Venus flybys, TCMs) are executed using pre-defined sequences that can be repeated with only small changes from one orbit to the next.
- Streamlined interfacing with a single PI-led science and instrument team as on New Horizons.

- Decoupling of science planning and spacecraft operations as on STEREO and other missions
- Autonomous, “lights out,” unstaffed operation of the mission operations center except during critical events such as launch, TCMs, Venus flybys, solar encounters, or emergencies

Each of these measures will greatly simplify mission operations, reduce mission risk, and reduce mission planning and operations costs.

4.3 Mission Environment

Solar Probe+ must be able to operate and survive under near-Sun environmental conditions, which present significant challenges for the engineering design of the spacecraft. As the spacecraft approaches and flies past the Sun, it will be exposed to intense solar flux and bombardment by particles from the circumsolar dust cloud. In addition, the effects of coronal lighting and solar scintillation in the near-Sun environment had to be included in the design of attitude control and telecommunications systems.

4.3.1 Solar Flux. The most challenging spacecraft design driver is the intense solar flux to which Solar Probe+ will be exposed. At perihelion, the flux will be roughly 510 times that at Earth orbit. As discussed in detail below (Section 4.6), the Thermal Protection System (TPS), consisting of a ceramic-coated carbon-carbon shield, protects the instruments and spacecraft bus from direct exposure to this flux. Immediately after launch and spacecraft separation, the TPS will point toward the Sun, and this attitude will be maintained through the mission. Except for the secondary solar arrays and the end segments of the PWI electric field antennas, instruments and spacecraft components will reside within the umbra of the TPS at all times within solar encounter. The only other components intended to extend beyond the umbra are the primary solar arrays and HGA, which are extended only in portions of the orbit away from the solar encounter.

4.3.2 Radiation. The radiation environment to which Solar Probe+ will be exposed consists of solar energetic protons, which are responsible for total dose damage in spacecraft components, and galactic cosmic rays (GCRs), which are the source of most single event effects (SEE) that spacecraft experience.⁵ Solar energetic protons can also cause SEEs in spacecraft systems.

With a 2015 launch, during the declining phase of solar cycle 24, much of the Solar Probe+ mission will occur during a period when the total dose due to solar energetic protons is expected to be small.

⁵With the new mission and spacecraft designs, Solar Probe+ will not, in contrast to Solar Probe 2005, be exposed to the intense radiation environment of Jupiter’s inner magnetosphere or to gamma radiation from RTGs.

Significant radiation damage would be expected to occur only toward the end of the nominal mission, around solar maximum (~2022). The total dose requirement for Solar Probe+ is 30 krad behind 100 mils of Al shielding, based on the 95% worst-case JPL solar proton model (*Feynman et al.*, 1993; 2002) for the two years of maximum conditions and correcting for Sun-spacecraft distance through the orbit as defined above. The total dose requirement is the same as that of the MESSENGER mission and is achievable through a parts screening and qualification test similar to that used for MESSENGER and other recent programs. During the design phase, a three-dimensional shielding analysis will be conducted to allow mass reduction in electronics enclosures and spacecraft structure without compromising total dose survivability.

The rate of GCR-induced SEEs that Solar Probe+ may experience is expected to be similar to that experienced by near-Earth missions, while the rate of SEEs caused by solar energetic protons is expected to be no worse than that experienced by missions such as MESSENGER and STEREO. Use of parts similar to those used in previous missions with an equivalent or worse environment, together with the parts screening and qualification program used for recent interplanetary missions, will ensure that Solar Probe+ meets SEE requirements and that the system will function as needed for the life of the mission.

4.3.3 Coronal Lighting. Coronal lighting near the Sun is an environmental factor that can have significant consequences for maintaining attitude control. Excessive coronal lighting can increase background noise and degrade a star tracker's ability to detect star constellations needed to determine spacecraft attitude. Although coronal lighting conditions can be estimated from data acquired by remote-sensing instruments in orbit from 1 AU, uncertainty about the actual lighting conditions will remain until a mission near the Sun is performed. Because of this uncertainty, Solar Probe+ uses three star trackers facing in orthogonal directions, a high-precision inertial measurement unit, and a Solar Horizon Sensor used to detect faults in attitude control and initiate corrective autonomous recovery.

4.3.4 Solar Scintillation. The effects of solar scintillation have been well characterized based on mission data from the Near Earth Asteroid Rendezvous (NEAR) mission as well as from the Magellan and Galileo missions. During the NEAR mission, measurable telemetry losses in the X-band downlink were experienced around solar conjunction once the angle between the Sun, the Earth and the spacecraft came within 2.3°. Although chosen for its increased data rate, Ka-band is less sensitive to scintillation effects as well. Thus, Solar Probe+ will use Ka-band for telecommunications, both for low-rate command and telemetry during the solar encounter and during high-rate science data downlink outside the solar encounter. X-band capability is baselined in the telecommunications subsystem design as a backup for redundancy and periods when Ka-band is unavailable due to ground station conditions.

4.3.5 Micrometeoroid and Dust. Solar Probe+ will encounter dust particles ranging in diameter from submicron up to several hundred microns and consisting of highly refractory carbon and silicate species with a typical bulk density of $\sim 2.5 \text{ g/cm}^3$. The particles will be traveling at relative speeds as high as 350 km/s. To define the shielding requirements for Solar Probe+, a dust model was developed based primarily on the work of *Mann et al.* (2004). The model employs the following assumptions:

1. The number density of the dust in ecliptic orbits (within $\pm 30^\circ$ inclination) varies with distance as $1/r$ between 10 R_S and 1 AU.
2. 5% of the dust within 30° of the ecliptic is in retrograde orbits.
3. All dust trajectories close to the Sun are circular.
4. As the distance from the Sun decreases to within 10 R_S , the number density of dust particles remains constant because of dust destruction.

Mann et al. (2004) estimated that significant dust particle collisions (see *Ishimoto*, 2000) in the inner heliosphere redistribute the particle flux greatly in favor of smaller particles. **Figure 4-6** provides a quantitative comparison of models with and without collisions. To account for uncertainties in the actual circumsolar dust environment, the Solar Probe+ study team conservatively assumed that there are no collisions between particles to establish the critical particle size used in the engineering model.

A comprehensive study of the inner heliospheric dust environment will be performed as part of the Solar Probe+ development effort; however, a preliminary comparison of the Solar Probe+ trajectory with that of Solar Probe 2005 (as well as those of earlier mission concepts) indicates that during a single near-Sun pass Solar Probe+ will encounter about five to six times more particles than would Solar Probe 2005 during either of its encounters. Because Solar Probe+ will make ~ 10 times more passes than Solar Probe 2005, its total dust exposure will be about 50 to 60 times higher than that defined for Solar Probe in the 2005 study. However, compared to the Solar Probe 2005 study, the vast majority of these collisions will occur at much lower relative speeds since both the Solar Probe+ and 95% of the dust are in prograde orbits. For a typical impact speed $\sim 1/4$ of that in the previous study, the kinetic energy is $\sim 1/16$ as large. Thus, despite this increased fluence, the mitigation factors baselined in the 2005 study are sufficient to protect the Solar Probe+ spacecraft. A detailed analysis is given in Section 4.14.

4.4 Spacecraft Overview

The spacecraft concept is illustrated in **Figure 4-7**, and the major components are shown in the block diagram in **Figure 4-8**. This section provides an overview of the baseline design, discusses the reliability and fault management approach, and summarizes the Solar Probe+ mass and power requirements. Individual subsystems are discussed in subsequent sections.

4.4.1. Spacecraft Description. Solar Probe+ is a three-axis-stabilized spacecraft. Its most prominent feature is the Thermal Protection System (TPS), a large flat ceramic-coated carbon–carbon (C-C) shield that is 2.7 m in diameter, with a thermally isolating structure used to attach the shield to the spacecraft. The TPS protects the bus and payload within its umbra during solar encounters. The instruments are mounted either directly to the bus, on a stand-off bracket near the fairing attachment, or on a science boom extended from the rear of the spacecraft. The science boom also carries a solar horizon sensor (SHS) for backup attitude safing during the solar encounters. Three deployable C-C plasma-wave antennas are mounted 120° apart on the side of the bus. These antennas will protrude beyond the umbra during solar encounters. Instrument low-voltage power and data processing are provided by a common data processing unit (DPU). The hexagonal bus carries the spacecraft subsystems and provides an efficient mechanical structure to handle launch loads and integrate with the launch vehicle.

Power is provided by two separate solar array systems. MESSENGER-heritage solar panels are baselined for the primary solar arrays, which will be used outside 0.25 AU. Array temperature is controlled by including optical surface reflectors (OSRs) with cells and tilting the arrays with respect to the Sun to keep the cell temperature within qualification limits. Inside 0.25 AU, the primary arrays will be folded inside the TPS umbra, and the spacecraft will be powered by the secondary solar arrays, two panels of high-intensity solar cells mounted on moveable, liquid-cooled base plates. At the start of a solar encounter, at 0.25 AU, the secondary panels are fully extended outside the TPS; as the spacecraft approaches the Sun, they will be partially retracted behind the TPS to maintain constant temperature and power output. A lithium-ion battery is included as a secondary power source to handle transient loads and power the spacecraft during launch and ascent until the primary solar arrays are deployed. The power system electronics (PSE) box controls spacecraft power and battery charging, and provides the primary power bus voltage for the bus.

The Solar Probe+ avionics suite consists of redundant integrated electronic modules (IEMs) that house the command and data handling (C&DH) processor, solid-state recorders (SSR), guidance and control (G&C) instrument interface, and payload interface. The avionics suite also includes the power distribution unit (PDU), an internally redundant box that includes all power switching as well as pulsed loads to thrusters and single-event actuators. Remote input/output (RIO) devices are used to collect spacecraft telemetry and communicate with the avionics suite through serial data links.

The G&C subsystem consists of three star trackers and one internally redundant inertial measurement unit (IMU) as the primary attitude determination sensors, with an internally redundant SHS used as a check on the primary G&C sensors and as a backup safing sensor. Four reaction wheels are used for attitude control.

The telecommunications subsystem consists of a high-gain antenna (HGA), which is the primary antenna for Ka-band science data downlink, and two low-gain antennas (LGAs). The HGA is gimbaled and mounted on an arm that extends it beyond the umbra for Earth-pointing. Within 0.59 AU, however, the HGA is stowed within the TPS umbra. In this region, command and housekeeping telemetry will be transmitted in the Ka-band via the LGAs. X-band communication through the LGAs is provided as backup for periods when Ka-band communication is not available. Science data collected during the solar encounters will be stored on the redundant SSRs for subsequent downlink via the HGA once the spacecraft is beyond 0.59 AU. No real-time science data downlink is planned inside 0.25 AU.

The propulsion subsystem is a blowdown monopropellant hydrazine system consisting of a single tank, 12 0.9-N and two 4.4-N thrusters used for momentum control and trajectory correction maneuvers (TCMs), and associated plumbing and electrical hardware. The hydrazine propellant tank is in the center of the bus.

4.4.2. Spacecraft and Mission Reliability. Solar Probe+ uses both hardware and functional redundancy to reduce the risk of failure and to ensure mission reliability (**Tables 4-5 and 4-6**). Because mechanisms and deployables represent potential sources of failure, a major emphasis during the development of the baseline spacecraft design was to reduce the number of mechanisms and to ensure that the remaining mechanisms incorporate fail-safe features. Additional studies will be undertaken during Phase A to further mitigate this potential source of mission risk (see Section 4.14.4).

4.4.3. Fault Management. The Solar Probe+ fault management system incorporates numerous elements successfully demonstrated on MESSENGER (perihelion at ~ 0.3 AU) and is distributed throughout the spacecraft design as hardware, software, autonomy, and mission operations requirements. The primary objective of the Solar Probe+ fault management system is to maintain a thermally safe attitude during the solar encounter. Attitude control must be maintained to avoid exposing instruments and spacecraft to direct solar flux. At perihelion, the maximum off-pointing allowed is 2° . Inability to recover quickly from an attitude control fault could result in loss of mission. Attitude control is rendered more difficult by uncertainties in the solar environment such as coronal lighting effects on star trackers or torques induced by high-speed dust impacts (cf. Section 4.3). In addition, the fault management system is responsible for

responding to time-critical fault scenarios, maintaining a power-positive spacecraft configuration, and, if necessary, reconfiguring the telecommunications system for emergency data rate communications.

4.4.4. Mass and Power Budget Summaries. **Table 4-7** summarizes the Solar Probe+ mass budget for instruments, instrument support hardware, mechanisms, and spacecraft subsystems. The values used in the table are the best current estimates for each item at launch. Launch mass is based on performance for an Atlas V 551 launch vehicle with a STAR-48BV third stage. The mass summary includes 30.1% margin to account for unanticipated growth and launch reserves. Because specifics of the launch vehicle have not yet been set, propellant mass is based on the need to achieve the required ΔV after inclusion of the full margin. A more detailed mass budget is provided in Appendix A. The engineering team has identified a collection of Phase A trade studies, shown in **Table 4-8**, to increase mass margin beyond 30% within 6 months of the start of Phase A.

The power subsystem is designed to provide 482 W of load power between 0.9 AU and 9.5 R_{\odot} . (Less power will be available immediately after launch and around aphelion during the first few orbits when the spacecraft is between 0.9 AU and 1 AU; during these intervals the reduction in available power will be compensated for by a reduction in the power allocated to the telecommunications subsystem, which, in this early part of the mission, will have no significant impact on the science data return.) **Table 4-9** summarizes the average power needed during solar encounters based on current best estimates. A more detailed breakdown of the power budget for all modes of spacecraft operation is provided in Appendix A.

4.5 Mechanical Design

The Solar Probe+ mechanical subsystem consists of two main elements: (1) the spacecraft bus, which carries the payload, the subsystems, and the thermal protection system (TPS); and (2) the transition structure assembly (TSA), which couples the TPS to the bus and supports the secondary solar arrays and elements of the cooling system. **Figure 4-9** (foldout) shows several spacecraft views and identifies the locations of the instruments and spacecraft components.

4.5.1. Spacecraft Bus. The Solar Probe+ bus is a conventional hexagonal structure with aluminum honeycomb side panels and a 37-inch-diameter cylindrical adaptor ring (**Figure 4-10**). The design baselined for the bus structure requires no new technology development and is very low risk. **Figure 4-11** shows Solar Probe+ in launch configuration enclosed in the 5-meter fairing of the Atlas V launch vehicle. The spacecraft is attached to the payload adaptor by the bus's cylindrical adaptor ring. Clean load paths efficiently transfer the launch and flight loads from the TPS support trusses and bus-mounted components

through the bus structure corners and into the payload adaptor. The payload adaptor couples the Solar Probe+ to the STAR 48B third stage and provides electrical and instrument purge interfaces to the spacecraft.

4.5.2. Transition Structure Assembly. The TSA consists of six carbon graphite/cyanate ester (Gr/CE) trusses that connect the TPS and the bus and that provide mechanical support for the secondary array deployment mechanisms and radiators (**Figure 4-12**). (The secondary array mechanisms and cooling system are described in Section 4.8.1.) The TPS and radiators are connected to the trusses by titanium flexures. The TSA trusses, secondary solar arrays, slider mechanisms, radiator panels, cooling system hoses, and spacecraft forward deck with the control electronics and cooling system pumps will be assembled, processed, and qualified as a single assembly.

A finite element model (FEM) of the TSA (**Figure 4-13**) was used to determine the truss geometry and sizing needed to meet launch load requirements. Three static load cases—15 g separately in X, Y, and Z—were run, and 15 iterations were completed (**Figure 4-14**). The results of the analysis, summarized in **Table 4-10**, demonstrate that the TSA design meets all load requirements with positive margins.

4.5.3 Instrument Accommodation. The Solar Probe+ mechanical design accommodates the baseline instrument payload specified by the STDT (Section 3.2 and Table 3.2). Instrument placement is shown in **Figure 4-9**, and the instrument fields of view (FOVs) are illustrated in **Figures 4-15, 4-16, 4-17, and 4-18**. (The Neutron Gamma-ray Spectrometer, not shown, is located just behind the heat shield.)

The Fast Plasma Instruments (Fast Ion Analyzer, one of the two Fast Electron Analyzers, and the Ion Composition Analyzer) are co-mounted on a bracket on the +X/−Y panel of the spacecraft; the bracket allows viewing very near the edge of the TPS umbra, in the ram direction, during closest approach to the Sun. The Coronal Dust instrument is mounted on the −Y panel looking in the ram direction to collect the maximum number of dust impacts. The second Fast Electron Analyzer is mounted directly to the spacecraft body, on −X/+Y panel, and angled to view in the anti-ram (wake) direction. The Hemispheric Imager is located on this panel as well; because the HI is mounted on the wake side of the spacecraft, the bus will protect the imager from the coronal dust flux.

The high-energy and low-energy energetic particle sensors (EPI-Hi and EPI-Lo) are mounted on the spacecraft's −Y and +X/−Y panels such that they view particles incident from both the sunward and antisunward hemispheres. The apertures of EPI-Hi's two high-energy telescopes (HET) are aligned with spacecraft Z axis so that they point sunward and antisunward. The apertures of the EPI-Hi medium energy telescopes (MET) are oriented orthogonal to the X axis (**Figure 4-15**). The EPI-Lo's FOV is angled to the edge of the TPS to maximize the FOV for incoming energetic particles.

The Magnetometer is mounted on a deployable, non-retractable axial boom extending from the aft deck of the spacecraft ($-Z$). The boom will be stowed at launch and deployed after separation from the third stage. The MAG sensor will be located on the boom close to the plasma wave search coils. The three PWI antennas are mounted 120° apart around the lower part of the bus. For launch the antennas will be stowed against the spacecraft bus in the $+Z$ direction. As shown in **Figure 4-19**, all of the instruments remain within the TPS umbra during the solar encounters except for the PWI antennas, each of which extends ~ 1 meter outside the shadowed volume into sunlight. Heat input into the bus from the exposed antennas is initially estimated to be 19 W (Section 4.7). However, because of its mission critical effects on the thermal environment, the PWI flight antennas must be implemented and controlled as an integrated part of the spacecraft's overall thermal protection system.

4.5.4 Subsystem Accommodation. Most of the subsystem electronics are mounted to the internal surfaces of the hexagonal spacecraft structure. The subsystem components, along with the associated harnesses and connectors, can be fully accommodated within the volume of the bus structure (**Figure 4-20**). Three side panels are removable, giving easy access to the spacecraft interior.

Power. The primary and secondary solar arrays and their accommodation on the spacecraft are described in detail in Section 4.8. The primary arrays are mounted on the $+X/+Y$ and $-X/-Y$ panels of the bus; the secondary arrays and cooling system are integrated with the TSA.

Telecommunications. The telecommunications subsystem consists of the high-gain antenna (HGA), two X-band low-gain antennas (LGAs), and the associated electronics. The LGAs are hard-mounted to the bus, separated by 180° and canted fore and aft. The HGA is mounted to a dual-axis gimbaled mast attached to bottom of the $+Y$ panel. The HGA remains stowed within the shadow of the umbra when Solar Probe+ is inside 0.59 AU; outside this distance, the HGA is deployed and the antenna is pointed to Earth for science data downlink (**Figure 4-21**). RF signals are transmitted across flight-heritage rotary joints and along the mast via rigid waveguide. The mast is a lightweight carbon-composite tube with bonded titanium end fittings at the attachment points and is a design with substantial flight heritage.

Propulsion. The hydrazine propulsion tank is located at the center of the hexagonal bus structure, supported by simple machined mounting brackets (**Figure 4-20**). The placement of tank at the center of the bus helps minimize the center of gravity travel as propellant is expended. Propellant lines internal to the bus run to the thrusters, which are placed meet to momentum control requirements and provide attitude control during TCMs. The thrusters are positioned so as to minimize impingement on the instrumentation and spacecraft.

4.6 Thermal Protection System

The increase in the minimum perihelion distance from $4 R_S$ to $9.5 R_S$ results in a reduction by almost a factor of 6 in the intensity of the solar flux to which Solar Probe+ will be exposed at closest approach, from 400 W/cm^2 at $4 R_S$ to 70 W/cm^2 at $9.5 R_S$. This reduction in the incident solar flux allows Solar Probe+ to use a simpler, less massive Thermal Protection System (TPS) than that baselined for Solar Probe in the 2005 study. Solar Probe 2005 required both a conical primary shield and a secondary shield; in contrast, Solar Probe+ needs only a single shield, the design of which is based on the secondary shield design developed for Solar Probe 2005. The requirements for the Solar Probe+ TPS are given in **Table 4-11**.

4.6.1 TPS Design. The Solar Probe+ TPS is a carbon-carbon (C-C) composite Sun shield, 2.7 meters in diameter and approximately 17 cm thick. The shield is a shell consisting of a flat top cover and a pan that is filled with a 15-cm thick layer of reticulated vitreous carbon (RVC) C-C insulating foam. The carbon foam is the primary thermal block in the TPS, and its thickness is determined by the surface temperature and the allowable heat flow through the shield. The forward face of the shield is coated with a low (<0.6) α/ϵ ceramic optical coating to reflect some of the incident solar energy. An additional layer provides protection against micrometeoroid impact. The side wall of the heat shield is angled to reduce the exposure to solar flux when the spacecraft is at closest approach, allowing the wall to radiate into space heat conductively transferred to it from the front face. The portion of the TPS shield just above each secondary solar array forms a straight knife edge to ensure the uniform illumination of the cells in the TPS penumbra when the array is partially retracted (cf. Section 4.8.1).

At closest approach, the Sun shield is exposed to a total incident flux of $\sim 4 \text{ MW}$ and reaches a temperature of $\sim 1700 \text{ K}$. Heat is transferred to the spacecraft both radiatively from the bottom of the shield and conductively through the shield supports. To ensure that the spacecraft does not exceed its maximum safe operating temperature of 40°C (cf. Section 4.7), the shield must reduce the heat flow transmitted to the spacecraft to 50 W or 0.001% of the original flux. The target temperature for the bottom of the shield is 350°C .

As discussed in the preceding section, the TPS is supported by the six trusses of the TSA. Because the temperatures at the base of the Sun shield are expected to be below 350°C , Ti flexures can be used to support the entire shield. These flexures transfer the mechanical loads to the TPS truss system and provide additional thermal resistance, so the temperatures at the top of the truss supports are beneath 300°C . At these temperatures, normal composites can be used to reduce the mass of truss members.

4.6.2 TPS Development. The design on which the Solar Probe+ heat shield is based was extensively studied as part of a Solar Probe Thermal Protection System Risk Mitigation Study carried out by the Applied Physics Laboratory in 2006.⁶ The thermal and structural analyses performed as part of this study have been updated for Solar Probe+ and demonstrate that the baseline Solar Probe+ TPS design can meet all of the thermal requirements and stiffness and strength requirements. Further trade studies, analysis, and testing will be undertaken during Phase A to develop options for saving mass and maximizing reliability in the TPS overall system. Coupon testing of the C-C and insulating materials and analog testing of representative structures will provide the basic engineering information needed for the TPS design. To bring the TPS technology up to a TRL of 6 by the time of the Program PDR, a full-sized TPS will be built and mechanically tested. In parallel with this activity, a segment of the shield will be built and tested to verify its thermal performance. This parallel testing approach is necessitated by the limitations of the available test facilities and the fact that the driving mechanical and thermal design cases are different. Both the mechanical and thermal tests are to be completed by PDR, allowing any design modifications to be incorporated into the flight units.

Finally, it should be noted that the new mission design significantly reduces the risk of mission loss resulting from a catastrophic failure of the TPS. The gradual lowering of perihelion from 35 R_s to 9.5 R_s over the course of the 7-year mission makes it possible to test the TPS system incrementally. Should some potentially catastrophic point of failure be found, the mission trajectory can be altered to keep the spacecraft at a slightly larger distance from the Sun.

4.7 Thermal Control System

The Solar Probe+ thermal control system uses both active and passive control measures to maintain the instruments and spacecraft systems at safe operating temperatures over the range of solar flux to which the spacecraft will be exposed between 1 AU and 9.5 R_s . The thermal control hardware consists of temperature sensors, heaters, MLI, heat pipes, and deck radiators plus the heat exchangers, radiators, mechanical pumps, and hoses used in the secondary solar array's dedicated active cooling system (see Section 4.8.1). The allowed temperatures for the spacecraft bus, as determined by thermal requirements of the propulsion system, range from 20°C to 40°C. All bus components, including instrument interfaces, are held to these limits. Battery, HGA, the star trackers, and solar array temperatures are controlled independently of the bus. (Thermal control of the primary and secondary arrays is discussed in Section

⁶*Solar Probe Thermal Protection System Risk Mitigation Study: FY 2006 Final Report*, prepared by The Johns Hopkins University Applied Physics Laboratory under Contract NAS5-01072, Laurel, MD (November 30, 2006).

4.8.) **Table 4-12** gives the temperature limits (both operational and survival) for the spacecraft subsystems.

4.7.1 TPS/Bus Interface. The TPS/bus interface is designed such that the combined radiative and conductive heat flow from the TPS to the spacecraft bus will not exceed 50 W. The TPS is thermally isolated from the bus by the six high-temperature composite support trusses and titanium flexures of the TSA. Blanket “blockers” are used as well to reduce the radiative heat transfer between the TPS and the bus as much as possible. At closest approach (the worst thermal case), the radiative heat transfer from the TPS directly to the bus is 14 W; the heat input from the support trusses is 4 W (conductive) and 6.1 W (radiative) (cf. **Table 4-13**).

4.7.2 Instrument Interface. The instruments are conductively coupled to the spacecraft bus with an interface temperature range of 20°C to 40°C. The magnetometer and aft boom remain within the TPS shadow during closest approach and will thus not be a significant source of heat to the bus. The three PWI antennas, on the other hand, will extend beyond the umbra into intense sunlight, with the exposed sections reaching temperatures as high as 1500°C at closest approach. However, current calculations show that the total conductive and radiative heat input from the three antennas into the bus should be only 19 W.

4.7.3 Thermal Analysis. Thermal analysis of the Solar Probe+ spacecraft design was performed for worst-case conditions near minimum perihelion (“hot case”) and 1 AU (“cold case”) to determine the required radiator area and heater power. Heat sources assumed in the hot case were the solar flux at 9.5 R_S (70 W/cm²) and the heat dissipated by the spacecraft electronics. For the hot case, the analysis showed that at least 0.64 m² of radiator area is required to maintain the bus temperature below 40° C. To maintain the bus temperature above 20°C, the overall heat into the bus cannot be less than 270 W. In the cold case, the solar flux heat input is minimal (0.13 W/cm²), while the spacecraft electronics dissipate 170 W. Heaters must therefore be used to compensate for the heat loss from the radiators and to maintain the required 270 W heat input into the bus. With the baseline minimum bus power of 170 W, the maximum heater power required in the cold case is 100 W. The results of the thermal analysis are presented in **Table 4-13** and **Figure 4-22**.

In the baseline design the radiators are located near the bottom of the spacecraft bus. Once the final location of all the components has been determined and the TPS final design has been completed, the thermal analysis will be repeated, and the final radiator size and placement will be determined. The final placement of components inside and outside the spacecraft depends on component footprints, fields of view, and thermal criteria.

4.8. Power Subsystem

The Solar Probe+ power subsystem (**Figure 4-23**) consists of primary and secondary solar arrays, two solar array junction boxes, a lithium-ion battery, and power systems electronics (PSE). The power distribution unit (PDU) is part of the avionics subsystem. The subsystem is sized to accommodate the loss of a battery cell or a string of solar cells without affecting mission performance. The power subsystem is single-fault tolerant, with fully redundant power control electronics and command/telemetry paths.

4.8.1. Solar Arrays. Solar Probe+ uses two different solar cell arrays, a primary array and a secondary array, each optimized for use over a different range of Sun-spacecraft distances. The primary array, which is based on the MESSENGER high-temperature solar array design (**Figure 4-24**), is used at distances greater than 0.25 AU. Inside 0.25 AU, Solar Probe+ will use the secondary array, which consists of high-intensity concentrator solar cells mounted on an actively cooled panel. The two solar array systems are diode-isolated from each other, and both feed the common set of peak power tracking modules within the PSE.

Primary Solar Array. The primary solar array consists of two retractable, articulated wings that are attached to the spacecraft bus via a two-axis Schaffer-Moog Type II biaxial harmonic drive stepper motor, a set of interface brackets, and a pyrotechnic-activated pin puller. After launch, the primary array will be deployed from behind the TPS and oriented at an angle to the Sun (**Figure 4-25**). As Solar Probe+ approaches the Sun, the array will be tilted up to $\sim 75^\circ$ off the Sun to limit the incident solar flux and maintain the array within allowable thermal limits ($<180^\circ\text{ C}$) while meeting spacecraft power requirements. When the spacecraft is within 0.25 AU of the Sun, the arrays will be folded back into stowed position within the TPS umbra and will stay in the shadow until the spacecraft reaches 0.25 AU again, when they will be re-deployed. The retractable, rotating wing, two-panel design baselined for Solar Probe+ combines flight-heritage components from TIMED's four-panel design with the Solar Probe+ requirement for a retractable design. (A similar design incorporating a retraction and redeployment capability similar to that described here for Solar Probe+ was developed to the preliminary design review (PDR) level for TIMED but was ultimately not used as the mission design evolved.)

Each solar panel contains 32 strings of solar cells. Each string has 39 series cells and a string isolation diode. The solar cells are triple-junction, GaAs-based cells with an active area of 12 cm^2 , and each cell includes an individual bypass diode. The cover glass is 0.15-mm-thick cerium-doped microsheet, type CMG, with dual antireflective coating. The total active area of cells on each solar panel is $\sim 1.5\text{ m}^2$. Although improved solar cells with increased efficiency are expected in the future, the power analysis

performed for the Solar Probe+ study conservatively assumed a 28% minimum average efficiency (under standard test conditions of 28° C, 1 Sun, air mass zero, beginning of life), as such space-flight-quality production-run cells are presently available and have been qualified and flown. Although the spacecraft performance could benefit from further improvements in solar cell efficiency, any newly developed cells would need to be qualified for the unique environment of this mission.

In order to survive at higher solar flux, optical surface reflectors (OSRs) are evenly distributed among the cells at a ratio of two OSRs for each solar cell (for a “packing factor” of 33%). MESSENGER has successfully used OSRs and panel tilt of up to 74° off the Sun to maintain the primary array solar cell temperature below 180° C.

Secondary Solar Array. The secondary solar array will be used when Solar Probe+ is between 0.25 AU and 9.5 R_S and the primary array is stowed. The secondary array system is integrated with the TSA (Section 4.5.2). Its key components are illustrated in **Figure 4-26** (see also **Figure 4-12**). It consists of two small retractable panels of concentrator photovoltaic cells on an actively cooled substrate that maintains cell junction temperatures below 120° C. Each panel is attached to a linear positioner actuated by a stepper motor. During operations outside or at 0.25 AU, the secondary solar arrays will be fully extended to maintain temperature and minimize heater power needed for thermal balance. As the spacecraft moves sunward from 0.25 AU, the secondary array panels will be retracted into the umbra in fine increments (a small fraction of a cell width), shadowing increasingly more strings behind the two knife edges in the TPS (**Figure 4-27**). The knife edge and secondary array panel radial and axial positions are designed so that, at 9.5 R_S , one row of exposed cells will see half of the solar disk, reducing by almost a factor of two the solar flux incident on the panel and allowing the cooling system to reject the heat. At closest approach (9.5 R_S), the secondary array panels will expose a total equivalent cell area of 34.04 cm² (**Figure 4-28**). This operation provides constant power generation while maintaining the heat flux on the concentrator array at manageable levels. The temperature of the cell substrates (and resulting power conversion efficiency) is controlled as the spacecraft gets closer to the Sun by a closed-loop fluid management system. The system is designed to keep the cells, mechanisms, drive motors, and other components within typical spacecraft operating temperature limits.

Concentrator Photovoltaic Cells. The solar cells baselined for the secondary solar array are triple-junction GaAs-based concentrator cells optimized for high-intensity illumination and high current density.⁷ Each cell has an active “aperture” area of 0.989 cm². The cell front-side metallization, dual bus

⁷The specific cell design proposed for the secondary solar panels has not been space-qualified; however, the epitaxial growth process used in its manufacture is the same as that used for next-generation triple-junction solar cells that have flight heritage. According to the manufacturer, the cells baselined for Solar Probe+’s secondary array will undergo spaceflight-qualification testing during 2008 in accordance with the American Institute of Aeronautics

bars, and gridlines are designed to minimize resistive losses to accommodate the relatively high current. The gridlines and contact metallization are the same as those used for concentrator photovoltaic cells employed in terrestrial applications with optics having a very high concentration ratio. Wide electrical interconnects with stress-relief and multiple-welded contact points conduct the relatively high current between cells. OSRs and electrical insulation cover the cell-to-cell electrical interconnects to minimize thermal load.

The cover glass, which is used for radiation protection and optical filtering, is cerium-doped microsheet with dual antireflective coating. The baseline solar cell stack up used in terrestrial applications is baselined for the secondary arrays: a germanium substrate, Kapton, cell, and cover glass (with adhesive between layers). The stack up design is critical because of thermal gradients built up through the different layers and the maximum allowable temperature of the cell (120°C) **Figure 4-29**). Trade studies will be performed to optimize the cover glass thickness and type of coating, and other possible cell stack ups will be tested to determine which one will result in the lowest cell temperature and the lowest temperature difference through the stack.

The secondary solar array panels each contain 50 parallel strings of solar cells with 27 cells per string and an isolation diode in series. A bypass diode is connected in parallel with each cell, and the diodes are located on the back side of the panel. The cell strings are arranged so that their series direction is parallel to the edge of the heat shield, ensuring that all cells within each string will be exposed to approximately the same illumination level. This becomes more important closer to the Sun, where only one or two strings are exposed on a panel and the illumination level on those strings is varied by fine positioning of the panel. The portion of the spacecraft heat shield just above each secondary solar array panel forms a straight knife edge, which improves the uniformity of illumination on the cells within the strings that are in the penumbra between full exposure and the umbra.

The illumination to which the secondary arrays will be exposed will vary in intensity between 16 and ~250 equivalent Suns, which is well within the range for which concentrator photovoltaic cells have been designed. Characterization tests for concentrator photovoltaic cells have been performed at up to 1000 equivalent Suns. Under the predicted range of operating conditions, the effective conversion efficiency of the secondary array cells will vary between 13% and 20%, with a junction temperature of 120° C, resulting in an additional 2259 to 1897 W of thermal energy absorbed by the cells. Effective conversion efficiency was estimated by using a conservative combination of specifications for spaceflight-qualified solar cells and concentrator photovoltaic cells at a 120° C operating temperature. Estimated efficiency

and Astronautics (AIAA) standard S-111. This qualification testing includes temperature/humidity exposure, top and bottom contact-weld integrity, electron and proton irradiation, and accelerated life.

included derating for losses caused by assembly, cover glass and coating, ultraviolet radiation, charged particle radiation, and micrometeoroid impacts. The power calculations for the concentrator photovoltaic cells also include a loss factor to account for the difference in spectral characteristics between the terrestrial (air mass 1.5) conditions for which these cells have been characterized and the space environment (air mass zero). In addition, the effect of peak power tracker inaccuracy was included.

Array Deployment/Retraction System. The key components of the linear positioning (retraction) system are a drive motor and a slider mechanism (**Figure 4-26**). The slider mechanism baselined for Solar Probe+ uses linear bearings and a recirculating ball lead screw system and is derived from numerical controlled machine tools for which debris tolerance, millions of problem-free cycles, precision, and tolerance of thermally induced misalignments are the normal operating requirements. Modifications are planned to reduce slider mass and to ensure that lubricants and selected components meet spaceflight requirements. The selected drive motor is a Schaeffer-Moog stepper motor with extensive flight heritage. The rated life, available torque, and positional accuracy (resolution) of the motor exceed mission requirements. The arrays will be released from launch lock by activation of a flight-proven pin puller.

Cooling System. The secondary solar arrays will be exposed to intense solar flux inside 0.25 AU, requiring an active cooling loop system to maintain safe operating temperatures. The baseline cooling system consists of copper heat exchangers under the cells, flight-proven pumps with Mars Rover heritage, flexible hoses, ammonia cooling fluid, and six radiators. Each array panel has a dedicated mechanical pump and pump loop as well as three radiator panels providing 1 m² of radiator area. The radiators are honeycomb panels with aluminum face sheets; embedded heat pipes distribute the heat and increase efficiency of the radiators. The ammonia is pumped in a loop through the heat exchanger pipes into the radiator heat pipes and back to the heat exchangers. Flexible hoses (required because the secondary arrays are retractable) transfer the fluid between the exchangers and the radiators. To prevent the ammonia from freezing and to reduce the required heater power, a valve in the pumped loop system will be used to shut off the flow of fluid into the radiators whenever the spacecraft is outside 0.25 AU.

Design Optimization/Qualification. The secondary array system described here represents a novel design not flown before in space. A comprehensive program of trade studies, testing, and other risk mitigation activities (see Section 4.14.1) will therefore be carried out before and during Phase A to optimize the design and to ensure that the arrays and related components can withstand the challenging space environment in which Solar Probe+ will operate. Details about the planned trade studies and tests can be found in the appropriate sections of the *2008 Solar Probe+ Mission Engineering Study Report*.

4.8.2. Battery. The battery baselined for Solar Probe+ is a 20-Ah lithium-ion battery. Lithium-ion technology was chosen because of its high-energy density, good cycle life, use of nonmagnetic materials,

and successful spaceflight heritage.⁸ The battery consists of multiple parallel strings of eight cells in series. The cells have internal switches that will open and isolate a string in case of cell failure. The use of parallel strings allows battery requirements to be met even with a failed string. The battery is conservatively sized so that the depth of discharge (DOD) will not exceed 50%. The most significant discharge will occur during launch; no repetitive eclipses are expected, and there is no shadowing from appendages. The battery supports short-term peak loads and provides a low-impedance source to clear a fuse in case of a load current fault.

4.8.3. Power System Electronics The Solar probe+ PSE tracks the solar array peak power and controls battery charge. The PSE consists of six peak power tracking (PPT) modules, two PPT controller cards, two command/telemetry interface cards, and battery interface cards. Power bus filtering is also included within the PSE. The PSE provides primary power to the power distribution unit (PDU) in the avionics subsystem and is connected by a serial digital command/telemetry interface with the integrated electronic module (IEM), which contains the PPT algorithm. Two solar array junction boxes (SAJBs), one for the primary and one for the secondary array, feed power to the PPT modules. Included in the SAJBs are solar array string isolation diodes and solar array current sensors. The PPT modules and controller design as well as the PPT algorithm have been flown successfully on the MESSENGER and STEREO spacecraft, and the SAJB design is similar to that used by those two missions.

Each PPT module contains a pulse-width-modulated buck-topology DC/DC converter and can support up to 90 W at its output. The use of current mode control within each PPT and centralized control (on primary and redundant sides) of all PPTs ensure current sharing among the modules. This approach also allows the PSE to continue functioning, although with less total output power, in the event that one of the PPT modules fails.

The battery charge control electronics minimizes stress on the battery by reducing charge current when the battery approaches a high state of charge, based on ampere-hour integration. Also, battery voltage limiting causes the battery current to taper to a low value close to the end of charge. The battery charge control parameters are command-adjustable in case of drift in the control electronics or to help compensate for battery aging. Bus overvoltage protection is provided as an additional control loop.

4.8.4. Power System Performance. The power subsystem is designed to provide 482 W of power at distances between 0.9 AU and 0.044 AU (9.5 R_S) from the Sun. Less power will be available between 0.9 AU and 1 AU. The Solar Probe+ will operate in this region only immediately after launch and around

⁸Lithium-ion batteries are being flown on THEMIS, Rosetta, Mars Express, and Venus Express and will be flown on the Solar Dynamics Observatory and the Lunar Reconnaissance Orbiter.

aphelion of the first few orbits, however, and demands on the power subsystem will be reduced during these times through the use of the X-band rather than the Ka-band. Although the amount of data downlinked will also be reduced, the spacecraft will have spent less time below 0.2 AU in these earlier orbits, so the impact on the science return will be insignificant. Among the factors considered in the analysis of the system's performance were solar array optical, assembly, and wiring losses; temperature effects and degradation because of ultraviolet radiation; charged particle radiation; and intensity variations with distance from the Sun.

4.9 Avionics System

4.9.1. Avionics Suite. The Solar Probe+ Avionics Suite (**Figure 4-30**) is an integrated system that manages guidance and control (G&C), spacecraft fault protection, and command and data handling (C&DH) functions. It consists of two block redundant integrated electronics modules (IEMs), remote interface units (RIUs), and an internally redundant power distribution unit (PDU).

The IEM uses a standard 6U compact peripheral component interface (cPCI) card architecture, which allows great flexibility in combining appropriate processor, memory, and interface cards. Each IEM contains five cards: a flight processor, a spacecraft interface card, a G&C interface card, a solid state recorder (SSR) card, and a DC/DC converter card. Under most conditions, only one IEM is powered. The cPCI backplane bus baselined for Solar Probe+ is being used on MESSENGER and STEREO and is planned for the Radiation Belt Storm Probes (RBSP) mission.

The baseline flight processor is an on off-the-shelf RAD750 CPU card with 16 MB SRAM, 4 MB EEPROM, and 64-KB Fuse Link boot PROM. Various configurations are available, including SDRAM-based configurations that provide significantly more main memory and can be selected as needed.

The spacecraft interface card is the only IEM card that contains the “standard” spacecraft interfaces that are not mission-specific. Much of its design has heritage from previous programs. It contains the critical command decoder, which executes some commands directly in hardware and passes some directly to the PDU. It also contains the PDU, downlink, and RIU interface circuitry, the backup oscillator, and clock/timing circuitry.

The PDU switches loads and controls the thrusters by command from either IEM. It uses a slice-based relay-and-switch design that is based on the RBSP design and contains redundant slices for power, command, and telemetry. The PDU is internally redundant with two field-effect transistors (FETs) in each solid-state switch to ensure that every load can be turned off. The FET switches incorporate re-settable circuit breakers based on the power remote I/O (PRIO) ASIC.

The RIUs collect analog and digital telemetry and transmit the data to the IEM using an industry-standard I2C bus. They are small, lightweight units based on the Remote Input-Output (RIO) Application Specific Integrated Circuits (ASICs) flown on several previous missions.

The 128-Gbit SSR is based on stacked SDRAM modules. BAE has proposed such a design for several missions. An alternative approach is to use a flash-based SSR based on the one used on New Horizons.

The G&C interface card contains interfaces to the star trackers, inertial measurement unit (IMU), sun horizon sensor (SHS), reaction wheels, thrusters, and gimbal drive circuitry for the solar arrays. It also contains the fault protection module (FPM), which autonomously switches IEMs if the Sun is seen by the SHS on the aft boom or if other fault conditions occur. The FPM is powered by unswitched power. The FPM in the “off” IEM monitors health signals from the “on” IEM. When the FPM detects a fault, it follows a decision tree and can command the PDU to switch IEMs. The FPM disables itself after use with a latching relay in the PDU. The FPMs can be enabled or disabled by critical command from either IEM (powered or unpowered) at any time.

4.9.2 Flight Software. The Solar Probe+ C&DH software has direct heritage from RBSP and significant component heritage from previous missions, including MESSENGER, New Horizons, and STEREO. It is implemented in the C programming language under the VxWorks™ real-time operating system and uses NASA/GFSC’s core Flight Executive (cFE) middleware

The flight processor selected by ground command as the primary processor acts as the 1553 bus controller and controls the spacecraft, performing all G&C, C&DH, and autonomy and fault protection functions. The secondary flight processor, when powered, boots to a flight software configuration that operates as a remote terminal on the 1553 bus and will record science data to the standby SSR in parallel with the recording of data on the primary SSR by the primary processor. During critical phases of the orbit, the secondary flight processor will act as a hot spare in standby mode in the event of a fault in the primary flight processor. In this mode, the secondary processor executes the same G&C software as the primary processor.

G&C attitude estimation and attitude control algorithms are implemented as tasks executed concurrently within a single G&C application. Both processors receive attitude information from the three star trackers and IMU via the 1553 bus. The primary flight processor performs the attitude estimation and control functions, with the secondary processor in standby mode as a hot spare. The G&C attitude estimation and control algorithms are developed by using MATLAB Simulink™ models. MATLAB Real-Time Workshop (RTW) is used to generate C code from the Simulink™ models, which is then

compiled into the G&C flight software. This G&C software development approach has been used successfully on several previous missions

The ***C&DH software*** manages the telecommunications uplink and downlink using CCSDS protocols for data handling. Commands are received in CCSDS telecommand packets and, according to an operation code contained in the packet header, are either processed by the primary flight processor or dispatched to the other subsystems on the 1553 bus, including the secondary flight processor. The C&DH software supports receipt and storage of command sequences, or macros, which can be executed by a ground command, an autonomy event, or a time-tagged command stored in the flight processor's memory. Additionally, it maintains history logs, event logs, and anomaly logs that may be downlinked to support anomaly investigation. The C&DH software monitors the health of the various software subsystems and may initiate a failover to the secondary flight processor in the event of a critical software anomaly. The system also uses a hardware watchdog timer that triggers a reset of the processor and failover to the secondary flight processor should the software become unable to service the watchdog timer within a programmed timeout.

Instrument housekeeping and science data are routed through a common data processing unit (DPU) remote terminal on the 1553 bus to the flight processor. The DPU compresses and packetizes these data before sending them to the flight processor, where the C&DH software manages the storage of the data packets on the SSR in the form of files. The C&DH software is configured to interleave CCSDS transfer frames of real-time telemetry packets with frames of SSR playback data based on a commandable ratio. SSR playback is managed with the CCSDS File Delivery Protocol (CFDP) software, which is being used successfully on MESSENGER. The CFDP protocol helps automate contacts by ground stations, which increases reliability and reduces operating costs.

In addition to the G&C and C&DH software, the flight processor hosts an ***autonomy and fault protection application***. Data collected from all subsystems are stored in a memory buffer and can be referenced by uploaded autonomy rules to detect and respond to faults. Each rule can monitor one or more telemetry points, perform computations, and execute a specified command (e.g., to execute a stored macro that performs a corrective or maintenance action). This design allows for autonomy rules to be developed and uploaded without requiring software changes. Such systems have been successfully used on several previous missions and increase reliability, while reducing risk and cost for autonomy system changes.

4.10 Telecommunications

Several factors influence the design of the Solar Probe+ telecommunications system. First, the spacecraft remains near the ecliptic throughout the entire mission, which establishes the Sun-Earth-Probe geometry and determines the antenna pointing requirements. Second, the desired science data volume (128 Gbits) and the limited time for data return between subsequent perihelia (approximately 88-150 days apart) require a high data rate for downlink. Finally, the HGA must be protected from temperatures exceeding survival limits at all times; and when it is deployed, its temperature must remain within operating limits in order that pointing be maintained. These requirements ultimately establish the subsystem design and data management strategy to return the required science data. **Figures 4-31** and **4-32** illustrate the Sun-Earth-Probe (SEP) angle and Earth-Probe distance for the baseline mission.

4.10.1. Frequency Selection. Solar Probe+ uses both the Ka- and X-bands for downlink and the X-band for uplink. It is assumed that the DSN 34-m subnet, which possesses both Ka- and X-band capability, will be used for routine (non-emergency) communications. Roughly half of the post-perihelion contacts will occur when the spacecraft is on the far side of the Sun (Earth range greater than 1 AU). Solar scintillation effects (cf. Section 4.3.4) will interfere with communications at small SEP angles ($<3^\circ$ for X-band; $<1^\circ$ for Ka-band). To maximize the data return, Ka-band will be used as the primary science return link. Ka-band increases the achievable data rate by approximately a factor of four or five (including weather effects) compared with X-band; and the 1° SEP angle limit for the Ka-band, as opposed to 3° for the X-band, allows several more days of contact time. This advantage is critical for meeting the science data return requirements for post-perihelion contacts at distances greater than 1 AU from Earth, with reasonable RF transmit power levels and HGA diameters. However, we have also baselined a parallel downlink system that uses the X-band. This system provides better emergency performance, can use the DSN 70-m subnet (which does not have a Ka-band capability), is less sensitive to weather, enjoys greater technological maturity and flight heritage, and has a more forgiving pointing requirement for the same aperture size. These advantage outweigh the additional costs.

4.10.2 Subsystem Implementation. A block diagram of the Solar Probe+ telecommunications subsystem is shown in **Figure 4-33**. The telecommunications subsystem consists of redundant Ka- and X-band transmitters, redundant Ka- and X-band transponders, and three antennas: a high-gain antenna (HGA) mounted to a dual-axis gimballed mast, and two hard-mounted low-gain antennas (LGAs). The HGA is the prime antenna for the Ka-band science data downlink, while all three antennas provide X-band uplink and downlink capability. The HGA dual-gimballed deployment system positions the antenna outside the TPS umbra and, in combination with spacecraft roll, orients it toward Earth for science playback. Earth-pointing and data downlink are achieved across all SEP angles (0° to 180° degrees). Whenever the

spacecraft is within 0.59 AU of the Sun, the HGA is stowed within the umbra. The HGA's main reflector is 0.8-m in diameter and uses a dichroic subreflector to transmit a right-hand circularly polarized (RHCP) wave at Ka-band. A horn behind the subreflector provides bidirectional communications at X-band. With the 0.8-m aperture, HGA requires a pointing accuracy of 0.2°.

When the spacecraft is within 0.59 AU of the Sun, communications are maintained through the X-band LGAs, which are mounted to the bus 180° apart and canted forward and aft respectively. The LGAs provide some directivity, allowing for telemetry reception within the 0.59 AU limit and for emergency rate command and telemetry communications at distances out to 1.7 AU.

The Ka-band (32 GHz) high-power transmitters are 40W RF output power traveling wave tube amplifiers (TWTAs). The TWTAs are approximately 50% efficient (DC power of 80W) and build on heritage from TWTAs on the Kepler (35W at 32 GHz) and Lunar Reconnaissance Orbiter (40W at 26 GHz) missions. The X-band transmitters are 13W TWTAs with heritage from the New Horizons mission and are approximately 40% efficient (32W primary DC power).

The two RF transponders are based on the advanced digital receiver flown on the New Horizons mission, and on digital and Ka-band hardware developed for NASA on the CoNNeCT program. Each transponder requires only 4W primary power in receive-only mode, 8.7W in receive/X-band transmit mode, 9.7W in receive/Ka-band transmit mode, or 14.1W in receive/X- and Ka-band transmit mode.

The output from either of the X-band TWTAs may be steered to any of the antennas through a network of single-pole-double-throw (SPDT) and transfer (XFER) switches, which are themselves configured for redundant operation. The Ka-band TWTAs are similarly switched to the HGA. Hybrid couplers are used with each the X-band and Ka-band TWTA pairs to increase downlink system reliability

4.10.3 Performance. Link performance is determined primarily by the antenna used and by the relative distance from the spacecraft to the Earth. **Table 4-14** summarizes the estimated telemetry performance for the different antennas at varying distances. **Table 4-15** summarizes maximum command rates. No significant solar interference and the use of a 34-m DSN antenna for the ground link are assumed. In the case of the LGA, a 70-m DSN antenna and a worst-case LGA orientation (random tumble) are assumed to cover an emergency situation.

4.11 Data Management

Although the Solar Probe+ baseline instrument suite is fundamentally the same as that baselined in the 2005 study, the data management concept for Solar Probe+ differs from the 2005 concept in two important aspects. First, the Solar Probe+ mission design allows for repeated solar encounters at frequent

intervals, while the 2005 concept assumed only two solar encounters ~4.6 years apart. Second, the 2005 data management plan provided for the downlink of critical science data at a high data rate in real time during the solar encounter;⁹ in contrast, no real-time downlink of science data during solar encounters is planned for Solar Probe+.

From an operational perspective, Solar Probe+ orbits are divided into aphelion and perihelion segments. While some science data will be taken at a low-rate throughout an orbit, most of the science data will be acquired during the solar encounters around perihelion. Encounter data will be stored on the redundant SSRs and played back, along with any cruise data acquired since the last ground contact, when the spacecraft is outside 0.59 AU, in the aphelion segment of the orbit.

4.11.1 Science Data Collection. The average rates for instrument and housekeeping data are given in **Table 4-16**. The raw data rates represent the actual science data; the data rate to the recorders includes 30% margin and a 5% overhead for packetization performed in the DPU. The packetized data will be transferred over a standard 1553 data bus at a rate of 139.6 kbps to the two 128-Gbit SSRs simultaneously and stored for later playback. Actual data rates from the instruments will vary during the encounter; the integrated science payload will be responsible for managing these variations and staying within the total volume allocation.

4.11.2 Data Return. Science data downlink will occur when Solar Probe+ is beyond 0.59 AU and the HGA can be safely deployed. As shown in **Figure 4-32**, the Earth-Probe distance varies from 0.3 AU to 1.9 AU depending on the specific orbit. Assuming 10-hour contacts and average downlink rates for each aphelion downlink period, we have developed a day-by-day downlink schedule that allows the full SSR data volume to be downlinked (except for 6 orbits) and supports other operational aspects of the mission (such as Venus flyby navigation). The full dataset cannot be downlinked for six orbits in which the Sun-Earth-Probe geometry is not favorable. The data volume return shown for these six cases is a worst-case estimate, however, and more detailed modeling of the daily data rate in Phase A is expected to show an increase in the data volume returned. A trade study to be conducted in Phase A will optimize the return for these orbits by balancing science data cadence, DSN cost and schedule requirements, HGA thermal design to increase the window for HGA deployment, and RF transmit power. **Table 4-17** summarizes the contact plan and gives the total data volume downlinked in each aphelion segment.

⁹The intent was to allow a significant science return even if a catastrophic event should occur during the encounter. The Solar Probe+ mission design, with its gradual lowering of perihelion, will allow the mission ops team to familiarize themselves with the spacecraft's response to the inner heliospheric environment and to modify operational plans as necessary, thus reducing the risk of a catastrophic event during a near-Sun pass.

4.12 Guidance and Control System

The Solar Probe+ Guidance and Control (G&C) subsystem maintains the spacecraft attitude required to protect the spacecraft bus from the harsh solar environment, to point antennas for communications with Earth, to provide the desired viewing geometry for science instruments, and to point thrusters for trajectory correction maneuvers (TCMs). Three star trackers and a high-precision, internally-redundant, inertial measurement unit (IMU) provide attitude knowledge, while attitude control is provided by four reaction wheels and 12 0.9-N thrusters. The attitude determination and accuracy requirements derived from these different activities are summarized in **Table 4-18**. Pointing control is driven by the need to point the HGA within 0.2° when downlinking using the communication system. The pointing knowledge and jitter budget is driven by the remote sensing instruments. A functional block diagram of the system is shown in **Figure 4-34**.

4.12.1 Attitude Determination. Spacecraft attitude will be determined by the star trackers and the IMU. The use of star trackers in the near-Sun environment presents a unique design challenge, which the baseline design addresses by mounting the star trackers so that their fields of view are approximately orthogonal to the Sun as well as to each other. This configuration minimizes the chance that all three units will be blinded by a localized coronal lighting event at the same time (cf. Section 4.3.3).

The IMU will provide the spacecraft rate and translational acceleration information necessary for maintaining attitude control as well as for closed loop control during TCMs. The IMU can also be used as a backup to the star trackers to propagate attitude for brief period during a solar encounter if all three star trackers are temporarily blinded. The baselined IMU is a single integrated box with internal redundancy, although two separate units would also meet the needs of the mission.

In the event of long-duration star tracker blinding, system resets, or other attitude control anomalies, a new sensor design, the solar horizon sensor (SHS), is baselined for attitude safing when the spacecraft needs to be protected behind the TPS umbra. The detector is mounted at the end of the science boom and consists of a conical ring of carbon-carbon material, a mirrored conical reflector, and a detector array with pinhole lens. The detector array resides in a small electronics box, which contains readout electronics for both the detector and a set of thermistors. If an attitude error that reaches a designated threshold occurs, the edge of the conical ring becomes illuminated and is projected onto the detector. The processed signal can then be used to provide attitude control for safing during the solar encounter.

Most currently available attitude control hardware should meet the needs of the Solar Probe+ with little or no custom modifications. Special care must be taken to select star trackers that will perform well

in the intense coronal lighting environment. During the engineering study, one or more potentially suitable candidate star trackers were identified in existing product lines. The only attitude determination device that requires development is the SHS; it is, however, conceptually simple.

4.12.2 Attitude Control. Although the overall pointing requirement for the spacecraft is 0.2° , the G&C system has been preliminarily budgeted to about 0.05° since much of the error budget will go to HGA misalignments and actuator setting errors. Consequently, reaction wheel control, which offers very tight pointing control and can easily maintain spacecraft attitude at better than the budgeted 0.05° , has been baselined. Wheel control also interacts less with flexible modes and is more likely to control them to meet the jitter budget. (Thrusters were rejected in the study as the primary means of attitude control because achieving the required pointing accuracy of 0.05° would require frequent thruster firings, risking instrument contamination and structural excitation that could exceed jitter requirements.) Thrusters are used to control attitude during TCMs and for dumping accumulated angular momentum from the wheels when necessary.

4.12.3 Environmental Considerations. Solar Probe+ will be subjected to several environmental effects that must be taken into account in developing the design of the G&C subsystem. First, as the spacecraft approaches perihelion, sunlight reflected off of dust particles will be seen by a star tracker that is viewing the sky through the corona. Coronal lighting reduces the signal-to-noise ratio for a tracker using a CCD, thereby reducing the number of detectable stars and degrading the performance of the star tracker. As noted above, this effect will be mitigated by using multiple trackers and carefully selecting those that will perform well in the elevated background noise of the near-Sun environment.

Solar radiation pressure will be very high and change rapidly during solar encounters. Because the center of photon pressure is ahead of the center of mass, the solar pressure torque is destabilizing and is an important factor in the dynamics of the spacecraft near perihelion. The solar pressure torque, which decreases with distance r from the Sun as $1/r^2$, will require multiple momentum dumps on the day of a perihelion pass. Relatively small misalignments of the TPS could induce significant torque and momentum build-up, potentially requiring more frequent use of thrusters for momentum management. The center-of-pressure/center-of-mass offset will thus be carefully monitored during the design phase.

Dust impacts can also affect spacecraft attitude, especially near perihelion. Dust particles hitting the spacecraft will impart an instantaneous momentum impulse that the reaction wheels must remove. If the momentum impulse is too large for the wheels to handle, the thrusters will have to be fired to keep the spacecraft oriented so that the sensitive spacecraft systems remain safely within the protective shadow of

the TPS. During Phase-A, a more detailed analysis of the near-Sun dust environment will be performed and thruster selection optimized, as necessary.

4.12.4 Pointing Strategy. For most of the Solar Probe+ orbit, the spacecraft will point the TPS toward the Sun. However, as long as sensitive instruments and subsystems are not exposed to the Sun, some off-pointing from solar nadir is expected in order to keep the antennas pointed earthward, to minimize solar torques, or to optimize instrument viewing. During TCMs, the spacecraft will be pointed off the Sun so that the larger 4.4-N thrusters can be used to impart the desired change in velocity. TCMs will occur near aphelion, where the spacecraft bus and instruments can safely be exposed to solar flux for the duration of the TCM. Upon completion of a TCM, the TPS will again be pointed sunward.

Momentum dumping will occur much more frequently during perihelion because of the intense solar radiation pressure. Each momentum management maneuver will be completed quickly, within ~3-5 minutes. For these short periods the thrusters will fire to remove angular momentum, and the control requirements for instrument pointing may not be maintained.

Solar pressure torques can be used as a means of passive momentum control and were considered in the engineering study as a possible augmentation of the Solar Probe+ attitude control system during closest approach. However, successful employment of this method is highly dependent on accurate modeling of solar pressure effects. Given the uncertainties in the models, it was decided that all momentum control would be done with thrusters, and the baseline propulsion system was sized accordingly.

4.12.5 High Gain Antenna Control. The HGA will be pointed by rotating the spacecraft about the spacecraft-Sun line and rotating the antenna to keep it oriented toward Earth. The G&C subsystem will compute the necessary positioning of the gimbal for the HGA based on on-board ephemeris models for the Earth, Sun, and the spacecraft. If on-board ephemeris knowledge is lost or other fault conditions occur, the HGA will be commanded to its safe stowed position.

4.13 Propulsion System

The Solar Probe+ propulsion subsystem is a blowdown monopropellant hydrazine system that provides ΔV and attitude control capability for the spacecraft. It consists of twelve 0.9-N thrusters, two 4.4-N thrusters, a spherical propellant tank, and components required to control the flow of propellant and monitor system health and performance. The baseline propellant load is 49.7 kg of hydrazine. For a 554-kg launch wet mass, this translates to 190 m/s of ΔV . The propellant and pressurant are stored in the same

tank, separated by a diaphragm. As propellant is expelled, the pressure of the pressurant decreases; thus the thrust and specific impulse of the thrusters decrease as the mission progresses. All valves will maintain temperatures above 5°C to protect the soft seals. The propulsion system schematic is shown in **Figure 4-35**.

Several flight-proven options exist for each propulsion subsystem component. A representative set of heritage components has been baselined for preliminary performance evaluation and to demonstrate that the system requirements can be achieved. The propellant tank is a 91-liter titanium tank containing an elastomeric diaphragm to push the propellant out through an outlet in the tank bottom. The maximum expected operating pressure for the Solar Probe+ mission is 300 psi. The tank is manufactured by ATK-PSI and has flight heritage on the DSCS III spacecraft. The thrusters baselined for Solar Probe+ are of the catalytic monopropellant hydrazine type. When the thruster valve is opened, propellant flows through the thruster into a catalyst bed, where the hydrazine spontaneously decomposes into hot gases, which then expand through a nozzle and exit the thruster, producing thrust. The Aerojet MR-103G thruster, with heritage from Voyager, Magellan, New Horizons, Cassini, and several other missions, is baselined for the 0.9-N attitude control thrusters; the Aerojet model MR-111C, flown on New Horizons, STEREO, and MESSENGER, is baselined for the two ΔV thrusters. The actual steady-state thrust produced from both thrusters varies as the tank pressure decreases. **Figure 4-36** illustrates thruster steady-state performance between BOL and EOL. The components used to monitor and control the flow of propellant—latch valves, filters, service valves, and pressure and temperature transducers—all have flight heritage from New Horizons and STEREO.

4.14 Technical Challenges

The Solar Probe+ mission involves significant new development. The engineering study therefore included a preliminary assessment of program risks and identification of risk mitigations in order to develop a mission implementation that balances risk with the ability to achieve performance requirements at low cost and on schedule. The four risk areas described below were identified, and the team has already expended significant effort to mitigate the risks in each area. Formal management of these and any other identified risks will begin in Phase A.

4.14.1 Secondary Solar Arrays. The secondary solar arrays are used to generate power during solar encounters when the primary arrays cannot be used. The technology for this system exists at TRL 5-9 (depending on element), including the temperature control system for the secondary arrays. However, the

near-Sun environment presents unique challenges that the detailed design of the secondary solar arrays must accommodate. Mitigations include

- Increased power margin for the secondary solar arrays in the encounter operational modes to allow for greater than anticipated degradation (Phase A)
- Increased margin in the temperature control system in the secondary solar array subsystem to allow for greater than anticipated heat loads (Phase A)
- Detailed qualification program for mechanisms, temperature control elements, and solar cells (pre-Phase A/Phase A)
- More detailed thermal modeling to optimize the design of the secondary solar array, including the temperature control subsystem (Phase A)
- A mission design that includes the gradual lowering of perihelion from 35 R_S to 9.5 R_S over a 6.5-year interval, allowing for the secondary solar array to be thoroughly characterized and the operations concept to be tailored before the worst-case environmental exposure (incorporated in baseline concept)

4.14.2 Mass Margin. The Solar Probe+ orbit presented in this study requires a high C_3 , and maximum launch vehicle lift mass is constrained. We have baselined the Atlas V 551 launch vehicle with a STAR-48BV third stage for cost; however, the mass margin for this configuration is lower than usually desired at this stage of a program. If significant mass growth occurs, the spacecraft may exceed the lift capability of the baselined launch vehicle and third stage. Mitigations include

- Optimize mechanical structure mass by using composite elements instead of the baselined all-aluminum structure (Phase A)
- Optimize power usage on the spacecraft and the power subsystem design to shrink both primary and secondary solar arrays (Phase A)
- Optimize launch vehicle tailoring and margins to increase lift mass available to spacecraft (Phase A)
- Retain compatibility with Delta IVH launch vehicle with higher lift mass for this orbit (Phase A/B)

4.14.3 TPS Design and Manufacturing. The TPS is a critical element of the Solar Probe+ mission. Extensive risk mitigation work has been performed to ensure that the TPS concept will provide the needed protection from the solar environment. However, detailed design of the TPS has not been completed given the early phase of the program. If unforeseen problems occur during the design,

manufacturing, or testing of the TPS occur, the ability to protect the spacecraft and payload from the near-Sun thermal environment may be compromised. Mitigations include

- Longer than normal development phases for the Solar Probe+ program, with required schedule margin to allow for recovery should problems occur
- Detailed thermal modeling to be completed early in the program, with sufficient margins on thermal design maintained through program (Phase A)
- Full TPS qualification program included in the cost and schedule as early in the program as reasonably possible to allow for modifications that may be needed (Pre-Phase A/Phase A)
- Modular design of TPS and spacecraft interface allows for late delivery of the shield to spacecraft integration (incorporated in baseline concept)

4.14.4 Mechanism Reliability. Mechanisms in the space environment carry some degree of risk, and failures in space of mechanisms have caused problems for missions in the past. The thermal environment of the near-Sun portion of the orbit provides additional challenges to the use of mechanisms. Mitigations include

- Use of high-heritage mechanisms, including detailed analysis of the suitability of each mechanism for the Solar Probe+ environment
- Increased margins on mechanisms and detailed analysis of potential failure mechanisms, including wear and lifetime issues
- Trade study to eliminate mechanisms where possible (Phase A)
- Detailed qualification program for all mechanisms used in flight
- Study to identify workarounds for failure that may occur in flight (Phase A/B)

Table 4-1. Preliminary ΔV /Fuel Budget

Usage	Event	ΔV (m/s)
Trajectory Correction Maneuver	Launch error correction	90
	Venus flyby 1	8
	Venus flyby 2	12
	Venus flyby 3	12
	Venus flyby 4	12
	Venus flyby 5	12
	Venus flyby 6	12
	Venus flyby 7	12
Attitude Maneuver	Momentum management	6
Margin		14
Total ΔV		190
Usable propellant (kg)		52.3
Residual (kg)		0.3
Pressurant (kg)		0.1
Total propellant mass (kg)		52.7
Spacecraft wet mass (kg)		610.0

Table 4-2. Total time spent by Solar Probe+ inside various heliocentric distances

Distance	Time (hrs)
30 R_S	2149
20 R_S	961
15 R_S	434
10 R_S	30

Table 4-3. Comparison of 2005 Solar Probe and 2008 Solar Probe+ mission designs

	2005 Solar Probe	Solar Probe+
Minimum perihelion	4 R_S	9.5 R_S
Aphelion	5.5 AU	1 AU
Inclination	90° from ecliptic	3.4° from ecliptic
Number of solar encounters	2	24
Total time within 20 R_S	~ 96 hours	~ 961 hours
Time between perihelia	4.6 years	88 - 150 days
Time from launch to first perihelion	4.1 years	3 months
Mission duration	8.8 years	6.9 years

Table 4-4. Venus flybys and planned TCMs

Event	Date
Launch	05/21/2015
TCM 1	06/05/2015
TCM 2	07/05/2015
Venus flyby 1	07/19/2015
TCM 3	09/20/2016
Venus flyby 2	10/11/2016
TCM 4	01/25/2017
TCM 5	04/16/2017
Venus flyby 3	04/26/2017
TCM 6	09/10/2017
TCM 7	11/27/2017
Venus flyby 4	12/07/2017
TCM 8	07/11/2018
Venus flyby 5	08/01/2018
TCM 9	08/09/2019
TCM 10	05/15/2020
Venus flyby 6	06/05/2020
TCM 11	05/23/2021
TCM 12	08/12/2021
Venus flyby 7	08/22/2021

Table 4-5. Hardware Redundancy

Functional Area	Hardware Redundancy
Avionics	2 IEMs Internally redundant PDU
Payload	Internally redundant Payload DPU
Attitude Determination	3 star trackers Internally redundant IMU Internally redundant Solar Horizon Sensor
Attitude Control	4 reaction wheels
Propulsion	Redundant thrusters in each axis
Data Bus	Redundant 1553 bus Redundant serial interfaces
Data Storage	2 SSRs
Telecommunications	2 uplink/downlink cards 2 LGAs 2 X-band and 2 Ka-band TWTAs
Thermal Control	2 thermistor harnesses 2 heater harnesses
Power	Internally redundant PSE Spare solar cell strings on each array

Table 4-6. Functional Redundancy

Functional Area	Primary System Failure	Functional Redundancy	Mission Impact
C&DH Processing	C&DH software fault	Second IEM operates in safe mode	Software must be promoted back into operational mode
G&C Processing	G&C software fault	Second IEM operates in safe mode	Software must be promoted back into operational mode
Attitude Determination	Star tracker	IMU: short duration Solar Horizon Sensor	Communications through LGA instead of HGA
	IMU	Star tracker-low rates Solar Horizon Sensor	Degraded pointing performance
Attitude Control	Reaction wheels	Thrusters	Increased propellant usage Increased outgassing
Telecommunications	Ka-band downlink	X-band downlink	Loss of communications P \pm 8 hours. Reduced science data volume
	HGA	LGA	Significant reduction in data rate.
Power	Battery	Solar Arrays	More difficult management of switchover between primary and secondary solar arrays.

Table 4-7. Mass summary

Name	CBE (kg)	Total (kg)
Instruments	47.2	51.9
Accommodation Hardware	7.4	8.4
Telecommunications	31.8	34.8
Guidance and Control	30.4	32.0
Power	119.2	134.8
Thermal Protection System	68.5	78.8
Thermal Control	15.7	18.1
Avionics	12.7	14.0
Propulsion	20.5	21.9
Structure	58.9	67.7
Harness	18.5	21.2
Dry Mass	430.8	483.6
Propellant		49.7
Wet Mass		533
Launch Mass		610
Unallocated Margin		76.7
Total Mass Reserve		30.1%

Table 4-8. Mass margin risk mitigation.

ID No.	Subsystem	Task Description	Current Best Estimate Expected Mass (kg)
1	Launch vehicle	Identify launch vehicle mass hold-backs, etc., based on historical experiences and comparison of mission-unique items across programs	23.00
2	TPS	Decrease the shield diameter via a bus repackaging	5.00
3	Power, solar array	decrease the substrate required area/perform a a cell-string layout	2.00
4	Power, solar array	Perform a historical margin analysis for in-flight systems and decrease the derating penalties	3.0
5	Thermal	Investigate lightweight radiators	2.00
6	Thermal/mechanical	Perform design cycle on transition structure assembly (TSA) fluid/mechanical system	3.00
Total Potential Savings			38.00

Table 4-9. Summary of Solar Probe+ power requirements (in Watts).

Name	Post-Separation	Maneuver	Cruise	Checkout	Approach	Science
Instruments	0.0	0.0	0.0	28.6	0.0	57.2
Accommodation Hardware	0.0	0.0	0.0	0.2	0.0	0.0
Telecommunications	49.7	97.7	97.7	49.7	49.7	49.7
Guidance and Control	95.2	95.2	95.2	95.2	95.5	95.5
Power	18.8	18.8	18.8	18.8	18.8	18.8
Thermal Control	0.0	43.2	43.2	43.2	43.2	43.2
Avionics	35.0	35.0	35.0	35.0	35.0	35.0
Propulsion	2.9	35.9	2.9	2.9	2.9	2.9
Heaters	0.0	27.4	60.4	51.6	80.1	22.7
Harness Loss	3.0	5.3	5.3	4.9	4.9	4.9
Total	204.6	358.5	358.5	330.1	330.1	329.9
Solar Array	0.0	482.0	482.0	482.0	482.0	482.0
Power Reserves	-204.6	123.5	123.5	151.9	151.9	152.1
Margin	-100%	34.4%	34.4%	46.0%	46.0%	46.1%

Table 4-10. Results of three static load tests performed using a finite element model of the TSA. (MEMF = model equivalent mass fraction)

Frequency	Direction	MEMF	Comments
18.1 Hz	Lateral 1	16% X 30% Y	Truss bending
19.2 Hz	First Z	10% X 26% Y 20% Z	Bending of secondary array support panels and tubes
23 Hz	Lateral 2	36% X 13% Y	Truss bending

Table 4-11. TPS requirements.

Requirement	Value
Structural requirement	15 Hz lateral 35 Hz thrust
Ionizing radiation	44 krad Si
Solar flux	Max 70 W/cm ² Min 0.13 W/cm ²
Mission duration	7 years
Configuration	
TPS mass	70.5 kg
Shield diameter	2.72 m
Primary shield thickness	15 cm
Spacecraft orientation	Sun-pointing
Science measurements	
Mass loss	2.5 mg/s
Primary shield surface α/ϵ	0.6
Surface conductivity	Conductive
Heat flow into spacecraft	<50 W

Table 4-12. Temperature ranges (operational and survival) for Solar Probe+ components

Component	Temperature Range, °C
Spacecraft Bus	+20 to +40
Battery	+5 to +30
HGA	−90 to +250
Star tracker	−20 to +60
Primary Array	−90 to +180
Secondary Array	+20 to +100

Table 4-13. Spacecraft bulk temperature as a function of heat input into the bus

Heat Source	Heat Input	
	Cold Case (1 AU)	Hot Case (9.5 R _S)
Electrical dissipation	170.0 W	300 W
Strut (conduction)	0.0 W	4.0 W
Strut (radiation)	0.0 W	6.1 W
Shield thorough bus sides	0.0 W	4.0 W
Shield through top MLI	0.0 W	10.0 W
PWI antennas	0.0 W	19.0 W
Heaters	100 W	0.0 W
Total	270 W	343.1 W
Spacecraft bulk temperature	20°C	38°C

Table 4-14. Maximum telemetry rates vs Earth range

Downlink Rates vs. Earth Range			
Earth-Spacecraft Distance (AU)	Estimated Maximum Telemetry Rate		
	0.8-m HGA, X-band to 34-m DSMS antenna 13-W TWTA	0.8-m HGA, Ka-band to 34-m DSMS antenna 40-W TWTA	LGA, X-band to 70-m DSMS antenna 13-W TWTA
0.5	92 kbps	932 kbps	167 bps
1	23 kbps	233 kbps	42 bps
1.5	10 kbps	104 kbps	10 bps
1.8	7 kbps	72 kbps	6 bps

Table 4-15. Maximum command rates vs Earth range

Uplink Rates vs. Earth Range		
Earth-Spacecraft Distance (AU)	Estimated Maximum Command Rate	
	34-m DSMS antenna to 0.8-m HGA X-band	70-m DSMS antenna to LGA X-band
0.5	>10 kbps	389 bps
1	>10 kbps	97 bps
1.5	>10 kbps	43 bps
1.8	>10 kbps	30 bps

Table 4-16. Instrument and housekeeping average data rates.

Instrument	Raw Data Rate (bps)	Data Rate to Recorder (bps)
Fast Ion Analyzer (FIA)	10,000	13,650
Fast Electron Analyzer (FEA)	20,000	27,300
Ion Composition Analyzer (ICA)	10,000	13,650
Energetic Particle Instrument Low Energy (EPI-Lo)	5000	6825
Energetic Particle Instrument Low Energy (EPI-Hi)	3000	4095
Neutron Gamma-ray Spectrometer (NGS)	500	683
Coronal Dust Detector (CD)	100	137
Magnetometer (MAG)	1100	1502
Plasma Wave Instrument (PWI)	10,000	13,650
Hemispheric Imager (HI)	40,800	55,692
Housekeeping	1800	2457
Total	10,230	139,640

Table 4-17. Orbit data return summary.

Orbit	1	2	3	4	5	6	7	8	9	10	11	12	13	14	15	16	17	18	19	20	21	22	23	24	Total
Days in orbit	168	149	139	119	112	108	101	99	99	96	95	95	96	95	95	94	92	91	91	87	87	87	87	87	2554
Venus flyby	Y			Y	Y		Y			Y							Y				Y				7
Downlink days	81	42	42	81	6	42	59	6	6	56	54	6	6	54	42	6	42	37	42	6	42	29	42	6	844
Avg. data rate (kbps)	44	86	86	44	583	86	44	583	583	44	44	583	583	44	86	583	86	44	86	583	86	44	86	583	92
Data return (Gbits)	128	128	128	128	128	128	94	128	128	90	86	128	128	86	128	128	128	59	128	128	128	46	128	128	2765

Table 4-18. Solar Probe+ pointing budgets

System	Pointing requirements (per axis)		
	Control degrees, 3 σ	Knowledge degrees, 3 σ	Jitter degrees, 3 σ
Communication (HGA)	² 0.2 y,z	N/A	N/A
In situ instruments (<0.3 AU)	² 1 x,y,z	² 0.3 x,y,z	² 0.3 x,y, z over 10 s
Magnetometer (<0.3 AU)	² 1 x,y,z	² 1 x,y,z	² 1 x,y, x over 0.05 s
Plasma Wave Instrument (<0.3 AU)	² 1 x,y,z	² 1 x,y,z	N/A
Hemispheric Imager (<20 R _S)	² 1.0 y,z	² 1.0 y,z	² 0.3 y, z over 1 s

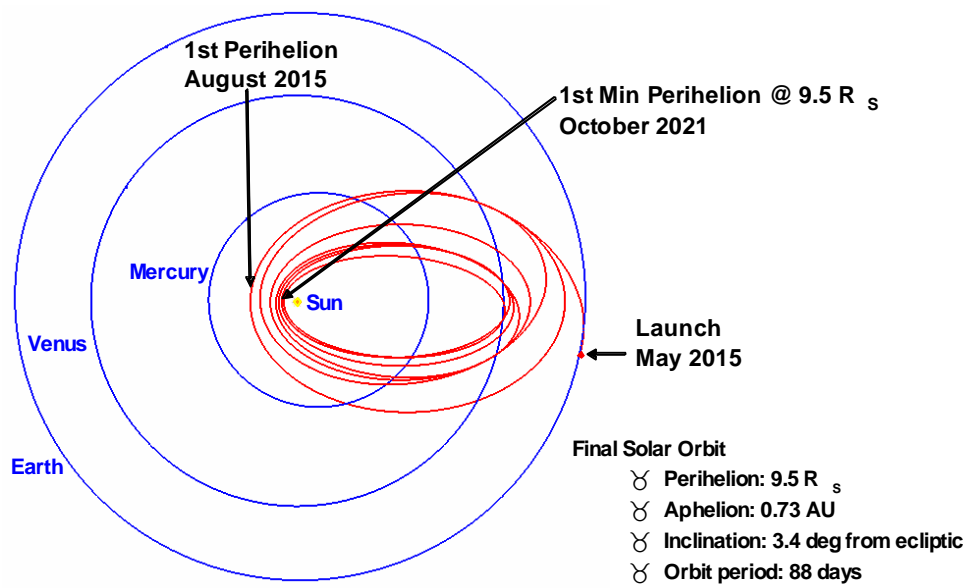


Figure 4-1. Baseline Solar Probe+ trajectory.

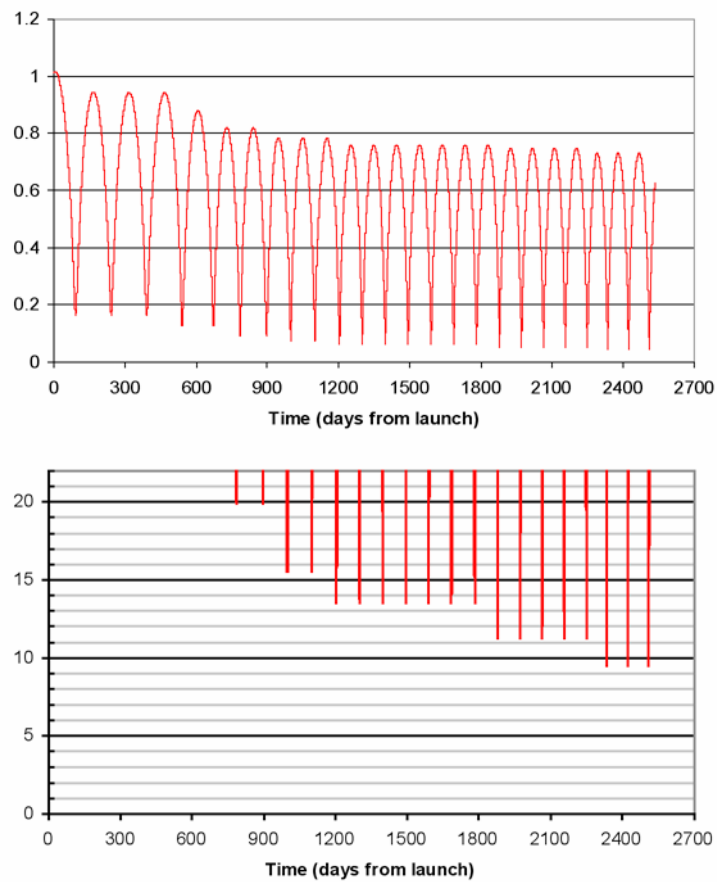


Figure 4-2. Solar distance profile for baseline trajectory for each entire orbit in AU (top) and each of the 21 perihelion encounters at ≤20 R_s.

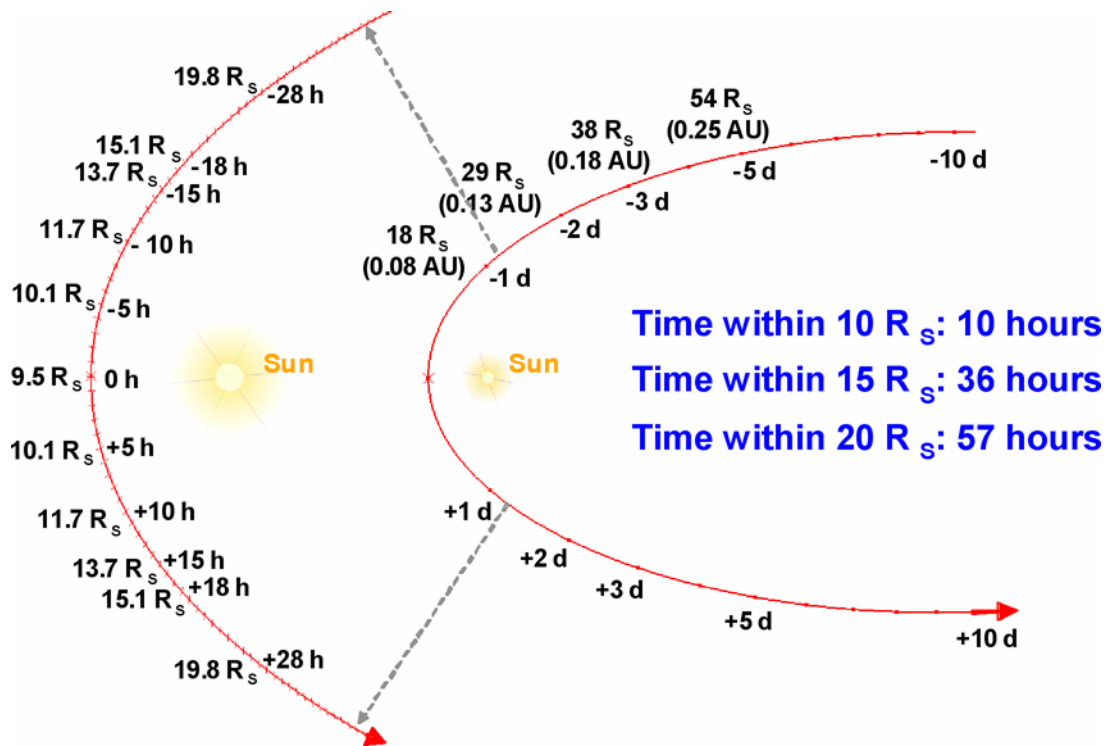


Figure 4-3. The Solar Probe+ trajectory for one of the three minimum perihelion passes. The view is from above the Sun's north pole looking down onto the plane of the ecliptic.

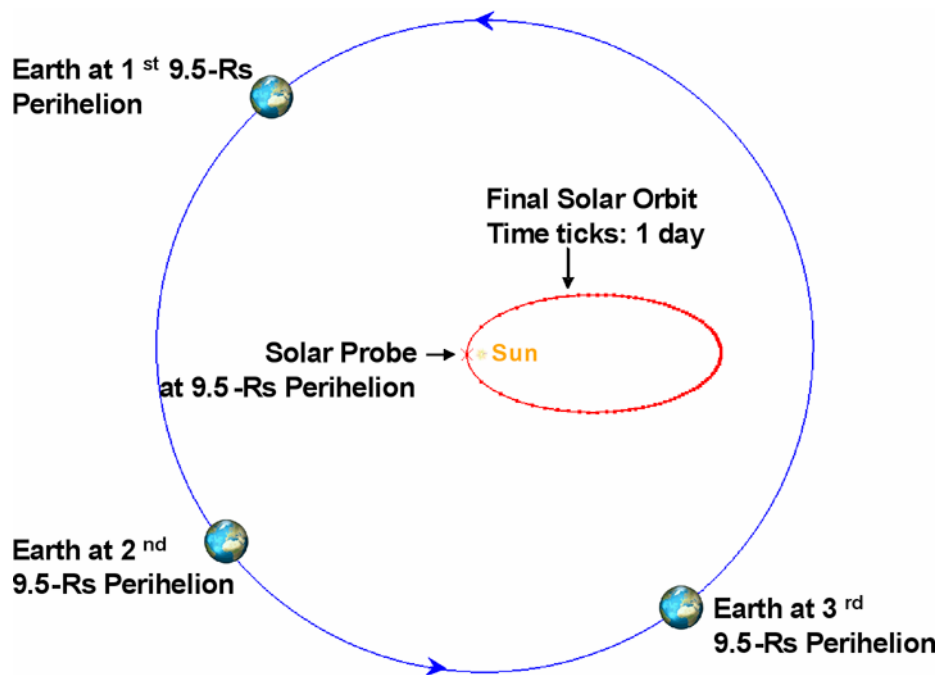


Figure 4-4. Location of Earth during solar encounters with perihelion below 10 R_s .

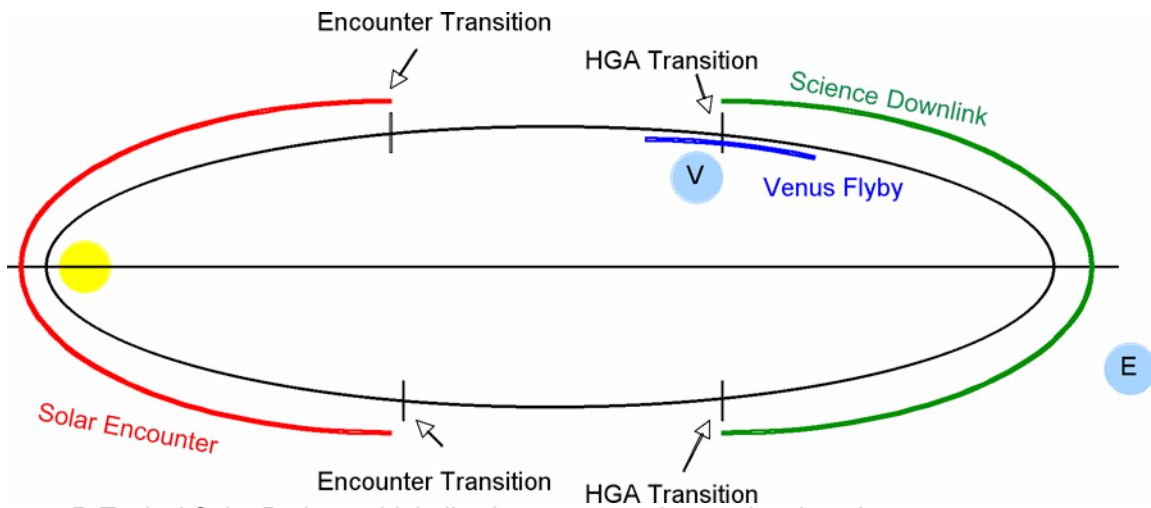


Figure 4-5. Typical Solar Probe+ orbit indicating events and operational modes.

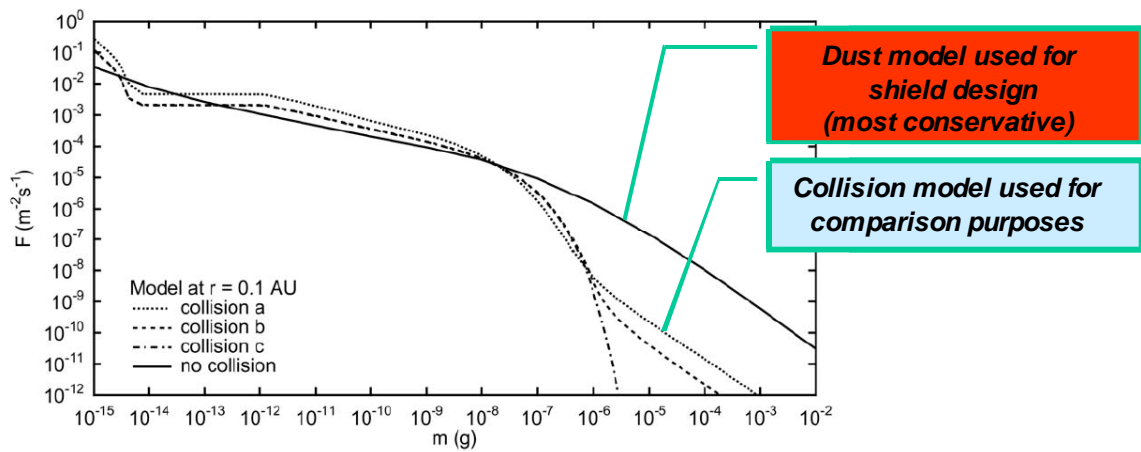


Figure 4-6. Predicted dust environment at 0.1 AU ($20 R_S$) (from Mann et al., 2004 and Ishimoto, 2000)

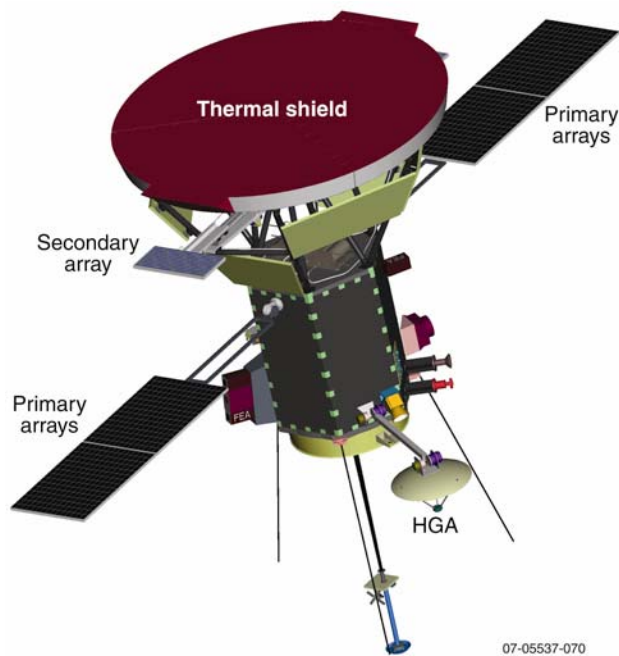


Figure 4-7. Solar Probe+ spacecraft.

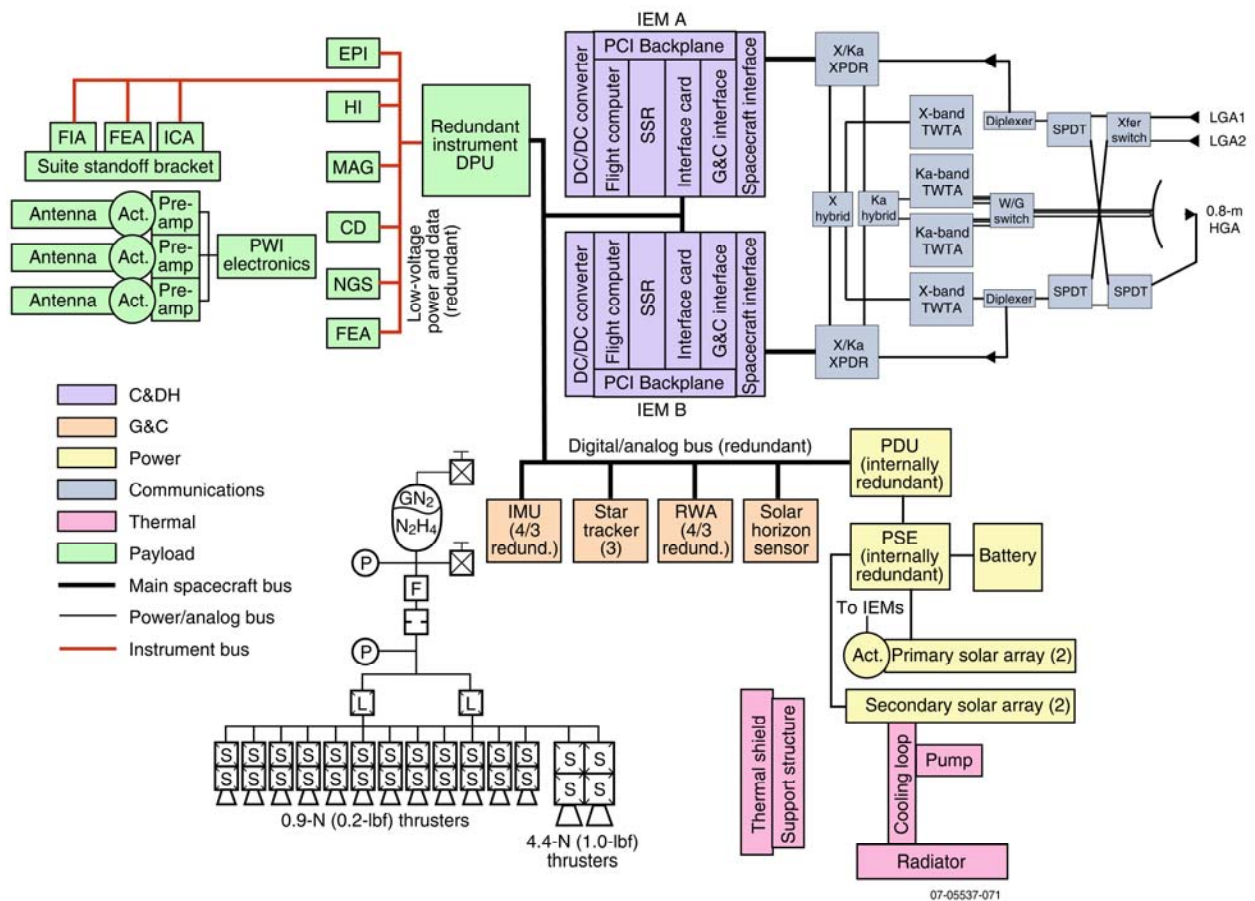


Figure 4-8. Block diagram

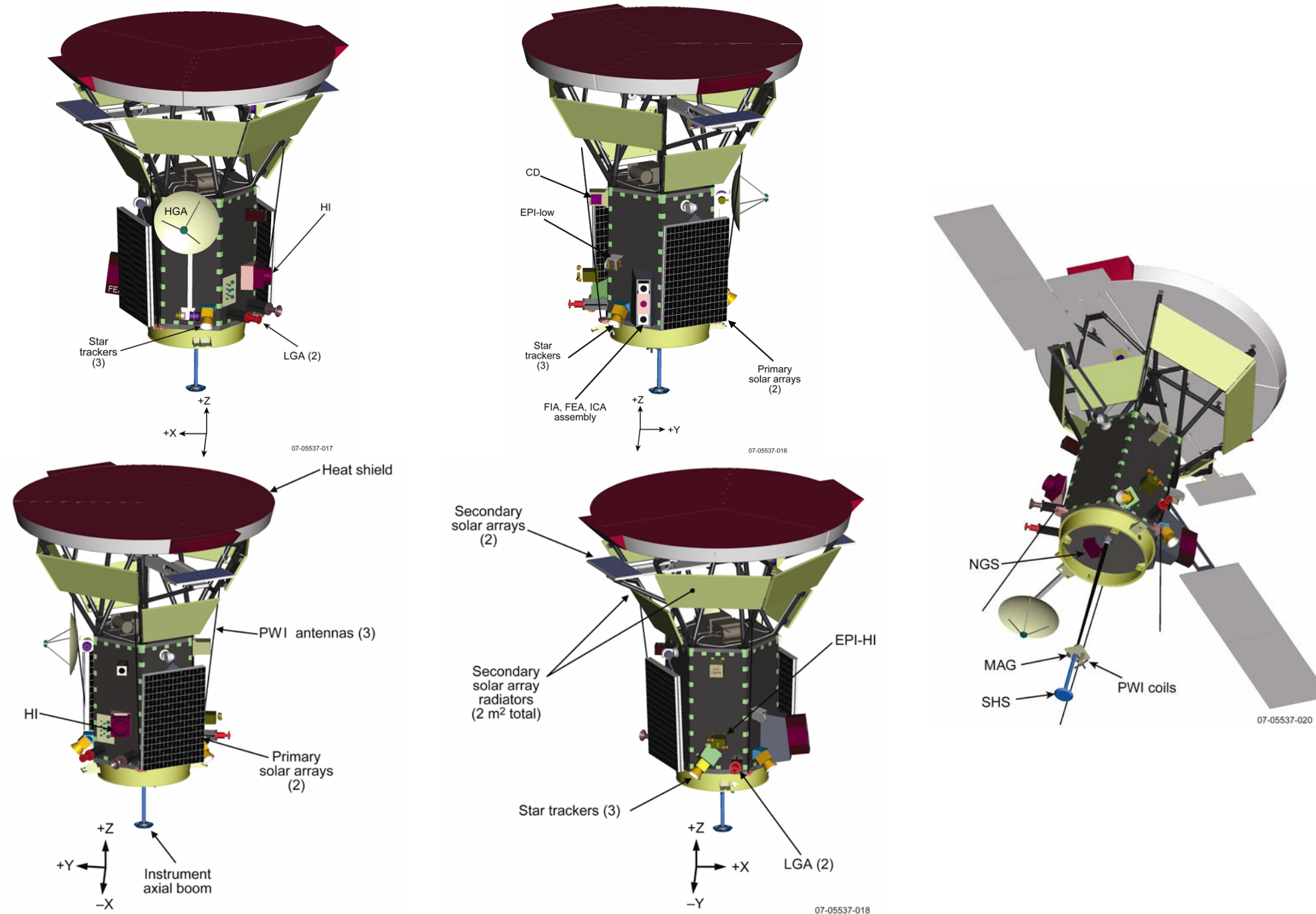


Figure 4-9. Solar Probe+ instrument and component layout

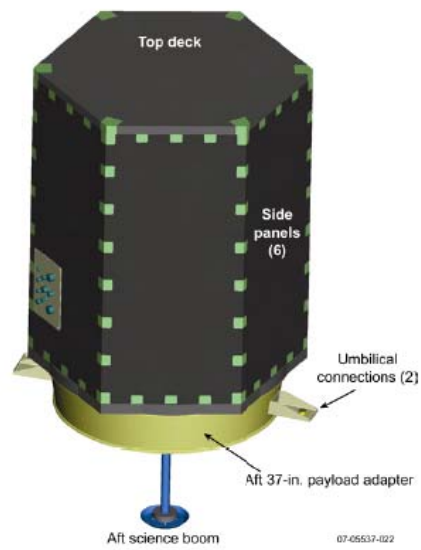


Figure 4-10. The hexagonal bus structure with the payload adaptor ring and aft science boom. Embedded edge members and bond clips are used for interpanel connections.

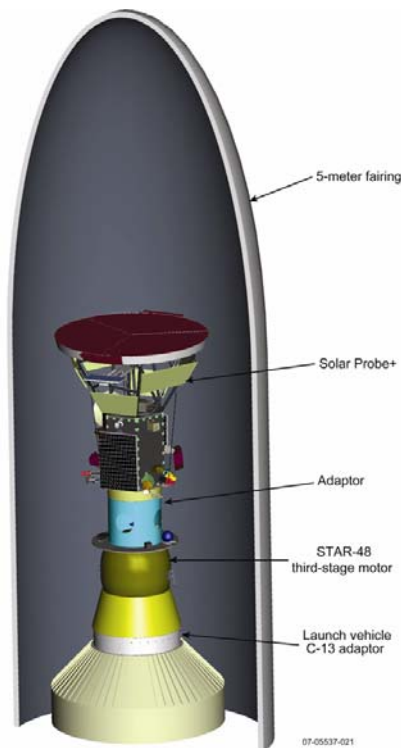


Figure 4-11. Solar Probe+ in launch configuration within the Atlas 551V 5-meter fairing.

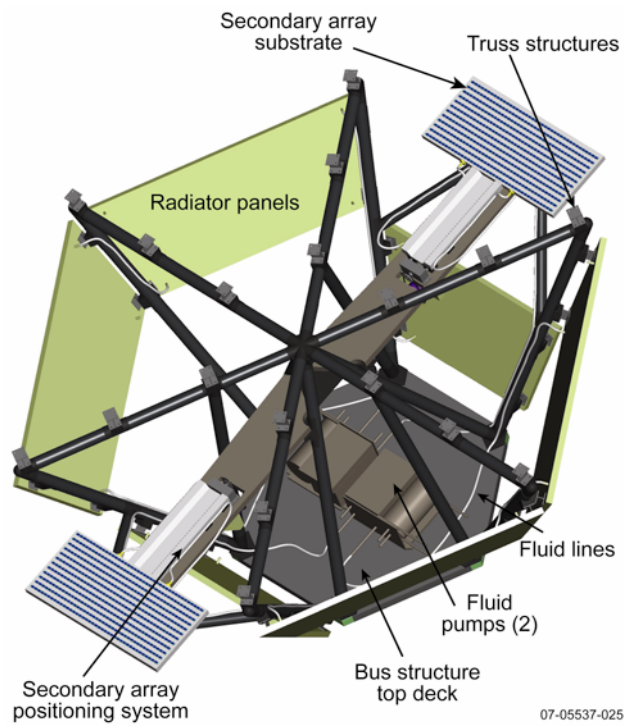


Figure 4-12. The transition structure assembly trusses and components of the secondary solar array system.

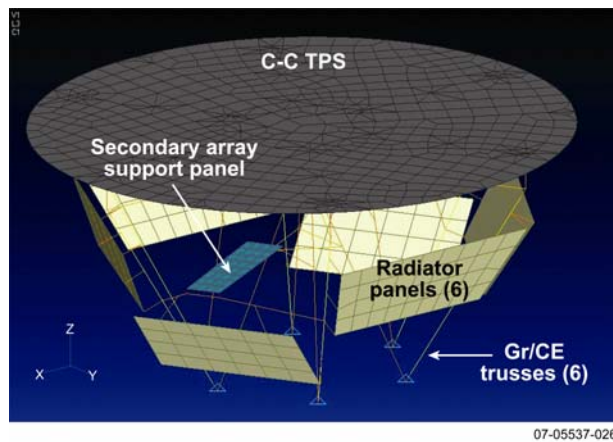


Figure 4-13. Primary components modeled in the finite element model (FEM) analysis.

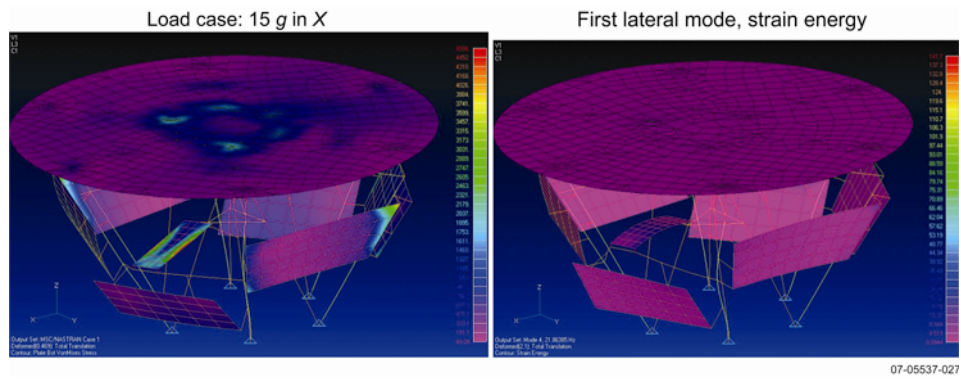


Figure 4-14. Representative results from two FEM analysis runs. All elements show positive margins of safety.

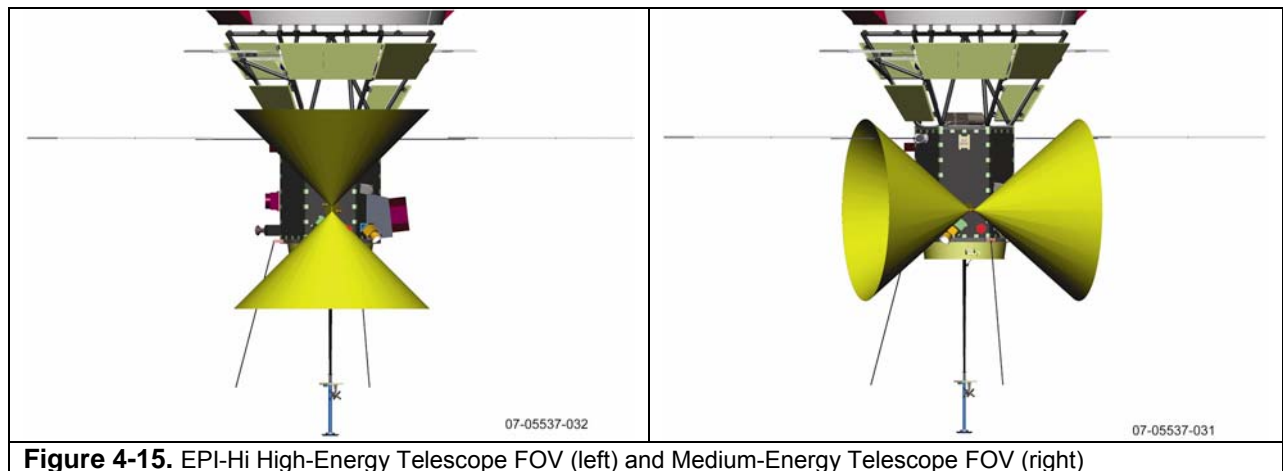


Figure 4-15. EPI-Hi High-Energy Telescope FOV (left) and Medium-Energy Telescope FOV (right)

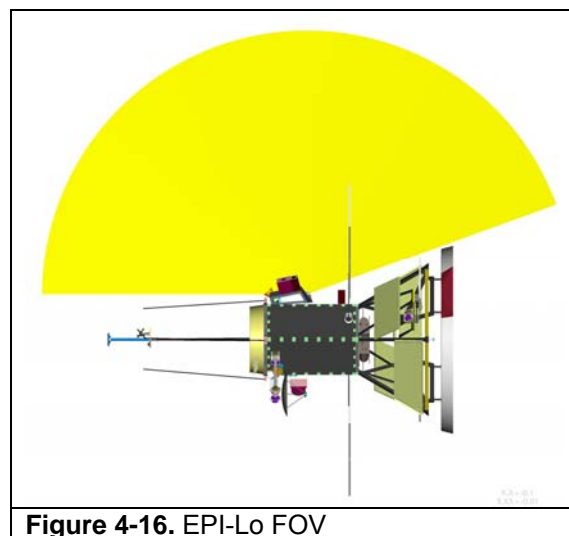


Figure 4-16. EPI-Lo FOV

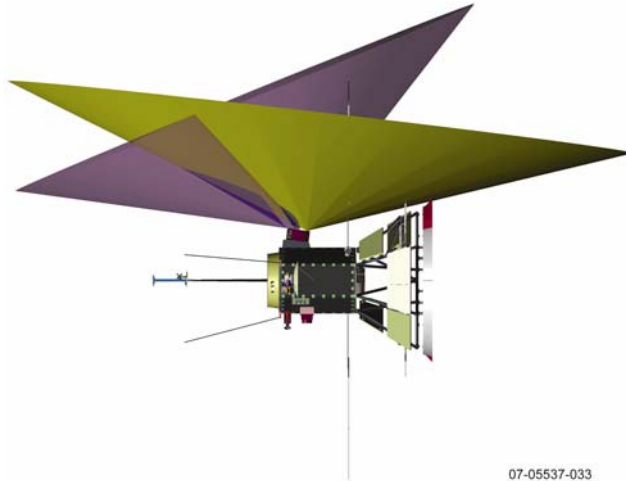


Figure 4-17. FPI FOV

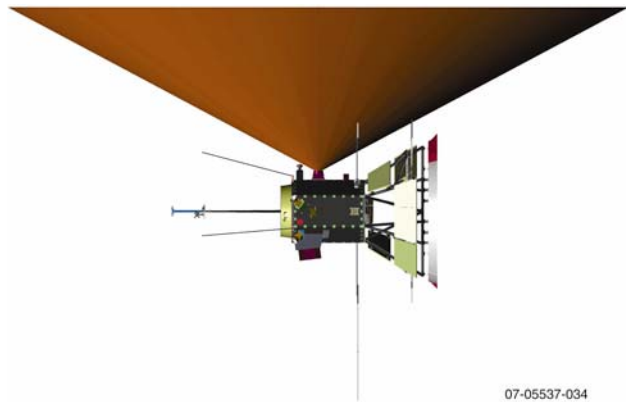


Figure 4-18. HI FOV

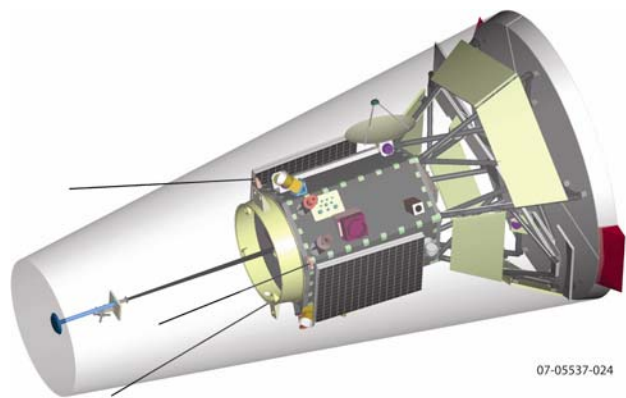


Figure 4-19. All of the instruments except for the PWI antennas remain within the TPS umbra during the solar encounters.



Figure 4-20. Interior view of the spacecraft.

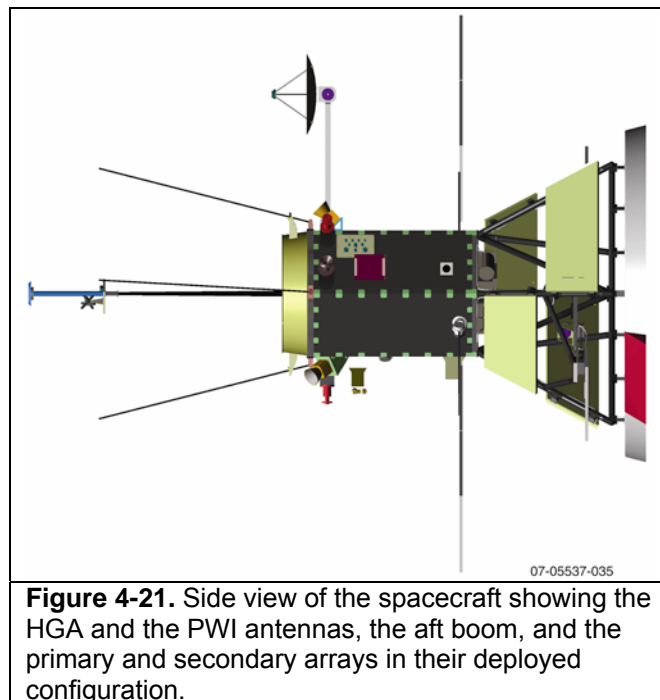


Figure 4-21. Side view of the spacecraft showing the HGA and the PWI antennas, the aft boom, and the primary and secondary arrays in their deployed configuration.

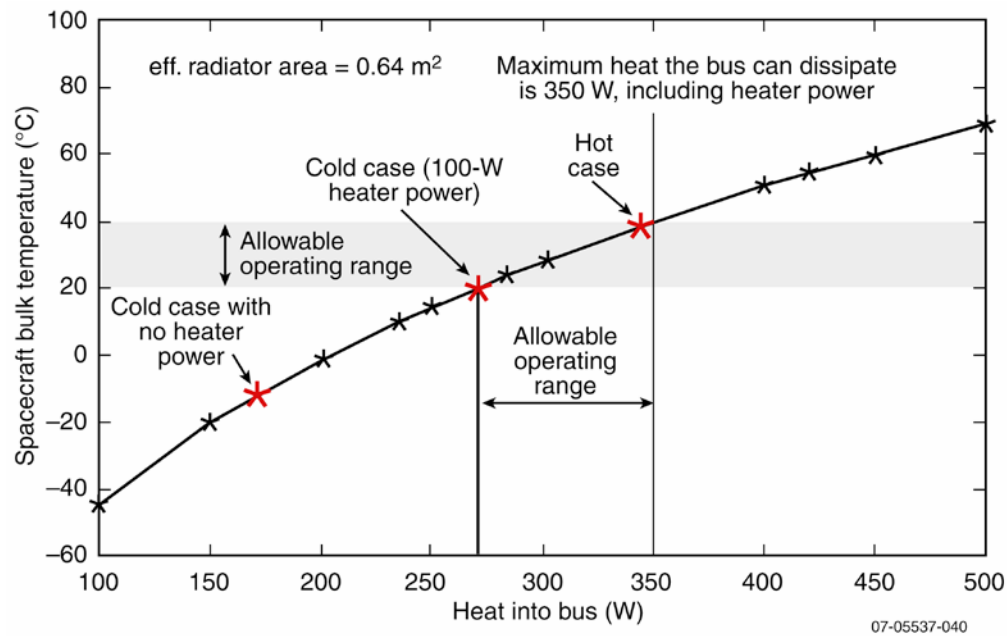


Figure 4-22. The bulk temperature of the spacecraft bus as a function of heat input into the bus, calculated for both Solar Probe+’s minimum perihelion distance of 9.5 R_S (hot case) and 1 AU (cold case).

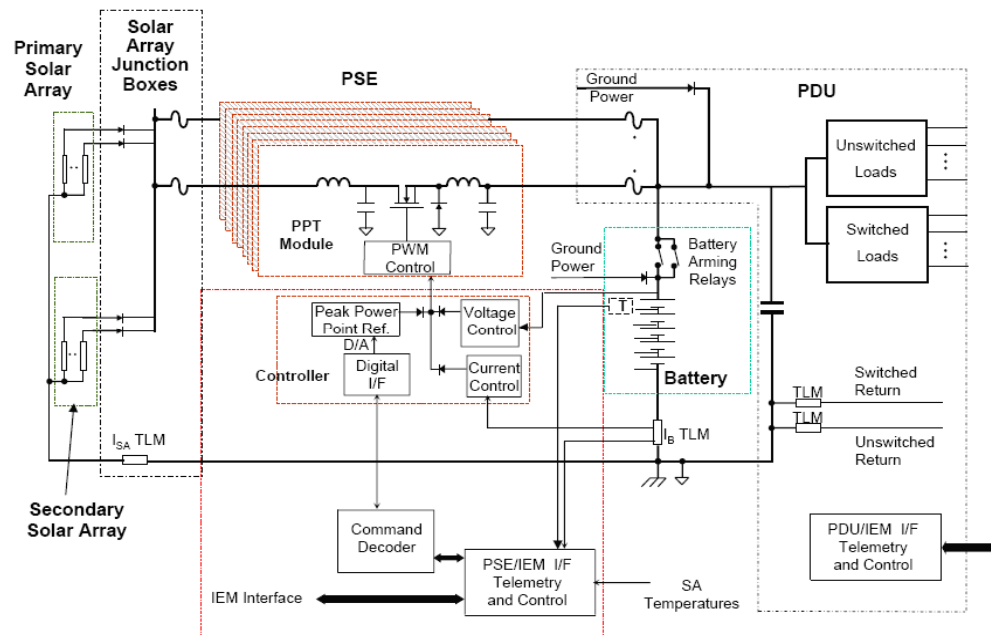


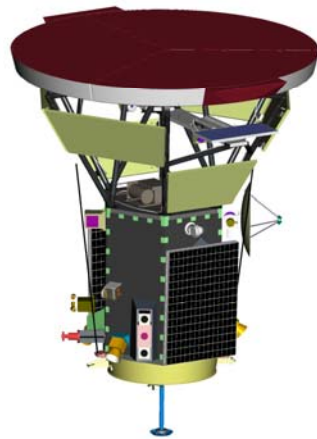
Figure 4-23. Power system block diagram.



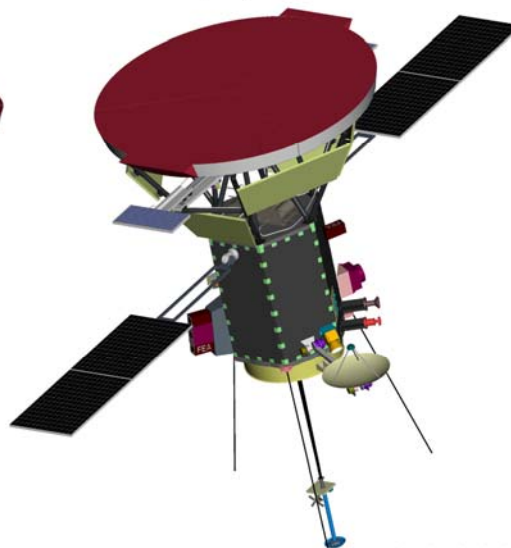
05-04829-35

Figure 4-24. MESSENGER solar array.

Primary solar array panel
in stowed position



Primary solar array panel
in deployed position



07-05537-012

Figure 4-25. The Solar Probe+ primary arrays in stowed (left) and deployed (right) configuration.

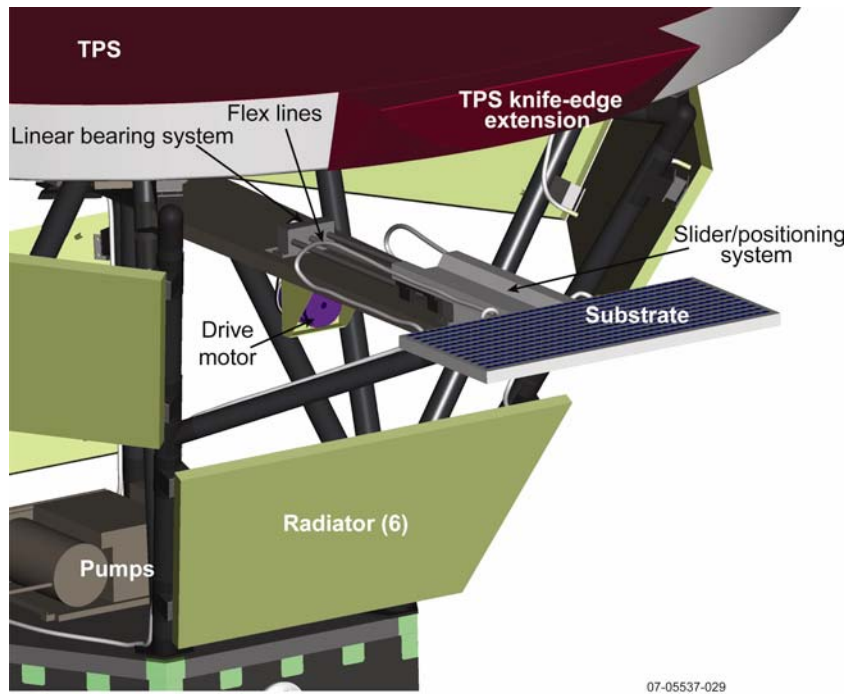


Figure 4-26. Key components of the secondary array system.

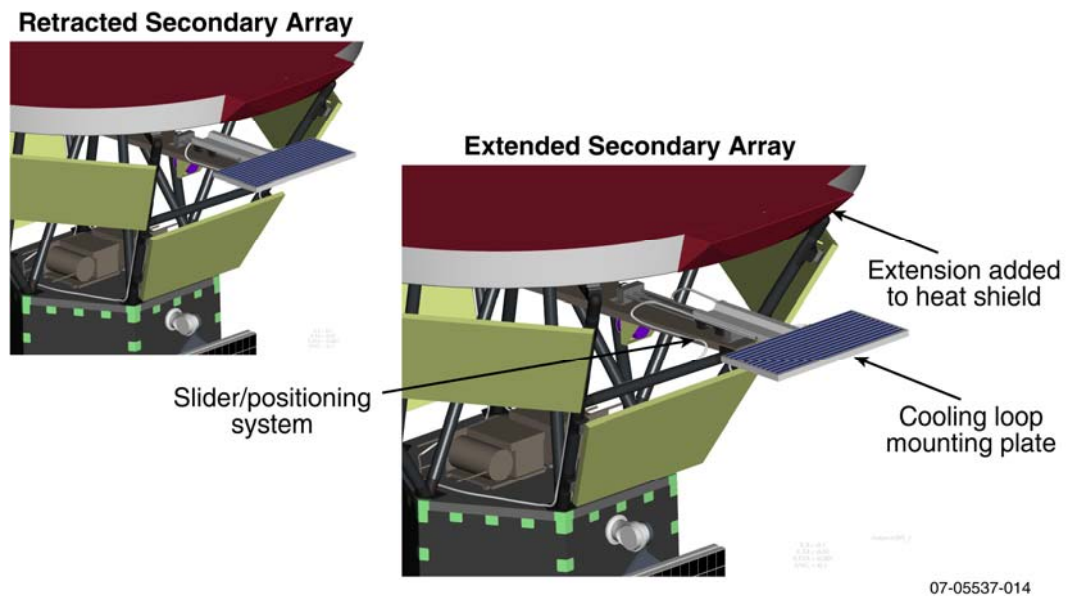


Figure 4-27. The secondary array in its retracted and extended positions.

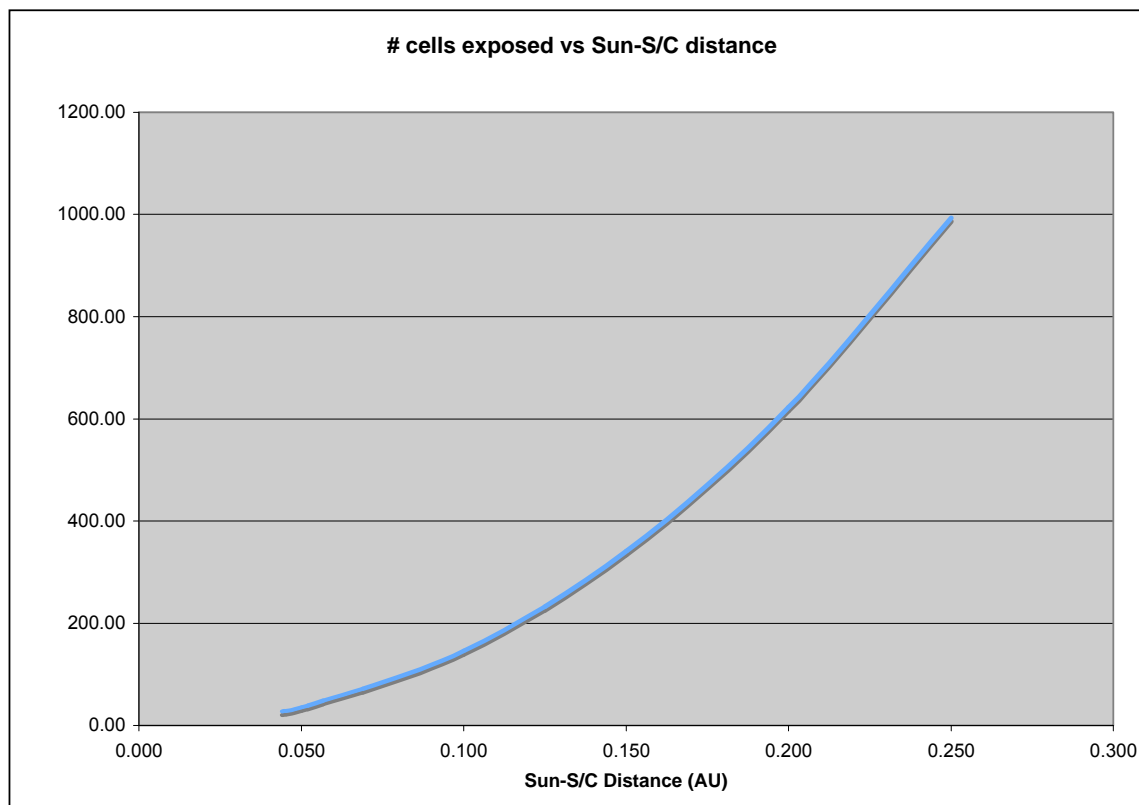


Figure 4-28. Secondary solar array (number of cells) illumination as a function of distance from the Sun from minimum perihelion (0.044 AU) to 0.25 AU. The secondary array is fully deployed and illuminated at and outside 0.25 AU.

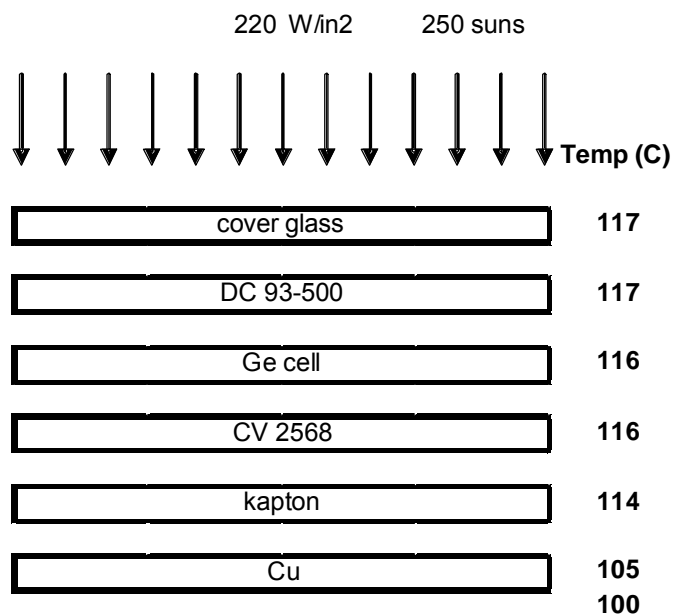


Figure 4-29. Baseline solar concentrator cell temperature stack up.

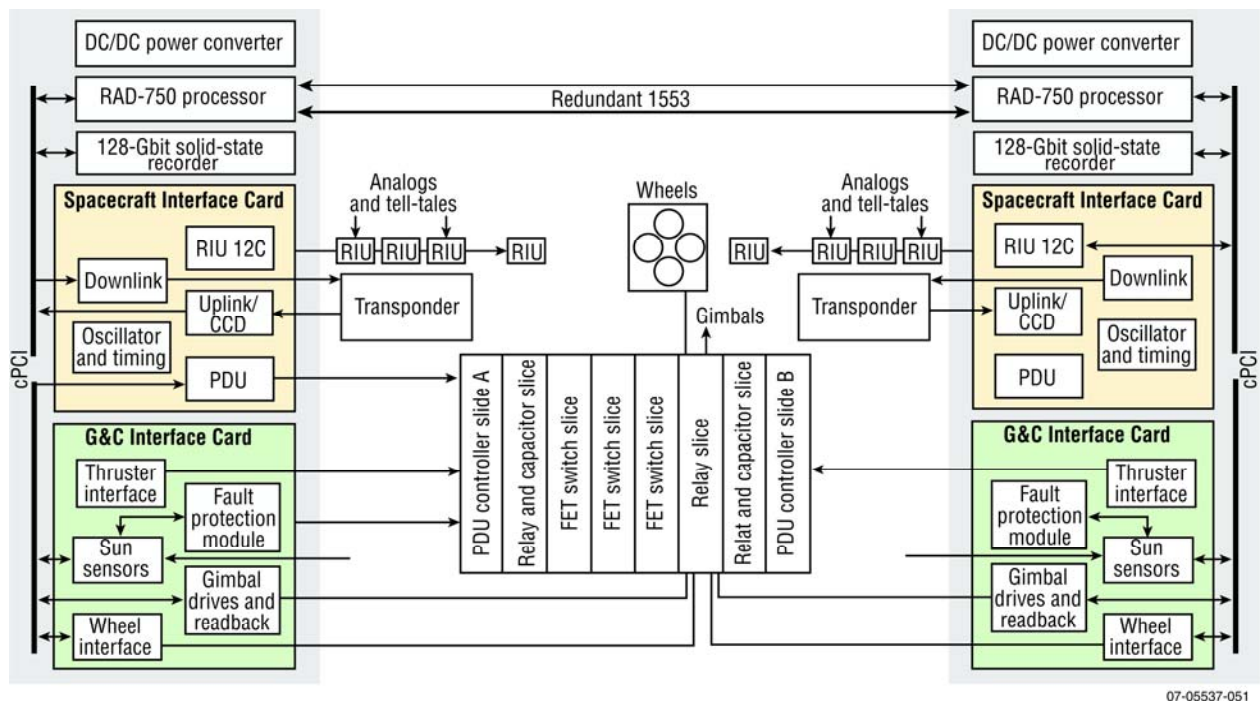


Figure 4-30. Avionics block diagram

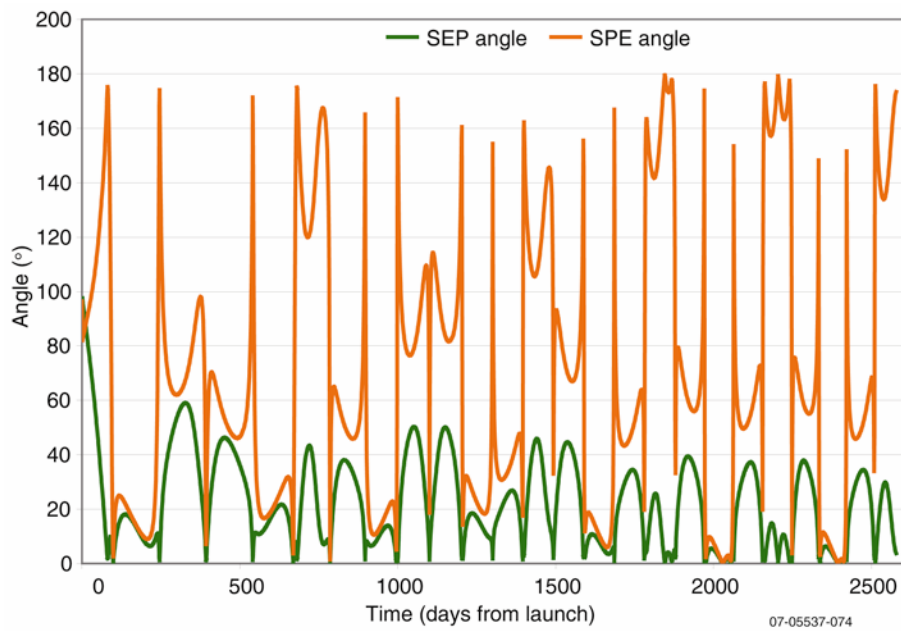


Figure 4-31. Solar-Earth-Probe (SEP) and Solar-Probe-Earth (SPE) angles.

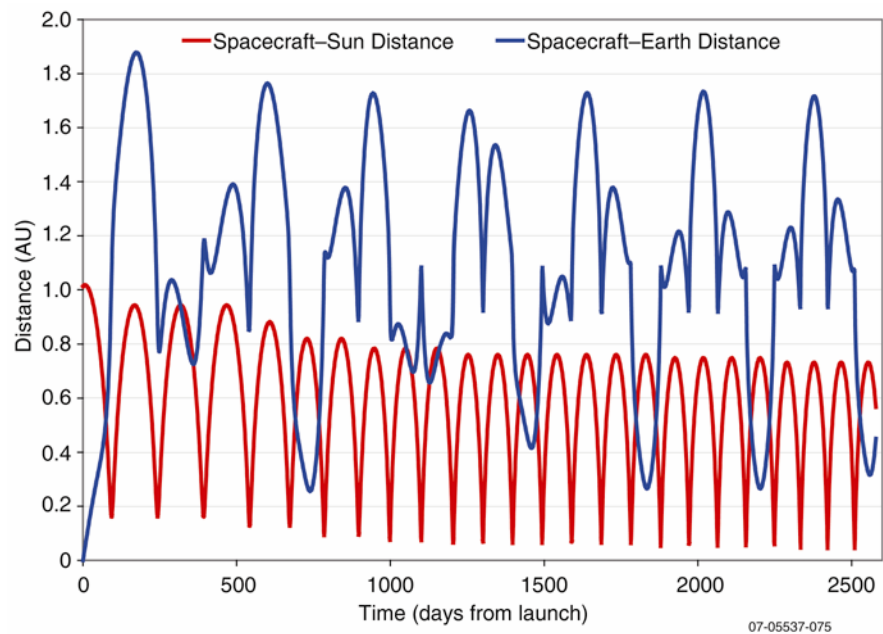


Figure 4-32. Distance of the spacecraft from Earth.

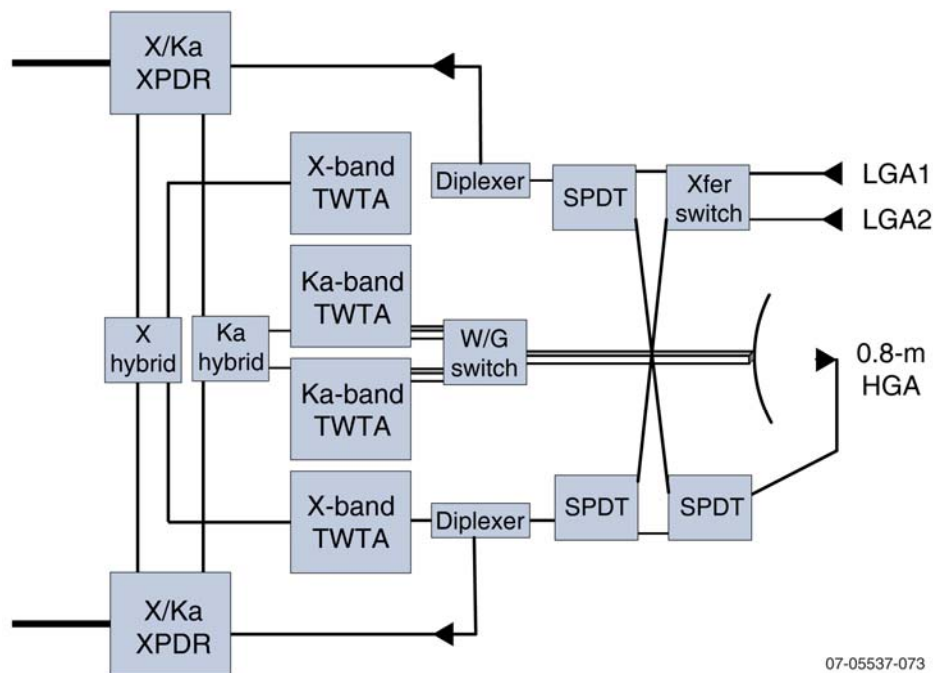


Figure 4-33. Solar Probe+ telecommunications system.

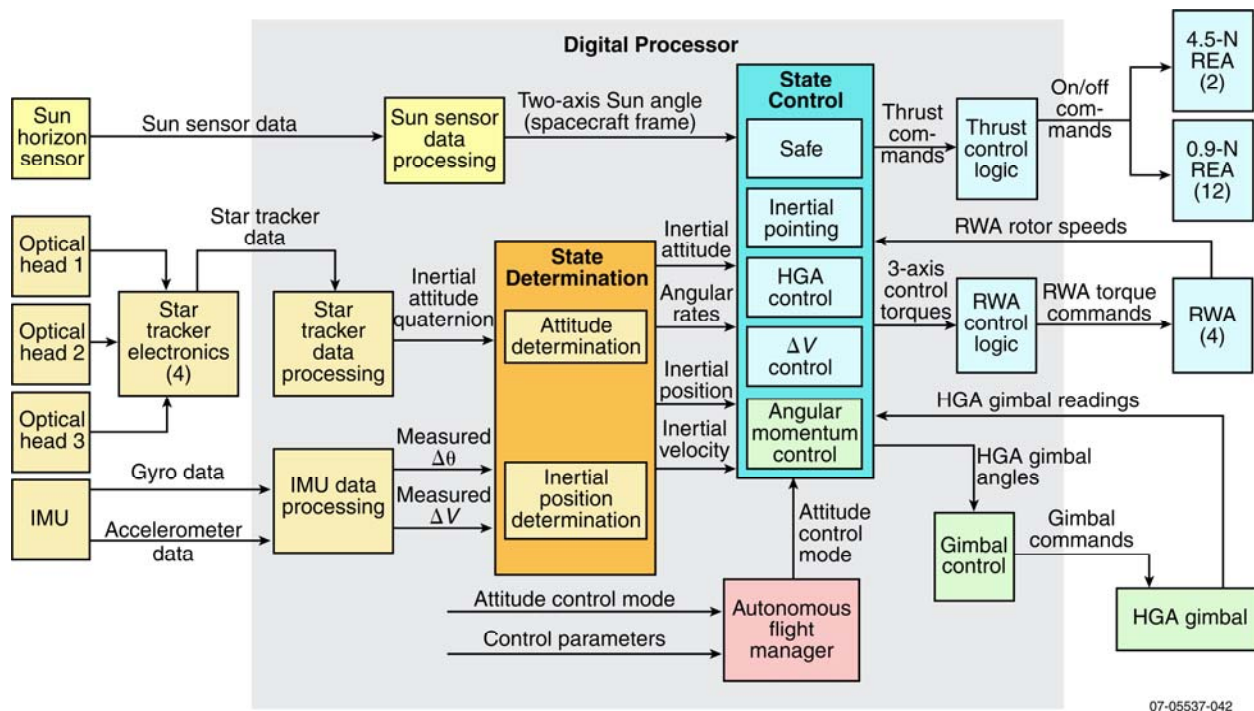


Figure 4-34. Solar Probe+ G&C subsystem functional block diagram.

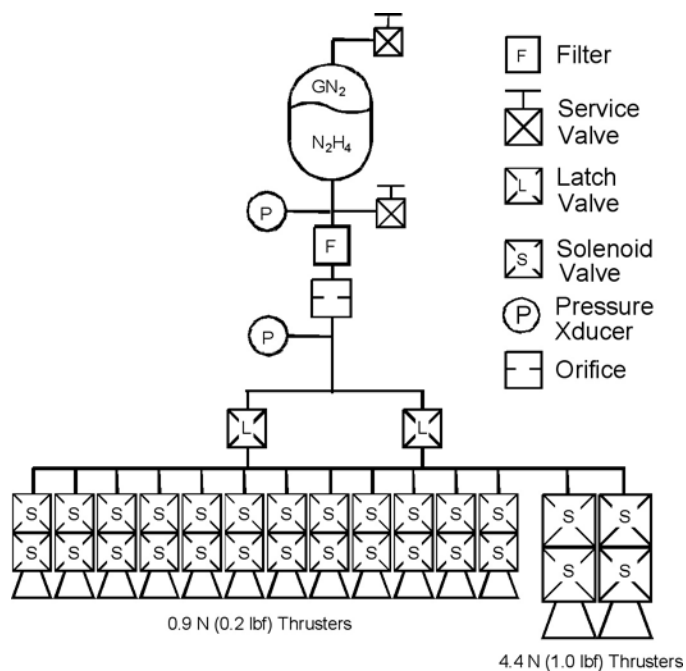


Figure 4-35. Propulsion subsystem block diagram.

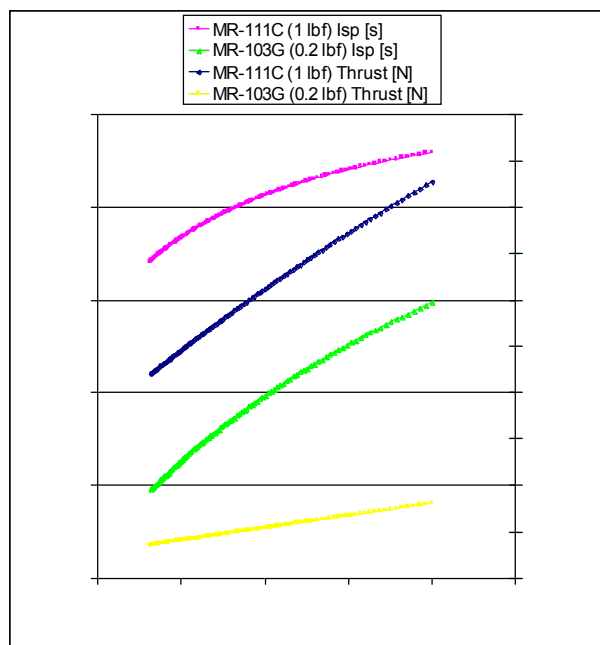


Figure 4-36. Blowdown curve.

5.0 References

- Ambrosiano, J., et al. (1988), Test particle acceleration in turbulent reconnecting magnetic fields, *J. Geophys. Res.*, **93**, 14383.
- Axford, W. I., and McKenzie, J. (1992), The origin of high speed solar wind streams, in: *Solar Wind Seven*, edited by E. Marsch and R. Schwenn, 1, Pergamon, Tarrytown, N. Y.
- Bemporad, A. et al. (2005), UVCS observation of sungrazer C/2001 C2: Possible comet fragmentation and plasma-dust interactions, *Astrophys. J.*, **620**, 523-536.
- Burns, J.A., P.L. Lamy, and S. Soter (1979), Radiation forces on small particles in the solar system, *Icarus*, **40**, 1.
- Canals, A., et al. (2002), Estimating random transverse velocities in the fast solar wind from EISCAT interplanetary scintillation measurements, *Ann. Geophys.*, **20**, 1265-1277.
- Cane, H.V., et al. (2003), Two components in major solar particle events, *Geophys. Res. Lett.*, 8017, DOI 10.1029/2002GL016580.
- Cane, H.V., et al. (2006), Role of flares and shocks in determining solar energetic particle abundances, *J. Geophys. Res.*, **111**, A06S90, doi: 10.1029/2005JA011071.
- Cargill, P.J., and J.A. Klimchuk (2004), Nanoflare heating of the corona revisited, *Astrophys. J.*, **605**, 911.
- Chae, J., U. Schühle, and P. Lemaire (1998), SUMER Measurements of nonthermal motions: constraints on coronal heating mechanisms, *Astrophys. J.*, **505**, 957.
- Chae, J., A.I. Poland, and M.J. Aschwanden (2002), Coronal loops heated by magnetohydrodynamic turbulence. I. A model of isobaric quiet Sun loops with constant cross-sections, *Ap.J.*, **581**, 726-735.
- Cliver, E.W., et al. (2004), Coronal shocks and solar energetic proton events, *Astrophys. J.*, **605**, 902-910.
- Cohen, C.M.S., et al. (1999), New observations of heavy-ion-rich solar particle events from ACE, *Geophys. Res. Lett.*, **26**, 2697, 1999.
- Coles, W.A., et al. (1991), Comparison of solar wind velocity measurements with a theoretical acceleration model, *J. Geophys. Res.*, **96**, 13849.
- Collier, M.R., et al. (2001), Observations of neutral atoms from the solar wind, *J. Geophys. Res.*, **106**, 24893-24906, doi: 10.1029/2000JA000382.
- Collier, M.R. et al. (2003), Dust in the wind: The dust geometric cross section at 1 AU based on neutral solar wind observations, in: *Solar Wind Ten: Proceedings of the Tenth Annual Solar Wind Conference*, AIP Conf. Proc. 679, edited by M. Velli, R. Bruno, and F. Malara, pp. 790-793, AIP, Melville, NY.

- Cranmer, S.R., and A. A. van Ballegoijen (2005), On the generation, propagation, and reflection of Alfvén waves from the solar photosphere to the distant heliosphere, *Astrophys. J. Supp.*, **156**, 265.
- Cummings, A.C., E.C. Stone, and C.D. Steenberg (2002), Composition of anomalous cosmic rays and other heliospheric ions, *Astrophys. J.*, **578**, 194.
- Decker, R. B. et al. (2006), Low-energy ions near the termination shock, in: *Physics of the Inner Heliosheath: Voyager Observations, Theory, and Future Prospects*, AIP Conf. Proc. 858, edited by J. Heerikhuisen et al., pp. 73-78, AIP, Melville, NY.
- DeForest, C.E., and J.B. Gurman (1998), Observation of quasi-periodic compressive waves in solar polar plumes, *Astrophys. J.*, **501**, L217.
- DeForest, C.E. et al. (2001), Observation of polar plumes at high solar altitudes, *Astrophys. J.*, **546**, 569.
- Del Zanna, G., and B. Bromage (1999), Characterization of solar coronal holes and plumes using spectroscopic diagnostic techniques applied to SOHO/CDS observations, *Space Sci. Rev.*, **87**, 169.
- Del Zanna, G., D. Chiuderi, and S. Parenti (2004), SOHO CDS and SUMER observations of quiescent filaments and their interpretation, *Astronomy and Astrophysics*, **420**, 307.
- De Pontieu, B. et al. (2007), Chromospheric Alfvénic waves strong enough to power the solar wind, *Science*, **318**, 1574, doi: 10.1126/science.1151747.
- Feldman, W.C., et al. (1974), Interpenetrating solar wind streams, *Rev. Geophys. Space Phys*, **12**, 715,.
- Feldman, W.C., et al. (1996), Constraints on high-speed solar wind structure near its coronal base: a ULYSSES perspective, *Astronomy and Astrophysics*, **316**, 355.
- Feldman, W.C., et al. (1997), Experimental constraints on pulsed and steady state models of the solar wind near the Sun, *J. Geophys. Res.*, **102**, 26905.
- Fisk, L.A. (1996), Motion of the footpoints of heliospheric magnetic field lines at the Sun: Implications for recurrent energetic particle events at high heliographic latitudes, *J. Geophys. Res.*, **101**, 15547.
- Fisk, L.A. (2003), Acceleration of the solar wind as a result of the reconnection of open magnetic flux with coronal loops, *J. Geophys. Res.*, **108** (A4), SSH 7-1, doi: 10.1029/2002JA009284.
- Fisk, L. A., and G. Gloeckler (2006), The common spectrum for accelerated ions in the quiet-time solar wind, *Astrophys. J.*, **640**, L79.
- Fisk, L. A., and G. Gloeckler (2007), Thermodynamic constraints on stochastic acceleration in compressional turbulence, *Proc. Nat. Acad. Sci.*, **104**, 5749-5754, doi: 10.1073/pnas.0700881104.
- Fisk, L.A., and N.A. Schwadron (2001), Origin of the solar wind: theory, *Space Science Rev.*, **97**, 221,.
- Gabriel, A.H., F. Bely-Dubau, and P. Lemaire (2003), The Contribution of polar plumes to the fast solar wind, *Astrophys. J.*, **589**, 623.
- Geiss, J, G. Gloeckler, and R. v. Steiger (1995), Origin of the solar wind from composition data, *Space Science Rev.*, **72**, 49.

- Geiss, J., G. Gloeckler, and R. v. Steiger (1996), Origin of C^+ ions in the heliosphere, *Space Science Rev.*, **78**, 43.
- Georgoulis, M.K., M. Velli, and G. Einaudi (1998), Statistical properties of magnetic activity in the solar corona, *Astrophys. J.*, **497**, 957.
- Gloeckler, G. (2003), Ubiquitous suprathermal tails on the solar wind and pickup ion distributions, in: *Solar Wind Ten: Proceedings of the Tenth Annual Solar Wind Conference*, AIP Conf. Proc. 679, edited by M. Velli, R. Bruno, and F. Malara, pp. 583-588, AIP, Melville, NY.
- Gloeckler, G., and L.A. Fisk (2007), Acceleration of pickup ions at quasi-stationary shocks, in *Turbulence and Nonlinear Processes in Astrophysical Plasmas*, AIP Conf. Proc. 932, edited by D. Shaikh and G. P. Zank, pp. 264-270, AIP, Melville, NY.
- Gloeckler, G., and J. Geiss (1998), Interstellar and inner source pickup ions observed with SWICS on Ulysses, *Space Science Rev.*, **86**, 127.
- Gloeckler, G., and J. Geiss (2001), Heliospheric and interstellar phenomena deduced from pickup ion observations, *Space Science Rev.*, **97**, 169.
- Gloeckler, G., et al. (1999), *Solar Probe: First Mission to the Nearest Star. Report of the Science Definition Team for the Solar Probe Mission*, The Johns Hopkins University Applied Physics Laboratory, Laurel, MD.
- Gloeckler, G., et al. (2000), Sources, injection, and acceleration of heliospheric ion populations, in: *Acceleration and Transport of Energetic Particles Observed in the Heliosphere: Proceedings of the ACE-2000 Symposium*, AIP Conf. Proc. 528, edited by R. A. Mewaldt et al., pp. 221-228, AIP, Melville NY.
- Gloeckler, G., T.H. Zurbuchen, and J. Geiss (2003), Implications of the observed anticorrelation between solar wind speed and coronal electron temperature, *J. Geophys. Res.*, **108** (A4), SSH 8-1, doi: 10.1029/2002JA009286.
- Goldstein, B.E., et al. (2000), Observed constraint on proton-proton relative velocities in the solar wind, *Geophys. Res. Lett.*, **27**, 53.
- Gopalswamy, N. (2001), et al., Near-Sun and near-Earth manifestations of solar eruptions, *J. Geophys. Res.*, **106**, 25261.
- Gopalswamy, N., et al. (2002), Interacting coronal mass ejections and solar energetic particles, *Ap.J.*, **572**, L103-L107.
- Gopalswamy, N., et al. (2004), Intensity variation of large solar energetic particle events associated with coronal mass ejections, *J. Geophys. Res.*, **109**, A12105.
- Grall, R.R. (1996), et al., Rapid acceleration of the polar solar wind, *Nature*, **379**, 429.
- Grün, E., et al. (1985), Collisional balance of the meteoritic complex, *Icarus*, **62**, 244.

- Grün, E., et al. (1992), Ulysses dust measurements near Jupiter, *Science*, **257**, 1550-1552.
- Gurnett, D.A., et al. (1983), Micron-sized particles detected near Saturn by the Voyager plasma wave instrument, *Icarus*, **53**, 236.
- Gurnett, D.A., et al. (1997), Micron-sized particles detected in the outer solar system by the Voyager 1 and 2 plasma wave instruments, *Geophys. Res. Lett.*, **24**, 3125,.
- Habbal, S.R., et al. (1997), Origins of the slow and the ubiquitous fast solar wind, *Astrophys. J.*, **489**, L103.
- Habbal, S.R., et al. (2003), On the detection of the signature of silicon nanoparticle dust grains in coronal holes, *Astrophys. J.*, **592**, L87-L90, doi: 10.1086/377678.
- Haggerty, D.K., and E.C. Roelof (2002), Impulsive near-relativistic solar electron events: delayed injection with respect to solar electromagnetic emission, *Astrophys. J.*, **579**, 841.
- Hansteen, V.H., E. Leer, and T.E. Holzer (1997), The role of helium in the outer solar atmosphere, *Astrophys. J.*, **482**, 498.
- Hassler, D.M., et al. (1999), Solar wind outflow and the chromospheric magnetic network, *Science*, **283**, 810.
- Heyvaerts, J., and E.R. Priest (1983), Coronal heating by phase-mixed shear Alfvén waves, *Astronomy and Astrophysics*, **117**, 220.
- Hollweg, J.V. (1974), Hydromagnetic waves in interplanetary space, *Astronomical Society of the Pacific*, **86**, 56.
- Hollweg, J.V. (1978), Alfvén waves in the solar atmosphere, *Solar Physics*, **56**, 305-333.
- Hollweg, J.V., and P.A. Isenberg (2002), Generation of the fast wind: A review with emphasis on the resonant cyclotron interaction, *J. Geophys. Res.*, **107** (A7), SSH 12-1, doi: 10.1029/2001JA000270.
- Igenbergs, E. et al. (1998), Mars Dust Counter, *Earth, Planets and Space*, **50**, 241-245.
- Ionson, J.A. (1978), Resonant absorption of Alfvénic surface waves and the heating of solar coronal loops, *Astrophys. J.*, **226**, 650.
- Isenberg, P.A. (2004), The kinetic shell model of coronal heating and acceleration by ion cyclotron waves: 3. The proton halo and dispersive waves, *J. Geophys. Res.*, **109**, doi:10.1029/2002JA009449.
- Ishiguro, M., et al. (2007), Dark red debris from three short-period comets: 2P/Encke, 22P/Kopff, and 65P/Gunn, *Icarus*, **189**, 169-183.
- Ishimoto, H. (2000), Modeling the number density distribution of interplanetary dust on the ecliptic plane within 5 AU of the Sun, *Astron. Astrophys.*, **362**, 1158.
- Jones, G.H., et al. (2003), Strong interplanetary field enhancements at Ulysses—evidence of dust trails' interaction with the solar wind?, *Icarus*, **166**, 297.

- Kahler, S.W. (1994), Injection profiles of solar energetic particles as functions of coronal mass ejection heights, *Astrophys. J.*, **428**, 837-842.
- Kahler, S.W., (2001) The correlation between solar energetic particle peak intensities and the speeds of coronal mass ejections: effects of ambient particle densities and energy spectra, *J. Geophys. Res.*, **106**, 20,947.
- Kahler, S.W. and D.V. Reames (2003), Solar energetic particle production by coronal mass ejection-driven shocks in solar fast-wind regions, *Astrophys. J.*, **584**, 1063.
- Kissel, J., and F.R. Krueger (1987), The organic component in dust from Comet Halley as measured by the PUMA mass spectrometer on board VEGA 1, *Nature*, **326**, 755.
- Kohl, J.L., et al. (1998), UVCS/SOHO empirical determinations of the anisotropic velocity distributions in the solar corona, *Astrophys. J.*, **501**, L127.
- Krimigis, S. M., et al. (2004), Energetic particle observations near the termination shock, in: *Physics of the Outer Heliosphere: Third International IGPP Conference*, AIP Conf. Proc. 719, edited by V. Florinski, N. V. Pogorelov, and G. P. Zank, pp. 133-138, AIP, Melville, NY.
- Krucker, S., and R.P. Lin (2000), Two classes of solar proton events derived from onset time analysis, *Astrophys. J.*, **542**, L61-L64.
- Krucker, S., et al. (2002), Hard x-ray microflares down to 3 keV, *Solar Physics*, **210**, 445.
- Lario, D., et al. (2005), Radial and longitudinal dependence of solar 4-13 MeV and 27-37 MeV proton peak intensities and fluences: Helios and IMP 8 observations, *Astrophys. J.*, **653**, 1531-1544, doi: 10.1086/508982.
- Leamon, R.J., et al. (1998), Contribution of cyclotron-resonant damping to kinetic dissipation of interplanetary Turbulence, *Astrophys. J.*, **507**, L181.
- Leinert, C., and B. Moster (2007), Evidence for dust accumulation just outside the orbit of Venus, *Astron. Astrophys.*, **472**, 335-340.
- Li, G., and G.P. Zank (2005), Mixed particle acceleration at CME-driven shocks and flares, *Geophys. Res. Lett.*, **32**, L02101.
- Li, X., et al. (1998), The effect of temperature anisotropy on observations of Doppler dimming and pumping in the inner corona, *Astrophys. J.*, **501**, L133.
- Longcope, D.W., D.S. Brown, and E.R. Priest (2003), On the distribution of magnetic null points above the solar photosphere, *Physics of Plasmas*, **10**, 3321.
- Mann, I., and A. Czechowski (2005), Dust destruction and ion formation in the inner solar system, *Astrophys. J.*, **621**, L73-L76, doi: 10.1086/429129.
- Mann, I., and E. Murad (2005), On the existence of silicon nanodust near the Sun, *Astrophys. J.*, **624**, L125-L128, doi: 10.1086/430701.

- Mann, I., et al. (2000), Dust cloud near the Sun, *Icarus*, **146**, 568.
- Mann, I., et al. (2004), Dust near the Sun, *Space Sci. Rev.*, **110**, 269, 2004.
- Mann, I., et al. (2005), Physical properties of the dust in the solar system and its interrelation with small bodies, in: *Asteroids, Comets, Meteors: Proceedings IAU Symposium No. 299*, edited by D. Lazzaro, S. Ferraz-Mello, and J.A. Fernández, pp.41-65.
- Mann, I., et al. (2007), Nanoparticles in the inner solar system, *Planet. Space Sci.*, **55**, 1000-1009.
- Marsch, E., and A. K. Richter (1984), Distribution of solar wind angular momentum between particles and magnetic field: Inferences about the Alfvén critical point from Helios observations, *J. Geophys. Res.*, **89**, 5386–5394.
- Marsch, E., and C.-Y. Tu (2001), Heating and acceleration of coronal ions interacting with plasma waves through cyclotron and Landau resonance, *J. Geophys. Res.*, **106**, 227.
- Marsch, E., et al. (1982), Solar wind protons: three-dimensional velocity distributions and derived plasma parameters measured between 0.3 and 1 AU, *J. Geophys. Res.*, **87**, 52.
- Mason, G.M., et al. (1989), Impulsive acceleration and scatter-free transport of ~1 MeV per nucleon ions in ³He-rich solar particle events, *Astrophys. J.*, **339**, 529-544.
- Mason, G.M., et al. (1999), ³He enhancements in large solar energetic particle events, *Astrophys. J.*, **525**, L133.
- Mason, G. M. et al. (2004), Abundances of heavy and ultraheavy ions in ³He-rich solar flares, *Astrophys. J.*, **606**, 555.
- Mason, G.M., et al. (2006), The role of interplanetary scattering in western hemisphere large solar energetic particle events, *Astrophys. J.*, **647**, L65-L68.
- Matthaeus, W.H., and M.L. Goldstein (1986), Low-frequency 1/f noise in the interplanetary magnetic field, *Phys. Rev. Lett.*, **57**, 495.
- Matthaeus, W.H., and S.L. Lamkin (1986), Turbulent magnetic reconnection, *Phys. Fluids*, **29**, 2513.
- Matthaeus, W.H., et al. (1999), Coronal heating by magnetohydrodynamic turbulence driven by reflected low-frequency waves, *Astrophys. J.*, **523**, L93.
- Matthaeus, W.H., et al. (2007), Density and magnetic field signatures of interplanetary 1/f noise, *Astrophys. J.*, **657**, L121-124.
- McComas, D.J., et al. (1998), Ulysses' return to the the slow solar wind, *Geophys. Res. Lett.*, **25**, 1-4, doi: 10.1029/97GL03444.
- McComas, D.J., et al. (2003), The three-dimensional solar wind around solar maximum, *Geophys. Res. Lett.*, **30** (10), 24-1, doi: 10.1029/2003GL017136.
- McComas, D.J., et al. (2005), *Solar Probe: Report of the Science and Technology Definition Team*, NASA/TM-2005-212786.

- McIntosh, S.W., et al. (2006), Simple magnetic flux balance as an indicator of ne VIII doppler velocity partitioning in an equatorial coronal hole, *Astrophys. J.*, **644**, L87-L91, doi: 10.1086/505488.
- McKenzie, D.E., and D.J. Mullan (1997), Periodic modulation of x-ray intensity from coronal loops: heating by resonant absorption, *Solar Physics*, 127.
- McKibben, R.B., C. Lopate, and M. Zhang (2001), Simultaneous observations of solar energetic particle events by IMP 8 and the Ulysses Cospin High Energy Telescope at high solar latitudes, *Space Science Rev.*, **97**, 257.
- Mewaldt, R.A., et al. (2003), Heavy ion and electron releases time in solar particle events, in: *Proceedings of the 28th Internat. Cosmic Ray Conference*, edited by T. Kajita et al., 3313.
- Mewaldt, R.A., et al. (2006), The source material for large solar energetic particle events, in: *Solar Eruptions and Energetic Particles*, Geophysical Monograph 165, edited by N. Gopalswamy, R.A. Mewaldt, and J. Torsti, 115-126, American Geophysical Union, Washington D.C.
- Meyer-Vernet, N., M.G. Aubie, and B.M. Pedersen (1986), Voyager 2 at Uranus: Grain impacts in the ring plane, *Geophys. Res. Lett.*, **13**, 617.
- Miller, J. A. (1998), Particle acceleration in impulsive solar flares, *Space Sci. Reviews*, **86**, 79.
- Miralles, M.P., S.R. Cranmer, and J.L. Kohl (2004), Low-latitude coronal holes during solar maximum, *Adv. Space Res.*, **33**, 696.
- Misconi, N.Y. (1993), The spin of cosmic dust: Rotational bursting of circumsolar dust in the F corona, *J. Geophys. Res.*, **98**, 18951.
- Murphy, N., E.J. Smith, and N.A. Schwadron (2002), Strongly underwound magnetic fields in co-rotating interaction regions: Observations and implications, *Geophys. Res. Lett.*, **29** (22), 23-1, doi: 10.1029/2002GL015164.
- Murphy, R.J., et al. (2007), Using gamma-ray and neutron emission to determine solar flare accelerated particle spectra and composition and the conditions within the flare magnetic loop, *Astrophys. J. Supp.*, **168**, 167-194, doi: 10.1086/509637.
- NASA (2005), *Sun-Solar System Connection: Science and Technology Roadmap 2005-2035*.
- NRC (1996), *Radiation Hazards to Crews of Interplanetary Missions: Biological Issues and Research Strategies*, p. 2, National Academy of Sciences, Washington D.C.
- NRC (2003), *The Sun to the Earth—and Beyond: A Decadal Research Strategy in Solar and Space Physics*, National Academy of Sciences, Washington D.C.
- Neubauer, F.M., et al. (1990), Hypervelocity dust particle impacts observe by the Giott magnetometer and plasma experiments, *Geophys. Res. Lett.*, **17**, 1809.
- Neugebauer, M. (1991), The quasi-stationary and transient states of the solar wind, *Science*, **252**, 404.

- Neugebauer, M., et al. (1995), Ulysses observations of microstreams in the solar wind from coronal holes, *J. Geophys. Res.*, **100**, 23389.
- Neugebauer, M., et al. (2002), Sources of the solar wind at solar activity maximum, *J. Geophys. Res.*, **107** (A12), SSH-13, doi: 10.1029/2001JA000306.
- Noci, G., et al. (1997), First results from UVCS/SOHO, *Adv. Space Res.*, **20**, 2219.
- Oberc, P., and W. Parzydło (1992), Impacts of dust particles M greater than 10^{-9} g in Halley's coma as seen in the electric field waveforms of VEGA 2, *Icarus*, **98**, 195.
- Ofman, L. (2000), Source regions of the slow solar wind in coronal structures, *Geophys. Res. Lett.*, **27**, 2885.
- Ofman, L., and T. Wang (2007), Hinode observations of propagating Alfvén waves in coronal loops, *Astrophys. J.*, submitted.
- Ofman, L., V.M. Nakariakov, and C.E. DeForest (1999), Slow magnetosonic waves in coronal plumes, *Astrophys. J.*, **514**, 441.
- Ofman, L., et al. (1997), Ultraviolet Coronagraph Spectrometer observations of density fluctuations in the solar wind, *Astrophys. J.*, **491**, L111.
- Ofman, L., et al. (2000), UVCS WLC observations of compressional waves in the south polar coronal hole, *Astrophys. J.*, **529**, 592.
- Okamoto, T.J., et al. (2007), Coronal transverse magnetohydrodynamic waves in a solar prominence, *Science*, **318**, 1577, doi: 10.1126/science.1145447.
- Parker, E.N. (1958), Dynamics of the interplanetary gas and magnetic fields, *Astrophys. J.*, **128**, 644.
- Parker, E.N. (1988), Nanoflares and the solar x-ray corona, *Astrophys. J.*, **330**, 474.
- Parsons, J.L., and L.W. Townsend (2000), Interplanetary crew dose rates for the August 1972 solar particle event, *Radiation Res.*, **153**, 729.
- Pizzo, V., et al. (1983), Determination of the solar wind angular momentum flux from the Helios data: an observational test of the Weber and Davis theory, *Astrophys. J.*, **271**, 335–354.
- Ragot, B.R., and S.W. Kahler (2003), Interactions of dust grains with coronal mass ejections and solar cycle variations of the F-corona brightness, *Astrophys. J.*, **594**, 1049.
- Raymond, J.C., et al. (1998), Solar wind at 6.8 solar radii from UVCS observation of comet C/1996Y1, *Astrophys. J.*, **508**, 410.
- Reames, D.V. (1999), Particle acceleration in the Sun and the heliosphere, *Space Sci. Rev.*, **90**, 413.
- Reames, D. V., and C. K. Ng (1998), Streaming-limited intensities of solar energetic particles, *Ap.J.*, **504**, 1002.
- Reames, D.V., and C. K. Ng (2004), Heavy element abundances in solar energetic particle events, *Astrophys. J.*, **610**, 510.

- Roberts, D.A., K.W. Ogilvie, and M.L. Goldstein (1996), The nature of the solar wind, *Nature*, **381**, 31-32, doi: 10.1038/381031a0.
- Sasaki, S. et al. (2002), Observation of interplanetary and interstellar dust particles by Mars Dust Counter (MDC) on board NOZOMI, *Adv. Space Res.*, **29**, 1145-1153.
- Schrijver, C.J, et al. (1997), Sustaining the quiet photospheric network: The balance of flux emergence, fragmentation, merging, and cancellation, *Astrophys. J.*, **487**, 424.
- Schwadron, N.A., and D.J. McComas (2003), Solar wind scaling law, *Astrophys. J.*, **599**, 1395.
- Schwadron, N.A. (2002), An explanation for strongly underwound magnetic field in co-rotating rarefaction regions and its relationship to footpoint motion on the the sun, *Geophys. Res. Lett.*, **29** (14), DOI 10.1029/2002GL015028, 8-1.
- Scudder, J.D. (1994), Ion and electron suprathermal tail strengths in the transition region: Support for the velocity filtration model of the corona, *Astrophys. J.*, **427**, 446.
- Sheeley, N. R., Jr., et al. (1997), Measurements of Flow Speeds in the Corona between 2 and 30 R_s, *Astrophys. J.*, **484**, 472.
- Simunac, K.D.C., and T.P. Armstrong. (2004), Solar cycle variations in solar and interplanetary ions observed with Interplanetary Monitoring Platform 8, *J. Geophys. Res.*, **109**, A10101, doi:10.1029/2003JA010194.
- Singh, J., et al. (2004), Existence of nanoparticle dust grains in the inner solar corona?, *Astrophys. J.*, **608**, L69-L72, doi: 10.1086/422138.
- Smith, E.J. (2001), The heliospheric current sheet, *J. Geophys. Res.*, **106**, 15819.
- Smith, E. J. et al. (2003), The Sun and heliosphere at solar maximum, *Science*, **302**, 1165.
- Sokolov, I.V., et al. (2004), A new field line advection model for solar particle acceleration, *Astrophys. J.*, **616**, L171.
- Sterling, A.C. (2000), Solar spicules: A review of recent models and targets for future observations, *Solar Physics*, **196**, 79.
- Teriaca, L., et al. (2003), The nascent solar wind: origin and acceleration, *Astrophys. J.*, **688**, 566.
- Thomson, D.J., C.G., MacLennan, and L.J. Lanzerotti (1995), Propagation of solar oscillations through the interplanetary medium, *Nature*, **376**, 139.
- Thomson, D.J., C.G., MacLennan, and L.J. Lanzerotti (1996), The nature of the solar wind, *Nature*, **381**, 32, doi: 10.1038/381032a0.
- Tomczyk, S., et al. (2007), Alfvén waves in the solar corona, *Science*, **317**, 1192, doi: 10.1126/science.1143304.
- Tsurutani, B.T., et al. (2003), Dust impacts at Comet P/Borrelly, *Geophys. Res. Lett.*, **30**, SSC 1-1, 2134, doi: 10.1029/2003GL017580.

- Tu, C.-Y., E. Marsch, and Z.-R. Qin (2004), Dependence of the proton beam drift velocity on the proton core plasma beta in the solar wind, *J. Geophys. Res.*, **109**, A05101 doi: 10.1029/2004JA010391.
- Tu, C.-Y., Pu, Z. and Wei, F. (1984), The power spectrum of interplanetary Alfvénic fluctuations: derivation of the governing equation and its solution, *J. Geophys. Res.*, **89**, 9695.
- Tu, C.-Y. et al. (2005), Solar wind origin in coronal funnels, *Science*, **308**, 519-523.
- Tylka, A. J., et al. (2005), Shock geometry, seed populations, and the origin of variable elemental composition at high energies in large gradual solar particle events, *Astrophys. J.*, **625**, 474-495.
- Velli, M. (1993), On the propagation of ideal, linear Alfvén waves in radially stratified stellar atmospheres and winds, *Astronomy and Astrophysics*, **270**, 304.
- Verdini, A., and Velli, M. (2007) Alfvén waves and turbulence in the solar atmosphere and solar wind, *Astrophys J.*, **662**, 669.
- Wang, Y.-M., and N.R. Sheeley, Jr. (2003), On the topological evolution of the coronal magnetic field during the solar cycle, *Astrophys. J.*, **599**, 1404-1417, doi: 10.1086/379348..
- Wang, Y.-M., et al. (1997), Solar wind stream interactions and the wind speed-expansion factor relationship, *Astrophys. J.*, **488**, L51.
- Wilhelm, K., et al. (1998), The solar corona above polar coronal holes as seen by SUMER on SOHO, *Astrophys. J.*, **500**, 1023.
- Wimmer-Schweingruber, R.F., and P. Bochseler (2003), On the origin of inner-source pickup ions, *Geophys. Res. Lett.*, **30**(2), 49-1, doi: 10.1029/2002GL015218.
- Withbroe, G.L., and R.W. Noyes (1977), Mass and energy flow in the solar chromosphere and corona, *Ann. Rev. Astron. Astrophys.*, **15**, 363.
- Witt, A.N., K.D. Gordon, and D.G. Furton (1998), Silicon nanoparticles: Source of extended red emission?, *Astrophys. J.*, **501**, L111, doi: 10.1086/311453.
- Yamauchi, Y, et al. (2004), The magnetic structure of Ha macrospicules in solar coronal holes, *Astrophys. J.*, **605**, 511.
- Zank, G.P., et al. (2000), Particle acceleration and coronal mass ejection driven shocks: a theoretical model, *J. Geophys. Res.*, **105**, 25079.
- Zhao, L., and T.H. Zurbuchen (2008), On the global distribution of the slow solar wind, *Astrophys. J.*, submitted.
- Zubko, V.G., T.L. Smith, and A.N. Witt (1999), Silicon nanoparticles and interstellar extinction, *Astrophys. J.*, **511**, L57-L60, doi: 10.1086/311831.
- Zurbuchen, T.H, et al. (2002), The solar wind composition throughout the solar cycle: A continuum of dynamic states, *Geophys. Res. Lett.*, **29** (9), 66-1, doi: 10.1029/2001GL013946.

Appendix A:

Solar Probe+ Mass and Power Budgets

Table A-1. Solar Probe+ mass budget.

Name	Qty	CBE Each (kg)	CBE Total (kg)	Contingency (%)	Total (kg)
Instruments					
Instruments Total:			47.2		51.9
Hemispheric Imager	1	1.5	1.5	10%	1.7
TBD Science Payload	1	5.0	5.0	10%	5.5
Fast Ion Analyzer	1	2.8	2.8	10%	3.1
Fast Electron Analyzer	2	2.5	5.0	10%	5.5
Ion Composition Analyzer	1	7.0	7.0	10%	7.7
Plasma Wave Electronics	1	2.0	2.0	10%	2.2
Plasma Wave Pre-amp	3	0.4	1.2	10%	1.3
Search Coils	3	0.6	1.8	10%	2.0
Magnetometer	1	2.5	2.5	10%	2.8
Energetic Particle Inst. High Energy	1	2.7	2.7	10%	3.0
Energetic Particle Inst. Low Energy	1	1.4	1.4	10%	1.5
Neutron-Gamma Spectrometer	1	2.0	2.0	10%	2.2
Coronal Dust Detector	1	1.5	1.5	10%	1.7
Common DPU	1	10.8	10.8	10%	11.9
Accommodation Hardware					
Accommodation Hardware Total:			7.4		8.4
Fast Plasma Actuator Bracket	1	2.2	2.2	15%	2.5
Plasma Wave Antenna, Actuator	3	1.2	3.6	15%	4.1
Magnetometer Boom	1	1.6	1.6	5%	1.7
Spacecraft					
Spacecraft Total:			373.7		420.1
Telecommunications					
Telecommunications Total:			31.8		34.8
High Gain Antenna	1	3.8	3.8	10%	4.2
HGA Actuator	2	2.0	4.0	5%	4.2
High Gain Arm, mounting bracket, rotary joints, etc.	1	2.9	2.9	15%	3.3
HGA Actuator Electronics	1	1.0	1.0	5%	1.1
K-Band TWT/EP	2	3.0	6.0	5%	6.3
X-Band TWT/EP	2	2.5	4.9	5%	5.1
Low Gain Antenna Assembly	2	0.7	1.4	15%	1.6
RF Plate	1	1.0	1.0	15%	1.2
Hybrids/Components	1	1.0	1.0	15%	1.2
Transponder	2	1.6	3.2	15%	3.7
Coax/Waveguide	1	2.6	2.6	15%	3.0
Guidance and Control					
Guidance and Control Total:			30.4		32.0
Inertial Measurement Unit	1	6.6	6.6	5%	6.9

Table A.1 Solar Probe+ mass budget (cont'd)

Name	Qty	CBE Each (kg)	CBE Total (kg)	Contingency (%)	Total (kg)
Reaction Wheel Assembly	4	4.2	16.8	5%	17.6
Star Tracker	3	2.0	6.0	5%	6.3
Solar Horizon Sensor	1	1.0	1.0	10%	1.1
Power					
Power Total:			117.2		132.2
Solar Array System (Primary)			25.1		27.2
SA Substrate	2	2.0	4.0	10%	4.4
SA Cells, wiring, etc	2	5.2	10.4	10%	11.4
Hinge/Damper	2	1.0	2.0	10%	2.2
Solar Array Drive	2	2.8	5.6	5%	5.9
Solar Array Drive Electronics	1	2.0	2.0	5%	2.1
Fasteners, pins, etc	2	0.6	1.1	10%	1.2
Solar Array System, Secondary			66.8		76.7
Radiator Panel, Al HC	6	1.5	9.0	15%	10.4
Radiator Panel, Heat Pipes	1	3.5	3.5	15%	4.0
Straps, Clamps, Inserts, Thermal Adhesive, etc.	1	3.0	3.0	15%	3.5
Cooling Tubes, fittings, flex lines, Fasteners, Fill/Drain Valves, etc.	1	8.6	8.6	15%	9.9
Pump	2	12.0	24.0	15%	27.6
Fluid	1	0.2	0.2	15%	0.2
Substrate Cooling/Mounting Deck	2	2.3	4.6	15%	5.3
Motor, Schaeffer-MOOG, Type 1	2	0.5	1.0	5%	1.0
Brackets, drive components, pins, fasteners, etc.	2	1.6	3.2	15%	3.7
Motor Drive Electronics	1	2.2	2.2	15%	2.5
Slider/Positioning System	2	0.91	1.8	15%	2.1
Substrate	2	1.0	2.0	15%	2.3
Cells/etc.	2	0.5	1.0	15%	1.2
Harness	2	0.8	1.5	15%	1.7
Center Deck Stiffener	1	1.2	1.2	15%	1.4
Power System Electronics			25.3		28.3
Power System Electronics	1	7.3	7.3	15%	8.4
Battery	1	8.0	8.0	5%	8.4
Power Distribution Unit	1	10.0	10.0	15%	11.5
Thermal Protection System					
Thermal Protection System Total:			68.5		78.8
Shield	1	52.0	52.0	15%	59.8
Support Structure	1	10.0	10.0	15%	11.5
Dust Protection	1	6.5	6.5	15%	7.5
Thermal Control					

Table A.1 Solar Probe+ mass budget (cont'd)

Name	Qty	CBE Each (kg)	CBE Total (kg)	Contingency (%)	Total (kg)
Thermal Control Total:			15.7		18.1
Multi-Layer Insulation	1	10.0	10.0	15%	11.5
Radiators	1	0.3	0.3	15%	0.3
Heater/Thermistor Harness	1	2.5	2.5	15%	2.9
Diode Heat Pipe	1	0.9	0.9	15%	1.0
Doublers, Gaskets, etc	1	2.0	2.0	15%	2.3
Avionics					
Avionics Total:			12.7		14.0
Integrated Electronics Module	2	6.0	12.0	10%	13.2
TRIO Units	14	0.1	0.7	10%	0.8
Propulsion					
Propulsion Total:			20.5		21.9
Hydrazine Tank	1	6.4	6.4	5%	6.7
5-lbf Thruster	2	0.7	1.5	5%	1.5
0.2-lbf Thruster	12	0.3	3.6	5%	3.8
Latch Valve	2	0.3	0.6	5%	0.6
Filter	1	0.0	0.0	5%	0.0
Fill/Service Valve	2	0.2	0.3	5%	0.3
Pressure Transducers	2	0.2	0.4	5%	0.4
Tubing/Fasteners/Clamps	1	3.0	3.0	10%	3.3
Electrical Connectors	1	0.3	0.3	10%	0.3
Cabling	1	3.0	3.0	10%	3.3
Orifice	1	0.0	0.0	10%	0.0
Propulsion Diode Box	1	1.5	1.5	10%	1.7
Mechanical					
Mechanical Total:			58.9		67.7
Primary Structure =			53.4		61.5
Top Deck	1	6.5	6.5	15%	7.5
Aft Deck	1	14.7	14.7	15%	16.9
Side Panels	6	3.6	21.6	15%	24.8
Fasteners	1	1.8	1.8	15%	2.1
Payload Adaptor, Umbilical Brackets, etc.)	1	8.1	8.1	15%	9.3
Tank Mounting Structure	1	0.8	0.8	15%	0.9
Secondary Structure =			5.5		6.3
Reaction Wheel Brackets	4	0.3	1.2	15%	1.4
Low Gain Antenna Bracket	2	0.2	0.4	15%	0.5
Medium Gain Antenna Bracket	1	0.3	0.3	15%	0.3
Star Tracker Bracket	3	0.5	1.5	15%	1.7
Solar Array Tie Down Brackets (All)	8	0.2	1.6	15%	1.8

Table A.1 Solar Probe+ mass budget (cont'd)

Name	Qty	CBE Each (kg)	CBE Total (kg)	Contingency (%)	Total (kg)
Balance Mass	0	8.0	0.0	15%	0.0
Purge Components	1	0.5	0.5	15%	0.5
Harness					
Harness Total:			18.0		20.6
Main Harness	1	16.5	16.5	15%	19.0
Plugs	1	1.0	1.0	10%	1.1
Grounding Straps	1	0.5	0.5	10%	0.6
Observatory					
Observatory Dry Mass			428.3		480.3
Propellant					
Propellant Total:					52.7
Useable					52.3
Residual					0.3
Pressurant					0.1
Observatory Wet Mass					533.0
Launch Mass					610.0
Unallocated Margin					77.0
Total Mass Reserves					30.1%

Table A-2. Solar Probe+ power budget.

				Post-Separation		Maneuver		Cruise		Checkout/Calibration		Approach		Science		Science Momentum Dump	
Name	Qty	CBE Each (W)	CBE Total (W)	Duty Cycle (%)	Total (W)	Duty Cycle (%)	Total (W)	Duty Cycle (%)	Total (W)	Duty Cycle (%)	Total (W)	Duty Cycle (%)	Total (W)	Duty Cycle (%)	Total (W)	Duty Cycle (%)	Total (W)
Instruments																	
Instruments Total:					0.0		0.0		0.0		28.6		0.0		57.2		57.2
Hemispheric Imager	1	4.0	4.0	0%	0.0	0%	0.0	0%	0.0	50%	2.0	0%	0.0	100%	4.0	100%	4.0
Polar Source Region Imager	1	4.0	4.0	0%	0.0	0%	0.0	0%	0.0	50%	2.0	0%	0.0	100%	4.0	100%	4.0
Fast Ion Analyzer	1	3.7	3.7	0%	0.0	0%	0.0	0%	0.0	50%	1.9	0%	0.0	100%	3.7	100%	3.7
Fast Electron Analyzer	1	7.2	7.2	0%	0.0	0%	0.0	0%	0.0	50%	3.6	0%	0.0	100%	7.2	100%	7.2
Ion Composition Analyzer	1	6.0	6.0	0%	0.0	0%	0.0	0%	0.0	50%	3.0	0%	0.0	100%	6.0	100%	6.0
Plasma Wave Electronics	1	5.0	5.0	0%	0.0	0%	0.0	0%	0.0	50%	2.5	0%	0.0	100%	5.0	100%	5.0
Magnetometer	1	2.5	2.5	0%	0.0	0%	0.0	0%	0.0	50%	1.3	0%	0.0	100%	2.5	100%	2.5
Energetic Particle Inst. High Energy	1	2.3	2.3	0%	0.0	0%	0.0	0%	0.0	50%	1.2	0%	0.0	100%	2.3	100%	2.3
Energetic Particle Inst. Low Energy	1	1.7	1.7	0%	0.0	0%	0.0	0%	0.0	50%	0.9	0%	0.0	100%	1.7	100%	1.7
Neutron-Gamma Spectrometer	1	3.0	3.0	0%	0.0	0%	0.0	0%	0.0	50%	1.5	0%	0.0	100%	3.0	100%	3.0
Coronal Dust Detector	1	3.8	3.8	0%	0.0	0%	0.0	0%	0.0	50%	1.9	0%	0.0	100%	3.8	100%	3.8
Common DPU	1	14.0	14.0	0%	0.0	0%	0.0	0%	0.0	50%	7.0	0%	0.0	100%	14.0	100%	14.0
Accommodation Hardware																	
Accommodation Hardware Total:					0.0		0.0		0.0		0.3		0.0		0.3		0.3
Fast Plasma Actuator/Arm	1	0.0	0.0	0%	0.0	0%	0.0	0%	0.0	5%	0.0	0%	0.0	5%	0.0	5%	0.0
Plasma Wave Antenna, Actuator	1	5.0	5.0	0%	0.0	0%	0.0	0%	0.0	5%	0.3	0%	0.0	5%	0.3	5%	0.3
Spacecraft																	
Spacecraft Total:					201.6		325.8		292.8		244.8		245.1		245.1		253.3
Telecommunications																	
Telecommunications Total:					49.7		97.7		97.7		49.7		49.7		49.7		49.7
Ka-band TWT	2	80.0	160.0	0%	0.0	50%	80.0	50%	80.0	0%	0.0	0%	0.0	0%	0.0	0%	0.0
X-band TWTA	2	33.0	66.0	50%	33.0	0%	0.0	0%	0.0	50%	33.0	50%	33.0	50%	33.0	50%	33.0
Transponder rcv only	1	4.0	4.0	100%	4.0	100%	4.0	100%	4.0	100%	4.0	100%	4.0	100%	4.0	100%	4.0
Transponder (rcv+X only)	1	8.7	8.7	100%	8.7	0%	0.0	0%	0.0	100%	8.7	100%	8.7	100%	8.7	100%	8.7

Table A.2 Solar Probe+ power budget (cont'd)

Name	Qty	CBE Each (W)	CBE Total (W)	Post-Separation		Maneuver		Cruise		Checkout/Calibration		Approach		Science		Science Momentum Dump	
				Duty Cycle (%)	Total (W)	Duty Cycle (%)	Total (W)	Duty Cycle (%)	Total (W)	Duty Cycle (%)	Total (W)	Duty Cycle (%)	Total (W)	Duty Cycle (%)	Total (W)	Duty Cycle (%)	Total (W)
Transponder (rcv+Ka only)	1	9.7	9.7	0%	0.0	100%	9.7	100%	9.7	0%	0.0	0%	0.0	0%	0.0	0%	0.0
Transponder (rcv+X+Ka)	1	14.1	14.1	0%	0.0	0%	0.0	0%	0.0	0%	0.0	0%	0.0	0%	0.0	0%	0.0
USO	2	2.0	4.0	100%	4.0	100%	4.0	100%	4.0	100%	4.0	100%	4.0	100%	4.0	100%	4.0
Guidance and Control																	
Guidance and Control Total:					95.2		95.2		95.2		95.2		95.5		95.5		95.5
Inertial Measurement Unit	1	29.5	29.5	100%	29.5	100%	29.5	100%	29.5	100%	29.5	100%	29.5	100%	29.5	100%	29.5
Reaction Wheel Assembly	4	11.0	44.0	100%	44.0	100%	44.0	100%	44.0	100%	44.0	100%	44.0	100%	44.0	100%	44.0
Star Tracker	1	21.7	21.7	100%	21.7	100%	21.7	100%	21.7	100%	21.7	100%	21.7	100%	21.7	100%	21.7
Solar Horizon Sensor	1	0.3	0.3	0%	0.0	0%	0.0	0%	0.0	0%	0.0	100%	0.3	100%	0.3	100%	0.3
Power																	
Power Total:					18.8		18.8		18.8		18.8		18.8		18.8		18.8
Primary Solar Array Drive	2	18	36.0	1%	0.4	1%	0.4	1%	0.4	1%	0.4	0%	0.0	0%	0.0	0%	0.0
Secondary Solar Array Drive	2	18	36.0	0%	0.0	0%	0.0	0%	0.0	0%	0.0	1%	0.4	1%	0.4	1%	0.4
Power System Electronics	1	10.0	10.0	100%	10.0	100%	10.0	100%	10.0	100%	10.0	100%	10.0	100%	10.0	100%	10.0
Power Distribution Unit	1	8.8	8.8	100%	8.8	100%	8.8	100%	8.8	100%	8.8	100%	8.8	100%	8.8	100%	8.8
Thermal Control																	
Thermal Control Total:					0.0		43.2		43.2		43.2		43.2		43.2		43.2
Secondary Array Pumps	2	21.6	43.2	0%	0.0	100%	43.2	100%	43.2	100%	43.2	100%	43.2	100%	43.2	100%	43.2
Heaters	1	0.0	0.0	0%	0.0	100%	0.0	100%	0.0	100%	0.0	100%	0.0	100%	0.0	100%	0.0
Avionics																	
Avionics Total:					35.0		35.0		35.0		35.0		35.0		35.0		35.0
Primary IEM	1	30.0	30.0	100%	30.0	100%	30.0	100%	30.0	100%	30.0	100%	30.0	100%	30.0	100%	30.0
Secondary IEM	1	5.0	5.0	100%	5.0	100%	5.0	100%	5.0	100%	5.0	100%	5.0	100%	5.0	100%	5.0
Propulsion																	
Propulsion Total:					2.9		35.9		2.9		2.9		2.9		2.9		11.1
Thrusters	1	33.0	33.0	0%	0.0	100%	33.0	0%	0.0	0%	0.0	0%	0.0	0%	0.0	25%	8.3
Cat Bed Heaters	1	11.5	11.5	25%	2.9	25%	2.9	25%	2.9	25%	2.9	25%	2.9	25%	2.9	25%	2.9

Table A.2 Solar Probe+ power budget (cont'd)

Name	Qty	CBE Each (W)	CBE Total (W)	Post-Separation		Maneuver		Cruise		Checkout/Calibration		Approach		Science		Science Momentum Dump	
				Duty Cycle (%)	Total (W)	Duty Cycle (%)	Total (W)	Duty Cycle (%)	Total (W)	Duty Cycle (%)	Total (W)	Duty Cycle (%)	Total (W)	Duty Cycle (%)	Total (W)	Duty Cycle (%)	Total (W)
Pressure Transducers	1	1.8	1.8	100%	1.8	100%	1.8	100%	1.8	100%	1.8	100%	1.8	100%	1.8	100%	1.8
Observatory																	
Observatory Power					201.6		325.8		292.8		273.6		245.1		302.5		310.8
Radiated RF Power																	
TWT radiated power Ka-band	1	40	40.0		0.0		40.0		40.0		0.0		0.0		0.0		0.0
TWT radiated power X-band	1	12	12.0		12.0		0.0		0.0		12.0		12.0		12.0		12.0
Cooling pumps isolated from bus																	
Bus Subsystem Dissipated Power					189.6		242.6		209.6		218.4		189.9		247.3		255.6
Bus Heaters				0%	0.0	100%	27.4	100%	60.4	100%	51.6	100%	80.1	100%	22.7	100%	14.4
Harness Loss					3.0		5.3		5.3		4.9		4.9		4.9		4.9
Bus Power					192.6		275.3		275.3		274.9		274.9		274.9		274.9
Total S/C Consumed Power					204.6		358.5		358.5		330.1		330.1		330.1		330.1
Solar Array							482.0		482.0		482.0		482.0		482.0		482.0
Power Reserves							123.5		123.5		151.9		151.9		151.9		151.9
Margin							34.45%		34.45%		46.03%		46.03%		46.03%		46.03%

Appendix B - Environmental Mitigation

B.1 Dust Protection

The Solar Probe+ spacecraft will include dust and micrometeoroid protection for the expected particle environment. The near-Sun dust environment and its impact on the SP spacecraft were a major focus of the 2005 Solar Probe STDT study (*McComas et al.*, 2005; Appendix B). Compared with Solar Probe 2005, Solar Probe+ will be subjected to a larger particle flux, but at lower relative velocities and thus significantly lower kinetic energies. The dust protection approach described in the earlier study is generally adequate for the new spacecraft design, and Solar Probe+ will employ a similar approach. It includes dust protection for the thermal protection system (TPS), spacecraft bus, and solar arrays. The Solar Probe+ approach is described below, but the planned effort includes a study both on the definition of the mission's dust exposure, and a characterization of the protection approaches for the key areas.

The dust environment in the ecliptic portion of the trajectory was used to establish a statistical dust environmental model (**Figure B.1-1**). Within 1 AU, the dust density is highest near the ecliptic plane and falls off at higher inclinations. Parametric studies of particle impacts were used to define the protection level provided for designs subject to different particle velocities and angles of attack. In this region, there will be thousands of small particle impacts (submicrometer), but there will only be one or two particles large enough to penetrate the TPS C-C shell.

In the Solar Probe+ study three key areas were identified that require particle protection: the TPS, the spacecraft bus, and the solar arrays. Impacts on the thermal protection system will be significantly reduced by the change from a conical to flat shield. The TPS cross-sectional area, in the ram direction, is reduced by a factor of almost 20. If there is a penetration of the TPS shell, the resulting damage could extend well into the insulating foam. To protect against this secondary damage, an extra C-C layer has been added to the TPS to shield the carbon foam. For the spacecraft bus, the Whipple-shield approach, where the multi-layer insulation (MLI) is spaced away from the underlying structure, will still provide the needed protection. The spacing between the MLI and spacecraft will be updated based on the new particle environment. The solar arrays are a new feature of the Solar Probe+ design; detailed dust environments will be generated for them in Phase A. However, there are several mitigating options that indicate adequate protection for them is available. Generally, the solar arrays are aligned parallel to the ram direction reducing their exposure to the dust environment. Flight experience from the MESSENGER mission has shown that the effect of particle impacts on solar arrays between 1.0 and 0.3 AU is minimal; the Solar Probe+ spacecraft will spend 88% of its mission within this range. Inside 0.3 AU, potential protection options for the solar arrays have been identified, such as turning the cell-face inward during

storage, or oversizing the arrays. With a $1/r$ dust particle dependency, the time spent within 0.3 AU is equivalent to a 6-year orbit at 1 AU. Existing solar array design rules, allowing for performance degradation factors, can account for the damage expected during the Solar Probe+ mission.

Methodology. An investigation was performed during the 2005 Solar Probe STDT study (*McComas et al.*, 2005; Appendix B), using an analysis and prediction methodology similar to that used for other NASA missions (both low-Earth orbit and deep space), to assess the risk of dust to the spacecraft and to develop a methodology for dust protection. Using conservative, worst-case assumptions for particle size, velocity, and obliquity, this study was performed by Dr. Cesar Carasco (at the University of Texas at El Paso) using state-of-the-art hydrodynamic codes (e.g., CTH) that resolve the highly dynamic, non-linear impact physics and include constitutive models of the materials of construction. His findings predicted that Whipple shielding consisting of MLI (i.e., 18 layers of Kapton) at a stand-off distance of 10 mm would be sufficient to break-up the largest particles and prevent penetration of the metallic spacecraft bus or instrument housings as illustrated in **Figure B.1-2**. Similarities in both bus and instrument configurations and statistical dust environment models suggest that this approach would also be effective for Solar Probe+. However, during Phase A, shielding studies need to be repeated with new trajectories (and corresponding dust environments) to predict whether the full MLI-based Whipple shielding approach is still required.

During the 2005 STDT study and subsequent Solar Probe Risk Reduction Study¹, the TPS was analyzed to determine the thermal-structural performance after dust impact and to predict the resulting effects on mission performance with respect to mass loss and contamination of sensitive instruments. The TPS evaluated in these studies consisted of a thin-walled, conical, ceramic coated carbon-carbon primary heat shield and a flat disk-shaped secondary heat shield (consisting of a thin-walled carbon-carbon shell packed with carbon foam insulation). The secondary heat shield of the 2005 TPS design is similar to the heat shield proposed in current Solar Probe+ study with the exception that the new design incorporates a ceramic coating (like the 2005 primary heat shield) for temperature control. In follow-on work by Dr. Carasco, the structural response of the conical heat shield to a matrix of dust particle size, impact speed, and impact angle of incidence was calculated with high-performance hydrodynamic codes. These predictions indicated that localized spallation footprints were greater in size than that of the impact particle. For a given particle size and impact speed, the spallation footprint varied with angle of incidence; the largest footprints occurred for normal angle of incidence impacts as shown in **Figure B.1-3**.

Although appearing large in the highly magnified figure, the spallation footprints are several orders of magnitude greater than the diameter of the particle, but still extremely small (tenths of cm^2). Penetration

¹*Solar Probe Thermal Protection System Risk Mitigation Study: FY 2006 Final Report*, prepared by the Johns Hopkins University Applied Physics Laboratory under contract to NASA, Laurel, MD, November 30, 2006.

through the heat shield includes both the ceramic coating and underlying carbon-carbon substrate. Predictions from thermal models of penetrated zones indicate localized temperature increases of several hundred degrees Kelvin, but the effect on predicted equilibrium heat shield temperatures would be negligible. Predictions also indicated that large dust particles would be mostly consumed during the penetration event and that the remaining dust fragments would be vaporized within the large volume of the hot primary heat shield—no solid dust would impact the secondary heat shield. The small, submicron dust particles were predicted to be vaporized on impact and not penetrate the conical heat shield.

The results of the earlier analyses are relevant to Solar Probe+. Dust will impact the flat surface of the coated heat shield directly. However, in contrast to the conical primary shield of Solar Probe 2005, Solar Probe+'s heat shield will not be hollow, but will be filled with foam insulation essential to maintaining control of the equilibrium temperature of the bus. As before, small dust particle impacts are not anticipated to be damaging; however, assessment of large particle impact damage will be more complex. In this case, the heat shield will most likely experience spallation footprints to those modeled for the 2005 design; however, unconsumed dust particles will penetrate into the insulating foam structure. This will most likely not affect overall heat shield equilibrium temperatures, but may induce localized hot spots with potential line of sight to the spacecraft bus. The number of impacts and size of the particles will also increase due to the increased number of orbits and the increased fluence. *However, as noted above, the relative velocities will be lower than in the 2005 case and the kinetic energy in a “typical” impact will be much reduced.*

Further studies will be conducted during Phase A to refine the dust fluence and the statistical size distribution of the particles predicted to impact the heat shield during the multiple ecliptic orbits and to quantify the effects of such impacts on thermal performance. Additional studies will be done to characterize the degree of insulation damage by large particle impacts and the resulting increase in heat conduction through the heat shield. In addition, the effect of spallation on overall spacecraft mass loss rates and the interaction of spallation plumes with the local dust environment will be studied further.

B.2 Spacecraft Charging

Studies of the Solar Probe charging date to the 1980 Starprobe report.² The analysis described here is a continuation of risk reduction studies carried out for the 2005 Solar Probe concept, adapted for the Solar Probe+ mission design. The analysis with NASCAP-2K provides estimates of differential charging,

²Goldstein et al., *Spacecraft Mass Loss and Electric Potential Requirements for the Starprobe Mission*, A Report of the Starprobe Mass Loss Requirements Group Meeting of September 29-30, 1980, NASA Jet Propulsion Laboratory, California Institute of Technology, Pasadena CA, December 1980.

taking the spacecraft geometry into account. We have considered a range of trajectory points, including closest approach and the range from 0.5 AU down to 0.1 AU. Furthermore, our modeling efforts make use of the material properties for the coatings of interest. These properties include elevated-temperature resistivity estimates and room temperature secondary electron emission and backscattered electron emission measurements. It should be noted that the NASCAP results are dependent on the accuracy to which these material properties are known. In particular, since resistivity is the material property that most drives the charging behavior, more precise temperature-dependent resistivity measurements are desirable.

Charging Results. The baseline coatings in the study are alumina (Al_2O_3) and pyrolytic boron nitride (PBN). The charging problem was studied for the following trajectory points: 0.5, 0.4, 0.3, 0.2, 0.1, and 0.0443 AU (closest approach). A solar absorptivity-to-infrared emissivity ratio (α/ϵ) of 0.6 was assumed in the study; previous efforts also included the lower α/ϵ of 0.2. The temperature of the heat shield will be lower for smaller values of α/ϵ , resulting in a higher resistivity and a change in the differential potential, so the results presented here are not a worst-case.

The differential charging results derived from NASCAP-2K are given in **Tables B.2-1** and **Table B.2-2**. Both materials experience differential charging at low levels, below 10 V, for all of the trajectory points considered. The absolute surface charging relative to plasma ground is also below 10 V for all of these points. The NASCAP-2K plot of the spacecraft potentials for Al_2O_3 and PBN for at the 0.1 AU trajectory point for $\alpha/\epsilon = 0.6$ are shown in **Figure B.2-1**. The shaded portion of the spacecraft tends to charge to a few volts negative, while the heat shield coating charges slightly positive and the solar cells charge to a few volts positive.

Impact of Spacecraft Charging. Historical trends indicate that surface charging potentials should be limited to the low hundreds of volts in order to protect the spacecraft electronics. Even for low differential potentials, however, spacecraft surface charging can effect science data collection. The buildup of a significant potential on the spacecraft relative to plasma “ground” may cause measurement contamination by disrupting instrument function and by disturbing the local environment. The level of charging should be kept as small as possible from the perspective of science data collection, however, good solar wind measurements are often made with spacecraft charging levels up to ~10V.

Mitigation Strategies. The charging results shown in **Figure B.2-1** indicate that the solar cells charge more positive than the heat shield. In order to mitigate their charging, it may be necessary to ensure that the solar arrays are conductive on the sunlit side, e.g, by the use of transparent conductive oxides. If it is also necessary to mitigate charging by the ceramic coating of the TPS, one mitigation option is to lower the resistivity of the heat shield coating by adding small quantities of impurities to the ceramic material. Another possible solution to reduce the differential charging of the heat shield is to expose small portions

of the heat shield to be bare carbon-carbon. It should be noted that the effects of both approaches—the effect of dopants on ceramic optical properties and the effect of C-C exposure on outgassing—must be investigated before either approach could be implemented.

Conclusions. A preliminary charging analysis has been performed for the Solar Probe+ spacecraft design and for two different heat shield coating materials. Initial results indicate that the spacecraft charges to a potential of several volts relative to the plasma “ground.” The differential charging situation is that the sunlit side of the solar arrays charge slightly positive, as does the heat shield, while the shaded portion of the spacecraft charges to a few volts negative. At these potential levels, arcing is not a concern, but mitigation strategies may be considered in order to prevent contamination of the data collected by the instruments. Possible mitigation approaches include, for the solar array, the use of conductive solar cells; and for the heat shield, doping ceramic coating or exposing portions of the shield to be bare C-C.

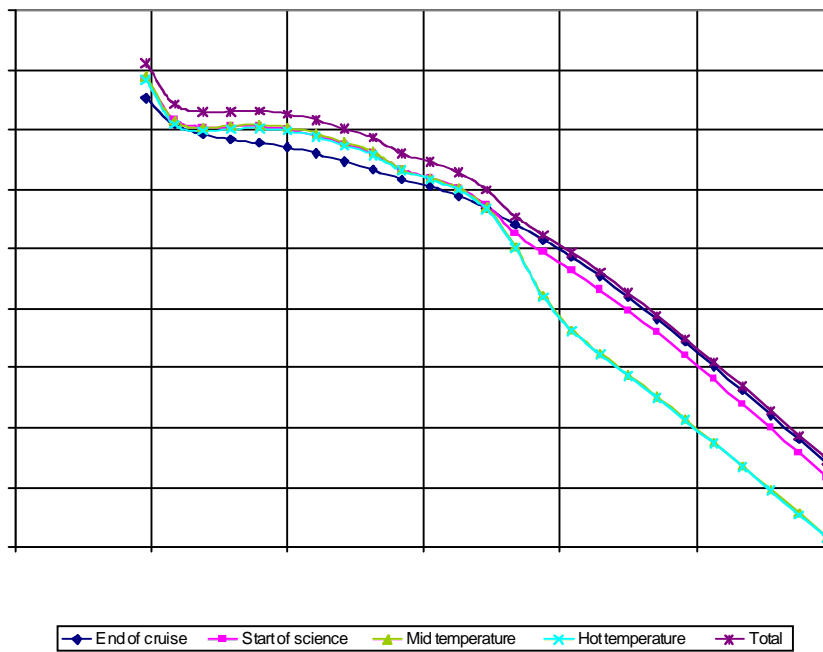


Figure B.1-1. Distribution of Dust Impact with Respect to Particle Size.

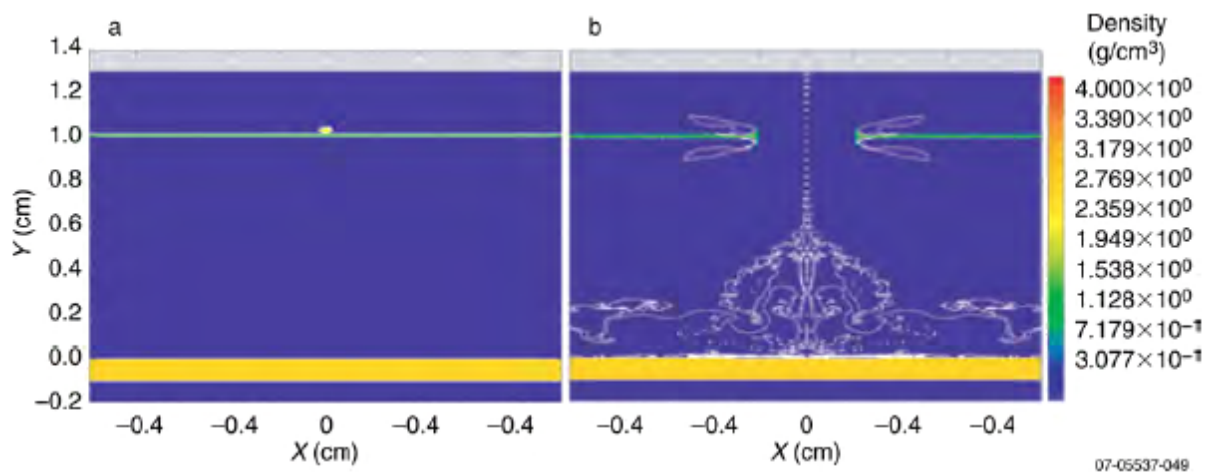


Figure B.1-2. Large Particle, High Speed Dust Impact on Whipple Shield.

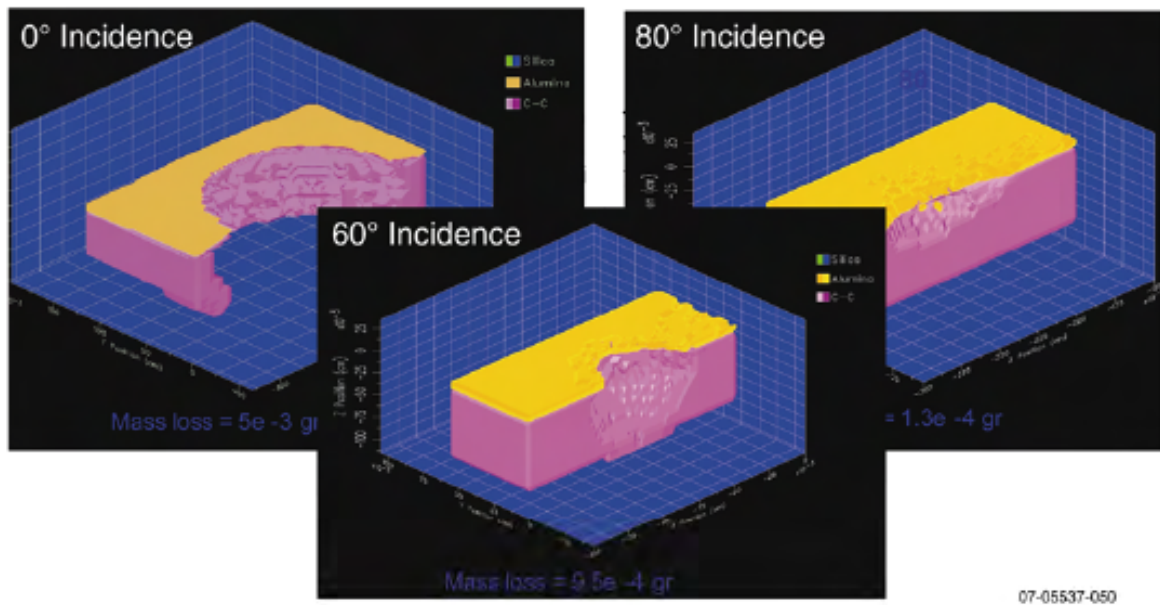


Figure B.1-3. Predicted Spallation Footprints for Particle Impact of Heat Shield.

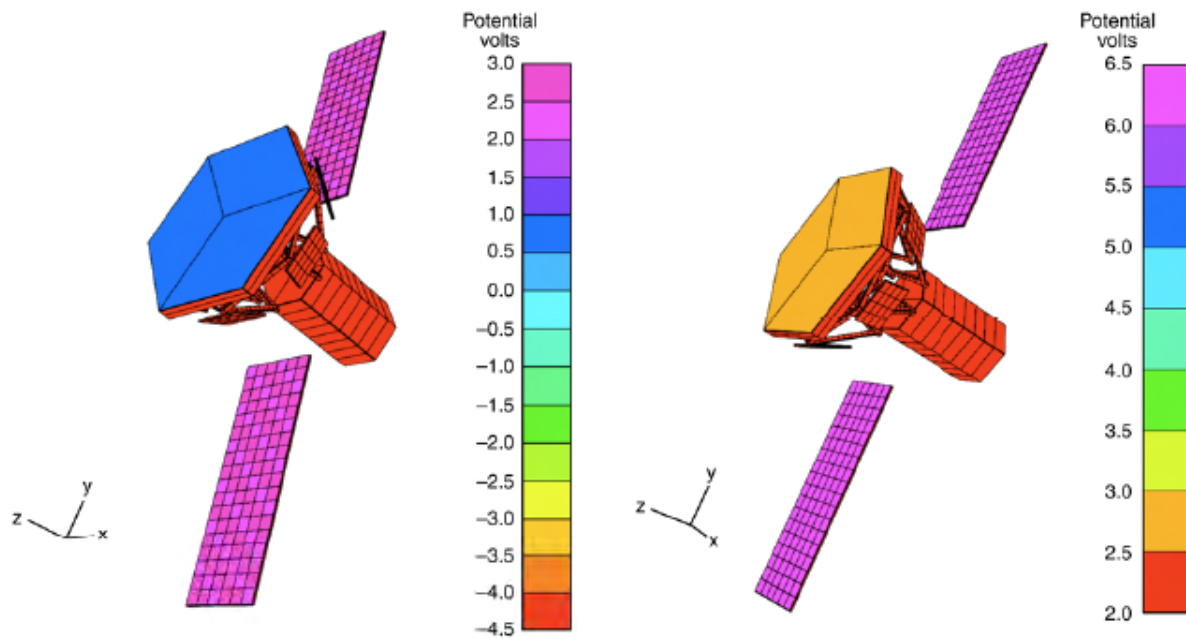


Figure B.2-1. Differential charging for Al_2O_3 (left) and PBN (right) at 0.1 AU.

Table B.2-1. Differential potentials for Al_2O_3 .

Trajectory point (AU)	Differential potential (V)
0.5	7
0.4	7.5
0.3	7
0.2	7
0.1	7.5
0.0443	3.8

Table B.2-2. Differential potentials for PBN.

Trajectory point (AU)	Differential potential (V)
0.5	7
0.4	7
0.3	6.5
0.2	7
0.1	4.5
0.0443	3.4

APPENDIX C

ACRONYMS AND ABBREVIATIONS

α	Absorptivity
ϵ	Emmissivity
AC	Alternating Current
ACE	Advanced Composition Explorer
AIU	Attitude Interface Unit
APL	The Johns Hopkins University Applied Physics Laboratory
AU	Astronomical Unit
BC	Bus Controller
BOL	Beginning of Life
BOM	Beginning of Mission
bps	Bits per Second
BaZP	Barium Zirconium Phosphate
C&DH	Command and Data Handling
C_3	Maximum Required Launch Energy
CBE	Current Best Estimate
C-C	Carbon–Carbon
CCSDS	Consultative Committee for Space Data Systems
CD	Coronal Dust Detector
CDPU	Common Data Processing Unit
CDS	Coronal Diagnostic Spectrometer on SOHO
CFDP	CCSDS File Delivery Protocol
CME	Coronal Mass Ejection
CONTOUR	Comet Nucleus Tour
COSPAR	Committee on Space Research
CTH	Coupled Thermodynamic and Hydrodynamic
DC	Direct Current
DPU	Data Processing Unit
DSAD	Digital Solar Aspect Detector
DSMS	Deep Space Mission System (formerly the Deep Space Network, DSN)
EISCAT	European Incoherent Scatter Radar
EIT	Extreme Ultraviolet Imaging Telescope on SOHO

EPI	Energetic Particle Instrument
ESA	European Space Agency
EUV	Extreme Ultraviolet
FAST	Fast Auroral Snapshot Explorer
FEA	Fast Electron Analyzer
FEM	Finite Element Model
FFT	Fast Fourier Transform
FIA	Fast Ion Analyzer
FIP	First Ionization Potential
FOV	Field of View
FPGA	Field-Programmable Gate Array
G&C	Guidance and Control
GCR	Galactic Cosmic Ray
GPHS	General Purpose Heat Source
GSFC	NASA Goddard Space Flight Center
HET	High-Energy Telescope
HGA	High-Gain Antenna
HI	Hemispheric Imager
I&T	Integration and Test
ICA	Ion Composition Analyzer
IEM	Integrated Electronics Module
IFE	Interplanetary Field Enhancement
IFM	Interplanetary Flux Model
IMU	Inertial Measurement Unit
IR	Infrared
IRAD	Independent Research and Development
ISEE	International Sun-Earth Explorer
JGA	Jupiter Gravity Assist
JHU/APL	The Johns Hopkins University Applied Physics Laboratory
JPL	Jet Propulsion Laboratory
kbps	Kilobits per Second
KSC	Kennedy Space Center
LASCO	Large Angle and Spectrometric Coronagraph on SOHO
LGA	Low-Gain Antenna
LOS	Line of Sight

LVPS	Low Voltage Power Supply
LWS	Living With a Star
MAG	Magnetometer
MDI	Michelson Doppler Interferometer
MESSENGER	MERcury Surface, Space ENvironment, GEochemistry, and Ranging
MET	Medium-Energy Telescope
MGA	Medium-Gain Antenna
MGS	Mars Global Surveyor
MIPS	Millions of Instructions per Second
MLI	Multilayer Insulation
MMRTG	Multi-Mission Radioisotope Thermal Generator
MSL	Mars Science Laboratory
N/A	Not Applicable
NASA	National Aeronautics and Space Administration
NEAR	Near Earth Asteroid Rendezvous
NGS	Neutron/Gamma Ray Spectrometer
NIST	National Institute of Standards and Technology
NRC	National Research Council
OSR	Optical Surface Reflector
PAF	Payload Attach Fairing
PBN	Pyrolytic Boron Nitride
PCI	Peripheral Component Interconnect
PDU	Power Distribution Unit
PHS	Primary Heat Shield
PNI	Probability of No Impact
PNP	Probability of No Penetration
PSE	Power System Electronics
PWI	Plasma Wave Instrument
QNS	Quasi-Thermal Noise Spectroscopy
RF	Radio Frequency
RHCP	Right Hand Circular Polarization
RHESSI	Reuven Ramaty High Energy Solar Spectroscopic Imager
R_J	Radius of Jupiter
rpm	Revolutions per Minute
R_S	Solar Radius

RT	Remote Terminal
RTG	Radioisotope Thermal Generator
RWA	Reaction Wheel
S/C	Spacecraft
S/N	Signal-to-Noise Ratio
SAIC	Science Applications International Corporation
SEC	Sun-Earth Connection
SEE	Space Environmental Effects
SEP	Solar Energetic Particle
SHS	Solar Horizon Sensor
SMEI	Solar Mass Ejection Imager
SOHO	Solar and Heliospheric Observatory
SPAS	Solar Probe Affiliated Scientist
SPDT	Single-Pole-Double-Throw
SPE	Solar Particle Event
SRG	Stirling Radioisotope Generator
SSPA	Solid-State Power Amplifier
SSR	Solid-State Recorder
STDT	Science and Technology Definition Team
STEREO	Solar-Terrestrial Relations Observatory
SUMER	Solar Ultraviolet Measurements of Emitted Radiation on SOHO
SWOOPs	Solar Wind Plasma Experiment on Ulysses
TCM	Trajectory Correction Maneuver
TGA	Thermal Gravimetric Analysis
TIMED	Thermosphere, Ionosphere, Mesosphere Energetics and Dynamics
TOF	Time of Flight
TPS	Thermal Protection System
TRACE	Transistion Region and Coronal Explorer
TRIO	Temperature Remote I/O
TSA	Transition Structure Assembly
TSS	Thermal Synthesizer Model
USO	Ultrastable Oscillator
UVCS	Ultraviolet Coronagraph Spectrometer on SOHO
VLBA	Very Long Baseline Array
XFER	Transfer